Age and Age Gradients in Pseudo-bulge Galaxies from CALIFA

Sandra Nogueira dos Reis
Astronomia
Departamento de Física e Astronomia
2014

Orientador
Jean Michel Gomes, Investigador, Centro de Astrofísica da Universidade do Porto

Coorientador
Polychronis Papaderos, Investigador Coordenador, Centro de Astrofísica da Universidade do Porto

U.PORTO

FACULDADE DE CIÊNCIAS
UNIVERSIDADE DO PORTO

Todas as correções determinadas pelo júri, e só essas, foram efetuadas.

O Presidente do Júri,

Porto, _____/_____/_____

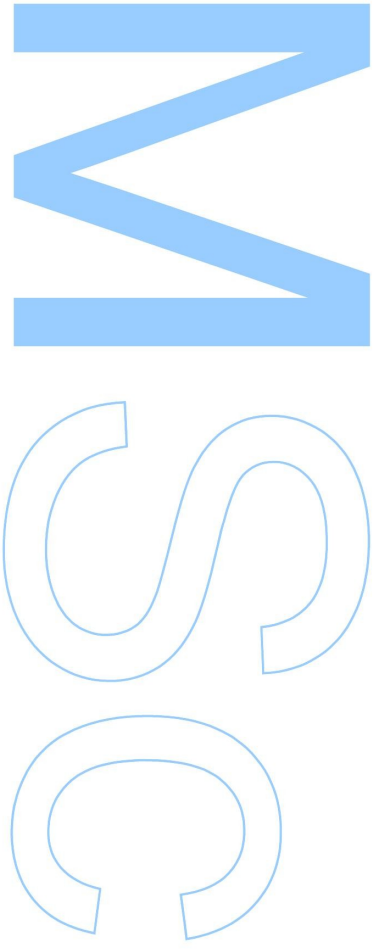

To my family, for their love and support.

Acknowledgements

I want to thank the guidance of both my supervisors, Dr. Jean Michel Gomes and PD Dr. Polychronis Papaderos, for their indispensable contribution, without which it would not be possible to complete this work. I also want to express my acknowledgement to the entire IA-CAUP team, specially to my friend and colleague Iris for all the assistance and support during the entire time framework.

I acknowledge funding from the FCT project *An exploration of the assembly history of galaxies with the novel concept of self consistent spectral synthesis* (FCOMP-01-0124-FEDER-029170 & PTDC/FIS-AST/3214/2012) and SELGIFS (Study of Emission Line Galaxies with Integral Field Spectroscopy) (P7-PEOPLE-2013-IRSES) project.

J.M. Gomes acknowledges support from the Fundação para a Ciência e a Tecnologia (FCT) through the Fellowship SFRH/BPD/66958/2009 and POPH/FSE (EC) by FEDER funding through the program Programa Operacional de Factores de Competitividade–COMPETE.

P. Papaderos acknowledges support from the Fundação para a Ciência e a Tecnologia (FCT) through the Investigador FCT Contract No. IF/01220/2013 and POPH/FSE (EC) by FEDER funding through the program Programa Operacional de Factores de Competitividade–COMPETE.

Abstract

This work is centered on the derivation of the age and radial age gradient in the stellar component of pseudo-bulges, using a new methodology that combines surface photometry and spectral synthesis. Using multi-band imaging data from the Sloan Digital Sky Survey (SDSS) for a sample of 66 nearly face on galaxies in the local universe, we have derived their surface brightness profiles and determined photometric and structural parameters of the (pseudo)bulge. Afterwards, Integral Field Spectroscopy (IFS) data from the Calar Alto Legacy Integral Field Area (CALIFA) Survey were modeled spaxel-by-spaxel with an in-house automated spectral synthesis pipeline Porto3D.

The photometric and structural analysis of the sample galaxies was performed with an in-house surface photometry code that permits derivation of surface brightness profiles, and their decomposition into the luminosity contribution of the (pseudo)bulge, disk and bar component. This code permits determination of several photometric parameters, such as the Sérsic index η, apparent and absolute magnitude of the structural components considered in the profile decomposition (bulge, disk and bar), the central surface brightness and exponential scale length of the disk, the mean surface brightness μ_{80} of the bulge within the radius enclosing 80% of its total luminosity and the effective radius $r_{\rm eff}$.

The spectroscopic data was modeled spaxel-by-spaxel with the aim of establish constraints on the age and star formation history of pseudo-bulges. The IFS data was processed with the automated spectral synthesis pipeline Porto3D, which enabled us, among other things, a spatially resolved determination of the luminosity- and mass-weighted stellar age (and metallicity) of the bulge and disk.

Following the considerations and defining criteria presented in Kormendy & Kennicutt (2004),

we conclude that only 3 out of 66 galaxies (NGC 5614, NGC 5656 and NGC 6004) have Sérsic index $\eta > 2$, being classified as classical bulges. It is worth pointing out that the surface brightness profile (SBP) decomposition carried out here explicitly includes the bar component in order to ensure a proper determination of the luminosity and structural properties of the bulge. Our spectroscopic analysis allowed us to determine the luminosity- and mass-weighted stellar ages within the bulge region, being 8.2 Gyr (σ=2.7 Gyr) and 10.1 Gyr (σ=1.7 Gyr), respectively. We further find that, with respect to their luminosity-weighted stellar age, pseudo-bulges are, on average, $\sim$2.7 Gyr older than the underlying disks. Another important conclusion drawn from this study is that the most massive and compact pseudo-bulges have formed the bulk of their stellar mass early on, whereas the less massive/compact ones are assembling over longer timescales. Interestingly, the mass-weighted age suggests significant growth of the stellar mass at a late cosmic epoch, being consistent with the secular evolution scenario. Our analysis also indicates that the age of pseudo-bulges tightly correlates with their stellar metallicity. Finally, the fact that our sample galaxies show in their majority negative age gradients in their pseudo-bulge component hints at an inside-out formation scenario.

Keywords

galaxy: spiral, galaxy: pseudo-bulge, galaxy: formation, galaxy: evolution, techniques: photometric and spectroscopic, Integral Field Spectroscopy, CALIFA

Resumo

Este trabalho é centrado na derivação de idades e gradientes radiais de idade na componente de pseudo-bojos, usando uma nova metodologia que combina fotometria de superfície e síntese espectral. Usando dados de imagem multi-banda do Sloan Digital Sky Survey (SDSS) para uma amostra de 66 galáxias no universo local, derivamos os seus perfis de brilho de superfície e determinamos parâmetros fotométricos e estruturais do (pseudo)bojo. Posteriormente, os dados de Espetroscopia de Campo Integral (IFS) do Calar Alto Legacy Integral Field Area (CALIFA) Survey foram modelados spaxel-a-spaxel com o código automatizado de síntese espectral, Porto3D, feito pela nossa equipa.

A fotometria e análise estrutural das galáxias da amostra foi realizada com um código da nossa equipa que permite a derivação de perfis de brilho de superfície, e a sua decomposição na contribuição de luminosidade dos componentes (pseudo)bojo, disco e barra. Este código permite a determinação de vários parâmetros fotométricos, tais como o índice de Sérsic índice η, magnitude aparente e absoluta das componentes estruturais consideradas na decomposição do perfil (bojo, disco e barra), o brilho da superfície central e o comprimento de escala exponencial do disco, a média da superfície de brilho μ_{80} dentro do raio que contém 80% da sua luminosidade total e o raio efetivo $r_{\rm eff}$.

Os dados espectroscópicos foram modelados spaxel-por-spaxel com o objectivo de estabelecer restrições sobre a idade e história de formação estelar de pseudo-bojos. Os dados IFS foram processados com o código automatizado de síntese espetral Porto3D, o que nos possibilitou, entre outras coisas, determinar espacialmente a idade (e metalicidade) estelar, ponderadas em luminosidade e em massa, do bojo e do disco.

Seguindo as considerações e critérios definidos por Kormendy & Kennicutt (2004), conclui-se

que apenas 3 das 66 galáxias (NGC 5614, NGC 5656 e NGC 6004) têm índice de Sérsic $\eta > 2$, sendo classificadas como tendo um bojo clássico. É importante salientar que a decomposição do perfil de brilho superficial (SBP) realizada aqui inclui explicitamente a componente da barra de modo a garantir uma correta determinação da luminosidade e propriedades estruturais do bojo. A nossa análise espectroscópica permitiu determinar as idades estelares, ponderadas em luminosidade e massa, dentro da região do bojo, sendo de 8.2 Gyr (σ=2.7 Gyr) e 10.1 Gyr (σ=1.7 Gyr), respetivamente. Encontramos ainda que, no que diz respeito à idade estelar ponderada em luminosidade, os pseudo-bojos são, em média, $\sim$ 2.7 Gyr mais velhos do que os discos subjacentes. Outra conclusão importante deste estudo é que os pseudo-bojos mais maciços e compactos formaram a maior parte da sua massa estelar mais cedo, ao passo que os menos massivos/compactos estão a formar-se em escalas de tempo mais longas. Interessante é que a idade estelar ponderada em massa sugere um significante crescimento da massa estelar numa época cósmica tardia, sendo consistente com o cenário de evolução secular. A nossa análise também indica que a idade dos pseudo-bojos está fortemente correlacionada com a sua metalicidade estelar. Por fim, o facto de que as galáxias da nossa amostra mostram, na sua maioria, gradientes de idade negativos na componente do pseudo-bojo, sugere um cenário de formação de dentro para fora.

Palavras chave

galáxia: espiral, galáxia: pseudo-bojo, galáxia: formação, galáxia: evolução, técnicas: fotometria e espectroscopia, Espectroscopia de Campo Integral, CALIFA

Contents

List of Figures

List of Tables

Chapter 1.

Introduction

The Universe emerged from a singularity giving rise to what is called today as the Big Bang. Then, the expansion of the Universe had begun, leading to the overall distribution of energy and matter we see today. As it expanded, the Universe progressively cooled, while the gravitational potential started to pull back together clumps of cold gas, until the first baryonic entities, i.e. the stars, appeared. These objects, together with gas, dust and dark matter, are responsible for the formation of the first galactic structures.

The study of the formation and evolution of galaxies is a keystone in astronomy and astrophysics to unravel the history of the Universe. In the last few years, with the advent of new astronomical instruments, such as the Integral Field Unit (IFU) spectrographs, much more powerful in terms of spatial and spectral resolution, we have entered a new prolific era in extragalactic astronomy, which aims at better understanding how galaxies form and evolve over cosmic time.

Since stars are the fossil records of successive star formation and chemical enrichment events in galaxies, we can use them as a proxy to better understand the evolution and formation of these systems. Unfortunately, the majority of galaxies that we observe cannot be resolved into individual stars, with a few exceptions in the Local Group (e.g., the Large and Small Magellanic Clouds, and a dozen of nearby dwarf spheroidals), where Color-Magnitude diagrams can be directly determined from Hubble Space Telescope (HST) data (see Figure 1.1). Therefore, one must rely on different methods that utilize the integrated (i.e. non-resolved) colors and spectra of the stellar component on spatial scales of typically hundreds pc^2, in order to reconstruct the star

formation history (SFH) of galaxies.

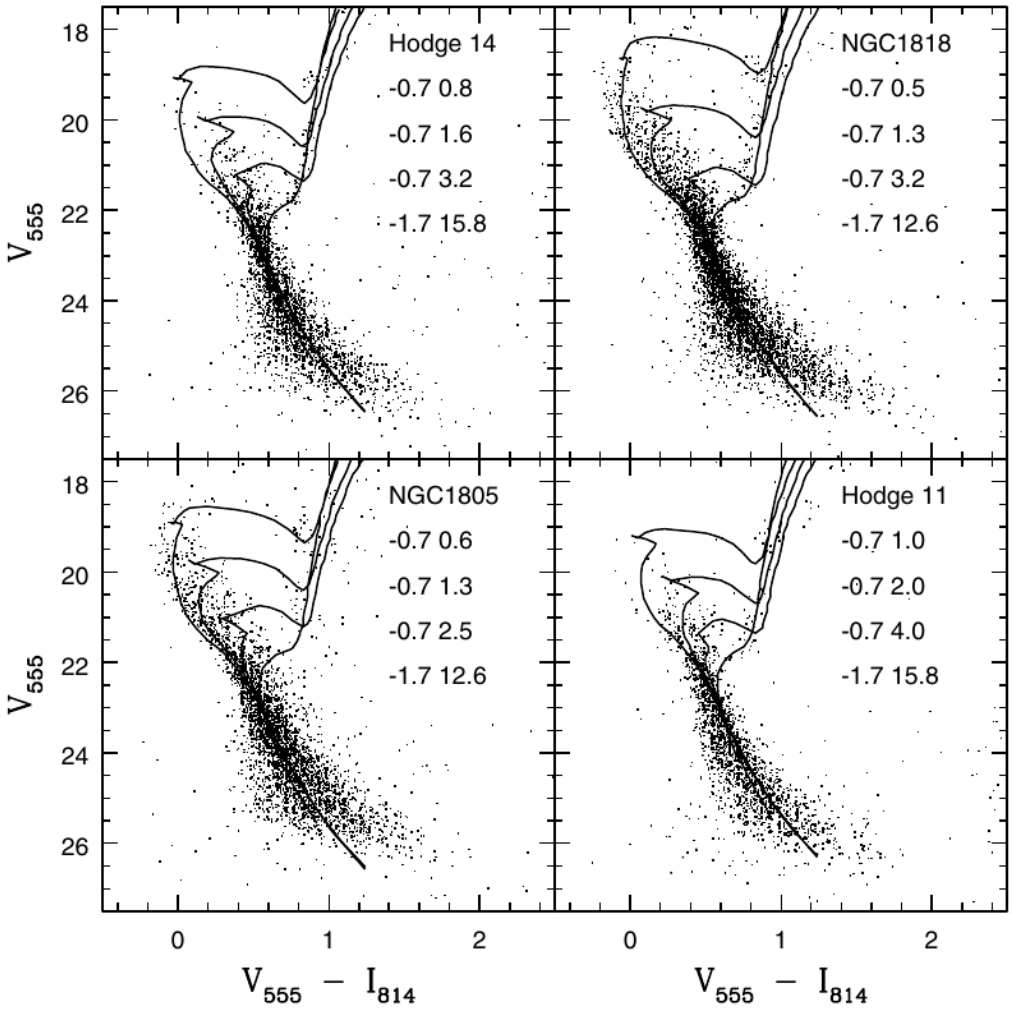

Figure 1.1: Color-Magnitude Diagrams of stellar clusters in the Large Magellanic Cloud, obtained through deep photometric measurements in the v and i bands with the Wide Field and Planetary Camera 2 on board of HST. The solid lines in each of the clusters (Hodge 14, NGC 1818, NGC 1805 and Hodge 11) represent isochrones referring to different metallicities (in units of $\left[\frac{Fe}{H}\right]$) and ages (in units of Gyr) (first and second column on the right-hand side of each diagram). Figure taken from Castro et al. (2001).

In this work, we use a combined methodology that takes advantage of surface photometry and spectral synthesis of stellar populations (to be briefly described in chapter 3). Our main motivation comes from studies of bulge formation in spiral galaxies, where classical bulges are thought to be formed in violent processes, such as mergers, whereas pseudo-bulges are built slowly via secular processes, as for example, disk instabilities or bar-driven inflow and collapse of gas. Our main goal is the determination of the age and age gradients in (pseudo)bulges using high-quality IFU data from the CALIFA survey (see `http://califa.caha.es` for details). This information is expected to offer new discriminators between pseudo-bulges and classical bulges, shedding light into the formation and evolution of these structures in galaxies.

1.1 MORPHOLOGICAL CLASSIFICATION OF GALAXIES

In 1936, Edwin Hubble set out a classification scheme for galaxies by means of their visual appearance, i.e. morphology. His new system considered three main group of galaxies: ellipticals (E), spirals (S) and lenticulars (S0) (see Figure 1.2). A fourth class of galaxies that did not fit into this scheme are irregulars (Irr), which do not show any regular, axis-symmetric shape.

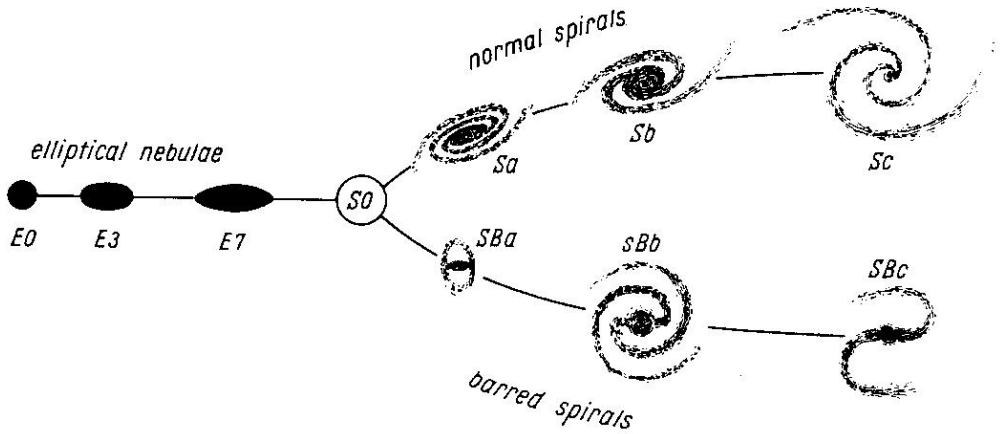

Figure 1.2: Hubble's tuning fork diagram. Three main branches of galaxies are depicted: one in the left containing elliptical (E) galaxies and the other two in the right for spiral (S) galaxies unbarred (top) and barred (bottom). Lenticular galaxies (S0) are placed in the node that connects, from left to right, early-type to late-type systems. Figure taken from *Realm of the Nebulae* (Hubble 1936).

Elliptical galaxies have approximately ellipsoidal smooth shapes and are preferentially found in clusters of galaxies. They don't have much substructure and are generally lacking cool gas, which means that they have very low, if any at all, ongoing star-forming activity. Several recent studies, using IFU data (see, e.g., Sarzi et al. (2010) and references therein) confirm in a very quantitative and precise way that stellar kinematics in ellipticals are dominated by random motions, with little rotational support in most cases.

Spiral galaxies are characterized by a thin, rotationally-supported disk, and a central concentration of stars known as the bulge. Their bright spiral arms are outlined by young and hot O and B stars, as well as ionized gas and dust. Many spiral and lenticular galaxies show a bar component (SB and SB0, respectively).

Lenticular galaxies are disk galaxies with a high Bulge/Disk ratio and little ongoing star formation, as compared to normal spiral galaxies (Johnston et al. 2012). These galaxies are generally regarded as a transition class between ellipticals and spirals.

The Hubble classification was later on extended by de Vaucouleurs (1959), who realized that features, such as rings are also important morphological indicators of galaxies. The classification scheme devised by de Vaucouleurs for late-type galaxies therefore complements Hubble sequence, taking into account not only the presence and prominence of spiral arms and bars, but also rings.

Often in extragalactic studies the term Early- and Late-Type galaxies is used to reflect the left and right part of the diagram in Figure 1.2, respectively. This is because, erroneously, there was a widespread belief that these two classes represent different stages of a galaxy evolutionary sequence. This study – ages and age gradients in (pseudo)bulges – is obviously closely linked to our understanding of galaxy formation and evolution.

1.2 SURFACE PHOTOMETRY

The understanding of the formation and evolution of galaxies requires quantitative information on the photometric properties of their structural parameters (i.e., disk, bar and bulge components). The technique of measuring the electromagnetic radiation emitted by point-like and extended celestial sources is called photometry.

In 1948, de Vaucouleurs stated the necessity to go beyond a visual representation of galaxies and obtain quantitative measurements of their light distribution. He obtained a law describing how the surface brightness profile I of an elliptical galaxy varies as a function of the galactocentric radius r:

$$\ln I(r) = \ln I_0 - kr^{1/4} \tag{1.1}$$

with k being a constant. However, measuring the size of a galaxy is not an easy task because it is not clear where the galaxy ends. Therefore, by convention, galaxy sizes are specified by a scale length that describes how sharply the light of a galaxy decreases with r. Another widely used measure of galaxy sizes is based on the effective radius $r_{\rm eff}$, i.e. the radius enclosing half of the

total luminosity of a galaxy. With this new parameter it is possible to rewrite de Vacouleurs' law as

$$\ln I(r) = \ln I_{\rm eff} + 7.669 \left[1 - \left(\frac{r}{r_{\rm eff}} \right)^{1/4} \right] \tag{1.2}$$

where $I_{\rm eff}$ is the intensity at $r_{\rm eff}$. Figure 1.3 shows an example of a profile with de Vaucouleurs' law (also referred to as the $r^{1/4}$ law).

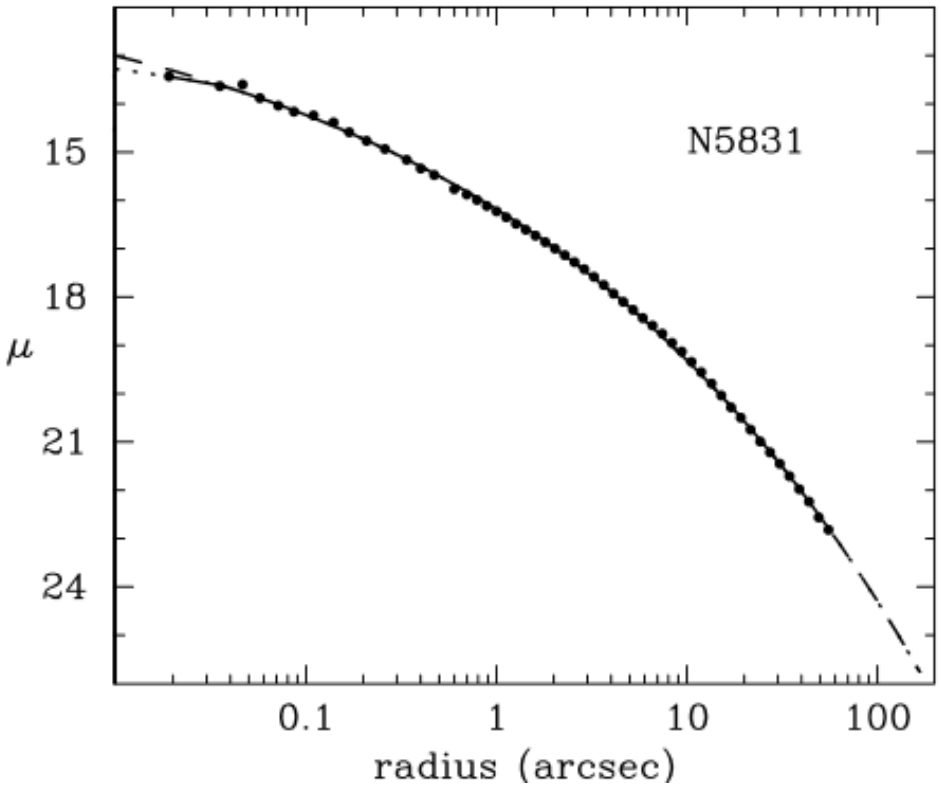

Figure 1.3: Example of the surface brightness profile of an elliptical galaxy (NGC 5831). The solid line represents the fit using an empirical model, with inner and outer extrapolations indicated by the dotted extensions. The profile is approximated by the de Vaucouleurs' law. Figure taken from Graham et al. (2003).

In 1963, José Luis Sérsic published a generalization of the de Vaucouleurs' law. His $r^{1/\eta}$ model has the form

$$I(r) = I_{\rm eff} \exp \left\{ -b_\eta \left[\left(\frac{r}{r_{\rm eff}} \right)^{1/\eta} - 1 \right] \right\} \tag{1.3}$$

with b_η being a parameter coupled to the Sérsic index or *shape parameter* η (Sérsic 1963). Figure 1.4 presents the variation of galaxy intensity profiles for different indices η.

Setting the Sérsic index to $\eta = 1$ gives an exponential profile, which is commonly assumed to describe spiral galaxy disks (Figure 4.8), whereas a $\eta = 4$ yields the de Vaucouleurs's law.

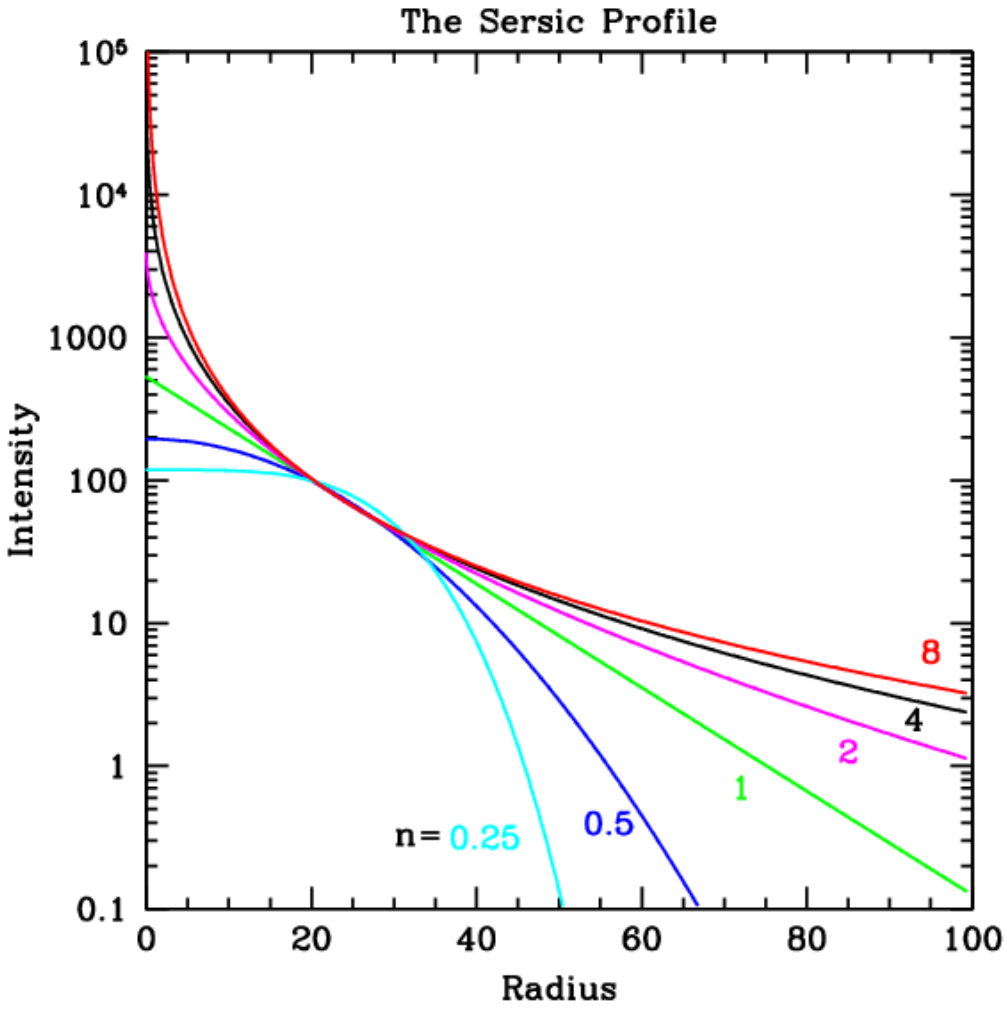

Figure 1.4: Sérsic intensity distributions for different Sérsic exponents η (from 0.25 to 8). Figure taken from Peng et al. (2010).

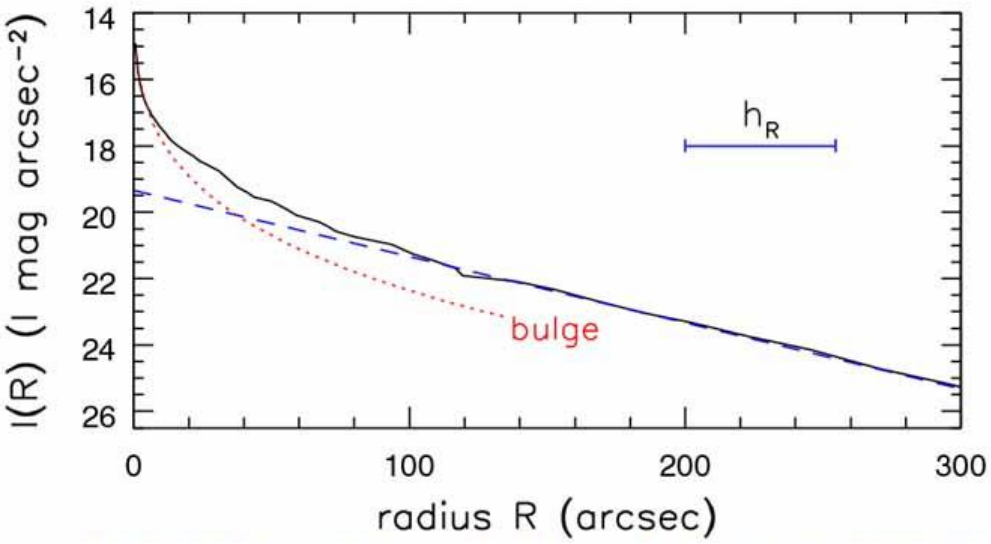

Figure 1.5: Example of a disk profile - exponential (η=1). The solid line represents the surface brightness in the I band, the dashed line shows the exponential fit to the disk-dominated outer part of the galaxy and the dotted line shows a Sérsic fit to the emission in excess to the disk. The exponential scale length h_R of the disk is depicted by the horizontal bar. Figure taken from *Galaxies in the Universe* (Sparke & Gallagher 2007) (Credits: R. Peletier).

Another useful quantity is the bulge-to-total light ratio B/T, which can be determined from the total (Sérsic-model dependent) luminosity of the bulge and the disk. This ratio shows a clear trend with the Hubble type, increasing from late-type towards early-type galaxies.

1.3 SPIRAL GALAXIES: BULGES

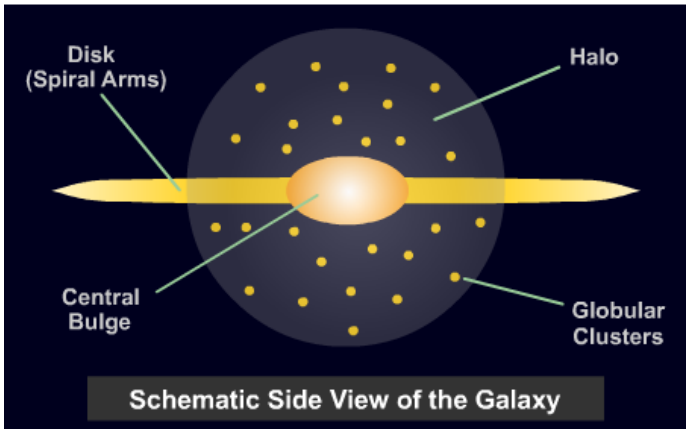

Figure 1.6: Basic structure of a late-type galaxy, as viewed edge-on. The main components are the disk (containing gas, dust and stars), the central concentration of stars known as the bulge, and the halo of stars and clusters. Note that the galactic halo extends beyond the disk, however, for representation purposes, it is shown in the figure smaller than the spiral arms. (Credits: Jones and Lambourne, 2003).

Bulges are often referred as a densely packed stellar system found in the center of spirals and lenticulars. When seen edge-on they can appear as round ellipsoids, as flattened (like bright central disks), or as bar-like.

Historically bulges were thought to have a common sense of rotation about the center and weren't expect to rotate very fast. However, high-resolution data have shown that many bulges rotate rapidly and are of comparable thickness to disks. Thus, today is thought that there are at least two kinds of bulges: classical elliptical-like bulges, and pseudo or disk-like bulges.

Classical Bulges

According to our current understanding, classical bulges have similar properties to elliptical galaxies (Renzini 1999) and are formed through violent and rapid processes, such as mergers (Eggen et al. 1962). Since these bulges have almost no ongoing star formation, they are mainly composed by a population of old stars, which is reflected on red broadband colors. The stars

are densely packed and have dispersed orbits probably due to violent relaxation associated with mergers, which are thought to be responsible for the formation of the bulge (Bender et al. 1992). In this scenario, classical bulges are expect to show little or no rotation.

These bulges have typically more concentrated surface brightness profiles, with a Sérsic index $\eta \geq 4$ (Drory & Fisher 2007). As one can see from the equation 1.3, the surface brightness is supposed to increase to the center, and thus the volume density of the stars would grow, packing them into a high-surface brightness nucleus. There is also a correlation between the bulge Sérsic index and the bulge-to-total ratio (Fisher & Drory 2008).

The majority of bulges are also consistent with the Faber-Jackson relation (Faber & Jackson 1976), which correlates the total luminosity L with stellar velocity dispersion $\sigma_\star$ as $L \propto \sigma_\star^4$. Although this power-law was first described for elliptical galaxies, one can use it also for classical bulges of disk galaxies.

Another discriminator proposed by Kormendy & Kennicutt (2004) is the bulge-to-total luminosity ratio of a galaxy. Whenever we have $1/3 \lesssim B/T \leqslant 1/2$, it can be concluded that it contains a classical bulge.

Pseudo-bulges

The development of technology has allowed astronomers to obtain high-resolution data, revealing that many bulges have properties similar to disk galaxies (Kormendy & Illingworth 1982). These bulges tend to be rotationally supported, and some show recent star formation (Kormendy & Kennicutt 2004). Sometimes they can be overimposed on bars and/or contain star-forming rings and/or spiral features (see, e.g., Kehrig et al. (2012)).

Theories for the formation of pseudo-bulges are more uncertain than those for classical bulges. Pseudo-bulges may be formed by a combination of different phenomena, such as for example, gravitational instabilities (Genzel et al. 2008, Bournaud et al. 2014), or gas inflow to galaxy centers and ensuing star formation in the course of galaxy secular evolution (Kormendy & Kennicutt 2004). The scenario that is investigated in this work is related with the one proposed by Kormendy & Kennicutt (2004), where secular processes are responsible for the formation of pseudo-bulges. This scenario involves disk instabilities and bar-driven gas inflows towards the center of the galaxy.

Based on integral optical colors (i.e. an estimate of the age of stellar populations in galaxies), Strateva et al. (2001) found a separation into a red and blue sequence for early and late-type galaxies, respectively. From this, one can expect that pseudo-bulges have younger and bluer stars than classical bulges. Kormendy & Kennicutt (2004) emphasizes that, although it is expected that stellar population ages of pseudo-bulges have a range between $\sim 0-5$ Gyr (Bouwens, Cayón & Silk 1999), one should not disregard the presence of an underlying older stellar population.

Kormendy & Kennicutt (2004) suggest that a pseudo-bulge has to show at least one feature among the following ones:

- Have disk morphology, like, e.g., embedded spiral arms.
- Contain a nuclear bar (in nearly face-on galaxies).
- Be box-shaped (in edge-on galaxies).
- Have a Sérsic index $\eta \lesssim 2$.
- Show on-going star formation, with no signs of recent mergers.
- Have stellar kinematics dominated by rotation with a large ratio $V_{\max}/\sigma$ of circular to random motion and a comparatively low velocity dispersion.
- Fall below the Faber-Jackson relation (Faber & Jackson 1976).

In photometric studies of large galaxy samples the simplified notion that the Sérsic index is in itself enough to clearly distinguish between classical and pseudo-bulges has received significant popularity. On the other hand, there is an ongoing debate among astronomers regarding the key criteria for distinguishing pseudo-bulges from classical bulges. As Kormendy & Kennicutt (2004) warn, it is important to verify that at least one, preferably several, of the above characteristics are evident for a safe identification of pseudo-bulges.

1.4 INTEGRAL FIELD SPECTROSCOPY

Traditional long-slit spectroscopy allows studies of galaxies only within the narrow strip that is mapped by the slit aperture. However, this technique is not efficient for all applications because it

lacks the necessary spatial resolution for an extended object. Obviously, the ideal case is to have a spectrum from each part of an extended extragalactic object.

The technique used to obtain spectra from each part of an object simultaneously is called Integral Field Spectroscopy (IFS). It divides the 2-dimension region of the sky into a nearly continuous array by means of: lenslet array, fibres (with or without lenslets), and image-slicer (see Figure 1.7). From IFS observations is generated a data cube containing many "images" (spatial pixels or spaxels) of the same part of the sky, each at a different wavelength.

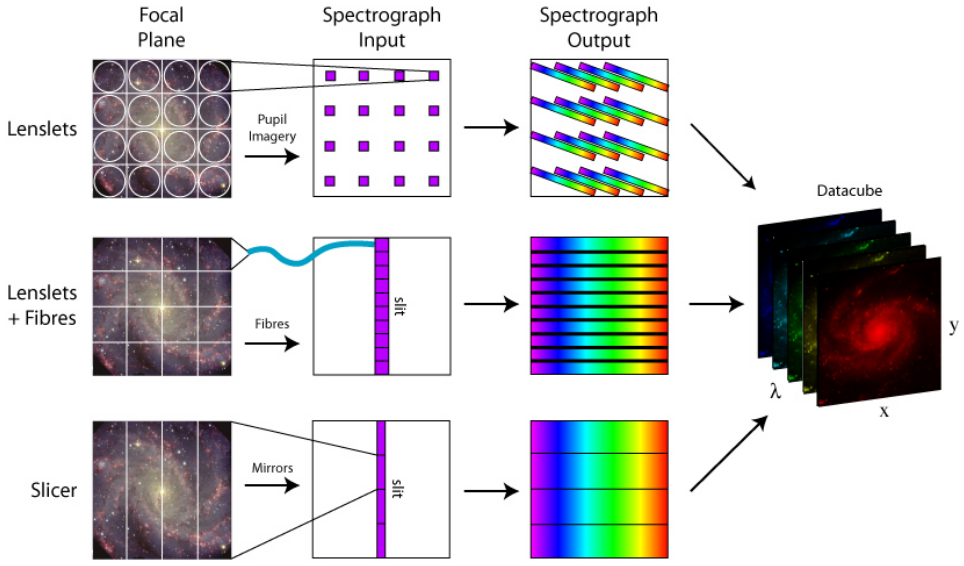

Figure 1.7: The three designs for achieving IFS. Credit: Westmoquette et al. (2009), adapted from Allington-Smith et al. (1998).

1.5 STELLAR POPULATIONS AND AGE GRADIENTS

During the WWII, Baade (1944) took advantage of the dark night sky to resolve, for the first time, stars of M31 and its companions, M32 and NGC 205, adding a new concept of populations of stars as building blocks of galaxies. He noted that the morphological classification of galaxies by Hubble (1936) required different relative contributions of distinct stellar populations. Following this concept, the building blocks of galaxies can be thought as a collection of distinct instantaneous bursts of stars with the same age and metallicity, i.e. Simple Stellar Populations (SSPs). The relative number of stars formed in each instantaneous burst is directly dependent on the assumed initial mass function (IMF). The latter describes the mass distribution of stars in a given burst.

Mathematically, one can derive a SSP spectrum by applying the following equation:

$$\text{SSP}(\lambda, t_\star, Z_\star) = \int_{M_{low}}^{M_{upp}} I^\star(\lambda, m_\star, t_\star, Z_\star)\phi(m_\star)dm_\star \tag{1.4}$$

where, $\phi(m_\star)$ gives the initial mass distribution of stars in a given burst, M_{low} and M_{upp} are, respectively, the lower and upper mass cutoff of the IMF and $I^\star(\lambda, m_\star, t_\star, Z_\star)$ is the spectrum, taken from a library of stars, that depends on the wavelength λ, the stellar mass $m_\star$, the age of the star $t_\star$ and the corresponding metallicity $Z_\star$.

A collection of SSPs can be used to derive the star formation history (SFH) of a galaxy by means of approximating the galaxy's spectrum by a linear combination of $N_\star$ SSPs. Therefore, the composite stellar population can be written as:

$$F(\lambda) = F(\lambda_0)\sum_j^{N_\star} x_j \times \frac{\text{SSP}(\lambda, t_{\star,j}, Z_{\star,j})}{\text{SSP}(\lambda_0, t_{\star,j}, Z_{\star,j})} \tag{1.5}$$

where, x_j is the fractional contribution of SSPs at the normalization wavelength λ_0, $F(\lambda_0)$ is a normalization constant whereas $\text{SSP}(\lambda, t_{\star,j}, Z_{\star,j})$ stands for the spectrum of a simple stellar population and $\text{SSP}(\lambda_0, t_{\star,j}, Z_{\star,j})$ is the value of the SSP flux at the normalization wavelength λ_0.

From spectral fitting one can obtain stellar ages radial profiles and age gradients. The latter provide a way of studying galaxy formation (inside-out vs outside-in galaxy formation). In this work a gradient is defined as the slope of a fitted linear regression to radial profiles, indicating how the age changes as a function of galactocentric radius.

1.6 OUTLINE OF OUR STUDY

There are so far very few spatially resolved studies of stellar populations of galaxies with IFS, which renders statistical statements on age gradients in pseudo-bulges very uncertain. In the present work we follow the perspective of Kormendy & Kennicutt (2004), classifying pseudo-bulges as the ones with Sérsic index $\eta \lesssim 2$ and verifying the bulge-to-total light ratios between 1/3 – 1/2, then studying their main properties and estimating their physical parameters. This investigation can lead to a better understanding of formation and evolution of galaxies in general,

for instance on how pseudo-bulges are buildup over several Gyrs of secular galactic evolution, as well as whether they form in an inside-out or outside-in mode.

To conduct this study we make use of late-type galaxies from the CALIFA Survey (Sánchez et al. 2012, Walcher et al. 2014). This work is organized as follows: Chapter 2 describes the selection criteria to build our sample and present it. Chapter 3 is divided in two sections, being detailed our methodology that combines surface photometry and spectral synthesis. Chapter 4 is divided in three Sections, being Section 4.1 relative to the results from the photometric technique and Section 4.2 to the results from spectroscopy, whereas Section 4.3 provides a discussion of the age behavior with other physical quantities. Finally, in Chapter 5 we briefly comment the main results and conclusions from this study.

Additionally, we supplement this work with two Appendices: Appendix A presents the color maps computed for our entire sample, and Appendix B displays all the age maps and radial profiles.

Chapter 2.

Sample Selection and Data Characterization

The observational data used in this work is from Calar Alto Legacy Integral Field Area (CALIFA) Survey, which currently comprises a sample of 426 galaxies in the local universe ($0.005 < z < 0.03$), observed with an Integral Field spectroscopy Unit (IFU) in order to obtain spatially resolved spectral information. When complete, the Survey will have 600 observed galaxies. The CALIFA sample takes advantage of a large hexagonal field of view (FoV > 1 arcmin^2), observed with the Potsdam Multi Aperture Spectrophotometer (PMAS) spectrograph in the PPak-mode (Roth et al. 2005, Kelz et al. 2006), mounted at the 3.5m telescope at the Calar Alto Observatory. For each galaxy of the sample, there are two overlapping versions of CALIFA IFS data cubes: an high (V1200) and a low resolution mode (V500), with a spectral coverage between $3700 - 7500$ Å, which were processed with the CALIFA IFS reduction pipeline (Sánchez et al. 2012). In our data analysis we used the low resolution V500 data cubes in order to cover the entire optical spectral range.

We have selected 66 out of 337 targets already observed at that time with the CALIFA IFU Survey. The corresponding images were taken from the Sloan Digital Sky Server (SDSS; (York et al. 2000)) Data Release (DR) 7 (Abazajian et al. 2009).The SDSS is one of the most successful surveys in astronomy, having created three-dimensional maps of the Universe with images of more than a quarter of the entire sky, and the data is made available for the public in annual releases. The SDSS uses the 2.5 meter telescope that is located at Apache Point Observatory, in New Mexico, and it is equipped with two instruments: a 120-megapixel imaging camera and a

pair of optical fiber spectographs (Gunn et al. 2006).

To build the sample for this work, we primarily choose galaxies morphologically classified as disk galaxies, since our targets of study are galaxy pseudo-bulges. The morphological classification was performed using a visual analysis of the data images. After this preliminary selection and, in order to reduce biases due to intrinsic extinction within the disk, we visually selected low-inclination galaxies (nearly face-on). Then, all galaxies which presented recent signs of interaction were excluded, in order to avoid complex SBPs for the decomposition into bulge, disk and bar. Finally, galaxies with a clear evidence for an Active Galactic Nucleus (AGN) using classical diagnostic diagrams (Baldwin, Phillips & Terlevich 1981) were also excluded from our sample due to the uncertainties in the spectral fitting.

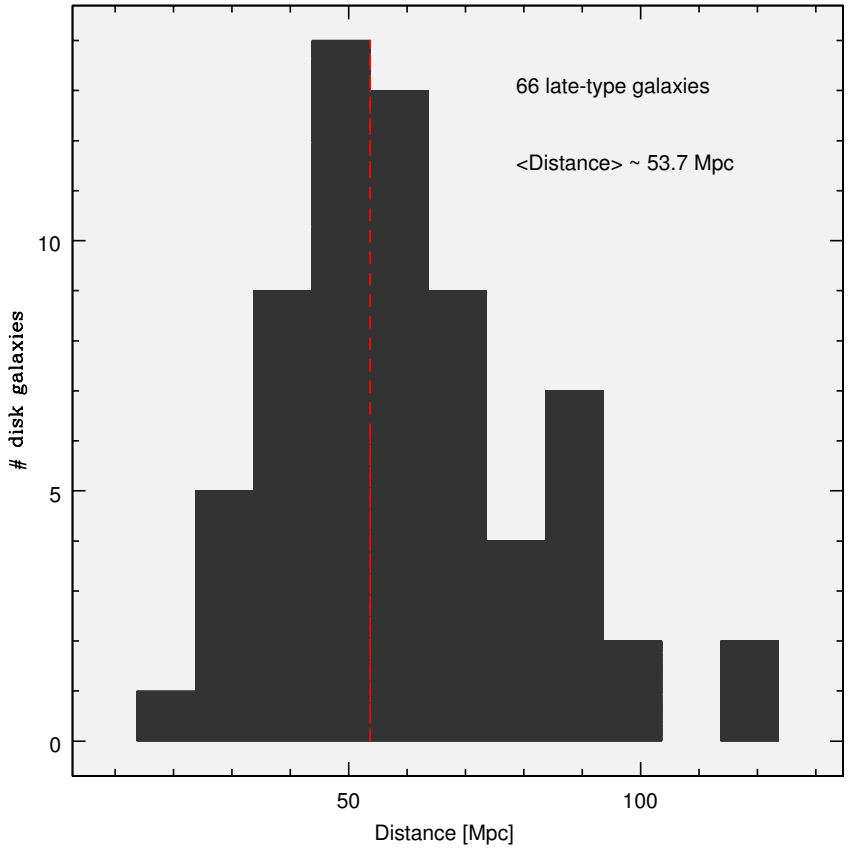

Figure 2.1: The histogram in grey color shows the distance distribution for our sample of 66 late-type galaxies, in units of Mpc. Combining the large FoV of CALIFA (> 1 arcmin^2) and the average distance of our galaxy sample, we can conclude that almost the full extend of our galaxies is spatially covered by the IFU, which is crucial for the precise derivation of radial profiles and age gradients.

With these selection criteria, we obtained a sample of 66 late-type galaxies, which are relatively nearby ($\sim$50 Mpc), as shown in Figure 2.1. Table 2.1 specifies the sample according to the

NASA/IPAC Extragalactic Database (NED)[1]. This table presents the name of the galaxy, relevant surveys that observed it, right ascension, declination, redshift, distance (Mpc), morphological classification, activity type, inclination (degrees), median ellipticity, foreground Galactic extinction in the V-band (mag), and computed absolute magnitude in the r-band.

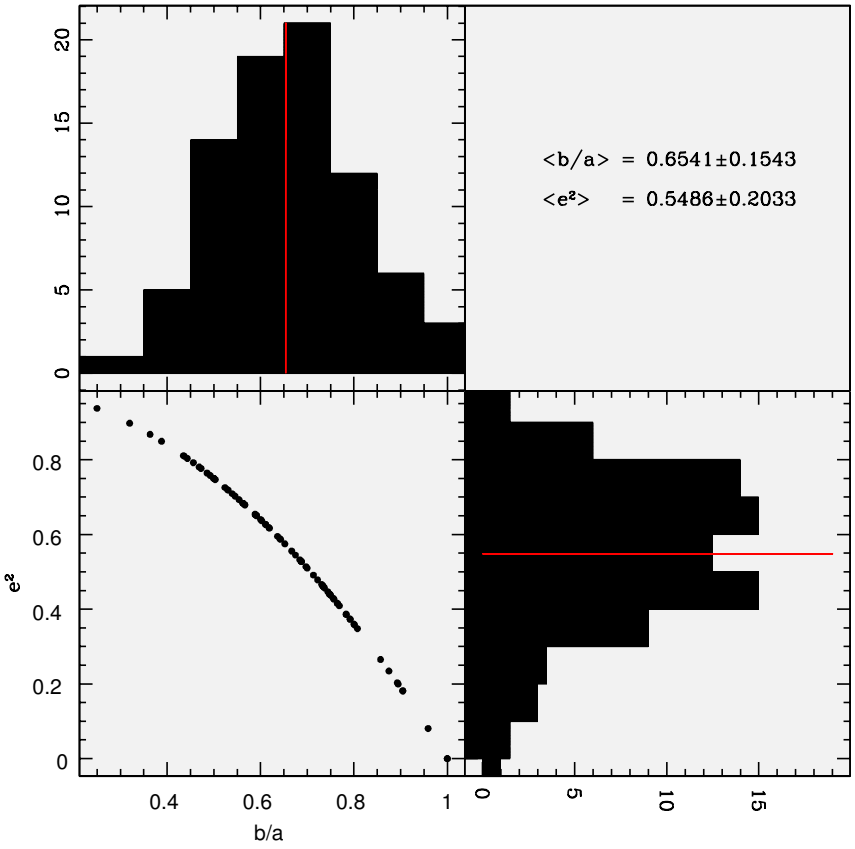

Figure 2.2: Top left panel: Histogram of b/a ratio. Top right panel: Mean values and standard deviation for the b/a ratio and the median ellipticity. Bottom left panel: b/a ratio as a function of the median ellipticity ε^2. Bottom right panel: Histogram of the median ellipticity. The solid red line refers to the mean value, which corresponds to 0.6541 ± 0.1543 for the b/a ratio and to 0.5486 ± 0.2033 for the median ellipticity.

The inclination i angle (in degrees) was derived with the following equation:

$$\cos^2 i = \frac{1 - q^2 - \varepsilon^2}{1 - q^2} \tag{2.1}$$

assuming $q = 0.13$ as an intrinsic ellipticity for disk galaxies (Giovanelli et al. 1995, 1997), and

[1]The NASA/IPAC Extragalactic Database (NED) is operated by the Jet Propulsion Laboratory, California Institute of Technology, under contract with the National Aeronautics and Space Administration.

where ε is the median ellipticity, defined as:

$$\varepsilon^2 = 1 - \left(\frac{b}{a}\right)^2 \tag{2.2}$$

being a and b the observed semi-major and semi-minor axes of the ellipse, respectively. Figure 2.2 shows the histograms of the median ellipticity and the b/a ratio, with the solid red line corresponding to the mean values. As expected, there is an inverse quadratic dependence between both values.

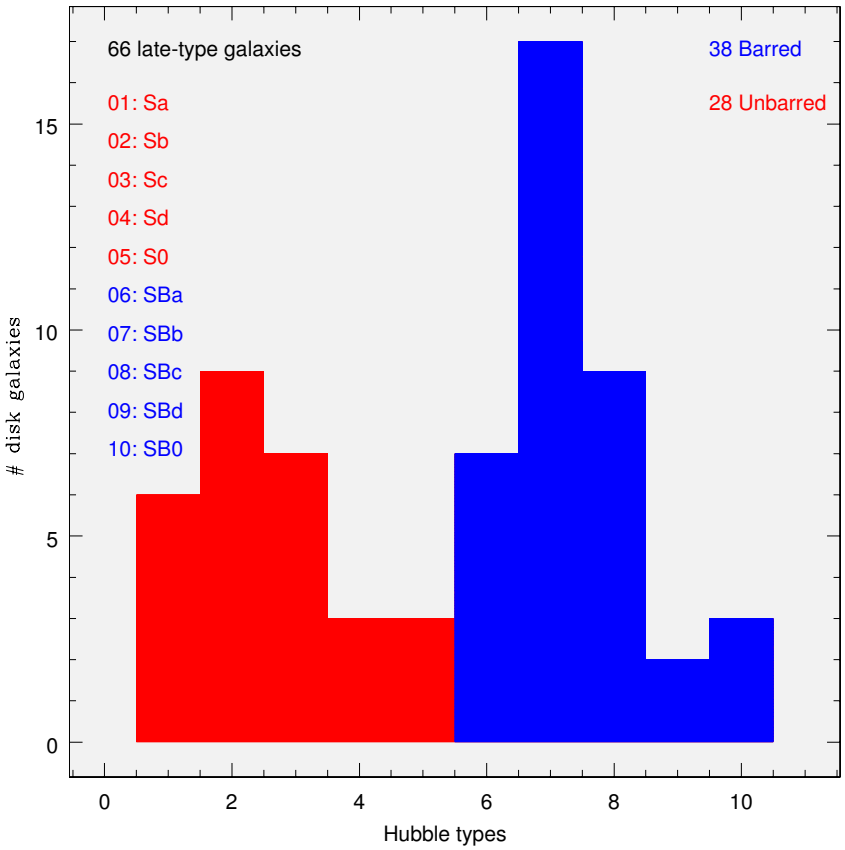

Figure 2.3: Histogram showing the different simplified Hubble-types of our sample. Blue color refers to galaxies classified with a bar, whereas red color correspond to unbarred galaxies. On the left side of the histogram is detailed the simplified morphological classifications, both for barred and unbarred galaxies.

To better visualize the morphological distribution of our sample, and since NED has a complex classification, we plot, in Figure 2.3, the histograms related to the different and simplified Hubble-types present in our sample. Furthermore, we have divided our sample in two main types: barred and unbarred galaxies. This subdivision was made according to the family classifications of Buta (2011), without concerning the stages. On one side we have the spiral unbarred galaxies (SA); on

the other side we have the spiral barred galaxies (SB), which include not only the barred galaxies, but also the intermediate cases (SAB).

Figure 2.4 displays five different random galaxies of our sample, with the remaining images of our sample included in Appendix A. For each galaxy there are four images: a) true-color image; b) logarithmic mean of the three SDSS filters gri; c) color map $r - i$; d) color map $g - r$. The blue/black bottom line in the figures represents 10 kpc. On the top of each figure one can find the name of the galaxy, NED's morphology, distance (Mpc), apparent magnitude (mag) and absolute magnitude in the SDSS r-band (mag).

The true-color images were generated with the Lupton et al. (2004) algorithm, that combines Red-Green-Blue (RGB) figures. To compute these true-color images we consider that $R = f(r)$, $G = f(g)$ and $B = f(b)$, where

$$f(x) = \begin{cases} 0 & x < m \\ \log_{10}(xm)/\log_{10}(Mm) & m \leq x \leq M \\ 1 & M < x \end{cases}$$

being m and M the minimum and maximum values to display, respectively. In order to avoid white pixels for values greater or equal to M it is imposed that $R = r * f(I)/I$, $G = g * f(I)/I$ and $B = b * f(I)/I$, where $I \equiv (r + g + b)/3$.

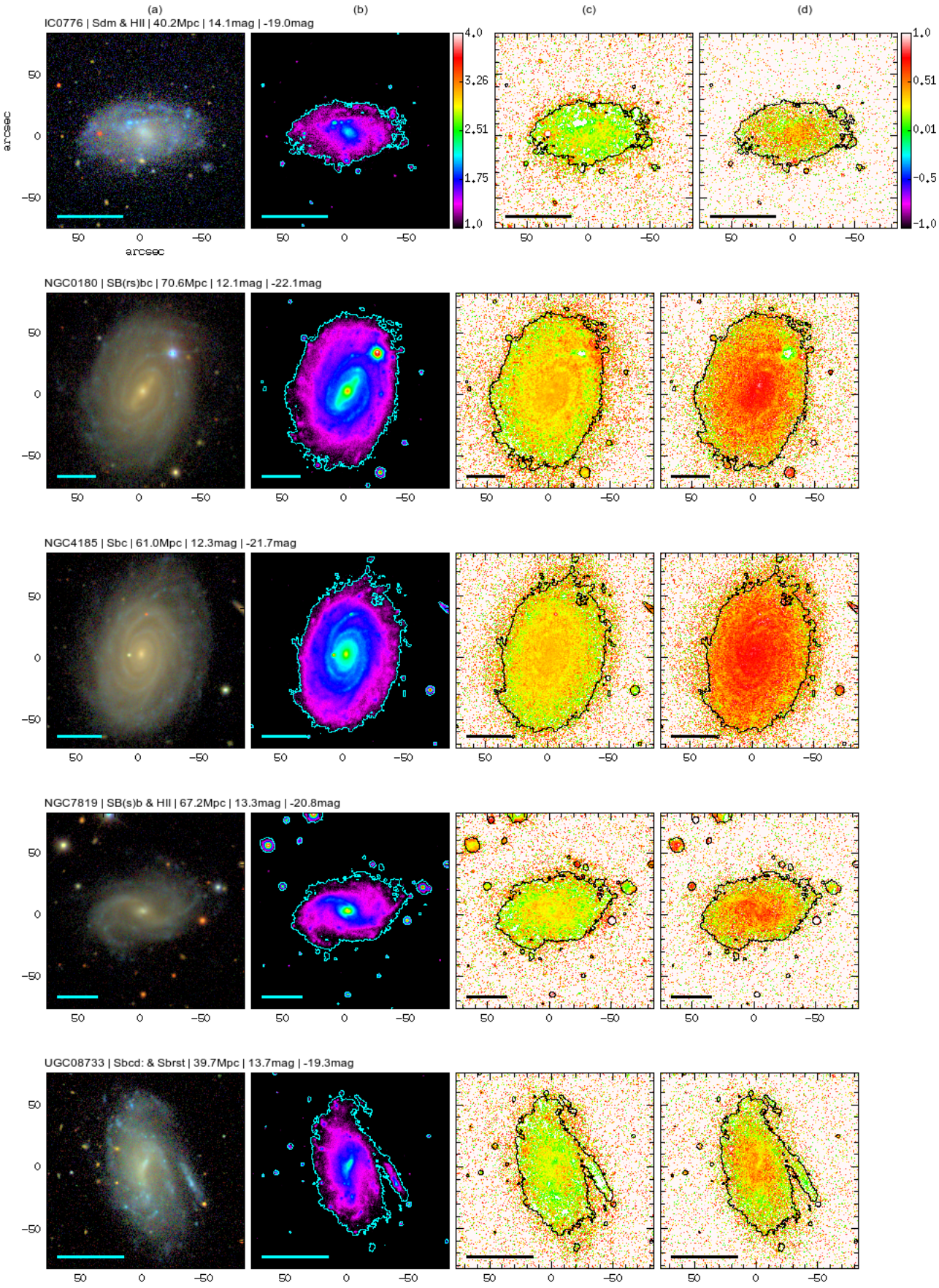

Figure 2.4: Five different random galaxies of our sample, showing: a) true-color RGB image; b) logarithmic mean of the SDSS filters gri; c) color map $r - i$; d) color map $g - r$. From the top to the bottom: IC0776, NGC0180, NGC4185, NGC7819 and UGC08733.

Table 2.1: Specifications of the galaxies in our sample, obtained in the NED Database: galaxy name, relevant surveys, right ascension, declination, redshift, distance (Mpc), morphological classification, activity type, inclination (degrees), median ellipticity, foreground galactic extinction in the V-band (mag), and total absolute magnitude in the r-band (mag).

Galaxy	Surveys	RA	DEC	z	Distance	Morph. Class.	Activity	Inclination	ε^2	Gal. Ext. V-band	r-band Abs. mag
IC0776	HIPASS J121ALFA 3-21	12h19m02.90s	+08d51m22.0s	0.008232	40.20	Sdm	HII	62.76	0.6265432099	0.06	-18.96
IC1256	KIG; UZC	17h23m47.31s	+26d29m11.5s	0.015778	72.10	Sb	-	59.78	0.52734375	0.13	-21.15
IC4566	USGC	15h36m42.16s	+43d32m21.6s	0.01926	86.30	Sab	-	59.23	0.51	0.07	-21.71
NGC0001	ALFALFA; KPG	00h07m15.84s	+27d42m29.1s	0.015177	61.60	SA(s)b:	-	56.79	0.4375	0.17	-21.43
NGC0023	ALFALFA; KUG	00h09m53.41s	+25d55m25.6s	0.015231	61.70	SB(s)a	Sbrst	62.48	0.6167800454	0.11	-22.28
NGC0160	UZC	00h36m04.06s	+23d57m28.4s	0.017525	70.50	(R)SA0$^+$ pec	-	64.22	0.6788888889	0.09	-21.96
NGC0165	NVSS	00h36m28.92s	-10d06m22.2s	0.019617	78.90	SB(rs)bc	-	56.41	0.4267346939	0.10	-21.35
NGC0171	HIPASS; VV	00h37m21.53s	-19d56m03.3s	0.013043	52.80	SB(r)ab	-	45.01	0.1814058957	0.06	-21.67
NGC0180	HIPASS	00h37m57.70s	+08d38m06.7s	0.017616	70.60	SB(rs)bc	-	54.41	0.3732638889	0.15	-22.11
NGC0214	ALFALFA; CXO	00h41m28.03s	+25d29m58.0s	0.015134	61.00	SAB(r)c	-	57.47	0.4570637119	0.10	-22.04
NGC0237	HIPASS; GALEXASC ; [VCV2006]	00h43m27.84s	-00d07m29.7s	0.013926	55.90	SAB(rs)cd	Sy?; LINER	64.35	0.68359375	0.05	-20.88
NGC0257	NVSS; GALEXASC	00h48m01.51s	+08d17m49.5s	0.017592	70.40	Scd:	-	59.93	0.5318559557	0.16	-22.00
NGC0477	NVSS	01h21m20.37s	+40d29m17.5s	0.0196	79.10	SAB(s)c	-	64.86	0.7024793388	0.15	-21.47
NGC0776	NVSS J015954+233839; UZC	01h59m54.49s	+23d38m39.8s	0.016415	65.50	SAB(rs)b	-	54.89	0.3856829803	0.27	-21.81
NGC1093	NVSS; UZC	02h48m16.15s	+34d25m11.2s	0.017646	70.80	SABab?	-	62.76	0.6265432099	0.24	-21.40
NGC1645	GALEXASC	04h44m06.38s	-05d27m56.2s	0.016345	65.90	(R')SB0$^+$(rs) pec	-	67.67	0.8109640832	0.15	-21.67
NGC2253	NVSS; [RC2]	06h43m41.84s	+65d12m22.6s	0.011885	51.30	Scd:	-	57.65	0.4622222222	0.19	-21.44
NGC2347	MRK; NVSS; KPG	07h16m03.69s	+64d42m32.1s	0.014747	63.00	(R')SA(r)b:	-	58.20	0.4783950617	0.22	-21.89
NGC2639	[VCV2001]; CXO; NVSS	08h43m38.08s	+50d12m20.0s	0.011128	49.60	(R)SA(r)a:?	LINER; Sy1.9	61.65	0.5884656461	0.07	-22.09
NGC2730	NVSS	09h02m15.83s	+16d50m17.9s	0.012782	56.70	SBdm:	-	55.99	0.4152249135	0.08	-20.66
NGC2906	NVSS; UZC	09h32m06.22s	+08d26m30.4s	0.007138	33.50	Scd:	-	61.60	0.5867346939	0.13	-20.71
NGC2916	HIPASS; UZC	09h34m57.60s	+21d42m19.0s	0.012442	56.00	SA(rs)b?	-	64.23	0.6794882562	0.07	-21.91
NGC3057	DDO; UZC	10h05m39.36s	+80d17m08.5s	0.005084	25.90	SB(s)dm	-	63.44	0.6508264463	0.07	-18.81
NGC3300	GALEXASC; UZC	10h36m38.44s	+14d10m16.0s	0.01027	48.00	SAB(r)0^0:?	-	66.04	0.7470674738	0.10	-21.27
NGC3381	[BKD2008]; NVSS	10h48m24.82s	+34d42m41.1s	0.005434	28.80	SB pec	WR; HII	36.58	0.0805029086	0.06	-19.83

Table 2.1 Continued.

NGC3614	GALEXASC; UZC	11h18m21.32s	+45d44m53.6s	0.007782	38.40	SAB(r)c	-	64.60	0.6929592774	0.04	-20.79
NGC3687	MRK; GALEXASC	11h28m00.61s	+29d30m39.8s	0.008362	41.10	(R')SAB(r)bc?	-	53.39	0.3480189807	0.06	-20.66
NGC4003	NVSS; GALEXASC; KPG	11h57m59.04s	+23d07m29.6s	0.021712	96.60	SB0	-	63.14	0.64	0.07	-21.77
NGC4047	NVSS; GALEXASC	12h02m50.68s	+48d38m10.3s	0.011375	53.30	(R)SA(rs)b:	-	57.65	0.4622222222	0.06	-21.67
NGC4185	HIJASS; UZC	12h13m22.20s	+28d30m39.5s	0.013022	61.00	Sbc	-	57.78	0.4659763314	0.06	-21.67
NGC4210	NVSS; UZC	12h15m15.83s	+65d59m07.2s	0.009113	43.20	SB(r)b	-	60.66	0.5555555556	0.05	-20.83
NGC4961	FAUST; [MO2001]; NFGS	13h05m47.57s	+27d44m02.9s	0.008456	42.50	SB(s)cd	-	59.78	0.52734375	0.03	-19.99
NGC5000	GALEXASC; FIRST; VV; ABELL	13h09m47.49s	+28d54m25.0s	0.018706	84.90	SB(rs)bc	Sbrst	59.35	0.5136772853	0.02	-21.45
NGC5016	HIPASS; KIG	13h12m06.68s	+24d05m42.0s	0.008713	43.50	SAB(rs)c	SBNG	55.99	0.4152249135	0.04	-20.86
NGC5205	UZC	13h30m03.58s	+62d30m41.7s	0.005891	30.90	Sbc	-	65.28	0.7183296401	0.06	-19.89
NGC5320	UZC	13h50m20.38s	+41d21m58.4s	0.008736	43.60	SAB(rs)c:	-	66.11	0.75	0.02	-20.85
NGC5378	UZC-CG	13h56m51.02s	+37d47m50.1s	0.010147	49.60	(R')SB(r)a	-	53.80	0.358127287	0.04	-21.10
NGC5406	GALEXASC; NVSS	14h00m20.12s	+38d54m55.5s	0.017352	79.00	SAB(rs)bc	-	65.04	0.7092464437	0.03	-22.32
NGC5480	NVSS; KPG	14h06m21.58s	+50d43m30.4s	0.006191	32.90	SA(s)c:	-	56.87	0.4397982611	0.05	-20.54
NGC5614	FIRST; VV; ARP	14h24m07.59s	+34d51m31.9s	0.012982	61.40	SA(r)ab pec	-	57.60	0.4606933594	0.04	-22.41
NGC5656	GALEXASC ; NVSS	14h30m25.51s	+35d19m15.7s	0.010551	51.40	Saab	LINER	60.33	0.5447815358	0.04	-21.45
NGC5735	UZC	14h42m33.24s	+28d43m35.2s	0.012482	59.60	SB(rs)bc	-	54.41	0.3732638889	0.05	-21.18
NGC5772	GALEXASC; FIRST; KIG	14h51m38.88s	+40d35m57.0s	0.016345	74.80	SA(r)b:	-	66.31	0.7577917272	0.05	-22.00
NGC5829	HIPASS; ARP; HCG	15h02m42.01s	+23d20m01.0s	0.018797	85.80	SA(s)c	HII	58.62	0.4912220646	0.12	-21.35
NGC6004	UZC	15h50m22.72s	+18d56m21.4s	0.012762	60.80	SAB(rs)bc	-	46.13	0.1994459834	0.11	-21.68
NGC6032	[WB92]; UZC	16h03m01.12s	+20d57m21.4s	0.014283	67.00	SB(rs)b:	-	66.80	0.7768451955	0.25	-21.13
NGC6154	UZC	16h25m30.48s	+49d50m24.9s	0.020064	88.70	SB(r)a	-	55.77	0.4091668523	0.06	-21.79
NGC6186	GALEXASC; ADBS	16h34m25.48s	+21d32m27.2s	0.009797	48.10	(R')SB(s)a	-	66.48	0.7644061421	0.13	-21.11
NGC6278	CXO; GALEXASC	17h00m50.33s	+23d00m39.7s	0.009447	45.80	S0	-	67.19	0.7921018014	0.17	-21.45
NGC6941	HIPASS; NVSS	20h36m23.47s	-04d37m07.5s	0.020761	88.60	SAB(rs)b	-	62.51	0.6181037748	0.17	-22.22
NGC7321	NVSS	22h36m28.02s	+21d37m18.5s	0.023833	97.90	SB(r)b	-	59.78	0.52734375	0.13	-22.32
NGC7489	NVSS; UZC	23h07m32.71s	+22d59m52.8s	0.020811	85.10	Sd	-	65.47	0.7256235828	0.63	-22.27

Table 2.1 Continued.

NGC7625	1WGA; NVSS; VV; ARP; CGPG	23h20m30.13s	+17d13m32.0s	0.005447	23.70	SA(rs)a pec	HII	48.11	0.234375	0.07	-20.14
NGC7653	TXS; GALEXASC	23h24m49.36s	+15d16m32.1s	0.014227	58.30	Sb	-	56.87	0.4398560184	0.18	-21.50
NGC7691	UZC	23h32m24.42s	+15d50m52.2s	0.013479	55.20	SAB(rs)bc	-	56.87	0.439743268	0.17	-21.01
NGC7716	HIPASS; KIG	23h36m31.45s	+00d17m50.2s	0.008604	35.60	SAB(r)b:	-	49.69	0.2653061224	0.09	-20.79
NGC7738	2XMM; NVSS; KIG	23h44m02.06s	+00d30m59.9s	0.022556	91.40	SB(rs)b	-	69.79	0.897729908	0.07	-21.86
NGC7819	NVSS; KUG	00h04m24.54s	+31d28m19.4s	0.016538	67.20	SB(s)b	HII	53.88	0.36	0.16	-20.83
UGC07012	KUG; UZC	12h02m03.15s	+29d50m52.8s	0.010277	49.40	Scd:	-	65.32	0.7197231834	0.06	-19.62
UGC08234	UZC; [RC2]	13h08m46.49s	+62d16m18.2s	0.027025	116.10	S0/a	-	69.07	0.867768595	0.04	-22.60
UGC08733	UZC	13h48m38.90s	+43d24m44.6s	0.007799	39.70	Sbcd:	Sbrst	61.24	0.5746691871	0.05	-19.33
UGC09067	NVSS; GALEXASC	14h10m45.46s	+15d12m33.9s	0.026151	116.30	Sab	-	66.11	0.75	0.05	-21.69
UGC09291	LCSB; UZC	14h28m36.89s	+38d59m56.9s	0.009657	47.60	Sd	-	67.48	0.8034409959	0.04	-20.29
UGC09476	UZC; KPG	14h41m32.02s	+44d30m45.9s	0.010881	52.30	SAB(rs)c	-	63.42	0.6501710291	0.05	-20.75
UGC10796	KUG; UZC	17h16m47.73s	+61d55m12.5s	0.010271	48.00	SB(s)b	-	68.62	0.8493334488	0.05	-19.28
UGC12224	HIPASS; GALEXASC; KIG	22h52m38.30s	+06d05m37.2s	0.011695	48.70	Scd:	-	45.01	0.1814058957	0.24	-20.63

Chapter 3.

Methodology

This chapter provides a description of the analysis methodology used in this work in order to investigate the stellar age and SFH of pseudo-bulges. The methodology employed here combines surface photometry with spectral synthesis of stellar populations, as described in the next sections.

3.1 PHOTOMETRY

The word *photometry* means *measure of light*. In the case of SDSS, the flux of galaxies can be measured by means of some photometric filters: u, g, r, i and z (see Figure 3.1). Surface photometry is applicable to *extended* sources (e.g., galaxies) and measures the flux received per solid angle, i.e. the (distance-independent) intensity of an object.

The following subsections give a description of the photometric methods that were used in this work in order to derive *surface brightness profiles* (SBPs) for our sample galaxies and to decompose them into the luminosity contributions of their disk, bulge and bar component.

Post-processing of SDSS imaging data

Imaging data from the SDSS are provided in reduced form, after several pre-reduction steps:

1. Removal of instrumental/detector effects (bias, dark and flat-field, saturation, bad pixels);

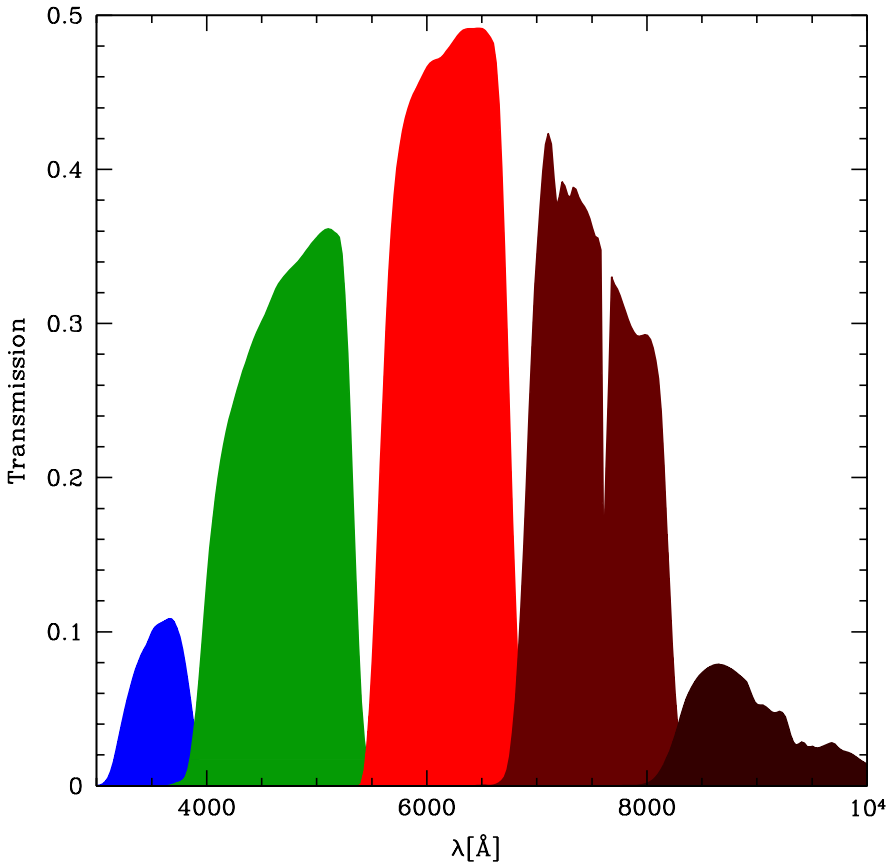

Figure 3.1: SDSS camera filter throughput curves. The central wavelengths for each band are: 3543 Å (ultraviolet u), 4770 Å (green g), 6231 Å (red r), 7625 Å (near infrared i) and 9134 Å (infrared z), with colors blue, green, red, dark red, and dark brown, respectively.

2. Correction for cosmic ray hits;

3. Computation of calibration constants;

4. Approximate subtraction of the sky background through a low-degree polynomial;

5. Co-registration of images in the five (u, g, r, i and z) SDSS bands.

However, the quality of reduction steps [4] & [5] is generally not sufficient for a precise surface photometry analysis and the determination of color maps. For example, a minor error of typically less than 20% of the sky photon noise in the removal of the local sky background can result in a down-bending or flattening of SBPs in their outer parts, leading then to significant errors in the determination of, e.g., the structural parameters of the disk component. Likewise, minor errors in the co-registration of images in two different bands can propagate into strong artifacts in color maps computed by division of these images. Finally, photometric bands are corrected for Galactic foreground extinction.

Due to these reasons a post-processing of the photometric SDSS data was made for all sample galaxies. For the task below a series of in-house codes written by P. Papaderos in the ESO-MIDAS script language was used in order to:

1. Perform a more accurate image co-registration using several Galactic foreground stars in each SDSS band. This alignment procedure has involved, e.g., translation and rotation of individual images, and their transformation to astronomical orientation (north to the top, and east to the left);

2. Accurately determine and subtract the sky background. For this the emission in up to 1600 sky positions of blank sky was automatically measured in each image, to which a higher-polynomial order (second or third degree) 2D model was fitted and finally subtracted;

3. Correct for the Galactic extinction: The extinction values for each galaxy were retrieved from the NED (Schlafly & Finkbeiner 2011);

4. Extract the useful portion of each SDSS image.

Following the above image post-processing steps, an iterative Gaussian convolution method was used in order to smooth the images of a given galaxy to the resolution of the image with the worse seeing (as defined by the mean value for the full width at half maximum (FWHM) of several non-saturated stars). Additionally, in cases of overlapping foreground/background sources, the latter were replaced by the mean value of the local galaxy surface brightness level.

Surface Photometry and Profile Decomposition

The derivation of SBPs, and their decomposition into the luminosity contribution of the bulge, disk and bar, was carried out with a code developed by our team. Technical details on this code can be found in Breda (2014). In the following, only a brief summary of the fitting formulae (based in Bender & Moellenhoff (1987)) used for the disk, bulge and bar is given.

The surface brightness $\mu(r)$ (in units of mag/arcsec^2) of a galaxy at the photometric radius r is defined as

$$\mu(r) = -2.5 \log_{10} \left(\frac{F(r)}{S^2} \right) \tag{3.1}$$

with $F(r)$ being the count rate per pixel at the corresponding isophote, S^2 the solid angle in arcsec^2 subtended by a pixel (0.396127^2 arcsec^2/pixel in the case of SDSS images).

The surface brightness of the disk is commonly approximated by the exponential law of Freeman (1970) modified as:

$$\mu(r) = \mu_0 + \left(\frac{2.5}{\ln 10}\right)\left(\frac{r}{\alpha}\right) + C \tag{3.2}$$

where μ_0 is the central disk surface brightness and α the disk scale length in arcsec. This process allow to subtract the modeled disk from the observed SBP, remaining the emission of the bar, when present, and of the bulge.

Next to the removal of the contribution of the disk, and when a bar-feature is evident in the profile, another equation is used to account for this extra emission. This way, the surface brightness of the bar can be approximated by a Sérsic (1963, 1968) distribution of the form

$$\mu(r) = \mu_0 + \left(\frac{2.5}{\ln 10}\right)\left(\frac{r}{\beta}\right)^{1/\eta} \tag{3.3}$$

with β being a pseudo scale-length and η its Sérsic exponent. The three free parameters of this formula are determined through an iterative χ^2 minimization procedure. The modeled bar is subtracted from the remaining emission obtained in the removal of the disk component.

After this process, it remains the emission of the bulge. The surface brightness of the bulge is estimated with a modified Sérsic formula by Ciotti (1991) as

$$\mu(r) = \mu_{\rm mod} + \left(\frac{2.5 b_\eta}{\ln 10}\right)\left[\left(\frac{r}{r_{\rm mod}}\right)^{1/\eta} - 1\right] \tag{3.4}$$

where $r_{\rm mod}$ is the effective radius of the Sérsic model that is integrated to infinity, $\mu_{\rm mod}$ is the surface brightness at $r_{\rm mod}$. For the constant b_η, Capaccioli (1989) provided one of the first analytical expressions that approximate its value, such that $b_\eta = 1.9992\eta - 0.3271$. It is worth pointing out that profile decomposition suffers from several degeneracies, specially between the Sérsic index η and the pseudo-scale length β (see, e.g., Noeske et al. (2003)). This can lead to ambiguities when basing the distinction between classical bulges and pseudo-bulges on the Sérsic index

only, as is common practice. Therefore, a new technique was devised by our team, stabilizing the degeneracy mentioned above, using observed quantities (such as the effective radius $r_{\rm eff}$ of the bulge and the surface brightness at $r_{\rm mod}$) to estimate the Sérsic index η, in order to give more stability and robustness to the structural parameters derived from SBP decomposition. In this way, there is no need to select points for the fit, but only the physical limit of the bulge. Then the modeled bulge is estimated automatically.

The relevant output from the decomposition procedure is exported into a MIDAS table format for the purpose of subsequent analysis. It has to be noted that the derived apparent and absolute magnitudes that results from here were integrated to a limiting surface brightness of 24 mag/arcsec^2 in the SDSS r band, since this value corresponds to when the detection efficiency of the CCD reaches 40%.

3.2 MODELING OF THE SPECTROSCOPIC DATA FROM CALIFA

The data set used in this study consists of wavelength and flux calibrated IFS data from the CALIFA Survey in the low-resolution (resolving power of $R \sim 850$ at 5000 Å) spectroscopic setup V500. The estimated limiting surface brightness of this data set in the V band is estimated to range between 23.4 and 23.9 mag/arcsec^2, permitting studies of the disk component well beyond one effective radius (see, e.g., Kehrig et al. (2012) for details). These data were modeled spaxel-by-spaxel with the spectral synthesis code STARLIGHT and the Porto3D automated spectral synthesis pipeline in the spectral range between 4000 Å and 6800 Å with the goal of placing constraints on the age and SFH of galaxy pseudo-bulges.

STARLIGHT

In section 1.5 we have discussed how Simple Stellar Populations can be used to derive the fractional contribution of $N_\star$ SSPs, i.e. the Star Formation History (SFH) expressed in terms of the population vector $\vec{x} = (x_1, ..., x_{N_\star})$ by means of population synthesis methods (equation 1.5).

STARLIGHT is one such population synthesis code presented in Cid Fernandes et al. (2005), which fits an observed spectrum O_λ as a linear superposition of coeval stellar populations with

homogeneous chemical abundances. This code allows one to estimate physical properties of galaxies, such as the total stellar mass, dust extinction, mean stellar age and metallicity, SFH, chemical enrichment history, among others quantities. In order to determine the best-fitting solution of a galaxy, the routines search for the minimum χ^2, using statistical mechanics technique (simulated annealing method) and multiple independent Markov Chains that are carried out in the parameter space to avoid being trapped in local minima solutions.

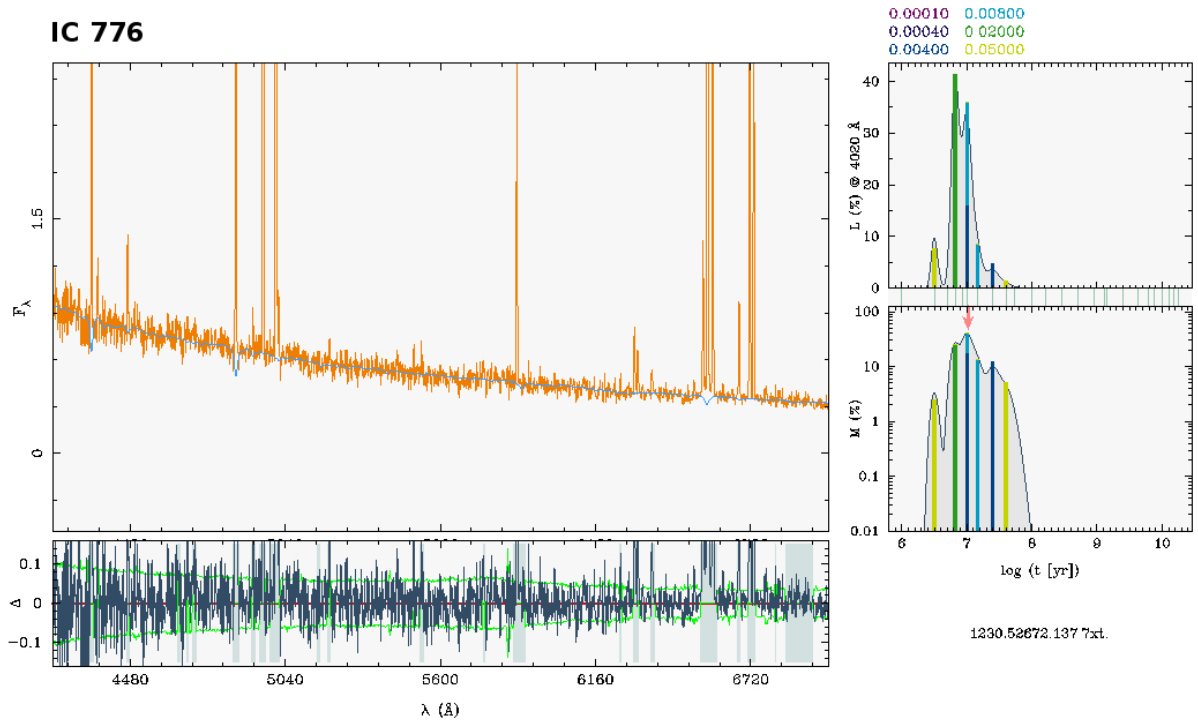

Figure 3.2: Example of STARLIGHT fit using equation 3.5 for one galaxy from our sample, IC776. Top left panel: SDSS observed spectrum (orange) and the best-fit model (blue). This example has used a linear combination of distinct SSPs with 6 metallicities and 25 age intervals. The bottom left panel shows the pure emission-line spectrum after subtracting the underlying stellar component. Flagged regions due to emission-lines and/or spurious pixels are shown as blue gray shaded areas. The right panels display the corresponding Star Formation Histories, i.e. the stellar light (top) and mass (bottom) fractions as a function of the stellar age.

The equation used for the best-fitting synthetic spectrum $F(\lambda)$ invokes more parameters than equation 1.5 discussed in the Introduction. This is done to model more realistically other effects commonly found in galaxies, like reddening and kinematics. Therefore, the final model contains $N_\star + 4$ parameters and can be expressed in the following form:

$$F(\lambda) = F(\lambda_0) \left(\sum_j^{N_\star} x_j \times \frac{\mathrm{SSP}(\lambda, t_{\star,j}, Z_{\star,j})}{\mathrm{SSP}(\lambda_0, t_{\star,j}, Z_{\star,j})} \times r(\lambda) \right) \otimes G(v_\star, \sigma_\star) \tag{3.5}$$

where the new terms $r(\lambda)$ and $G(v_\star, \sigma_\star)$ represent the reddening modeled as an uniform dust

screen and two kinematical parameters: the systemic velocity $v_\star$ and the velocity dispersion $\sigma_\star$. Kinematics is used with a Gaussian kernel function to smooth the modeled spectrum. The other terms have their usual meaning as discussed in the introduction (equation 1.5).

The first moments of the distribution, such as the mean luminosity- or mass-weighted stellar age $\langle t_\star \rangle_{L,M}$ can be computed from the light $\vec{x}$ or mass $\vec{\mu}$ population vectors. The latter is obtained after multiplying the light fractions of SSPs to their corresponding Mass-to-Light ratios. Therefore, we can express these quantities as:

$$\langle t_\star \rangle_L = \sum_{j=1}^{N_\star} x_j t_{\star,j} \tag{3.6}$$

whereas the mean mass-weighted age or metallicity is obtained by replacing x_j in the above equation by the mass fraction μ_j. For the case of mean stellar metallicities:

$$\langle Z_\star \rangle_L = \sum_{j=1}^{N_\star} x_j Z_{\star,j} \tag{3.7}$$

In our study, we use in our base the evolutionary synthesis models from Bruzual & Charlot (2003) for the spectral fitting described above. It comprises $N_\star = 152$ simple stellar populations, with 38 ages between 1 Myr and 13 Gyr and 4 metallicities (1/20, 1/5, 2/5 and 1 $Z_\odot$). This SSP library was computed using the Padova 2000 evolutionary tracks (Girardi et al. 2000) and the Salpeter (1955) initial mass function between 0.1 and 100 $M_\odot$. The elements in the base were selected to contain a large number of young stellar populations from 1 Myr to $\sim$ 100 Myr (12 out of 38 ages) and span a wide range of stellar ages from 1 Myr to 13 Gyr in order to account for rapid evolutionary changes in the SSP spectrum and also to include distinct evolutionary stages while fitting disks and (pseudo) bulges in late-type galaxies.

Porto3D

The V500 IFS data cubes for the sample galaxies were processed with the pipeline Porto3D that was developed by P. Papaderos and J.M. Gomes. Earlier versions of Porto3D were employed in Kehrig et al. (2012) and Papaderos et al. (2013), whereas a full description of the recently upgraded pipeline is presented in Gomes et al. (2014).

Porto3D is a suite of software modules written in the script language of ESO-MIDAS and GNU Fortran 2008, with secondary components invoking PGplot and CFITSIO routines. It was developed for the sake of automated processing and spectral modeling of IFS data of various formats and consists of different modules, where the two most relevant for this study are shown in Figure 3.3. The first one extracts spaxel-by-spaxel spectra from an IFS data cube, performs a number of pre-processing steps (flagging of spurious spectral features and emission lines, transformation of spectra to restframe and rebinning to a wavelength step of 1 Å per pixel; optionally, computation of noise statistics and errors, as well as binning to a minimum signal-to-noise ratio) and exports the spectra as ascii files, in a format that is suitable for their modeling with STARLIGHT. The second module of Porto3D, which is invoked after computation of the STARLIGHT models, computes emission-line fluxes and equivalent widths after subtraction of the best-fitting synthetic stellar spectrum, stellar and ionized-gas kinematics, and several quantities that are considered in this study, such as the luminosity- and mass-weighted stellar age and metallicity, and the mass and luminosity fraction of stars younger than 100 Myr.

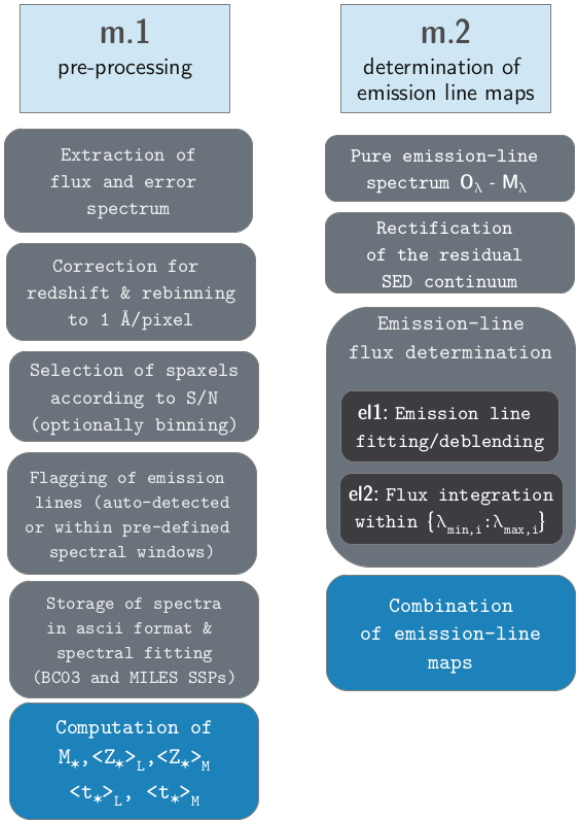

Figure 3.3: Schematic overview of the Porto3D pipeline with its two main modules: module 1 executes pre-processing steps and exports the spectra to model with STARLIGHT, and module 2 is used for measuring more accurately the emission-line maps.

Porto3D is supplemented by various auxiliary modules. One of those computes the Lyman continuum photon rate and the luminosity of Balmer recombination lines expected from a STARLIGHT population vector, and is being extensively used in studies of early-type galaxies by the Centro de Astrofísica da Universidade do Porto (CAUP) team (see, e.g., Gomes et al. (2014) for details). Additionally, Porto3D has an add-on routine for the computation of radial profiles of various quantities of interest, adapted from the surface photometry technique iv by Papaderos et al. (2002), i.e. *irregular isophotal annuli* method.

Chapter 4.

Results from our Analysis Methodology

This chapter discusses our main results obtained by applying our methodology (see Chapter 3) to our sample of 66 late-type galaxies selected from the CALIFA-IFU survey (Chapter 2). First, we discuss the structural properties of these galaxies, which were derived using an in-house surface photometry code developed by our team. This code was applied to SDSS images in order to decompose the SBPs of galaxies into a bulge plus disk component, when necessary, also including a bar contribution. The photometric parameters are then combined with the output from our Porto3D pipeline, which computes and stores several physical quantities of galaxies into spatially resolved 2D maps (e.g., stellar mass, stellar ages and metallicities). These 2D maps were then used in order to determine with the *irregular isophotal annuli* technique the distribution of several quantities of interest (e.g., light- and mass-weighted stellar age) as a function of galactocentric radius. Moreover, these profiles permitted determination of the mean stellar age and age gradient within the bulge and disk component.

4.1 SURFACE PHOTOMETRY: STRUCTURAL PARAMETERS

Our sample galaxies show a significant diversity with respect to their structural characteristics, as inferred from SBP fitting and decomposition (see Breda (2014) for an extended discussion on this subject).

Figure 4.1 illustrates the true-color composites of SDSS broadband imaging data (left panels)

and the correspondent profile decomposition (right panels) for three representative cases (UGC 9291, NGC 0477 and NGC 5000) out of our sample of 66 late-type galaxies.

In the profile decomposition panels, the black dots with the corresponding error-bars show the measured SBPs in the SDSS r-band. A non-weighted exponential fit to the disk (see Eq. 3.2) over the radius range delimited visual and manually by the two vertical lines can be seen as a solid black line and green open circles, and the emission in excess to the disk (i.e. the observed profile minus the exponential model to the disk) is shown with red open symbols. The blue solid curve shows the best-fitting Sérsic model (Eq. 3.4) to the bulge and/or the bar, with the latter depicted with green filed circles.

In all cases, the dashed horizontal line shows the adopted isophotal limit of 24 r mag/arcsec^2 down to which apparent and absolute magnitudes were determined. The values in the upper right corner of the plots are, from top to bottom, the observed and modeled surface brightness at the effective radius $r_{\rm eff}$, the $r_{\rm eff}$ in arcsec, and the derived Sérsic index of the bulge. The bottom panel shows the radial SDSS $r-i$ color profile.

Regarding the SDSS r-band SBP (Figure 4.1), each one shows distinct features that are detailed below:

- Compact bulge emission + no bar: UGC 9291. From a quick inspection of the RGB image one can see that a prominent bulge is absent, which is also confirmed from the profile and corresponding decomposition into a bulge + disk. This galaxy presents a central surface brightness of the bulge of ~ 22 mag/arcsec^2.

- Bulge + no bar: NGC 0477. This galaxy presents a central surface brightness of the bulge of ~ 20 mag/arcsec^2. There is an excess in the emission of the disk, probably due to regions of star formation, which can be seen in the true-color RGB image.

- Bulge + bar: NGC 5000. From the true-color image one can easily identify a strong bar, which is also evident in the profile decomposition, after the subtraction of the disk component. If the contribution of the bar was ignored, the contribution of the bulge would be overestimated, leading to a higher Sérsic index of the bulge.

Kormendy & Kennicutt (2004) not only proposed the widely used cutoffs of $\eta > 2$ for classical

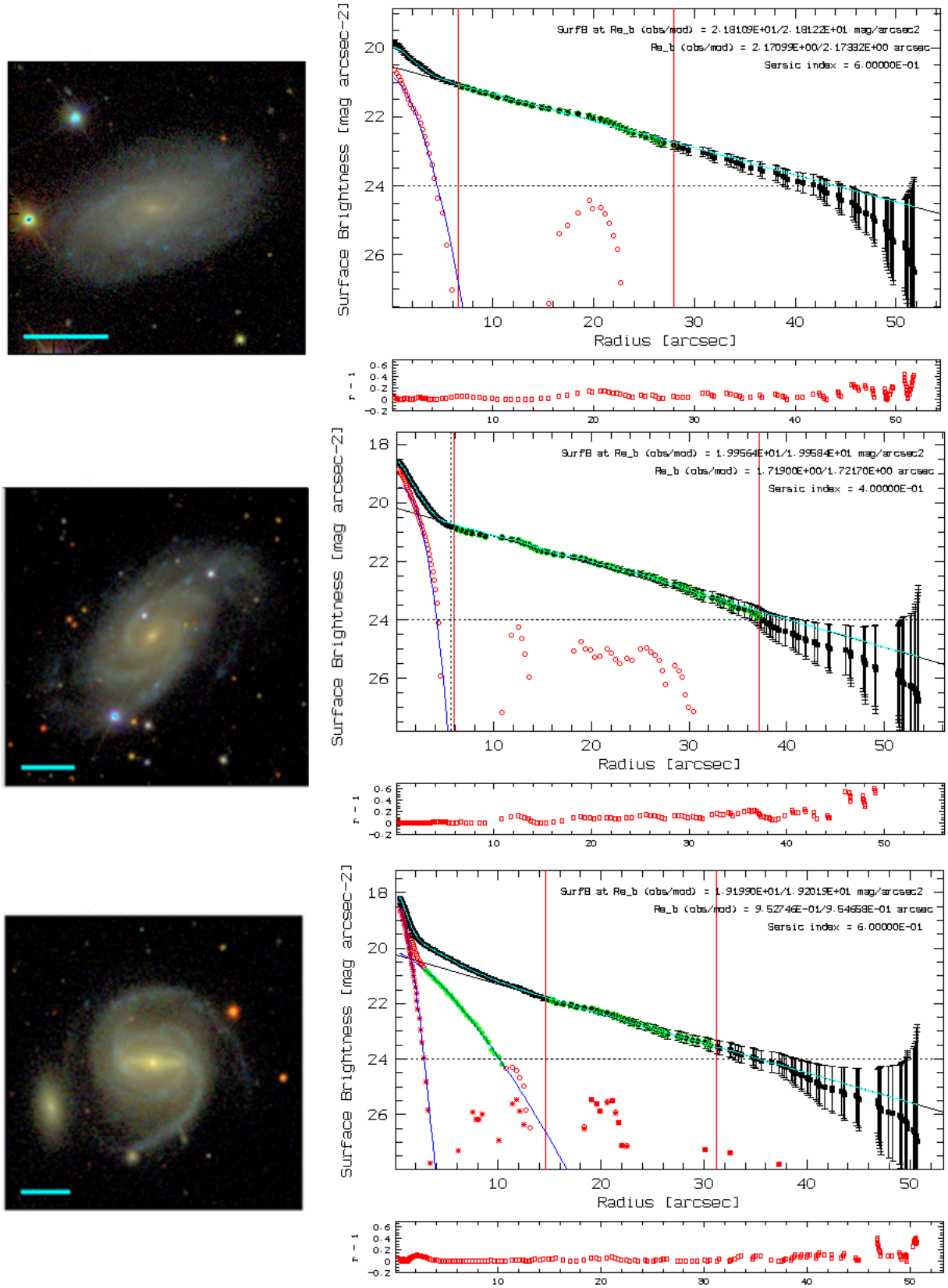

Figure 4.1: Three different galaxies of our sample: UGC 9291 (top panel), NGC 0477 (middle panel), NGC 5000 (bottom panel). Left panels: true-color RGB images. Right panels: surface photometry and corresponding radial SDSS $r-i$ color profile (in the bottom plots).

bulges and $\eta \lesssim 2$ for pseudo-bulges, they as well suggested that bulge-to-total light ratios between $1/3$ and $1/2$ could be considered as characteristic indicators of classical bulges. Figure 4.2 shows histograms for the Sérsic index η and the bulge-to-total B/T ratio, respectively on the left and right panels. We find that only three galaxies of our sample (NGC 5614, NGC 5656 and NGC 6004) have a Sérsic index of $\eta > 2$, an indicative of a classical bulge. Furthermore, the galaxies NGC 0001, NGC 0023 and NGC 6278 have bulge-to-total light ratios $1/3 < B/T < 1/2$, and could also be classified as having classical bulges. However, we did not further investigate the B/T as a discriminator, since we opted for a more conservative approach using the Sérsic index η only.

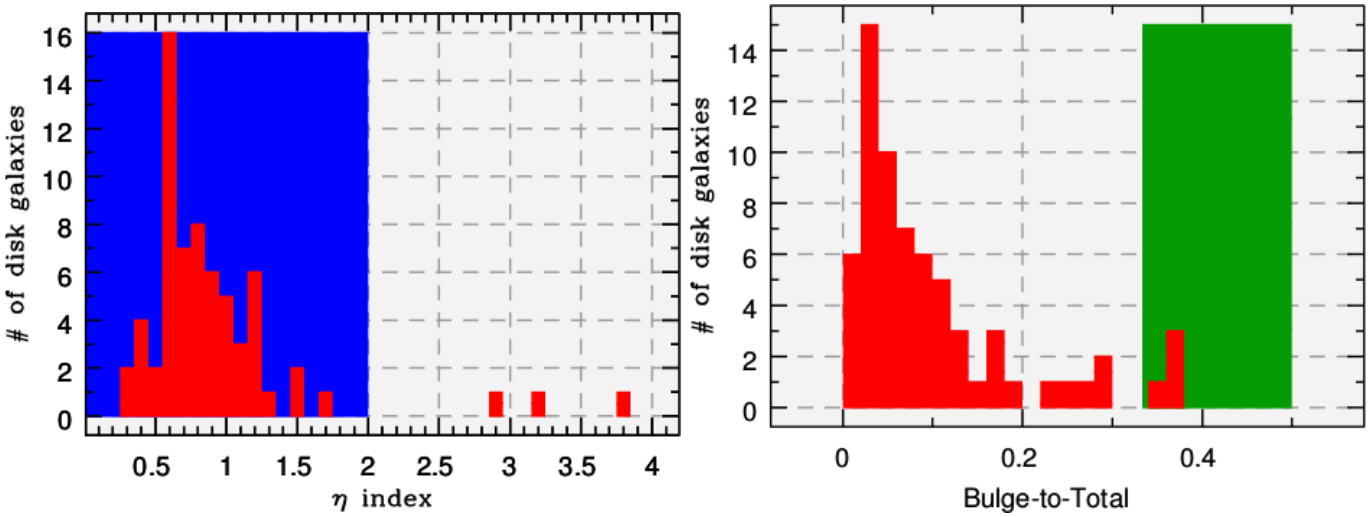

Figure 4.2: Left panel: histogram representation of the derived Sérsic index η. The shaded area in blue is where the criterion for pseudo-bulge galaxies can be applied ($\eta \lesssim 2$). From here we can easily detect three galaxies with $\eta > 2$ (NGC 5614, NGC 5656 and NGC 6004), being classified as classical bulges. Right panel: histogram for the bulge-to-total light ratio. The shaded area in green corresponds to where we could use B/T for classifying a classical bulge. This criterion leads to four galaxies that could be classified as having classical bulges (NGC 0001, NGC 0023, NGC 5614 and NGC 6278).

4.2 MEAN STELLAR AGE AND AGE GRADIENTS

Following our discussion in section 3.2.2, we are able to derive 2D maps for a variety of physical properties using the Porto3D pipeline. Our main motivation in this section is to derive the mean luminosity- and mass-weighted stellar age (see equation 3.6) profiles and age gradients of the bulge and disk for our sample of late-type galaxies. These two quantities seem to better characterize the stellar population mixtures as a function of galactocentric radius, invoking simple definitions and few parameters to describe our sample galaxies.

Figures 4.3, 4.4 and 4.5 show examples of 2D stellar age maps, both luminosity- and mass-weighted, and their corresponding mean stellar age radial profiles obtained using the *irregular isophotal annuli* technique from Papaderos et al. (2002). The remaining sample galaxies can be found in the Appendix B of this work. We also estimate the mean stellar age gradients of the bulge and disk components using the surface photometry in section 4.1. These values were calculated using the slope of the non-weighted linear regression fit to the data as a function of galactocentric radius. If the gradient is positive (for the bulge or disk component), then the stellar age tends to increase as a function of radius and *vice versa*.

The radial profiles have been normalized to the effective radius $r_{\rm eff}$ of each galaxy. From top to bottom, we see the underlying stellar continuum level between 6390–6490 Å, the luminosity and mass fraction of stellar populations younger than 100 Myr, and the mean luminosity- and mass-weighted stellar age as a function of galactocentric radius. The light-shaded area in red depicts the bulge radius $r_{\rm bulge}$ in units of $r_{\rm eff}$. The black empty squares and colored circles (bulge - red and disk - blue) are, respectively, the measured quantities for each irregular isophotal annulus and the result of a spline interpolation in steps of 1 arcsec.

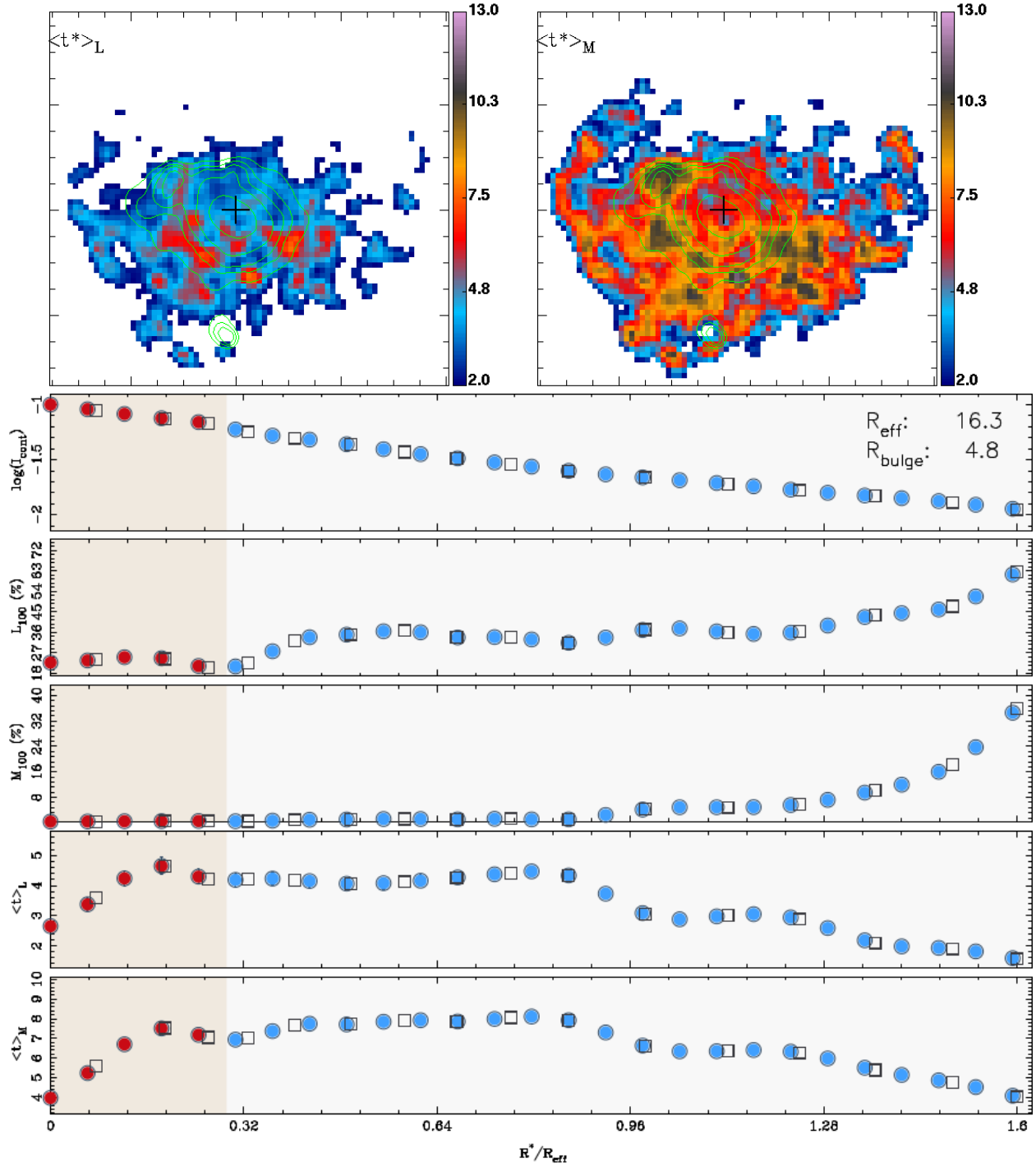

Figure 4.3: Galaxy IC 776. Top panels: 2D maps are from left to right luminosity- and mass-weighted stellar ages, respectively. From top to bottom, radial profiles of: logarithm of the emission-line free continuum between 6390–6490 Å; luminosity fraction of stellar populations younger than 100 Myr; mass fraction of stellar populations younger than 100 Myr; luminosity-weighted stellar age and mass-weighted stellar age. Inspection of the two lowest panels shows that this galaxy has both light- and mass-weighted stellar age gradients with positive values in the bulge region, which correspond to 7.459 $\pm$ 2.248 and 14.178 $\pm$ 3.305 Gyr / $r_{\rm eff}$, respectively. The bulge region is shown in red (light-shaded area). The black empty squares and colored circles (bulge - red and disk - blue) are, respectively, the measured quantities for each irregular isophotal annulus and the result of a spline interpolation in steps of 1 arcsec.

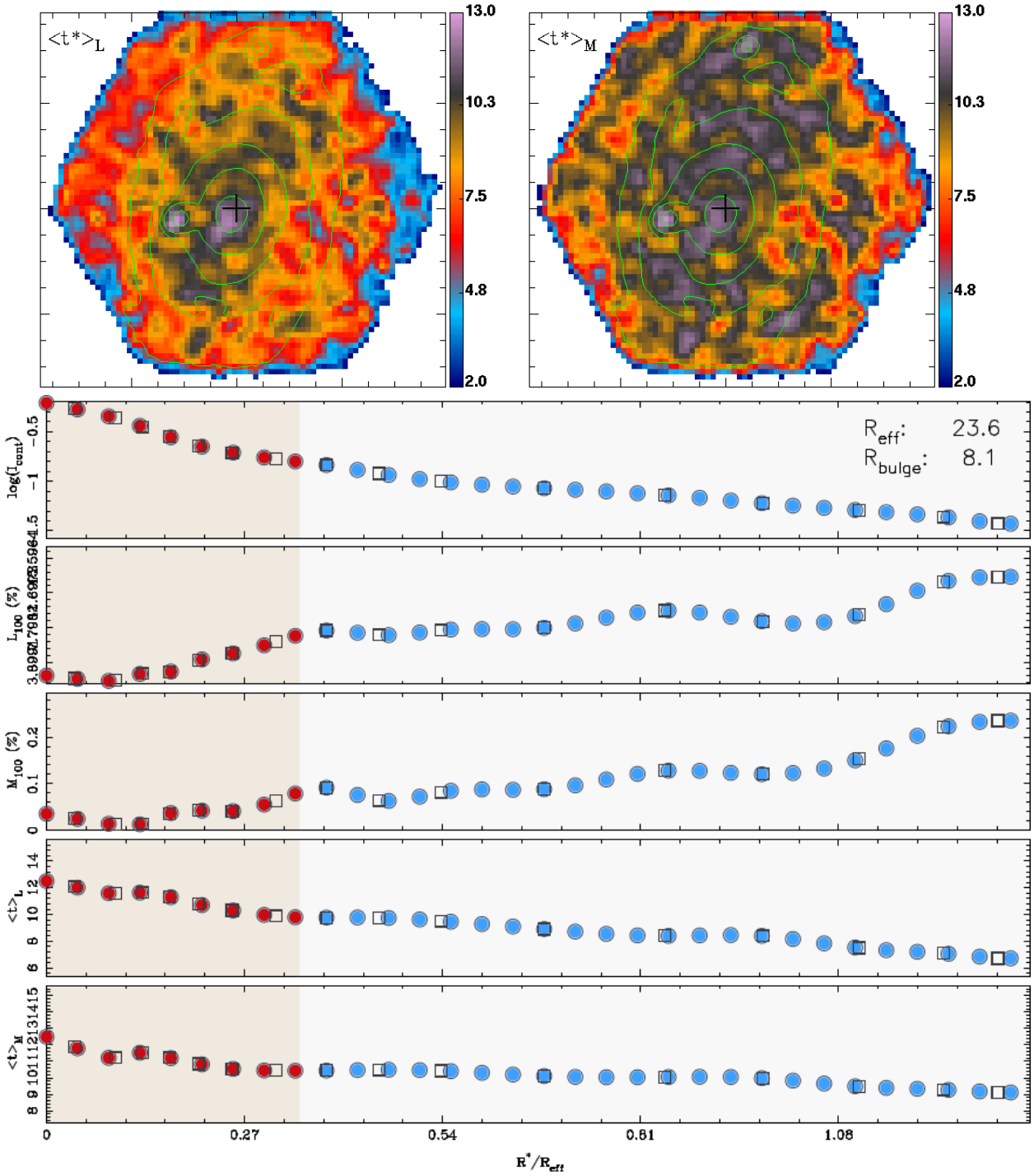

Figure 4.4: The same plots as in Figure 4.3, but for galaxy NGC 4185. This galaxy has both light- and mass-weighted stellar age gradients with negative values in the bulge area, which correspond to -8.050 $\pm$ 0.455 and -5.625 $\pm$ 0.755 Gyr / $r_{\rm eff}$, respectively.

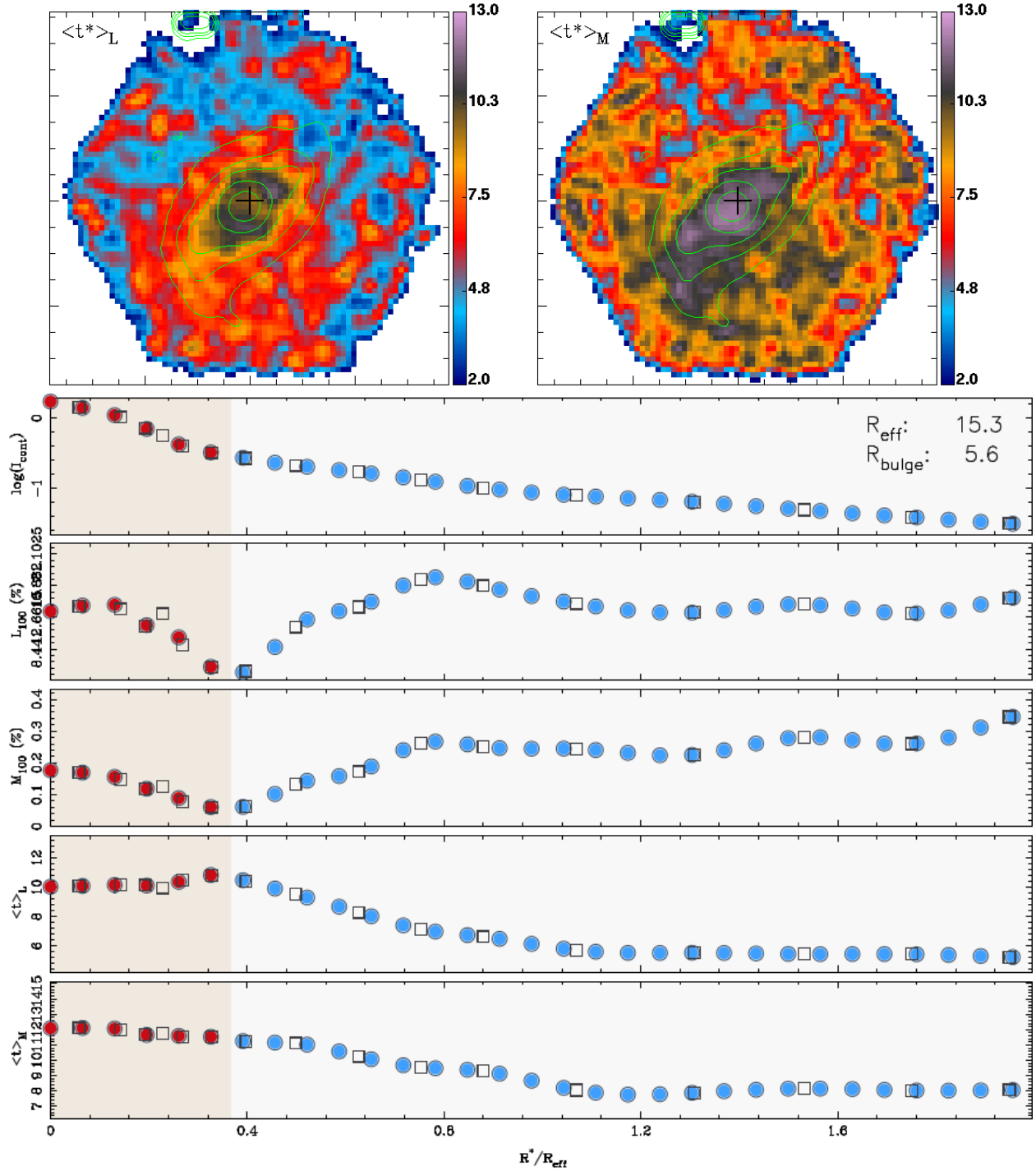

Figure 4.5: The same plots as in Figure 4.3, but for galaxy NGC 776. This galaxy has, in the bulge region, positive value of light-weighted stellar age gradient (2.099 $\pm$ 0.646 Gyr / $r_{\rm eff}$) and negative value of mass-weighted stellar age gradient (-2.074 $\pm$ 0.425 Gyr / $r_{\rm eff}$).

The selected galaxies can be summarized as follows:

1. IC 776 – The stellar population age gradients in Figure 4.3, both luminosity- and mass-weighted (last two panels), have positive values for the bulge region, meaning that the stellar age is increasing from the galactic center to the periphery of the bulge. The values found correspond to 7.459 $\pm$ 2.248 and 14.178 $\pm$ 3.305 Gyr / $r_{\rm eff}$, respectively.

2. NGC 4185 – The galaxy of Figure 4.4 shows negative gradients in the bulge region for light- and mass-weighted stellar age gradients, implying that the stellar age is decreasing from the center of the galaxy to the periphery of the bulge. The values for the bulge region correspond to -8.050 $\pm$ 0.455 for the light-weighted and -5.625 $\pm$ 0.755 Gyr / $r_{\rm eff}$ for the mass-weighted stellar age gradient.

3. NGC 776 – The stellar population age gradients in Figure 4.5, for the bulge area, have opposite signs for the luminosity- and mass-weighted values. The positive value of light-weighted stellar age gradient corresponds to 2.099 $\pm$ 0.646 Gyr / $r_{\rm eff}$, whereas the negative value of mass-weighted stellar age gradient corresponds to -2.074 $\pm$ 0.425 Gyr / $r_{\rm eff}$.

We list in tables C.2 and C.3 (see Appendix C) parameters related to luminosity and mass fractions of stellar populations younger than 100 Myr in the galaxy, luminosity- and mass-weighted stellar age for both regions, i.e. bulge and disk. Figure 4.6 shows two histograms directly related to table C.2. The histogram on the top panel refers to the luminosity fraction of stellar populations younger than 100 Myr, whereas the histogram on the bottom refers to the mass fraction of these populations. The shaded area in red corresponds to values of the bulge and the solid blue line to values of the disk. The units are given in percentage, being 100% all the stellar populations for each component.

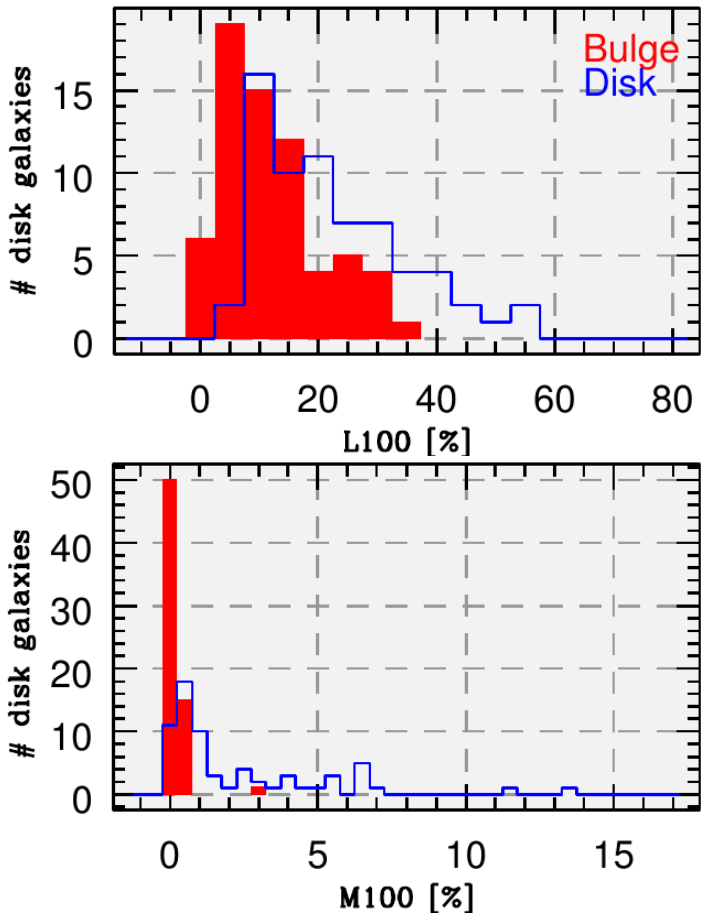

Figure 4.6: Histograms for luminosity (top) and mass (bottom) fractions of stellar populations younger than 100 Myr (in percentage, being 100% relative to all stellar populations). The red color corresponds to values of the bulge, whereas blue color corresponds to values of the disk.

4.3 CORRELATIONS AND TRENDS: AGE AND AGE GRADIENTS

In this section we investigate the most striking trends and correlations found for our late-type galaxy sample. Whereas we mainly focus on the mean stellar age and its radial gradients in the bulge, we also briefly discuss the values inferred for the disk and comment on how the latter compare with those in the bulge.

We start with the most prominent relations found between the mean stellar age and the photometric quantities of the bulge. Figure 4.7 shows that the mean stellar age, both luminosity- (left panels) and mass-weighted (right-panels), correlates well with two photometric properties of the bulge: its absolute magnitude in the SDSS r-band and the mean surface brightness μ_{80}. We recall that μ_{80} is defined to be the mean surface brightness within the radius R_{80} enclosing 80% of the total emission of the bulge. In each plot the bisector linear regression method (Isobe et al. 1990)

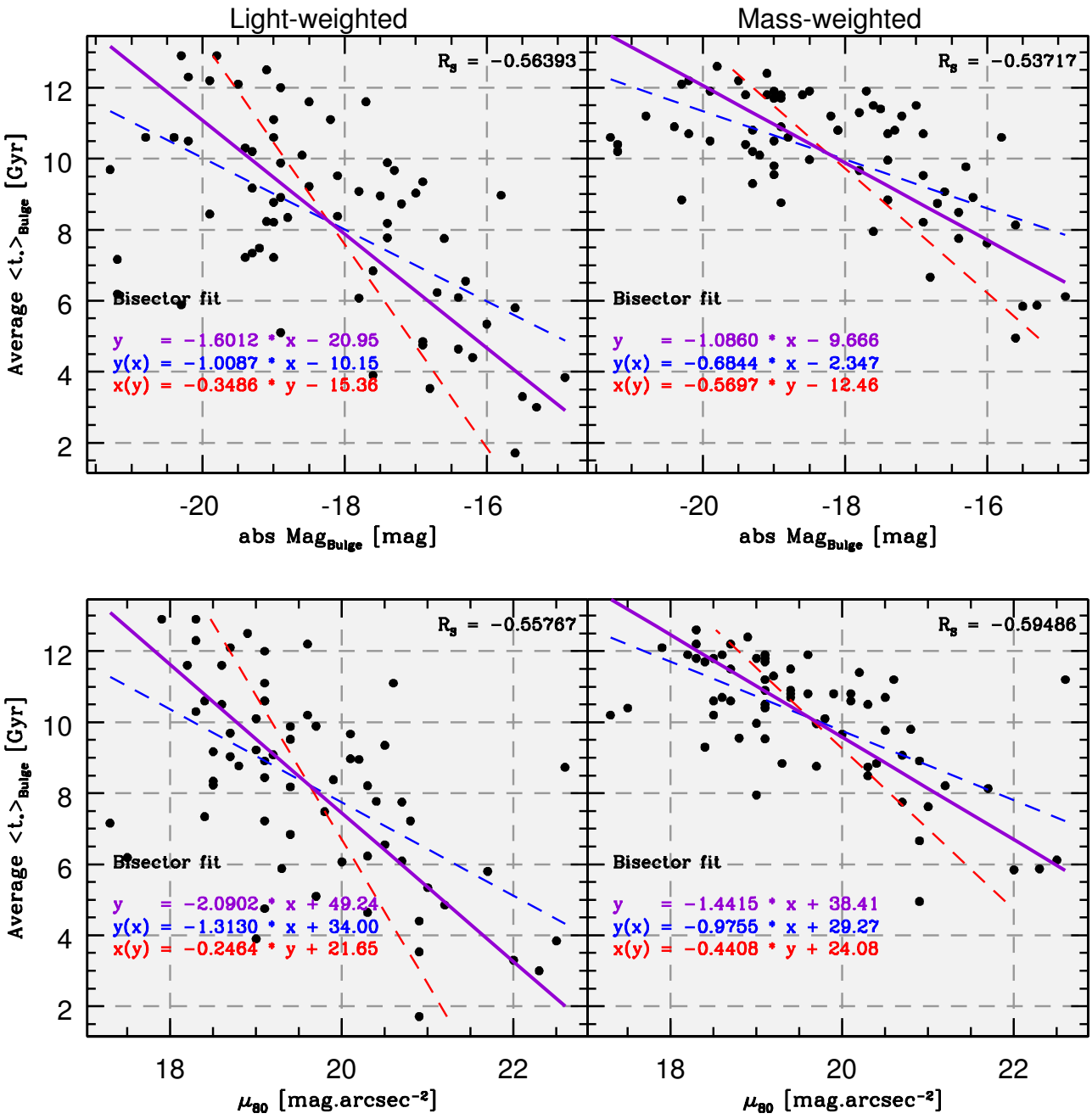

Figure 4.7: The average of the mean stellar age of the bulge, both light- (left panels) and mass- weighted (right panels), in units of Gyr as a function of two distinct photometric quantities: the absolute magnitude of the bulge in the SDSS r-band and the mean stellar surface brightness μ_{80} of the bulge within the radius enclosing 80% of the total luminosity R_{80}. We have used the bisector linear regression method which corresponds to the violet solid line in all plots. The dashed lines with colors blue and red are the functional forms $y(x)$ and $x(y)$, respectively. The R_S value corresponds to the Spearman's rank correlation coefficient to evaluate how well the data can be described by a monotonic function. The higher is the luminosity of the bulge and/or compactness of the bulge μ_{80}, the older are the stellar populations found in the bulge region.

was used in order to minimize the variation of linear fits when the latter do not involve an independent variable. For the sake of completeness, we also computed the Spearman's rank correlation coefficient R_S (Spearman 1904) to evaluate how well the data can be described by a monotonic function. R_S indicates the association of an independent variable x to the dependent one $y(x)$. If y increases when x increases, then R_S is positive, however if y and x are inversely related to each other, then R_S is negative. When there is no clear correlation between the variables then R_S is close to zero.

Despite the intrinsic spread seen in these discussed relations, the luminosity- and mass-weighted mean stellar age of the bulge and both photometric quantities, i.e. the absolute magnitude (top panels) and mean surface brightness μ_{80} of the bulge (bottom panels) are strongly correlated, as seen in Figure 4.7. The linear equations connecting $\langle t_\star \rangle_{\rm bulge}$, $\mathrm{Mag}_{\rm bulge}$ and μ_{80} can be expressed from the bisector regression analysis as follows:

$$\langle t_\star \rangle_{L,\rm bulge} = -1.6012 \times \mathrm{Mag}_{\rm bulge} - 20.95 \tag{4.1}$$

$$\langle t_\star \rangle_{M,\rm bulge} = -1.0860 \times \mathrm{Mag}_{\rm bulge} - 9.666 \tag{4.2}$$

$$\langle t_\star \rangle_{L,\rm bulge} = -2.0902 \times \mu_{80} + 49.24 \tag{4.3}$$

$$\langle t_\star \rangle_{M,\rm bulge} = -1.4415 \times \mu_{80} + 38.41 \tag{4.4}$$

where the mean stellar age of the bulge ($\langle t_\star \rangle_{\rm bulge}$) is in units of Gyr, the $\mathrm{Mag}_{\rm bulge}$ in magnitudes and μ_{80} in mag arcsec^{-2}.

The absolute magnitude $\mathrm{Mag}_{\rm bulge}$ may generally be regarded as a proxy for the total stellar mass $M_\star$ of the bulge, assuming that the latter is mainly composed of evolved stellar populations and

has not recently undergone significant star-forming activity (e.g., a starburst). On the other hand, μ_{80} gives a quantitative estimate on how densely packed is the stellar component in the bulge, i.e. a measure of the surface density of stars in the bulge and the steepness of the gravitational potential that they produce. The denser the bulge is the lower μ_{80} is and *vice versa*. This quantity was shown in Breda (2014) MSc thesis to be a more reliable/sensitive indicator of the physical properties (e.g. metallicity) of the bulge than the traditionally used Sérsic index. Putting together these considerations with respect to the relations derived, one can see that the higher is the luminosity and/or compactness[1] of the bulge, the earlier did the bulge form the dominant fraction of its stellar mass. In this regard, it is also worth pointing out that the empirically determined linear relations in equations 4.1 – 4.4, connecting spectral synthesis and photometric quantities, can readily be used to characterize and age-date the stellar component in the bulge of late-type galaxies – even when spectroscopic information is not available.

Concerning the spectroscopic quantities derived using Porto3D (Section 3.2.2), we also found some interesting trends and correlations. In Figure 4.8 we show, in the left panels, two plots for the histograms of the mean stellar age light- (top) and mass-weighted (bottom) for the disk (blue) and bulge (red) components. In general, the bulge region contains an older stellar population than the disk, specifically i.e. $\overline{\langle t_\star \rangle_{L,\mathrm{bulge}}} \sim 1.5\overline{\langle t_\star \rangle_{L,\mathrm{disk}}}$ and $\overline{\langle t_\star \rangle_{M,\mathrm{bulge}}} \sim 1.25\overline{\langle t_\star \rangle_{M,\mathrm{disk}}}$. The evidence from these histograms can be better appreciated when comparing the mean stellar age of the disk versus that of the bulge, as is done in the right panels. We can see that the older the stellar populations are in bulges the older they are also in disks. Then, by making use of the linear regression bisector method one obtains the following equations for $\langle t_\star \rangle_{\mathrm{bulge}}$ as a function of $\langle t_\star \rangle_{\mathrm{disk}}$:

$$\langle t_\star \rangle_{L,\mathrm{bulge}} = 1.5269 \times \langle t_\star \rangle_{L,\mathrm{disk}} - 0.21 \tag{4.5}$$

$$\langle t_\star \rangle_{M,\mathrm{bulge}} = 1.4067 \times \langle t_\star \rangle_{M,\mathrm{disk}} - 1.31 \tag{4.6}$$

[1] Note that for the absolute magnitude ($\mathrm{Mag}_{\mathrm{bulge}}$) and mean surface brightness within R_{80} (μ_{80}) one should read lower instead of higher, due to the minus sign convention used for these quantities in astronomy

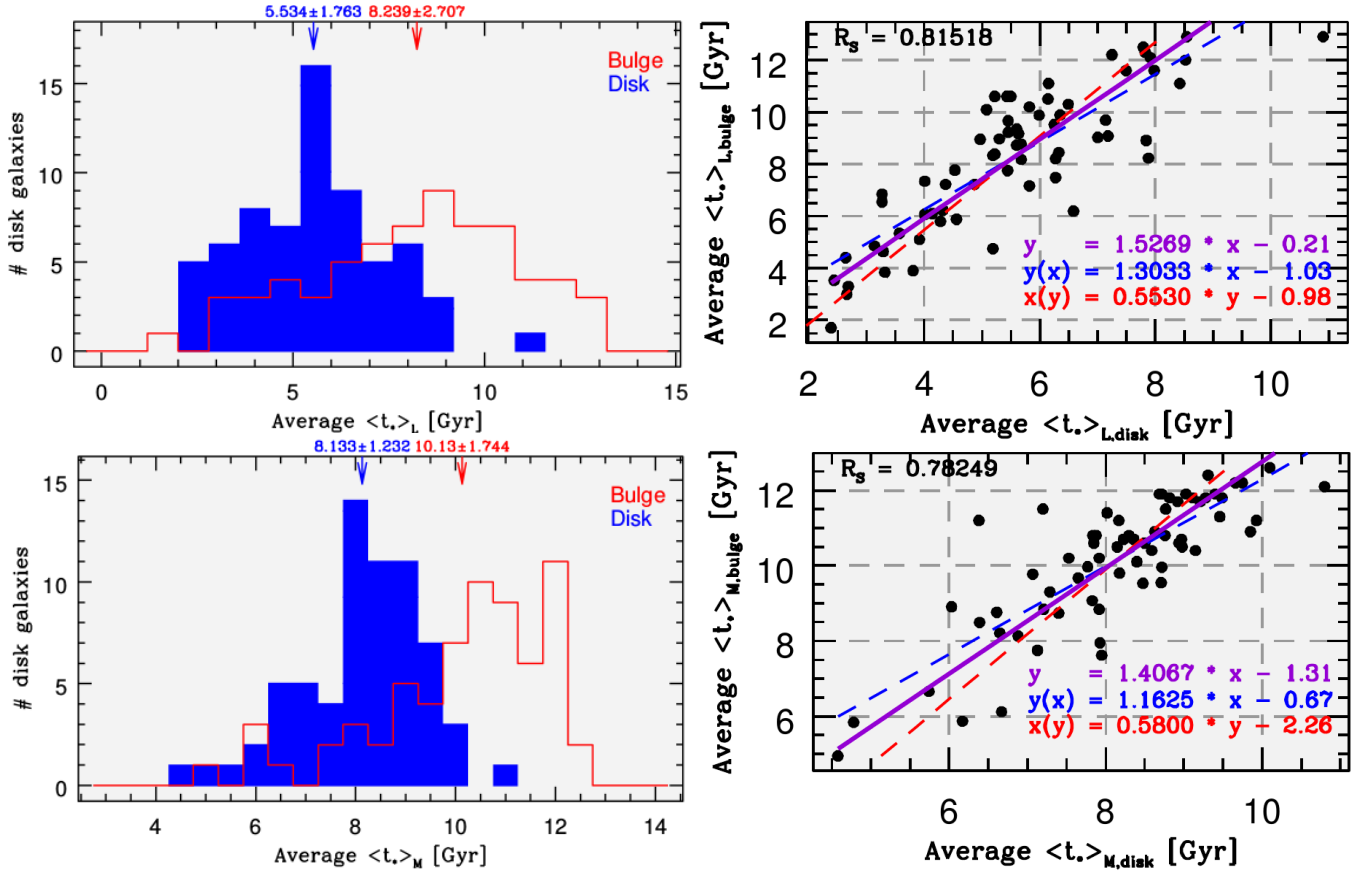

Figure 4.8: Left panels: histograms of the average of the mean stellar age of the bulge (red) and of the disk (blue). The arrows in the upper part of the histograms depict the average values and the standard deviation of the mean stellar age in Gyr, for both bulge and disk components. We can see that typically the bulge contains older stellar populations than the disk. Right panels: comparison between mean stellar age of the disk and the mean stellar age of the bulge. We can see that these quantities are strongly correlated, with a relation obtained by the bisector linear regression method shown through solid violet lines. The dashed lines feature the usual linear regression fits for $y(x)$ in blue and $x(y)$ in red. Top and bottom panels refer, respectively, to luminosity and mass-weighted quantities.

With the availability of huge, state-of-the-art extragalactic surveys, such as the SDSS, 2dF and 6dF, it has been possible in the past decade to study for the first time in depth and on the basis of robust statistics several fundamental galaxy relations. Some examples include the stellar age versus metallicity relations (Cid Fernandes et al. 2005), the mass versus metallicity relation (e.g., Tremonti et al. (2004)), and the bimodality of galaxies with respect to their integral colors and the main features of their SFH (e.g., Mateus et al. (2006)). However, these studies were based on single-aperture spectroscopy which, at low redshifts has been restricted to a minor portion of the nuclear component of galaxies, whereas at higher redshifts dealt with integral galaxy properties. Consequently, despite the tremendous benefit from these mega-surveys, their technical setup has inevitably introduced significant aperture biases in extragalactic studies (see, e.g., Gomes et al. (2014) for a discussion) that blur our understanding of the SFH and chemical enrichment history of

galaxies and their structural components. A second limitation stems from the fact that essentially all previous studies have addressed the nature of pseudo-bulges either from the spectroscopic or photometric point of view. For instance, much previous work has explored the relation between, e.g., the Sérsic index and the absolute magnitude of bulges, leaving aside the chemical and evolutionary properties of the latter. Conversely, a wealth of studies were dedicated merely to the chemical properties of bulges, mostly relying upon Lick indices, without attempting a combined interpretation of the chemical, evolutionary and structural properties of these entities.

A unique and distinctive feature of this project is the combined analysis of spatially resolved IFS that encompasses the total optical extent of galaxies with detailed structural information from broadband surface photometry and profile decomposition. This way, a foundation is now set for the investigation of the origin and the precise slope of fundamental galaxy relations by considering separately the bulge and the disk component, instead of addressing integral galaxy properties only. On the other hand, it should be born in mind that the limited time framework for this MSc thesis has not permitted full analysis and interpretation of the large output from our structural and spectral synthesis analysis. In this chapter we shall, therefore, only focus on a rather descriptive presentation of some of the main trends found, which will be further investigated in a PhD research project.

In Figure 4.9 we plot the total stellar mass of the galaxy, the light- and mass-weighted mean stellar metallicity of the bulge versus the mean stellar age of the bulge, both light- and mass-weighted. An important conclusion from these plots is that the more massive is the galaxy the older and metal-rich it tends to be the bulge and *vice versa*. The evidence from these diagrams implies an indirect relation for the mass-metallicity (MZ) relation obtained by Tremonti et al. (2004). However, in that case, the relation was used for the whole integrated spectrum from the SDSS fiber, and now is confirmed to be also valid for the bulge component. It is obviously worth investigating whether this is the case for any structural galaxy component, a fact that would be consistent with the conjecture of bulge, disk and bar building up in a synchronous manner. As apparent from the bisector fits in Figure 4.9 the three above quantities are tightly correlated as:

$$\langle t_\star \rangle_{L,\mathrm{bulge}} = 4.6681 \times \log M_\star - 41.95 \tag{4.7}$$

$$\langle t_\star \rangle_{M,\mathrm{bulge}} = 3.1450 \times \log M_\star - 23.69 \tag{4.8}$$

$$\langle t_\star \rangle_{L,\mathrm{bulge}} = 12.699 \times \langle Z_\star \rangle_{L,\mathrm{bulge}} + 0.22 \tag{4.9}$$

$$\langle t_\star \rangle_{M,\mathrm{bulge}} = 8.5480 \times \langle Z_\star \rangle_{M,\mathrm{bulge}} + 4.21 \tag{4.10}$$

where $\langle t_\star \rangle_{bulge}$ is again given in Gyr, $M_\star$ in solar masses $M_\odot$ and $\langle Z_\star \rangle_{\mathrm{bulge}}$ in solar metallicities $Z_\odot$.

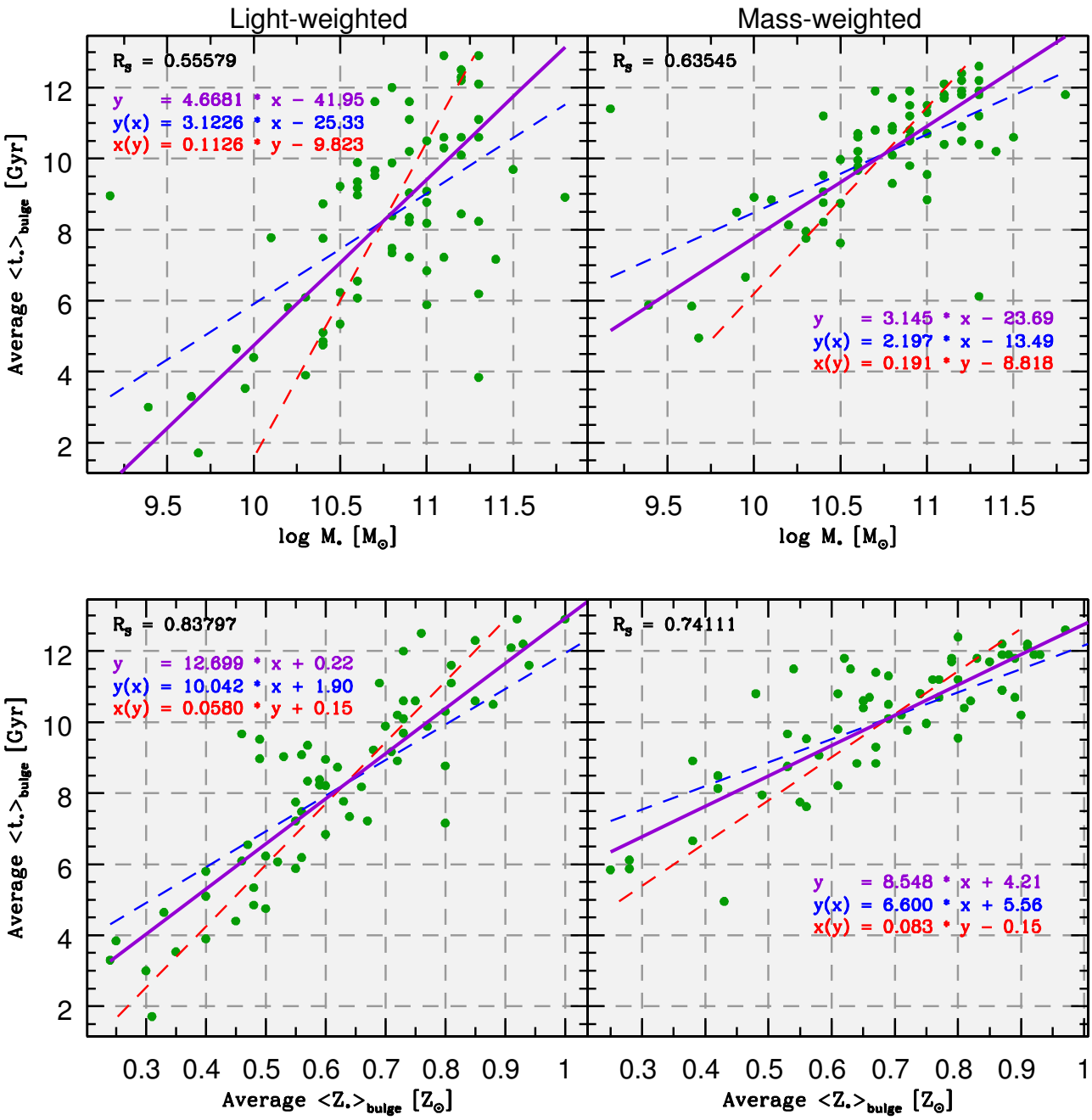

Figure 4.9: The average of the mean stellar age in the bulge region as a function of the total stellar mass of the galaxy (top) and the average of the mean stellar metallicity of the bulge (bottom). Luminosity- and mass-weighted quantities are in the left and right panels, respectively. These quantities show a strong correlation. In all plots, the violet solid line corresponds to the bisector linear regression method. The blue and red dashed lines are the usual linear regression fits $y(x)$ and $x(y)$, respectively.

Another relation to be investigated concerns the connection between the stellar age and the Hα equivalent width EW(Hα) of the bulge and the disk. EW(Hα) is a measure of the amplitude of ongoing star-forming activity, which in turn requires a gas supply of sufficient mass and surface density.

Going from integral to spatially resolved properties, we next inspect the EW(Hα) distribution, and its connection to the stellar age, separately in the bulge and in the disk. With regard to both, Figure 4.10 reveals a clear inverse trend, with old ($\sim$12 Gyr), massive and metal-rich (see Figure 4.9 and accompanying discussion) bulges showing an EW(Hα) $\lesssim$3 Å. This value is consistent with complete absence of ongoing star-forming activity and photoionization of gas purely by hot evolved (post-AGB) stars (e.g., Binette et al. (1994), Kehrig et al. (2012), Papaderos et al. (2013), Gomes et al. (2014)). On the opposite side of this sequence, one finds in Figure 4.10 bulges with an EW(Hα) exceeding 10 Åand a light- and mass-weighted stellar age being as low as $\sim$2 Gyr and $\sim$6 Gyr, respectively. Consideration of this extreme class of star-forming bulges together with the evidence from Figure 4.9 reveals that these entities are of low-luminosity and comparatively metal-poor. Summarizing, our analysis reveals a *local* downsizing trend, with more massive bulges evolving structurally and chemically faster than less massive ones, with the latter building up on much longer timescales and still sustaining significant star formation, in qualitative agreement with the secular formation scenario for pseudo-bulges. Interestingly, a similar trend is apparent from the lower panel of Figure 4.10 for the disk component, suggesting that old disks have efficiently converted most of their gas supply early on.

Bisector fits to our data yield the following relations:

$$\langle t_\star \rangle_{L,\mathrm{bulge}} = -4.4139 \times \log \mathrm{EW(H}\alpha)_{\mathrm{bulge}} + 11.88 \tag{4.11}$$

$$\langle t_\star \rangle_{M,\mathrm{bulge}} = -2.4999 \times \log \mathrm{EW(H}\alpha)_{\mathrm{bulge}} + 12.19 \tag{4.12}$$

$$\langle t_\star \rangle_{L,\mathrm{bulge}} = -6.7340 \times \log \mathrm{EW(H}\alpha)_{\mathrm{disk}} + 15.73 \tag{4.13}$$

$$\langle t_\star \rangle_{M,\mathrm{bulge}} = -4.1098 \times \log \mathrm{EW}(\mathrm{H}\alpha)_{\mathrm{disk}} + 14.70 \quad (4.14)$$

where the mean stellar age is given in Gyr and the Hα equivalent width in Å.

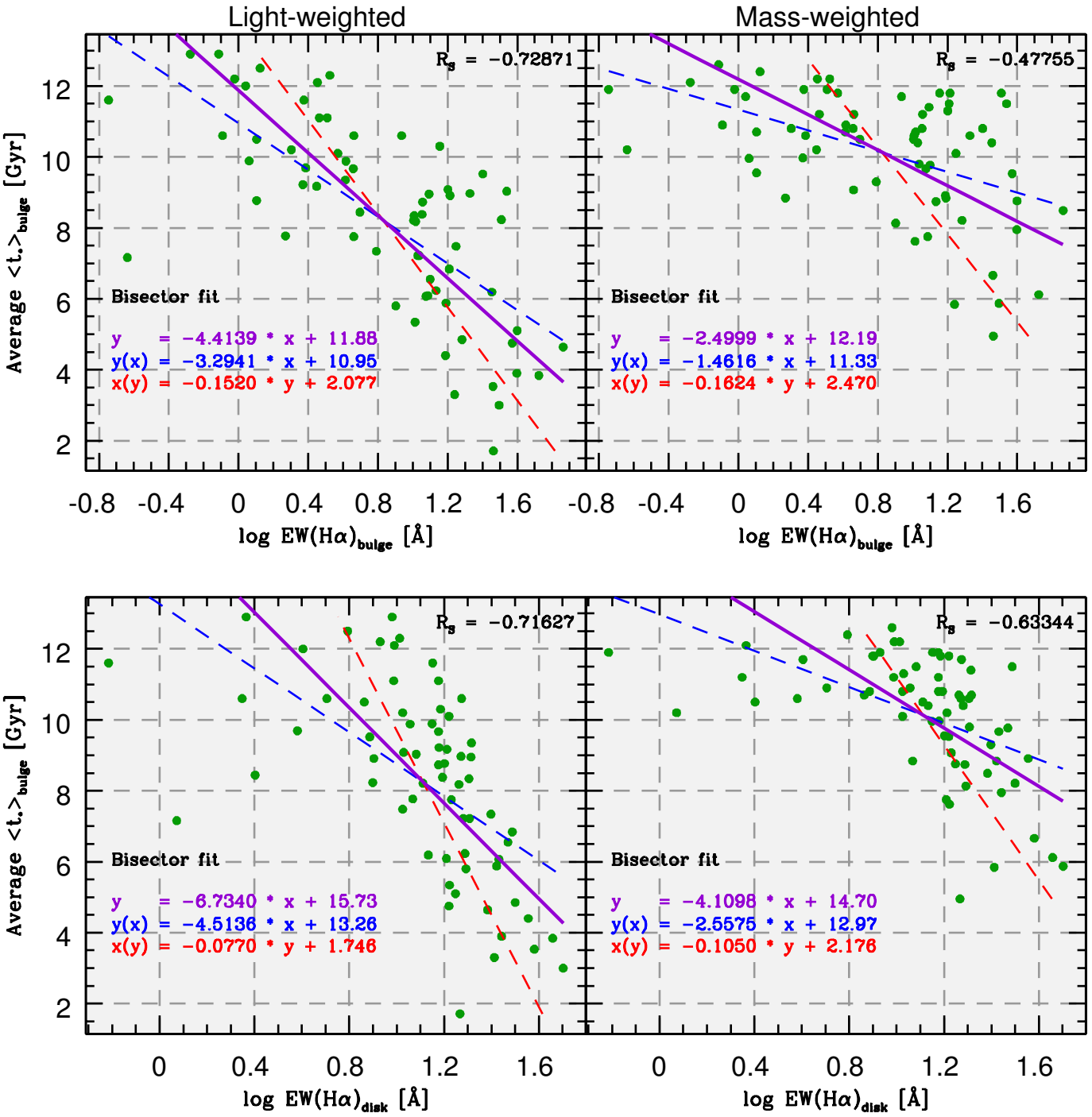

Figure 4.10: Equivalent width of Hα in emission versus average of the mean stellar age. Light- and mass-weighted quantities are respectively shown in the left and right panels, with the upper panel referring to the bulge and the lower panel to the disk. A clear correlation is apparent, indicating that the older is the bulge the lower is its bulge and disk Hα equivalent widths. The bisector linear regression method is shown through the violet solid lines. The dashed lines correspond the usual linear regression fits for $y(x)$ in blue and $x(y)$ in red.

The main results from this study may be summarized as follows: there is a strong trend for

increasing mean stellar age and metallicity in the bulge (both luminosity- and mass-weighted) with increasing galaxy stellar mass, bulge absolute magnitude and mean surface brightness (as expressed by μ_{80}) and mean stellar age in the disk. Additionally, the age of the bulge and the B/T are inversely related to the Hα equivalent width in the bulge.

Following our analysis to the age gradients, we show two histograms in Figure 4.11 for the mean stellar age gradient of the bulge weighted by light (solid line in blue) and mass (shaded area in red). We can see that they span a wide range of values from $\sim$ -16 to $\sim$ 12 in units of Gyr/$r_{\rm eff}$. The gradients were obtained by a linear fit to the data points corresponding to the bulge region. Therefore, a simple interpretation of the gradients is that whenever these values are positive we have an increase of the mean stellar age from the galactic center towards the periphery of the bulge and *vice versa*.

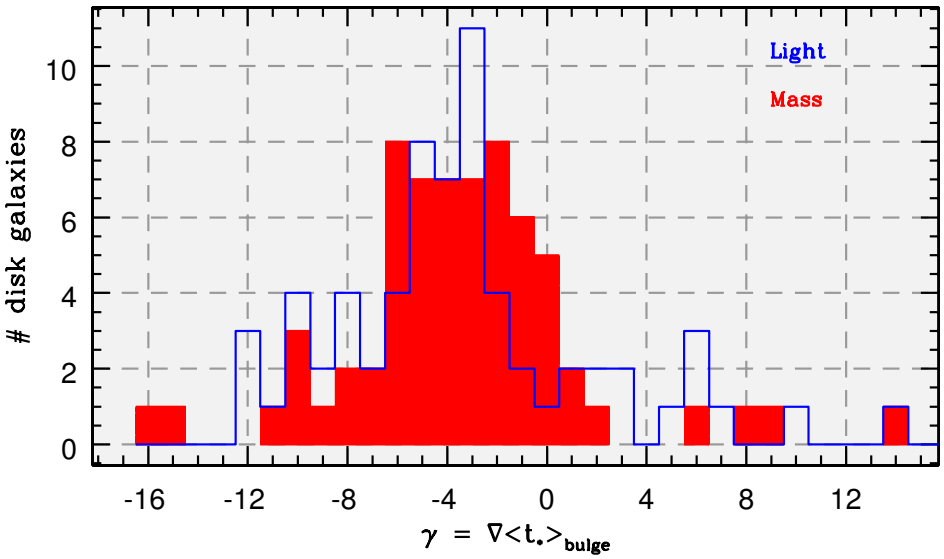

Figure 4.11: Histograms for the mean stellar age gradient of the bulge light-weighted (solid line in blue) and mass-weighted (shaded area in red). They span a huge set of values from $\sim$ -16 to $\sim$ 12 in units of Gyr/$r_{\rm eff}$. The gradients were obtained by a linear fit to the data points corresponding to the bulge region.

While investigating the age gradients pattern, we obtained weak trends with respect to the photometric/structural parameters and spectroscopic quantities. These trends can be considered and further analyzed in the framework of the four-class subdivision of our sample by Breda (2014) that primarily relies on the combined inspection of stellar metallicity and age gradients in bulges. The four classes envisaged in Breda (2014) are as follows:

Class 1 $\langle Z_\star \rangle_L$ (mean stellar metallicity) and $\langle t_\star \rangle_L$ (mean stellar age) gradients are positive: bar

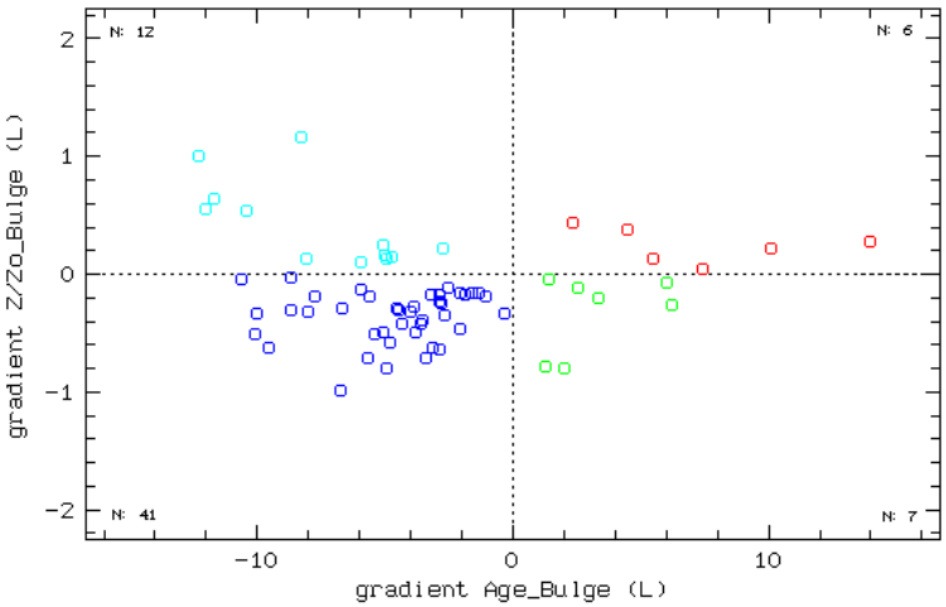

Figure 4.12: Distribution of the nature of the mean luminosity-weighted stellar gradients, both age and metallicity, in our entire sample of 66 late-type galaxies (units in Gyr/$r_{\rm eff}$ and dex/$r_{\rm eff}$, respectively). Red points correspond to Class 1 (both gradients are positive), blue points are for Class 2 (both gradients are negative), cyan points refer to Class 3 (negative age gradient and positive metallicity gradient) and green points correspond to Class 4 (positive age gradient and negative metallicity gradient). Image taken from Breda (2014).

dominated, with intermediate-to-low luminosity values ($\overline{\rm Mag_{bulge}} = -20.680$). The EW(H$\alpha$) of the bulge points to active star-formation bulges.

Class 2 $\langle Z_\star \rangle_L$ and $\langle t_\star \rangle_L$ gradients negative: faint to strong bars, with high luminosity values ($\overline{\rm Mag_{bulge}} = -21.449$). The three classical bulges (classified through the Sérsic index > 2) found in our sample belong to this class.

Class 3 $\langle Z_\star \rangle_L$ with positive gradient and $\langle t_\star \rangle_L$ with negative gradient: faint bars, with intermediate to high luminosity values ($\overline{\rm Mag_{bulge}} = -20.987$).

Class 4 $\langle Z_\star \rangle_L$ with negative gradient and positive gradient for $\langle t_\star \rangle_L$: strong or no bar, with low-to-intermediate luminosity values ($\overline{\rm Mag_{bulge}} = -20.602$), being actively forming stars.

However, the large dispersion found in **all** correlations involving radial age gradients, in most cases with a practically null R_S Spearman's rank coefficient (see Figure 4.13 for an example), suggests that an in-depth follow-up analysis is necessary for better understanding their origin and physical link to the evolutionary history of the bulge and the underlying disk. Important in this context is the fact that the large range of the determined age gradients suggests that they are extremely sensitive to the assembly history of bulges, making them potentially powerful diagnostics

of bulge formation and evolution. It should be noted, on the other hand, that wiggles seen in radial age profiles of many galaxies are suggestive of an underlying substructure in terms of multiple stellar populations with differing formation process. This substructure bears a resemblance to the embedded spiral or bar-like features found in bulges of early-type galaxies (e.g., Kehrig et al. (2012)), reaching, in many cases, only 1% of the total line-of-sight emission. Note that these features would be entirely missed if only (luminosity-weighted) colors (see Figure 4.14) were taken into account, the homogeneity of which could give the impression that a single coeval process has been responsible for the formation of the bulge component. The same applies to our results for the radial age profiles, where wiggles could reflect the presence of distinct stellar populations with differing SFHs. These considerations also suggest that simple linear fits to age profiles yield a merely first-order estimate of radial trends, and a multidimensional analysis is necessary for a full understanding of the origin of stellar age gradients in bulges. Whereas this is clearly beyond the scope of the present MSc thesis, it opens up a promising field of future investigation motivated and justified by the results of this study and those in Breda (2014).

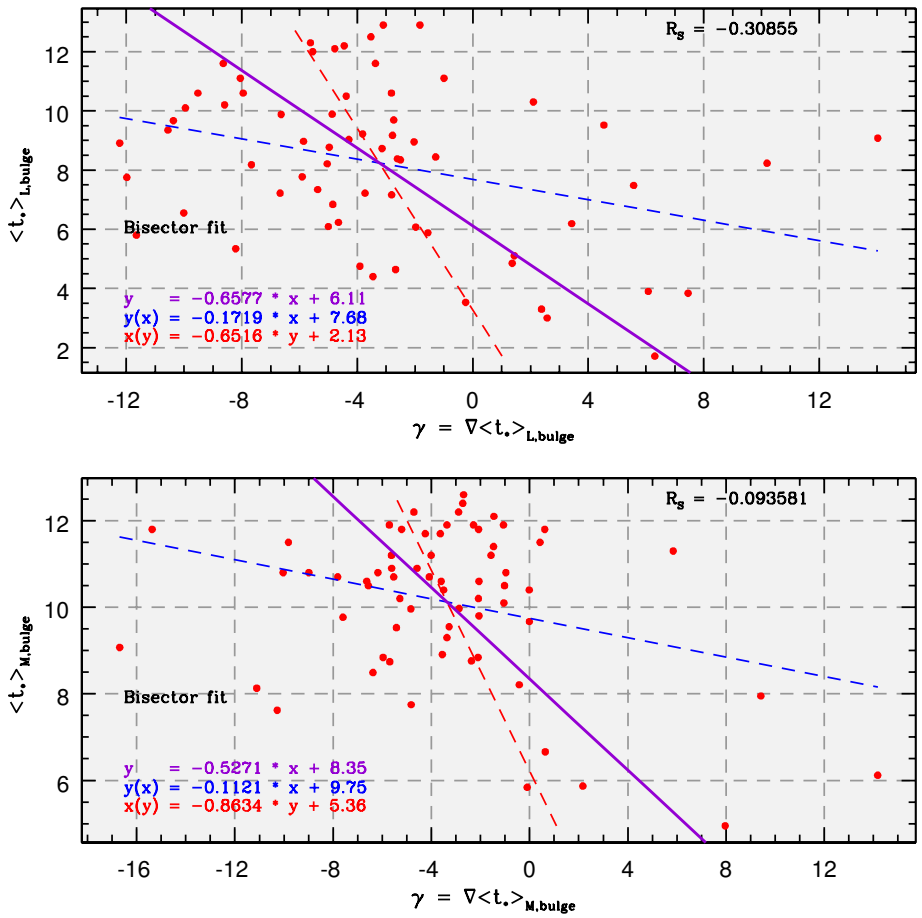

Figure 4.13: Mean stellar age as a function of the age gradient, both light- (top) and mass-weighted (bottom). A very weak correlation for the light-weighted and no correlation $R_S \sim 0$ for the mass-weighted quantities. The large spread indicates that a multidimensional analysis of the data is required to further investigate the relations with the age gradients.

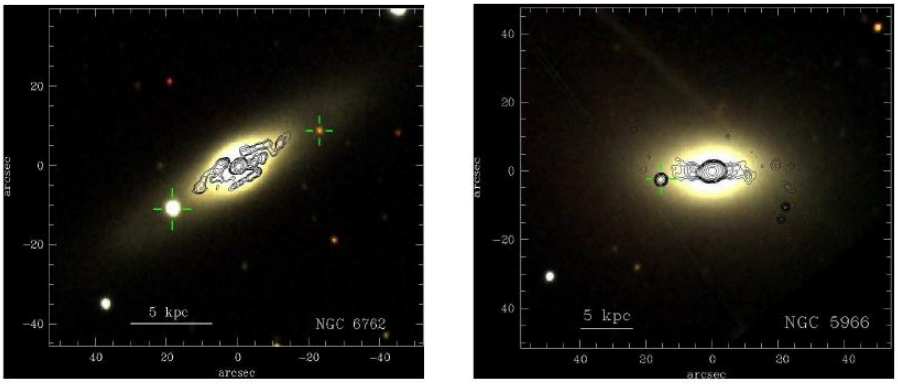

Figure 4.14: Three-color (g, r, and i) composite SDSS image of NGC 6762 and NGC 5966 from the CALIFA-IFU study on the warm interstellar medium in early-type galaxies (Kehrig et al. 2012). The contours delineate an extremely faint spiral- or bar-like feature disclosed by the unsharp-masking technique developed by Papaderos et al. (1998) in the bulge of the galaxies. To note that this features are not seen by only looking at the color images.

Chapter 5.

Summary and conclusions

This study employs a new methodology, which combines surface photometry with spectral synthesis, with the goal of gaining insight into the nature and formation history of pseudo-bulges in late-type galaxies.

The sample studied here consists of 66 nearly face on galaxies from the CALIFA integral field spectroscopy (IFS) survey, for which low-spectral resolution ($R \sim 850$) IFS data were modeled spaxel-by-spaxel with the automated spectral synthesis pipeline Porto3D (Section 3.2.2). Additionally, a structural analysis (Section 4.1) of this sample was performed using multiband imaging data from the Sloan Digital Sky Survey (SDSS).

Porto3D enabled us to study stellar age patterns in pseudo-bulges in a spatially resolved manner, based on a wealth of information that was extracted through spectral synthesis, such as the luminosity- and mass-weighted stellar age and metallicity, the mass fraction of stellar populations younger than 100 Myr, among others.

The photometric and structural analysis of the sample galaxies was performed with our in-house surface photometry code that permits derivation of surface brightness profiles (SBPs), and their decomposition into the luminosity contribution of the (pseudo)bulge, disk and bar component. A key feature of this code (see Breda (2014) for details) is the implementation of prescriptions allowing to mitigate the degeneracy between the Sérsic exponent η and the pseudo-scale length of Sérsic models. Besides η, this code permits determination of a multitude of photometric parameters, such as the apparent and absolute magnitude of the structural components considered in the

profile decomposition (bulge, disk and bar), the central surface brightness and exponential scale length of the disk, the mean surface brightness μ_{80} of the bulge within the radius enclosing 80% of its total luminosity, the effective radius $r_{\rm eff}$ and the isophotal radius $r_{\rm bulge}$ of the bulge component at 24 r mag/arcsec^2.

The main results and conclusions from this study may be summarized as follows:

- By adopting the widely used cutoff $\eta > 2$ for classical bulges and $\eta \lesssim 2$ for pseudo-bulges we identified only 3 classical bulges (NGC 5614, NGC 5656 and NGC 6004) in our sample. Furthermore, the galaxies NGC 0001, NGC 0023 and NGC 6278 have bulge-to-total light ratios between $1/3$ and $1/2$, and could be also classified as classical bulges. In approximately one half (35) of our sample galaxies a bar component was morphologically identified and included in the SBP decomposition in order to ensure a proper derivation of the photometric and structural properties of the bulge component.

- Using an adaptation of the *irregular annuli* surface photometry technique (Papaderos et al. 2002), we derived from the output of Porto3D radial profiles of various quantities of interest. These include the intensity of the emission-line free stellar continuum, the luminosity and mass fraction of the young stellar component with an age $\leq 10^8$ yr, and the luminosity- and mass-weighted stellar age. A follow-up analysis of these profiles within $r_{\rm bulge}$ was made with the goal of investigating the connection between the bulge mean stellar age and its radial gradient with the photometric/structural properties of late-type galaxies.

- The luminosity- and mass-weighted age of the stellar component within $r_{\rm bulge}$ was determined to be 8.2 Gyr (σ=2.7 Gyr) and 10.1 Gyr (σ=1.7 Gyr), respectively. On average, 0.23% of the stellar mass of (pseudo)bulges was built over the past 10^8 yr, a fact that, together with a low, yet not negligible Hα equivalent width (0.18 to 73.01 Å) indicates continuing growth of these entities through ongoing low-level star-forming activity. Pseudo-bulges, however, significantly differ from the disk component in their star formation history, being on average by $\sim$2.7 Gyr older with respect to their luminosity-weighted stellar age (5.534 $\pm$ 1.763 for the disk and 8.239 $\pm$ 2.707 for the bulge). We further find a clear trend for increasing bulge mean age with increasing bulge luminosity and compactness (as quantified by μ_{80}), as well

as with increasing galaxy stellar mass. This implies that the most massive and compact pseudo-bulges have assembled the bulk of their stellar mass early on, whereas the least massive/compact ones are forming over longer timescales. Interestingly, the mass-weighted age of the faintest bulges in our sample is as low as $\lesssim 10^8$ yr, suggesting rapid growth of the stellar mass at a late cosmic epoch. This downsizing trend is consistent with the hypothesis of the secular buildup of pseudo-bulges. Our analysis also indicates that the age of pseudo-bulges tightly correlates with their stellar metallicity. Taken all this together, the star formation and chemical enrichment history of pseudo-bulges appears to be governed both by their mass and stellar mass density.

- On average, light- and mass-weighted age gradients in pseudo-bulges show a large dispersion ($\sigma \sim 5$) of values around -3.3 Gyr/$r_{\rm eff}$ with no obvious correlation with integral or structural properties of galaxies. The fact that our sample galaxies show in their majority *negative* age gradients in their pseudo-bulge component hints at an inside-out formation scenario.

The analysis carried out here has demonstrated the feasibility of the methodology adopted in this project and contributes important observational constraints towards a better understanding of the formation history of pseudo-bulges.

5.1 OUTLOOK

This pioneer work takes advantage of surface photometry combined with spatially resolved analysis of stellar populations, allowing us to determine several structural and spectral synthesis parameters for the bulge component of our galaxy sample. However, there are several improvements foreseen in future works that can be summarized as follows:

- Use an improved decomposition scheme for the Surface Brightness Profiles to better estimate the physical properties of the bulge component.
- Extend the statistical analysis done in this work to the disk component.
- Do statistical analysis of the correlations between photometric and spectroscopic quantities.

- Do multidimensional analysis to investigate age and age gradients as a function of structural and spectral synthesis parameters.
- Increase the main galaxy sample of 63 pseudo-bulge galaxies.
- Select a comparison sample of classical bulges.
- Investigate the mass assembly history of pseudo-bulges as compared to classical bulges.

Bibliography

Abazajian K. N., Adelman-McCarthy J. K., Agueros M. A., Allam S. S., Allende Prieto C., An D., Anderson K. S. J., Anderson S. F., Annis J., Bahcall N. A., et al. 2009, ApJS, 182, 543

Allington-Smith J. R., Content R., Haynes R., 1998, in D'Odorico S., ed., Proc. SPIE Vol. 3355, p. 196-205

Baade, W. 1944, ApJ, 100, 137

Baldwin, J. A., Phillips, M. M., & Terlevich, R. 1981, PASP, 93, 5

Bender, R. & Moellenhoff. C., 1987, A&A, 177,71

Bender, R., Burstein, D., & Faber, S. M. 1992, ApJ, 399, 462B

Binette L., Magris C. G., Stasińska G., Bruzual A. G., 1994, A&A, 292, 13

Bournaud, F., Perret, V., Renaud, F., et al. 2014, ApJ, 780, 57

Bouwens, R., Cayón, L., & Silk, J. 1999, ApJ, 516, 77

Breda, I. 2014, in *On the metallicity of pseudo-bulges in the CALIFA galaxy Survey* Master Thesis

Bruzual G., Charlot S., 2003, MNRAS, 344, 1000

Buta, R. J. 2011, in *Planets, Stars, and Stellar Systems*, Vol. 6, Series Editor T. D. Oswalt, Volume editor W. C. Keel, Springer (arXiv:1102.0550)

Capaccioli, M. 1989, in *The World of Galaxies*, ed. H. G. Corwin, L. Bottinelli (Berlin: Springer-Verlag), 208

Castro R., Santiago B. X., Gilmore G. F., Beaulieu S., Johnson R. A., 2001, MNRAS, 326, 333

Cid Fernandes, R., Mateus, A., Sodré, L., Stasińska, G., Gomes, J.M. 2005, MNRAS, 358, 363

Ciotti, L. 1991, A&A, 249, 99

de Vaucouleurs, G. 1948, Annales d'Astrophysique, 11, 247

de Vaucouleurs, G. 1959, in *Handbuch der Physick*, Vol. 53, p. 275

Drory N., Fisher D. B., 2007, ApJ, 664, 640

Eggen OJ, Lynden-Bell D, Sandage AR., 1962, AJ, 136:748

Faber, S. M., and Jackson, R. E. 1976, AJ, 204, 668

Fernández Lorenzo, M., Sulentic, J., Verdes-Montenegro, L., et al. 2014, ApJ, 788, L39

Fisher, D. B. & Drory, N. 2008, AJ, 136, 773

Freeman, K. C. 1970, ApJ, 160, 811

Genzel, R., Burkert, A., Bouché, N., et al. 2008, ApJ, 687, 59

Giovanelli, R., Haynes, M. P., Salzer, J. J., et al. 1995, AJ, 110, 1059

Giovanelli, R., Haynes, M. P., Herter, T., et al. 1997, AJ, 113, 22

Girardi L., Bressan A., Bertelli G., Chiosi C., 2000, A&AS, 141, 371

Gomes, J. M., Papaderos, P. et al. 2014 A&A, received

Graham A.W., Erwin, P., Trujillo, I., Asensio Ramos, A. 2003, AJ, 125, 2951

Gunn, J. E., et al. 2006, AJ, 131, 2332

Hubble, E. P. 1936, in *Realm of the Nebulae*, Yale University Press

Husemann, B., Jahnke, K., Sánchez, S. F., et al. 2013, A&A, 549, A87

Isobe T., Feigelson E. D., Akritas M. G., Babu G. J., 1990, ApJ, 364, 104

Johnston E. J., Aragon-Salamanca A., Merrifield M. R., Bedregal A. G., 2012, MNRAS, 422; 2590-2599

Kehrig, C., Monreal-Ibero, A. & Papaderos, P. et al. 2012, A&A, 540, 11

Kelz, A., Verheijen, M.A.W., Roth, M.M. et al. 2006, PASP, 118, 129

Kennicutt, R. C. Jr, 1998, ARA&A, 36, 189

Kormendy J, Illingworth G., 1982, AJ, 256:460

Kormendy J., Kennicutt, Jr. R. C., 2004, ARA&A, 42, 603

Lupton, R., Blanton, M. R., Fekete, G., et al. 2004, PASP, 116, 133

MacArthur, L. A., González, J. J., & Courteau, S. 2009, MNRAS, 395, 28

Mateus, A., Sodré, L., Cid Fernandes, R., et al. 2006, MNRAS, 370, 721

Noeske, K. G., Papaderos, P., Cairós, L. M., & Fricke, K. J. 2003, A&A, 410, 481

Papaderos, P., Loose, H.-H., Fricke, K.J., Thuan, T.X. 1996, A&A 314, 59

Papaderos, P., Loose, H.-H., Fricke, K.J., Thuan, T.X., 1998, A&A 338, 43

Papaderos, P., Izotov, Y. I., Thuan, T. X. et al. 2002 A&A, 393, 461

Papaderos, P., Gomes, J. M., Vílchez, J. M., et al. 2013, A&A, 555, L1

Peng, C. Y., Ho, L. C., Impey, C. D., & Rix, H.-W. 2010, AJ, 139, 209

Renzini A. 1999. In *The Formation of Galactic Bulges*, ed. CM Carollo, HC Ferguson, RFG Wyse, p. 9. Cambridge: Cambridge Univ. Press

Roth, M.M., Kelz, A., Fechner, T. et al. 2005, PASP, 117, 620

Salpeter E.E., 1955, ApJ, 121, 161

Sánchez, S. F., Kennicutt, R. C., Gil de Paz, A., et al. 2012a, A&A, 538, A8

Sánchez-Blázquez, P., Ocvirk, P., Gibson, B. K., Pérez, I., & Peletier, R. F. 2011, MNRAS, 415, 709

Sánchez-Janssen R. et al., 2013, A&A, 554, A20

Sarzi M., et al., 2010, MNRAS, 402, 2187

Schlafly, E. & Finkbeiner, D. 2011, ApJ, 737, 103

Sérsic, J. L. 1963, In *Boletin de la Asociacion Argentina de Astronomia La Plata Argentina*, 6, 41

Sérsic, J. L. 1968, in *Atlas de Galaxias Australes* (Cordoba, Argentina: Observatorio Astronomico)

L.S. Sparke, J.S. Gallagher, III, 2007, in *Galaxies in the Universe: An Introduction* (Cambridge University Press, Cambridge)

Spearman C., 1904 The proof and measurement of association between two things. Am J Psychol 1904; 15:72–101.

Strateva, I., Ivezić, Ž., Knapp, G. R., et al. 2001, AJ, 122, 1861

Tremonti, C. A. et al. 2004, ApJ, 613, 898

Walcher, C. J., Wisotzki, L., Bekeraité, S., et al. 2014, A&A, 569, A1

Westmoquette, M. S., Exter, K. M., Christensen, L., Maier, M., Lemoine-Busserolle, M., Turner, J., Marquart, T., 2009. The integral field spectroscopy (ifs) wiki. arXiv 0905, 3054

York, D. G., Adelman, J., Anderson, Jr., J. E., et al. 2000, AJ, 120, 1579

Appendix A.

Color Maps

Figure A.1 shows a) the true-color image, b) the logarithmic mean of the three SDSS filters gri, c) the color map $r - i$, d) the color map $g - r$.

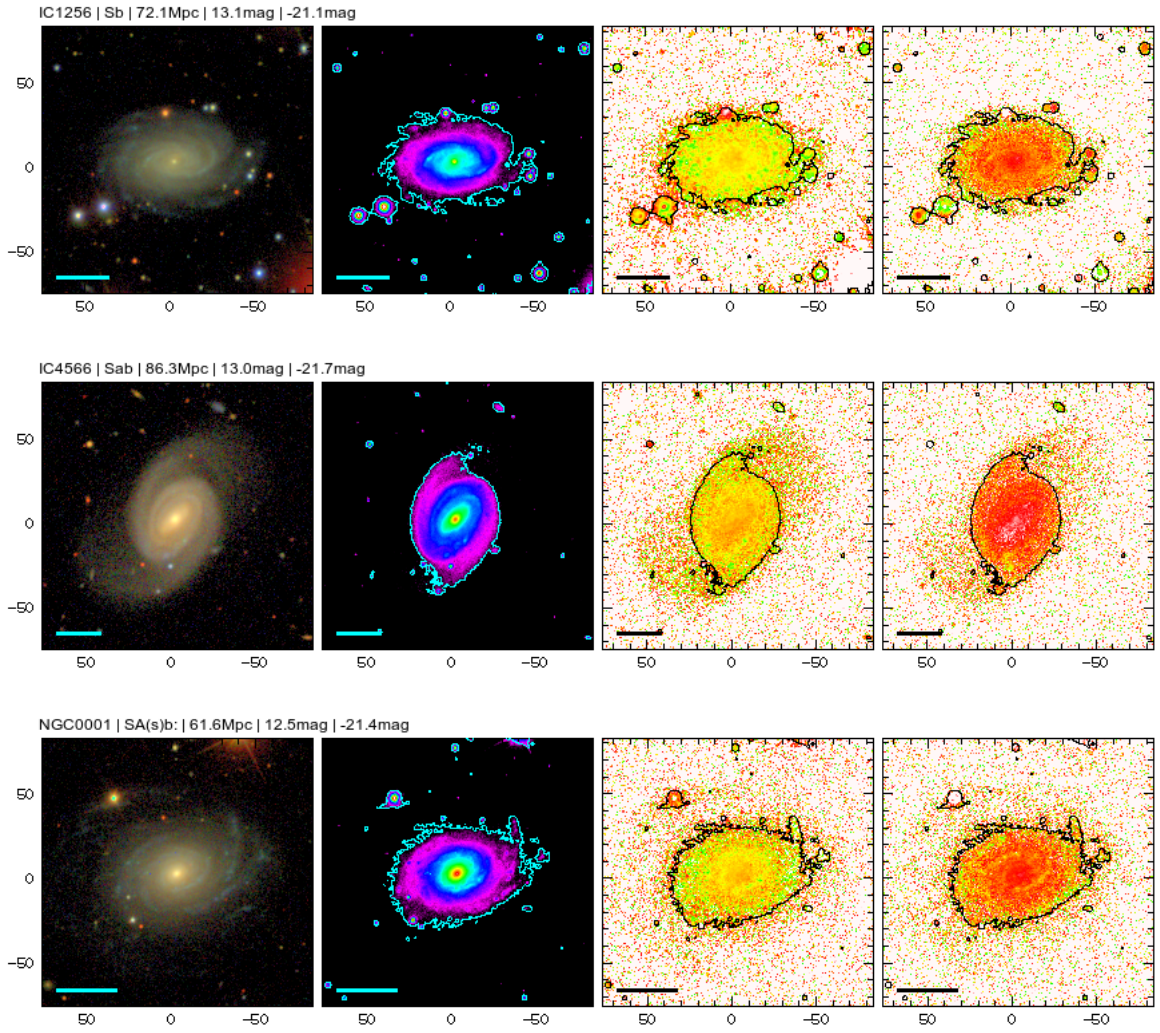

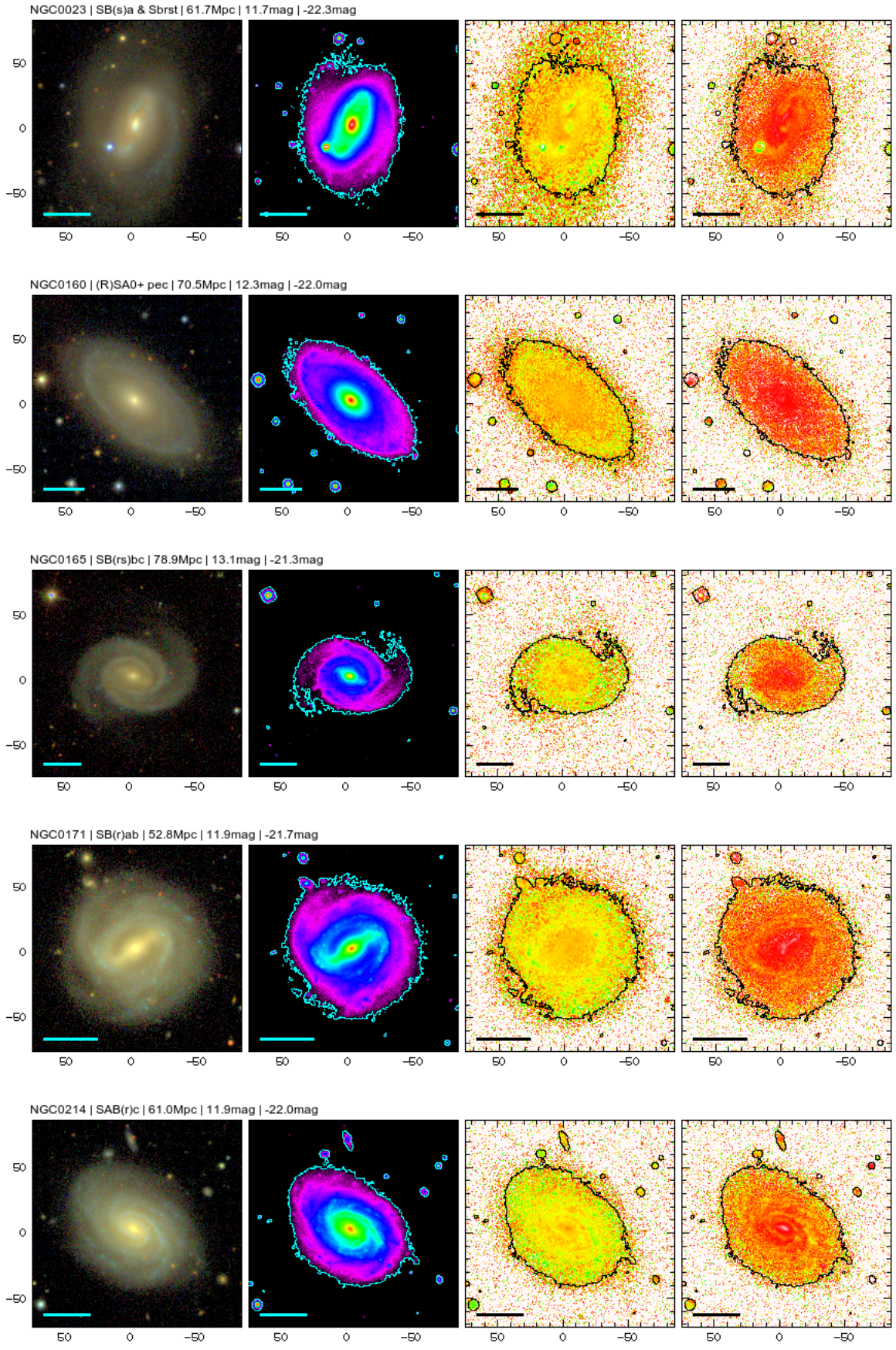
NGC0023 | SB(s)a & Sbrst | 61.7Mpc | 11.7mag | -22.3mag
NGC0160 | (R)SA0+ pec | 70.5Mpc | 12.3mag | -22.0mag
NGC0165 | SB(rs)bc | 78.9Mpc | 13.1mag | -21.3mag
NGC0171 | SB(r)ab | 52.8Mpc | 11.9mag | -21.7mag
NGC0214 | SAB(r)c | 61.0Mpc | 11.9mag | -22.0mag
50
0
−50

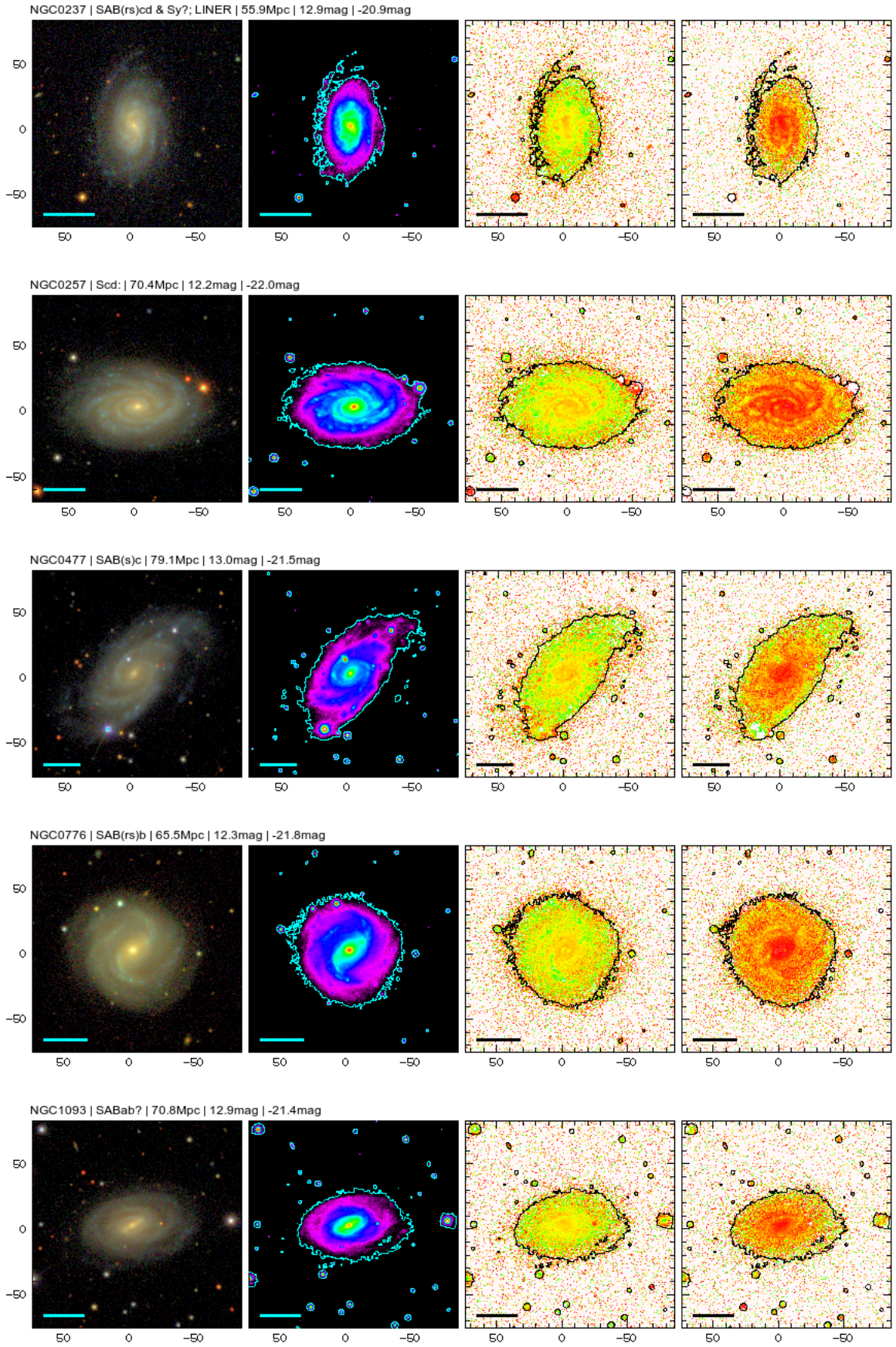
NGC0237 | SAB(rs)cd & Sy?; LINER | 55.9Mpc | 12.9mag | -20.9mag
NGC0257 | Scd: | 70.4Mpc | 12.2mag | -22.0mag
NGC0477 | SAB(s)c | 79.1Mpc | 13.0mag | -21.5mag
NGC0776 | SAB(rs)b | 65.5Mpc | 12.3mag | -21.8mag
NGC1093 | SABab? | 70.8Mpc | 12.9mag | -21.4mag
50
0
−50

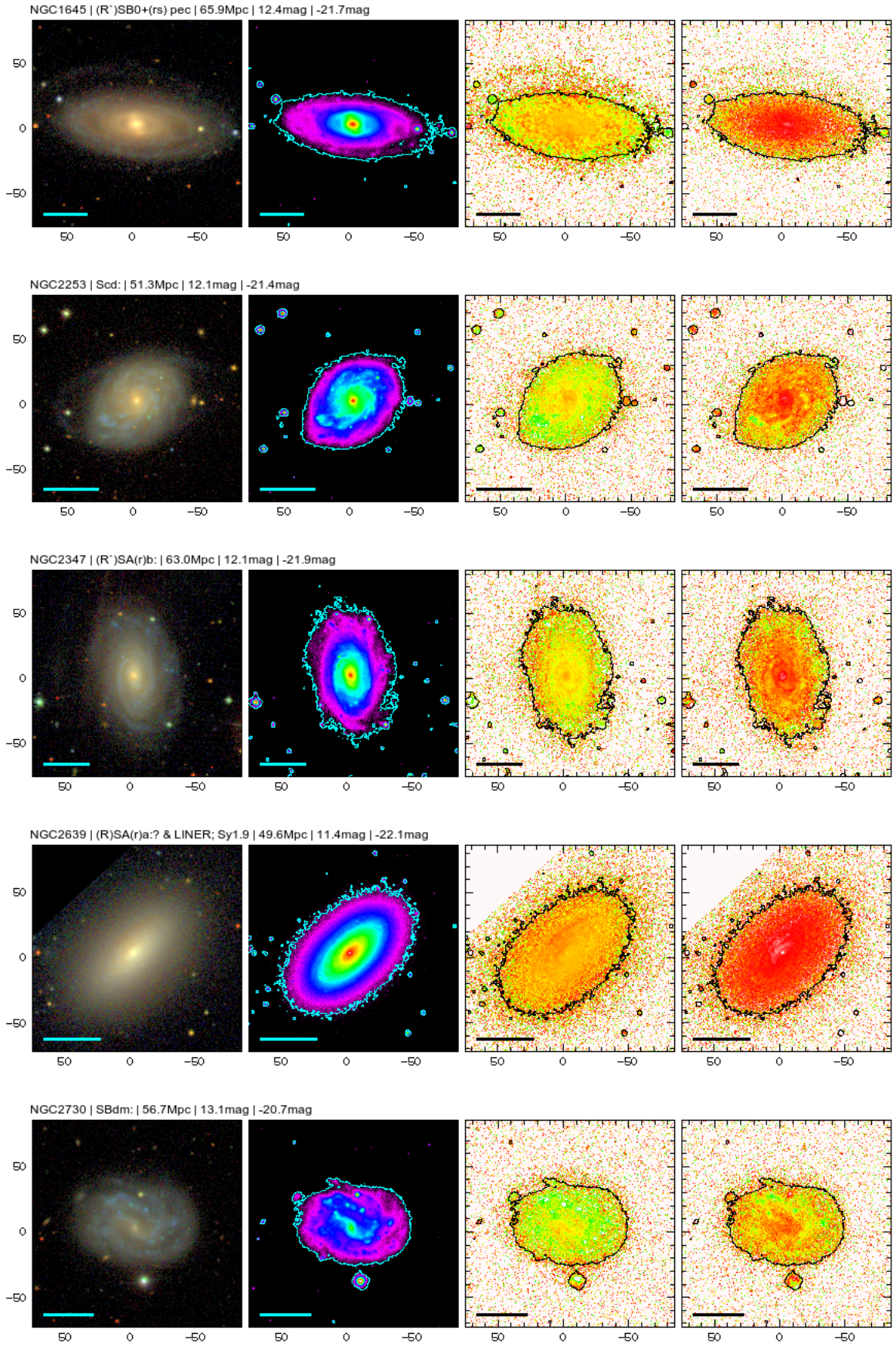
NGC1645 | (R`)SB0+(rs) pec | 65.9Mpc | 12.4mag | -21.7mag
NGC2253 | Scd: | 51.3Mpc | 12.1mag | -21.4mag
NGC2347 | (R`)SA(r)b: | 63.0Mpc | 12.1mag | -21.9mag
NGC2639 | (R)SA(r)a:? & LINER; Sy1.9 | 49.6Mpc | 11.4mag | -22.1mag
NGC2730 | SBdm: | 56.7Mpc | 13.1mag | -20.7mag
50
0
−50

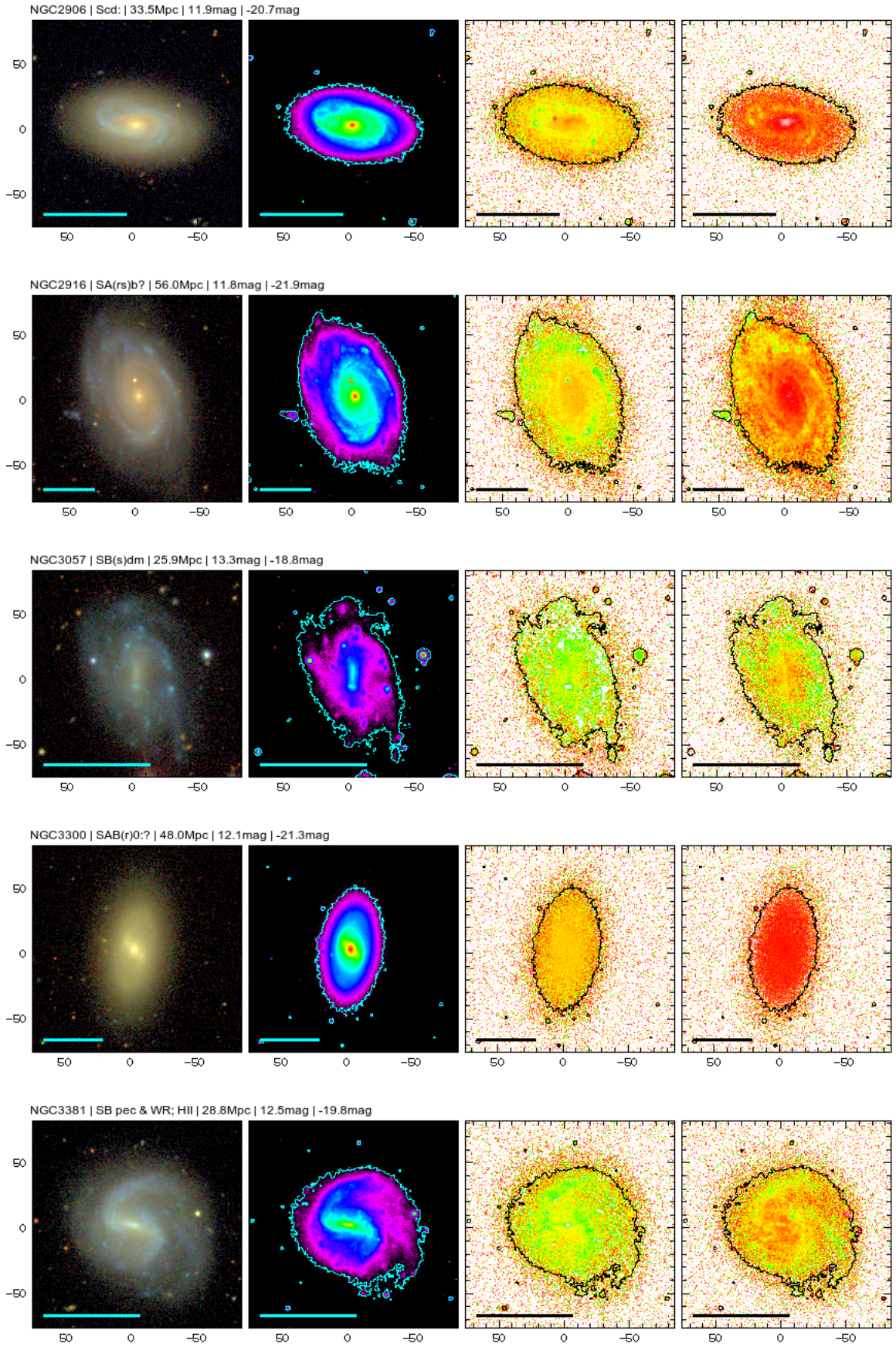
NGC2906 | Scd: | 33.5Mpc | 11.9mag | -20.7mag
NGC2916 | SA(rs)b? | 56.0Mpc | 11.8mag | -21.9mag
NGC3057 | SB(s)dm | 25.9Mpc | 13.3mag | -18.8mag
NGC3300 | SAB(r)0:? | 48.0Mpc | 12.1mag | -21.3mag
NGC3381 | SB pec & WR; HII | 28.8Mpc | 12.5mag | -19.8mag
50
0
−50

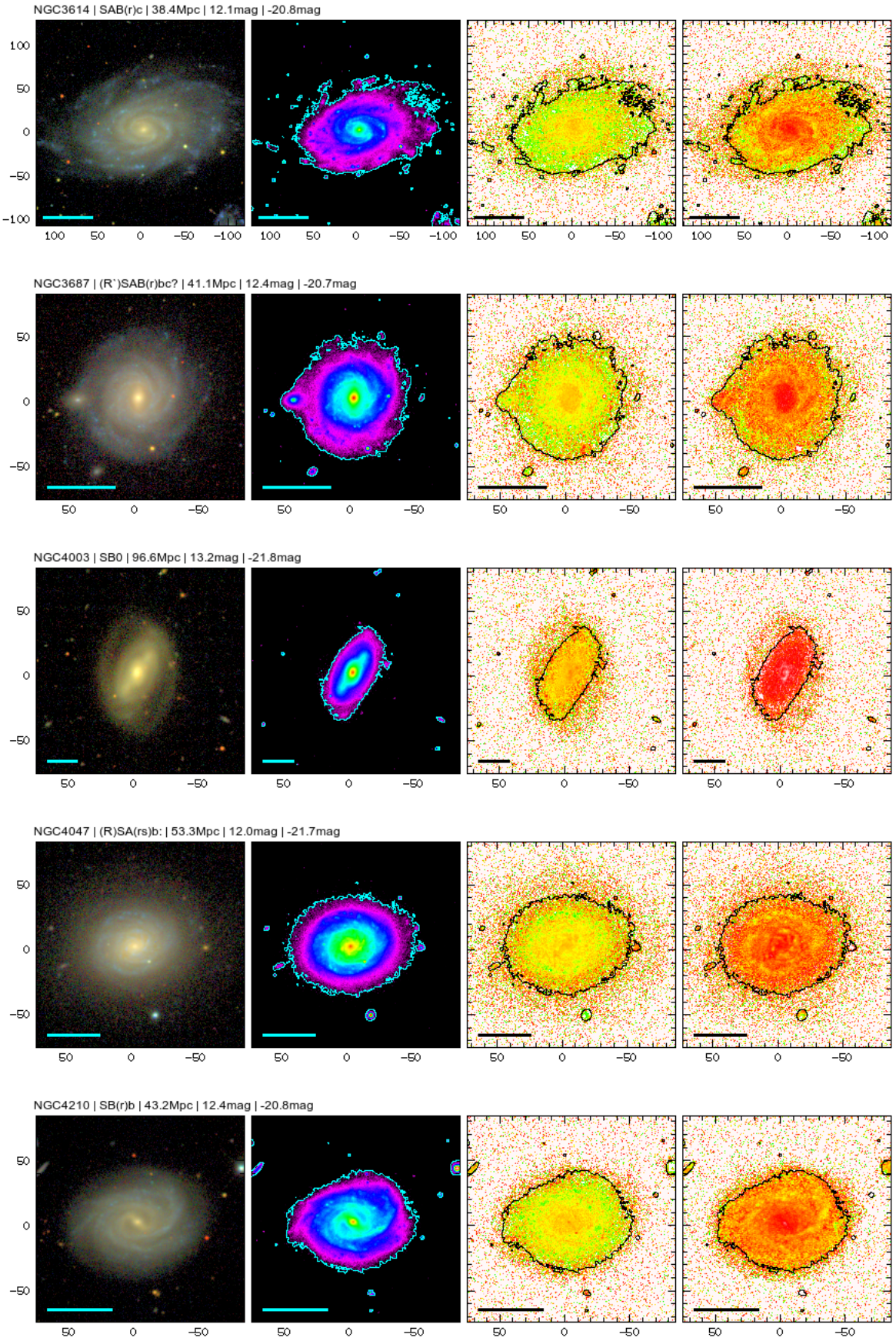
NGC3614 | SAB(r)c | 38.4Mpc | 12.1mag | -20.8mag
NGC3687 | (R')SAB(r)bc? | 41.1Mpc | 12.4mag | -20.7mag
NGC4003 | SB0 | 96.6Mpc | 13.2mag | -21.8mag
NGC4047 | (R)SA(rs)b: | 53.3Mpc | 12.0mag | -21.7mag
NGC4210 | SB(r)b | 43.2Mpc | 12.4mag | -20.8mag

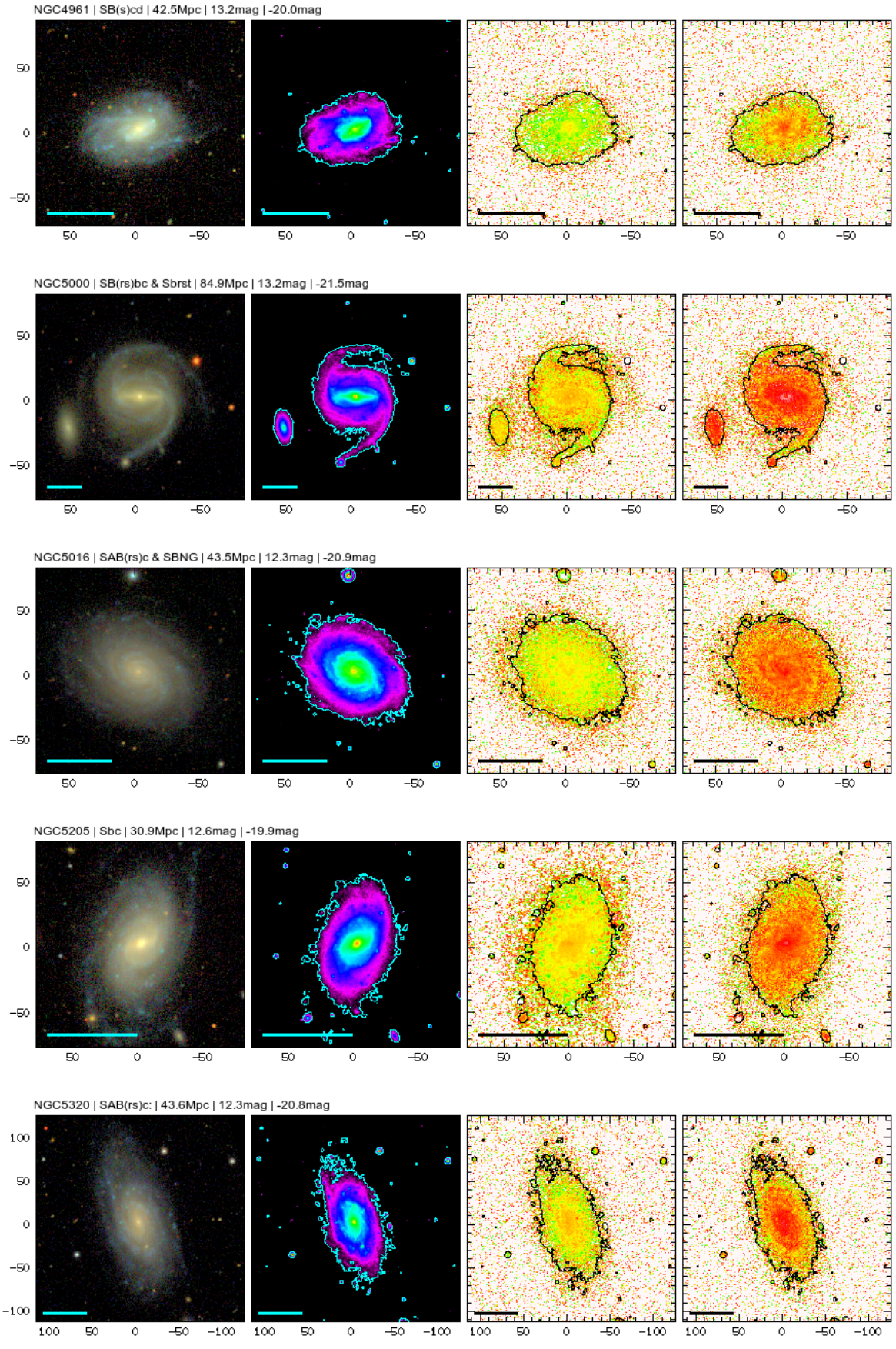
NGC4961 | SB(s)cd | 42.5Mpc | 13.2mag | -20.0mag
NGC5000 | SB(rs)bc & Sbrst | 84.9Mpc | 13.2mag | -21.5mag
NGC5016 | SAB(rs)c & SBNG | 43.5Mpc | 12.3mag | -20.9mag
NGC5205 | Sbc | 30.9Mpc | 12.6mag | -19.9mag
NGC5320 | SAB(rs)c: | 43.6Mpc | 12.3mag | -20.8mag

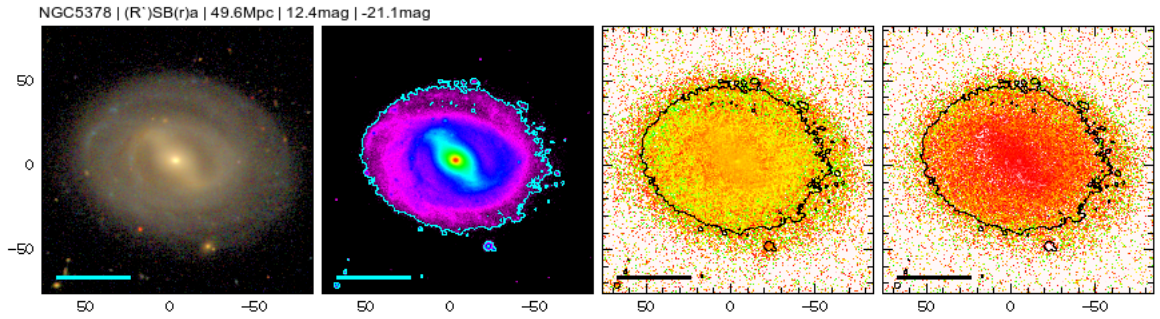
NGC5378 | (R`)SB(r)a | 49.6Mpc | 12.4mag | -21.1mag
50
0
−50
50
0
−50
50
0
−50
50
0
−50

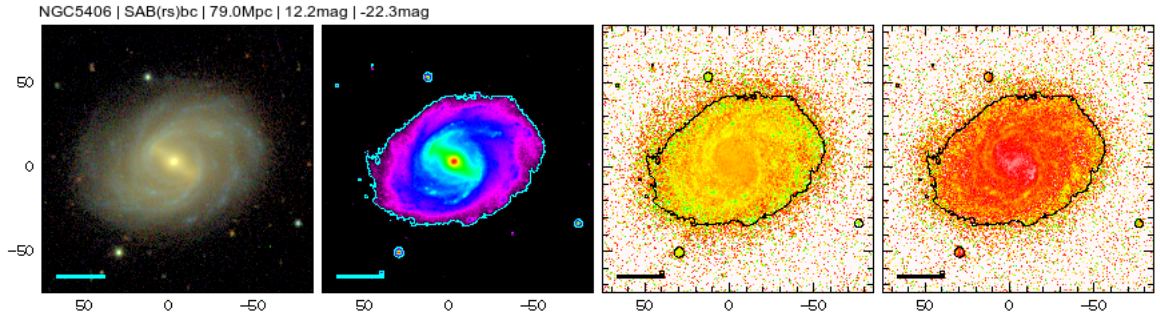
NGC5406 | SAB(rs)bc | 79.0Mpc | 12.2mag | -22.3mag
50
0
−50
50
0
−50
50
0
−50
50
0
−50

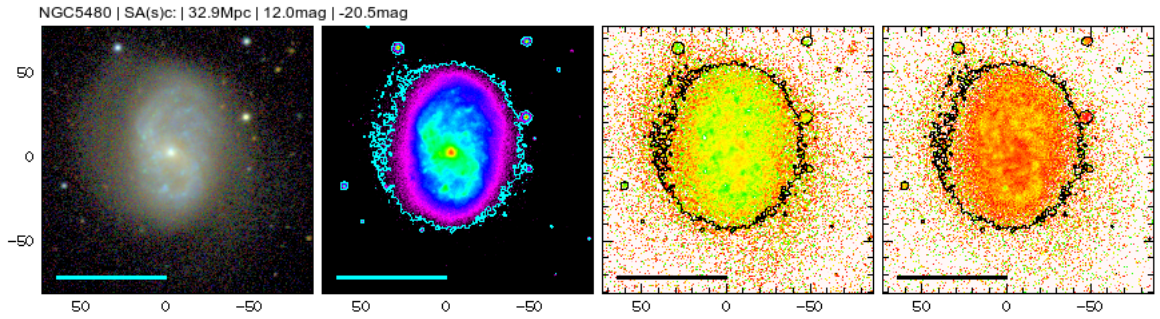
NGC5480 | SA(s)c: | 32.9Mpc | 12.0mag | -20.5mag
50
0
−50
50
0
−50
50
0
−50
50
0
−50

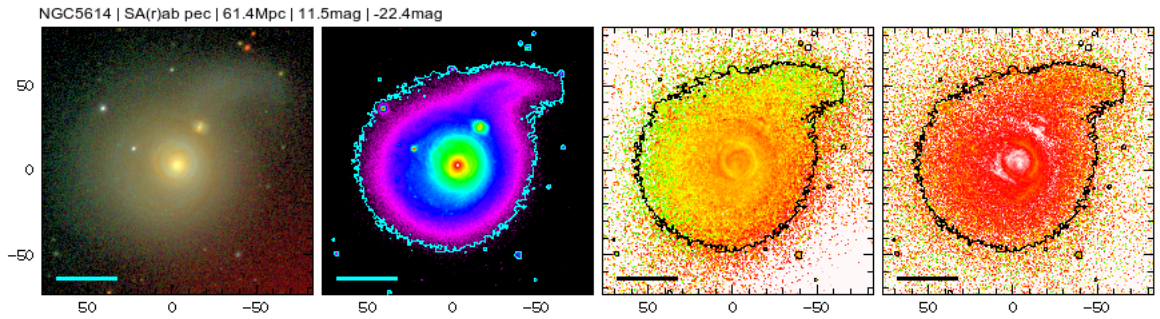
NGC5614 | SA(r)ab pec | 61.4Mpc | 11.5mag | -22.4mag
50
0
−50
50
0
−50
50
0
−50
50
0
−50

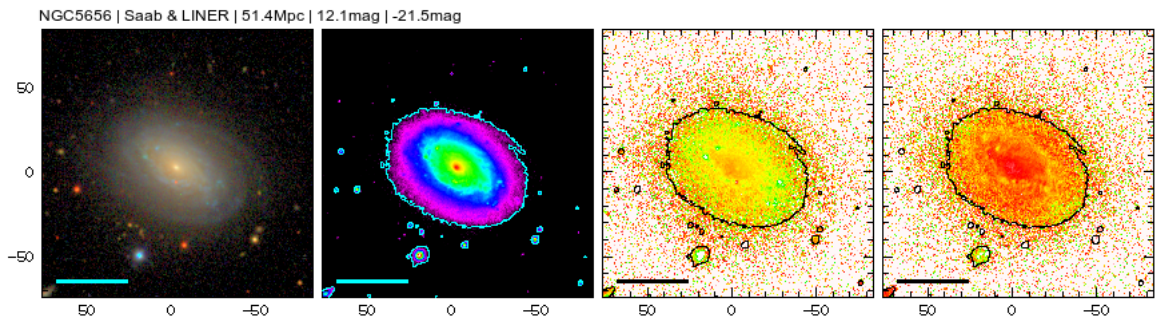
NGC5656 | Saab & LINER | 51.4Mpc | 12.1mag | -21.5mag
50
0
−50
50
0
−50
50
0
−50
50
0
−50

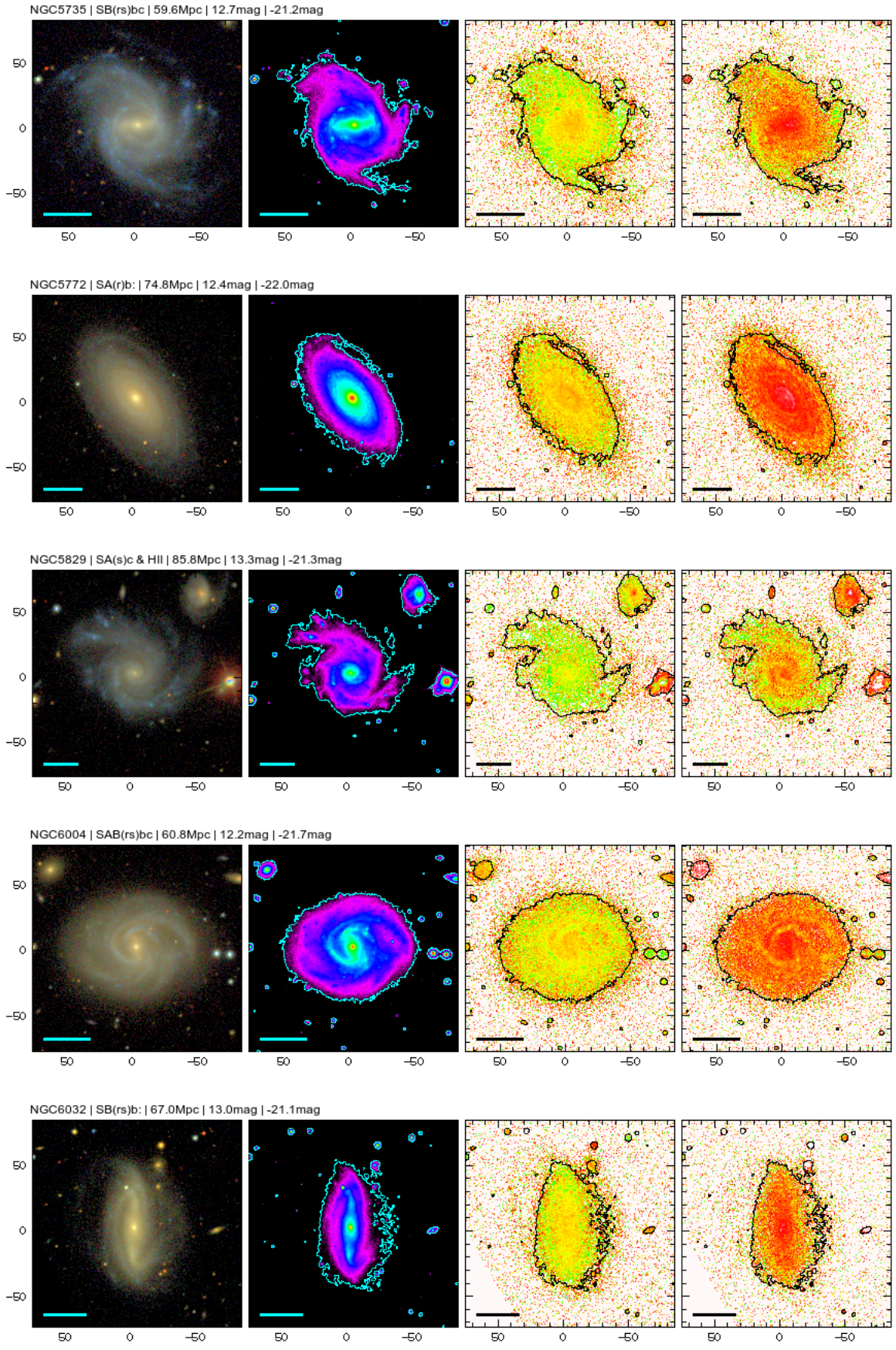
NGC5735 | SB(rs)bc | 59.6Mpc | 12.7mag | -21.2mag
NGC5772 | SA(r)b: | 74.8Mpc | 12.4mag | -22.0mag
NGC5829 | SA(s)c & HII | 85.8Mpc | 13.3mag | -21.3mag
NGC6004 | SAB(rs)bc | 60.8Mpc | 12.2mag | -21.7mag
NGC6032 | SB(rs)b: | 67.0Mpc | 13.0mag | -21.1mag
50
0
−50

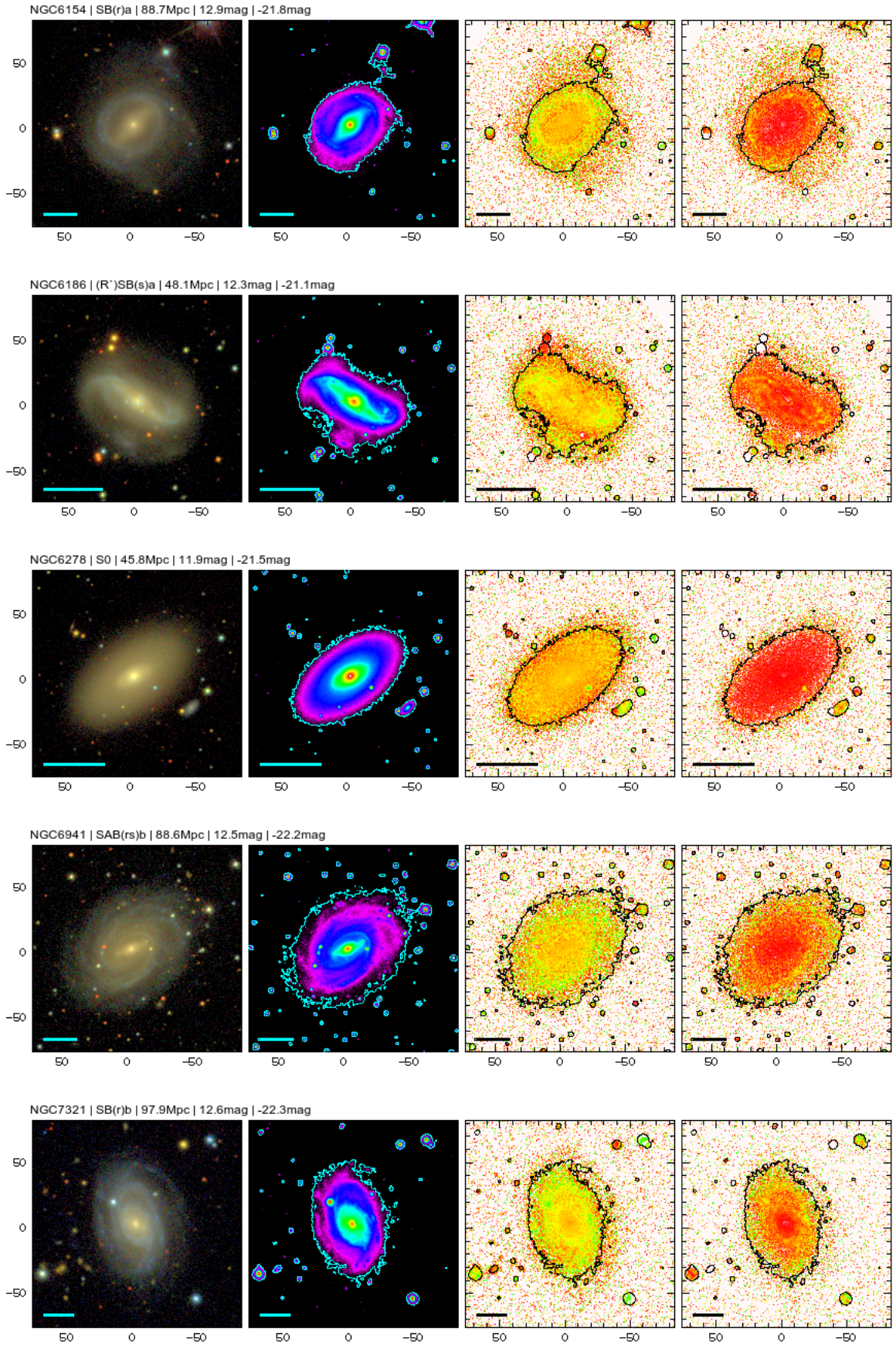
NGC6154 | SB(r)a | 88.7Mpc | 12.9mag | -21.8mag
NGC6186 | (R')SB(s)a | 48.1Mpc | 12.3mag | -21.1mag
NGC6278 | S0 | 45.8Mpc | 11.9mag | -21.5mag
NGC6941 | SAB(rs)b | 88.6Mpc | 12.5mag | -22.2mag
NGC7321 | SB(r)b | 97.9Mpc | 12.6mag | -22.3mag
50
0
−50

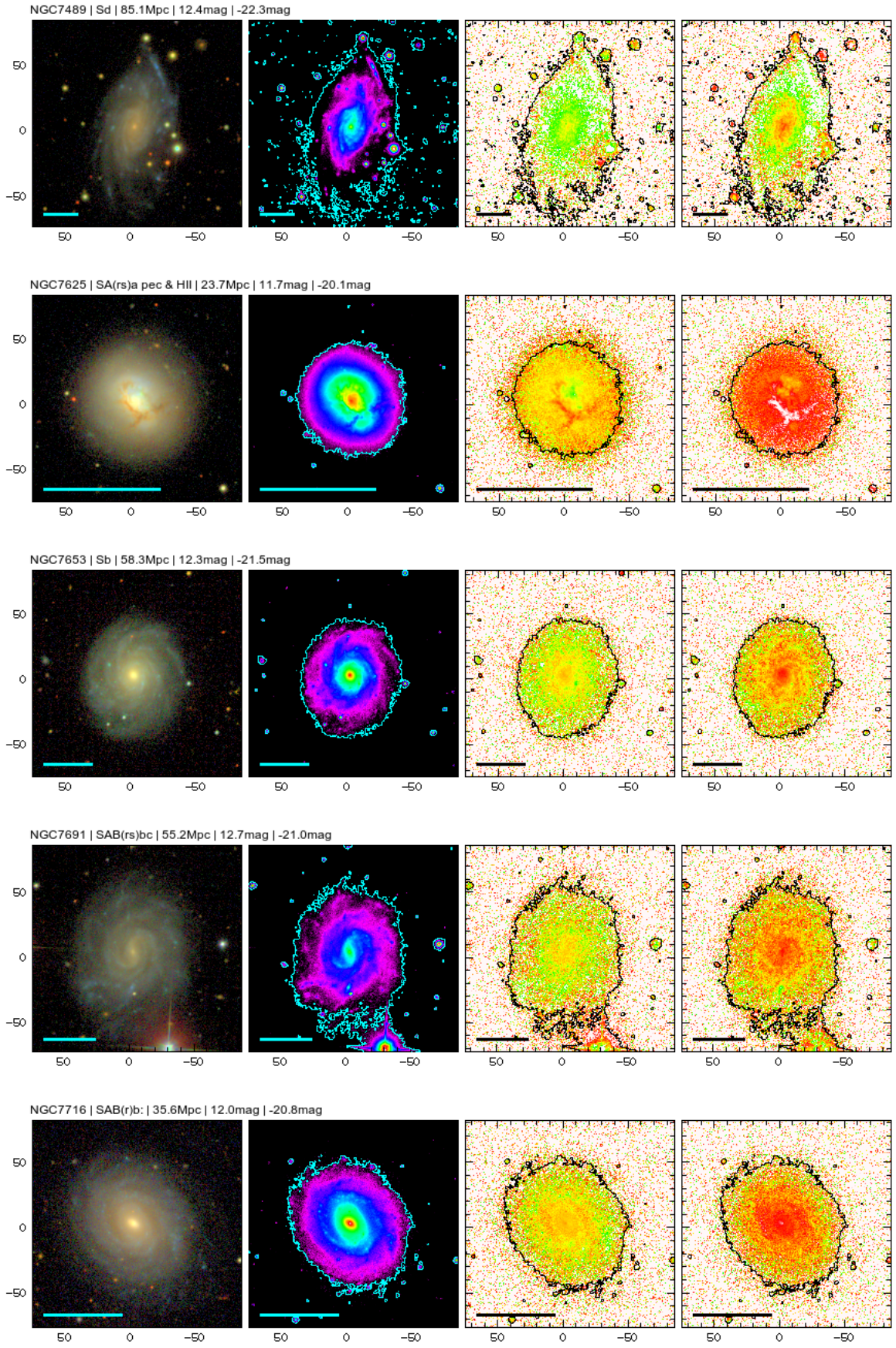
NGC7489 | Sd | 85.1Mpc | 12.4mag | -22.3mag
NGC7625 | SA(rs)a pec & HII | 23.7Mpc | 11.7mag | -20.1mag
NGC7653 | Sb | 58.3Mpc | 12.3mag | -21.5mag
NGC7691 | SAB(rs)bc | 55.2Mpc | 12.7mag | -21.0mag
NGC7716 | SAB(r)b: | 35.6Mpc | 12.0mag | -20.8mag
50
0
−50

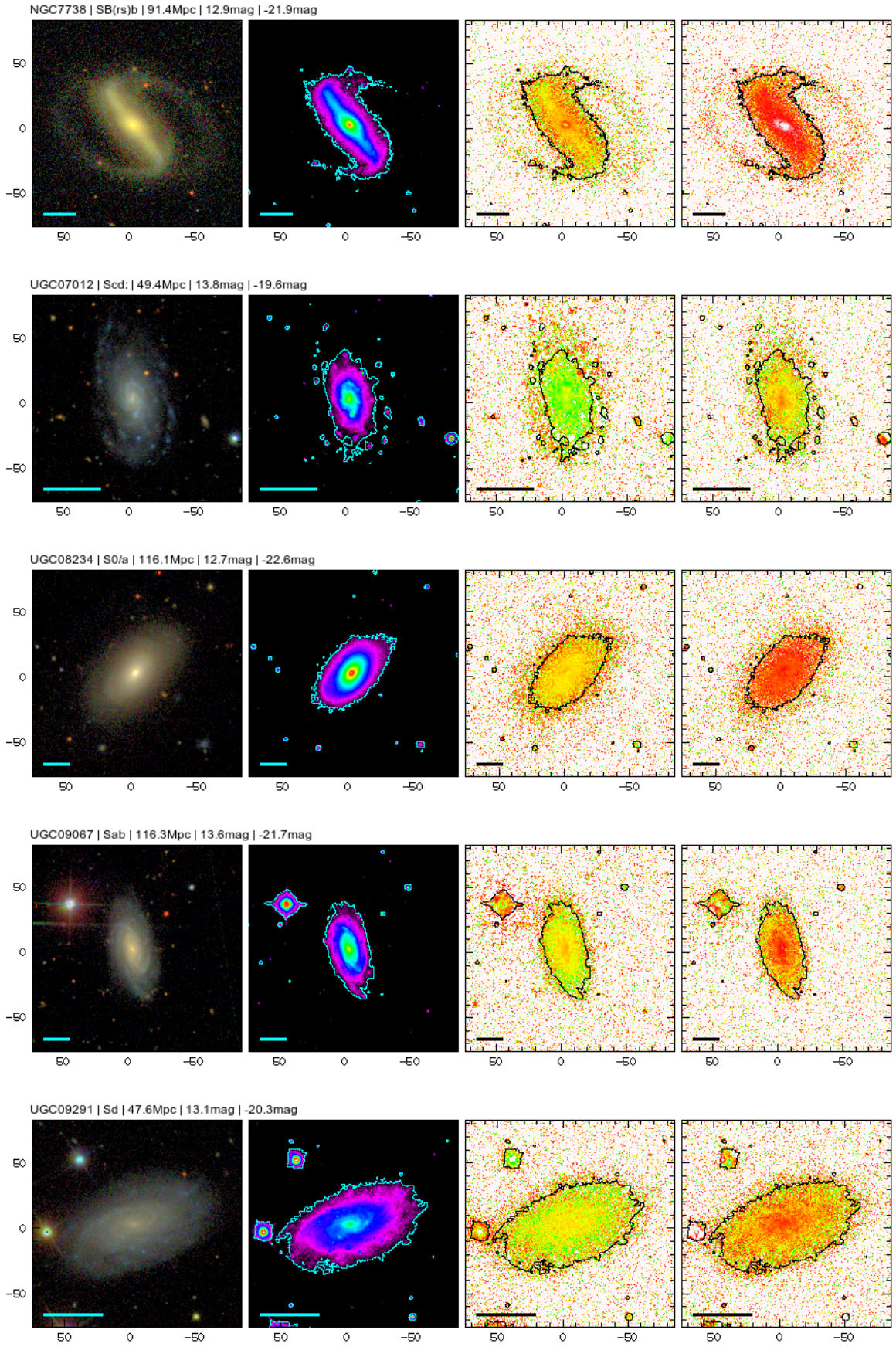
NGC7738 | SB(rs)b | 91.4Mpc | 12.9mag | -21.9mag
UGC07012 | Scd: | 49.4Mpc | 13.8mag | -19.6mag
UGC08234 | S0/a | 116.1Mpc | 12.7mag | -22.6mag
UGC09067 | Sab | 116.3Mpc | 13.6mag | -21.7mag
UGC09291 | Sd | 47.6Mpc | 13.1mag | -20.3mag
50
0
−50

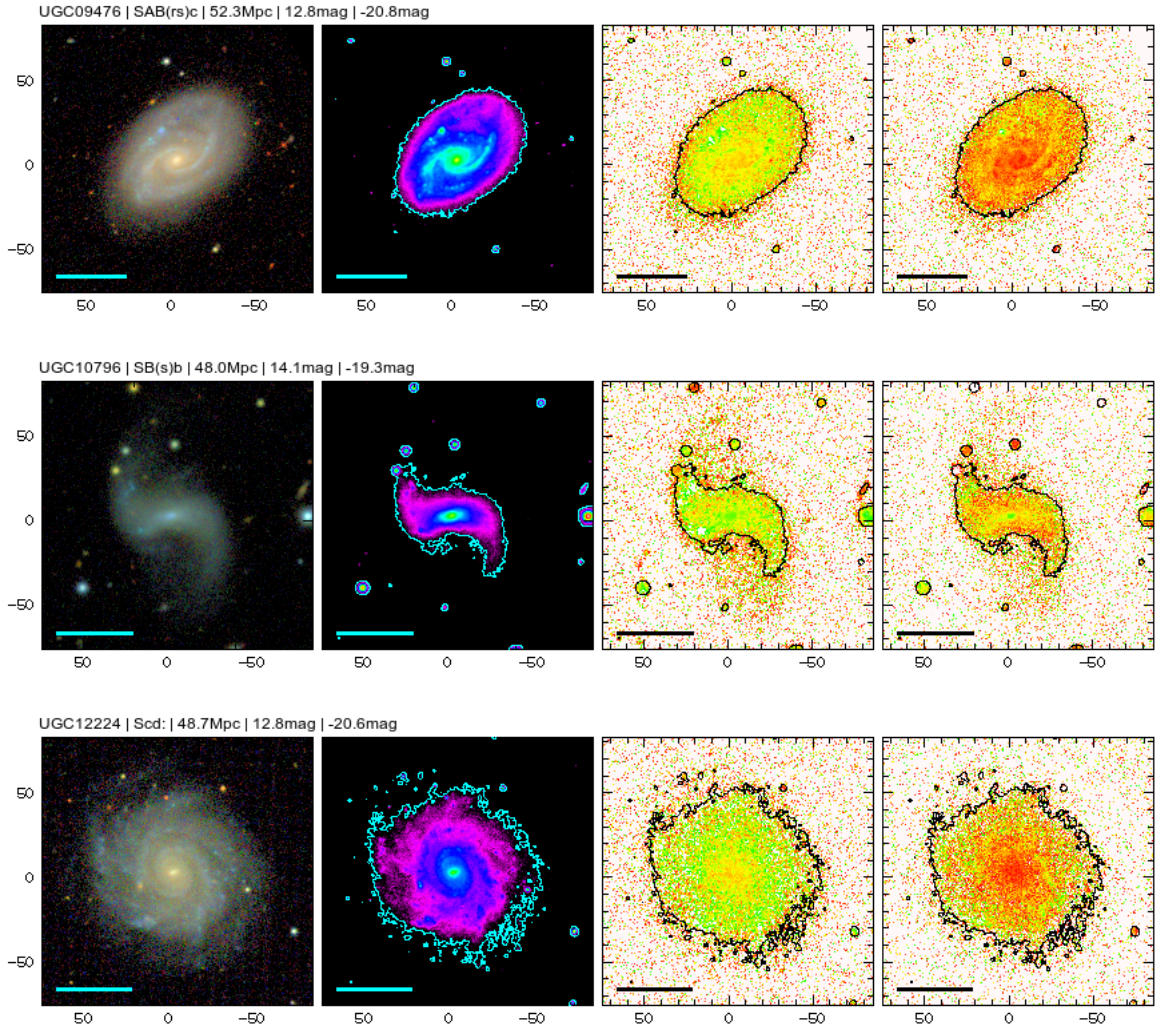

Figure A.1: For each galaxy are shown four images: a) true-color image; b) logarithmic mean of the three SDSS filters gri; c) color map $r - i$; d) color map $g - r$. The blue/black bottom line in the figures represents 10 kpc. On the top of each figure one can find the name of the galaxy, NED's morphology, distance (Mpc), apparent magnitude (mag) and absolute magnitude in the SDSS r-band (mag).

Appendix B.

Stellar Age Maps and Radial Profiles

Figure B.1 shows, on the top panels, 2D maps of stellar ages, both luminosity- and mass-weighted. On the bottom panels are represented the radial profiles of (from top to bottom): logarithm of the emission-line free continuum between 6390–6490 Å; luminosity fraction of stellar populations younger than 100 Myr; mass fraction of stellar populations younger than 100 Myr; luminosity-weighted stellar age and mass-weighted stellar age. The bulge region is shown in red (light-shaded area). The black empty squares and colored circles (bulge - red and disk - blue) are, respectively, the measured quantities for each irregular isophotal annulus and the result of a spline interpolation in steps of 1 arcsec.

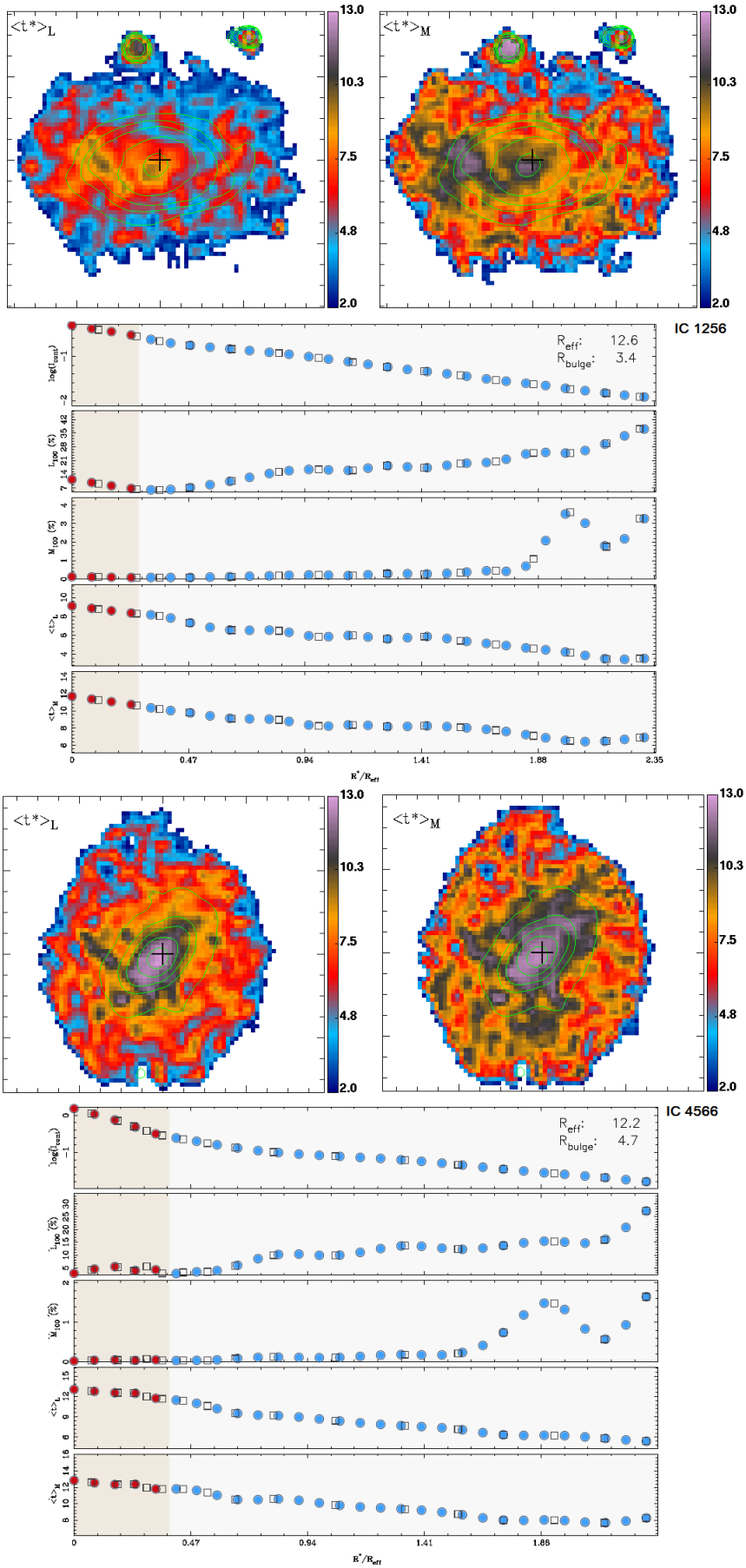
<t*>L
<t*>M
13.0
10.3
7.5
4.8
2.0
IC 1256
R_eff: 12.6
R_bulge: 3.4
log(I_tot)
I_100 (%)
M_100 (%)
<t>L
<t>M
0
0.47
0.94
1.41
1.88
2.35
R'/R_eff
IC 4566
R_eff: 12.2
R_bulge: 4.7

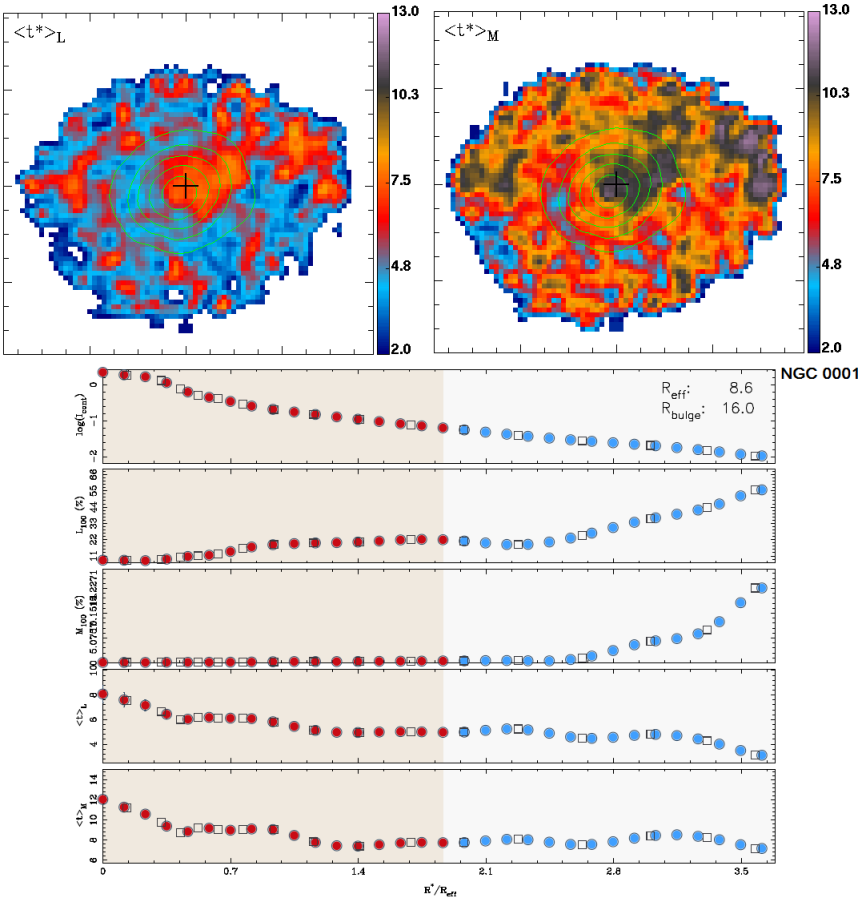
<t*>L
<t*>M
13.0
10.3
7.5
4.8
2.0
NGC 0001
R_eff: 8.6
R_bulge: 16.0
log(I_cont)
I100 (%)
M100 (%)
<t>L
<t>M
R*/R_eff

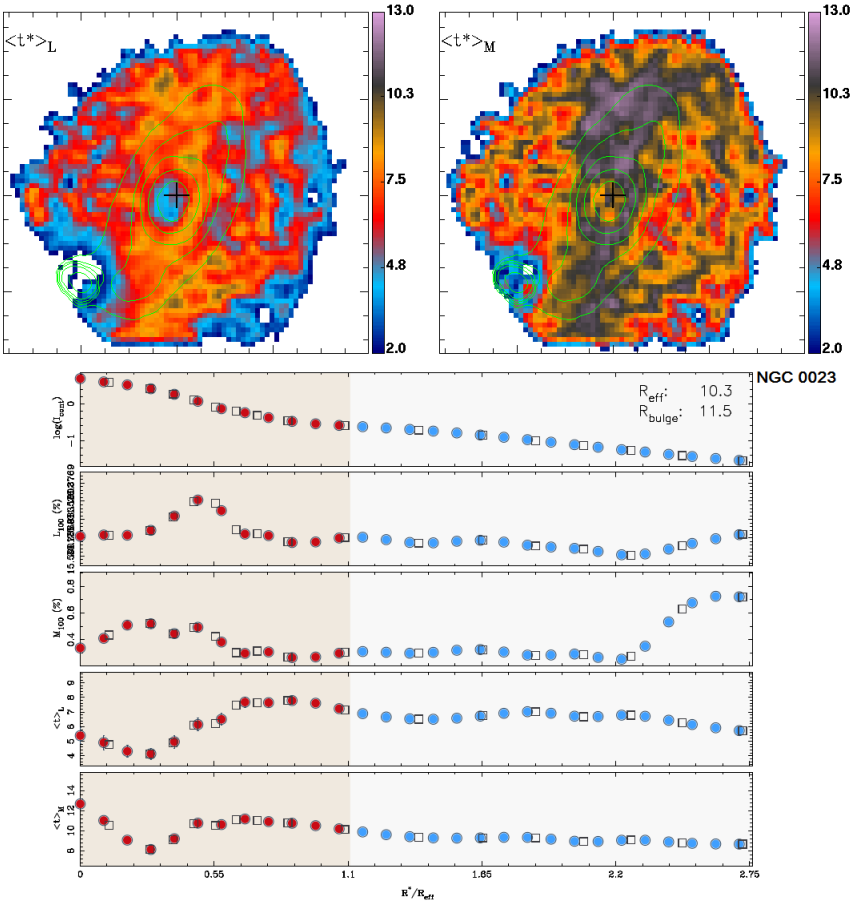
<t*>L
<t*>M
13.0
10.3
7.5
4.8
2.0
NGC 0023
R_eff: 10.3
R_bulge: 11.5
log(I_cont)
I100 (%)
M100 (%)
<t>L
<t>M
R*/R_eff

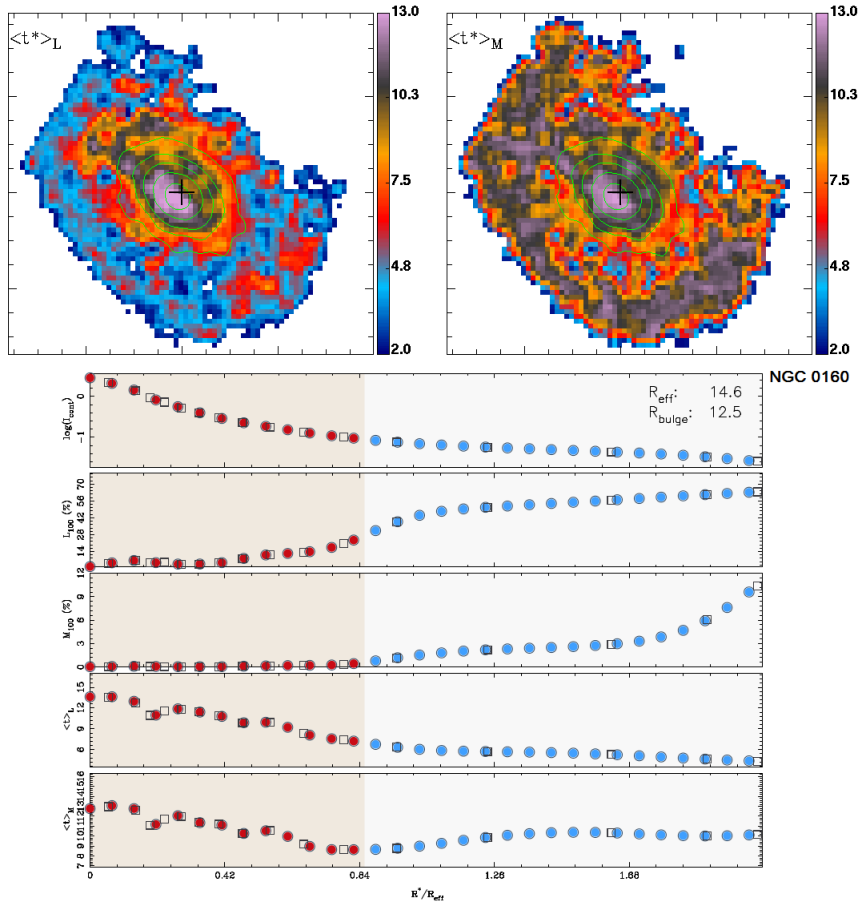
<t*>L
<t*>M
13.0
10.3
7.5
4.8
2.0
NGC 0160
R_eff: 14.6
R_bulge: 12.5
0
0.42
0.84
1.26
1.68
R*/R_eff

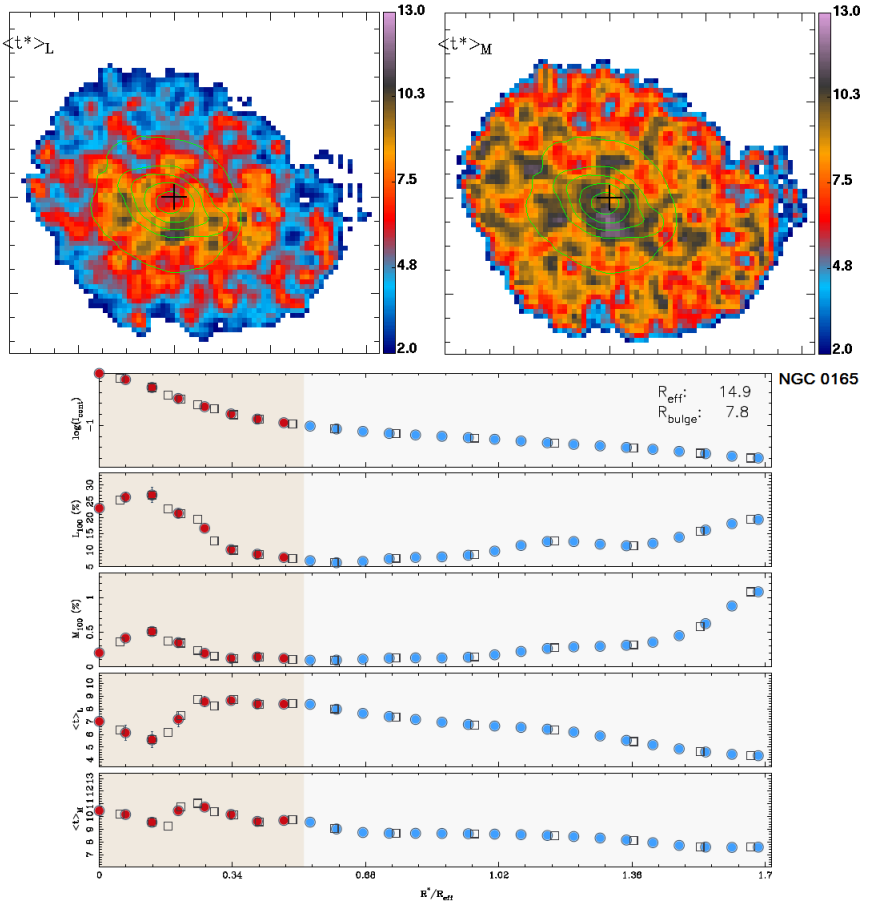
<t*>L
<t*>M
13.0
10.3
7.5
4.8
2.0
NGC 0165
R_eff: 14.9
R_bulge: 7.8
0
0.34
0.68
1.02
1.36
1.7
R*/R_eff

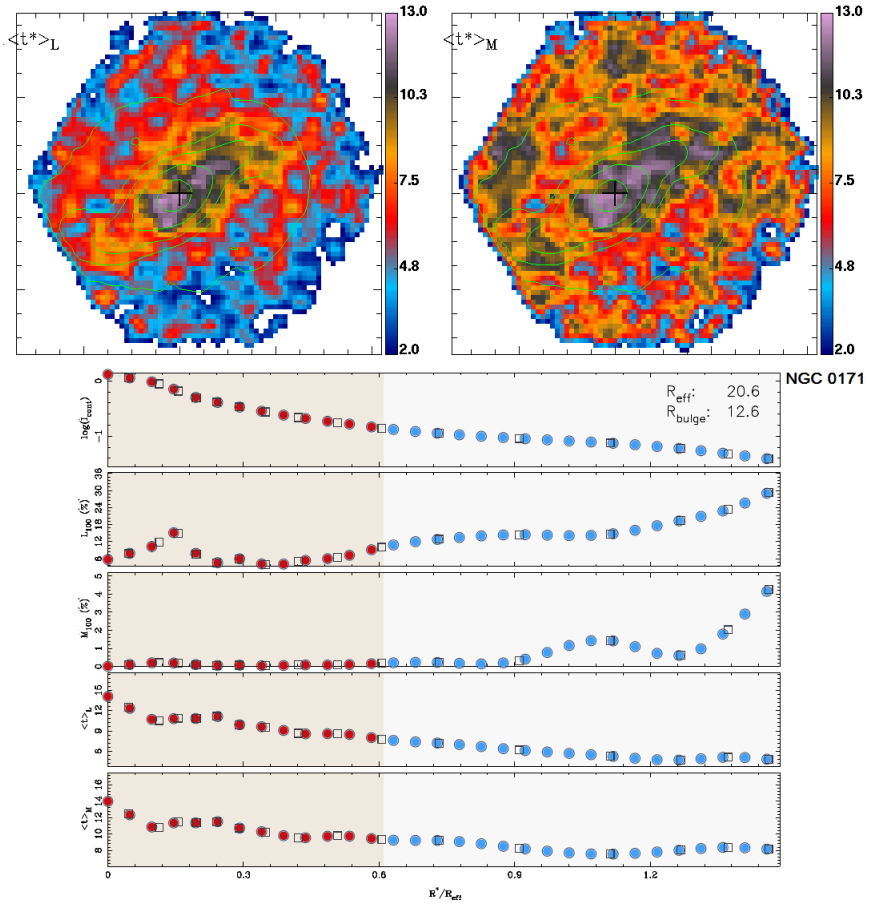
<t*>L
<t*>M
13.0
10.3
7.5
4.8
2.0
NGC 0171
R_eff: 20.6
R_bulge: 12.6
R'/R_eff

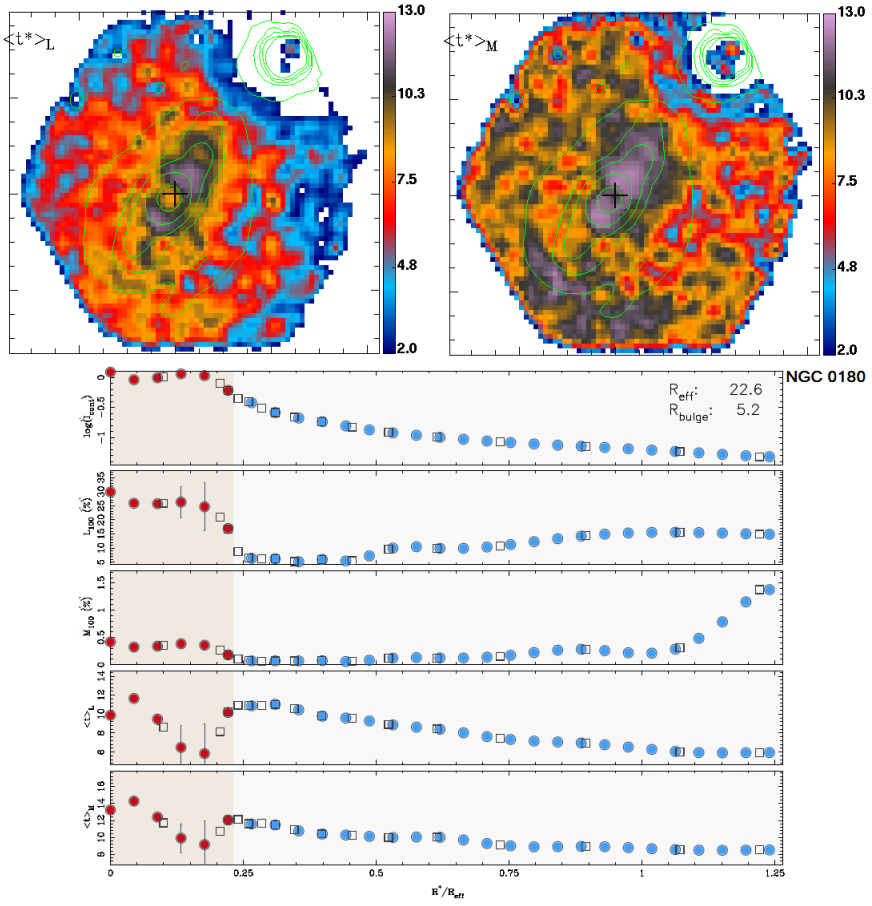
<t*>L
<t*>M
13.0
10.3
7.5
4.8
2.0
NGC 0180
R_eff: 22.6
R_bulge: 5.2
R'/R_eff

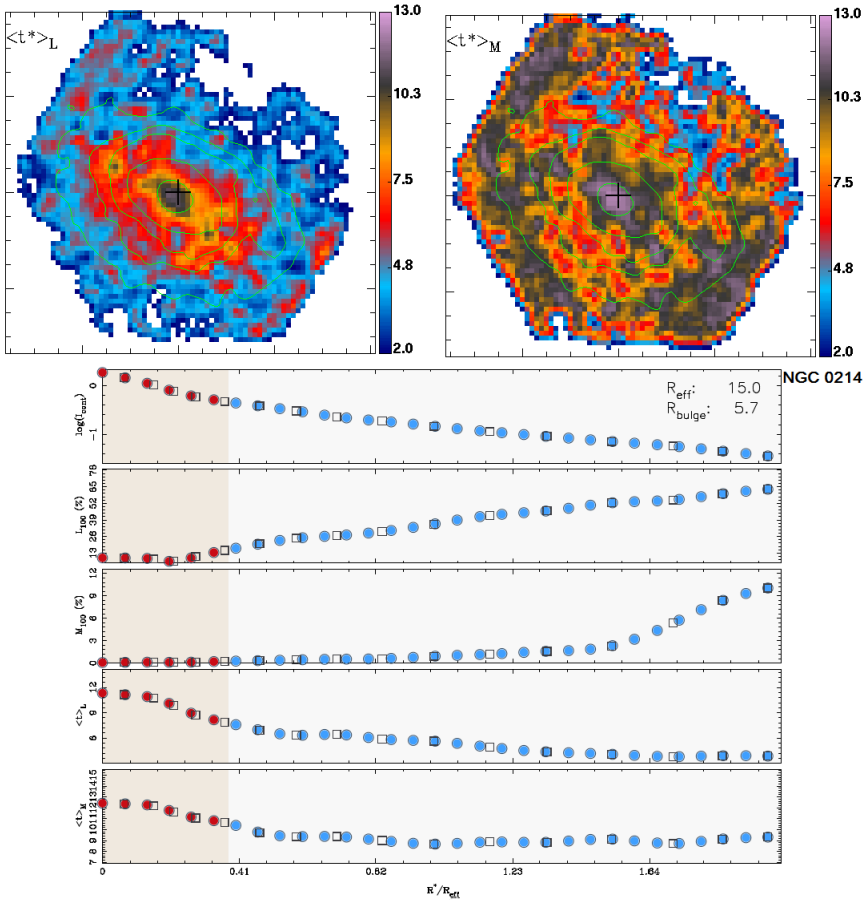
<t*>L
<t*>M
13.0
10.3
7.5
4.8
2.0
NGC 0214
R_eff: 15.0
R_bulge: 5.7
0
0.41
0.82
1.23
1.64
R*/R_eff

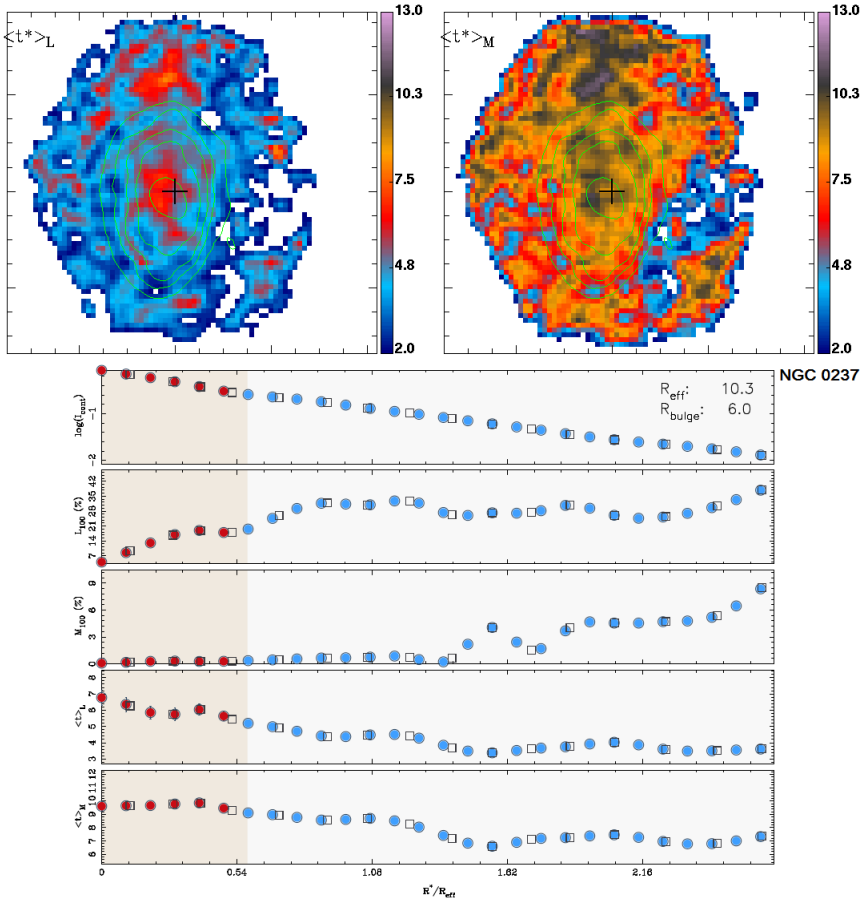
<t*>L
<t*>M
13.0
10.3
7.5
4.8
2.0
NGC 0237
R_eff: 10.3
R_bulge: 6.0
0
0.54
1.08
1.62
2.16
R*/R_eff

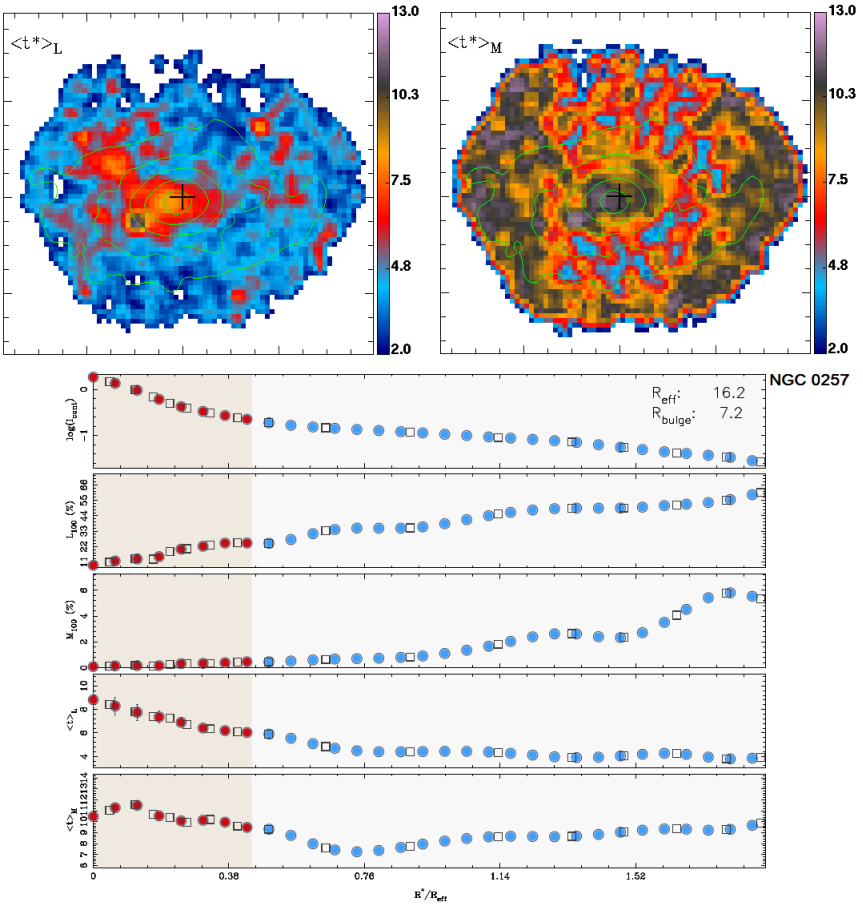
<t*>L
<t*>M
13.0
10.3
7.5
4.8
2.0
NGC 0257
R_eff: 16.2
R_bulge: 7.2
R*/R_eff

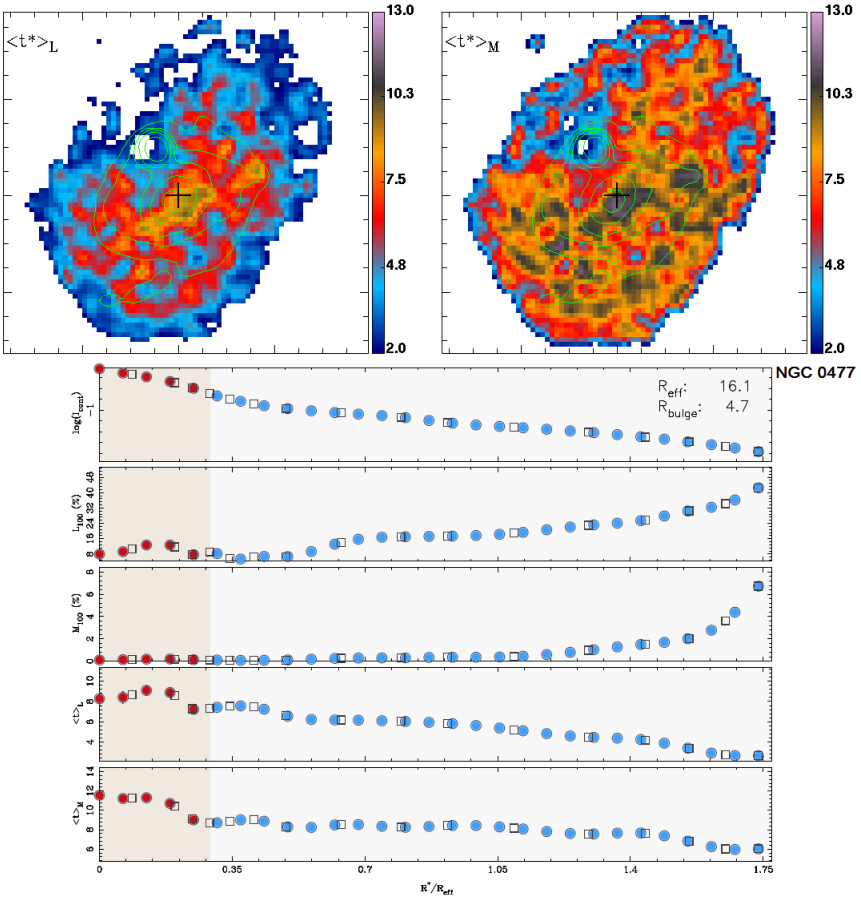
<t*>L
<t*>M
13.0
10.3
7.5
4.8
2.0
NGC 0477
R_eff: 16.1
R_bulge: 4.7
R*/R_eff

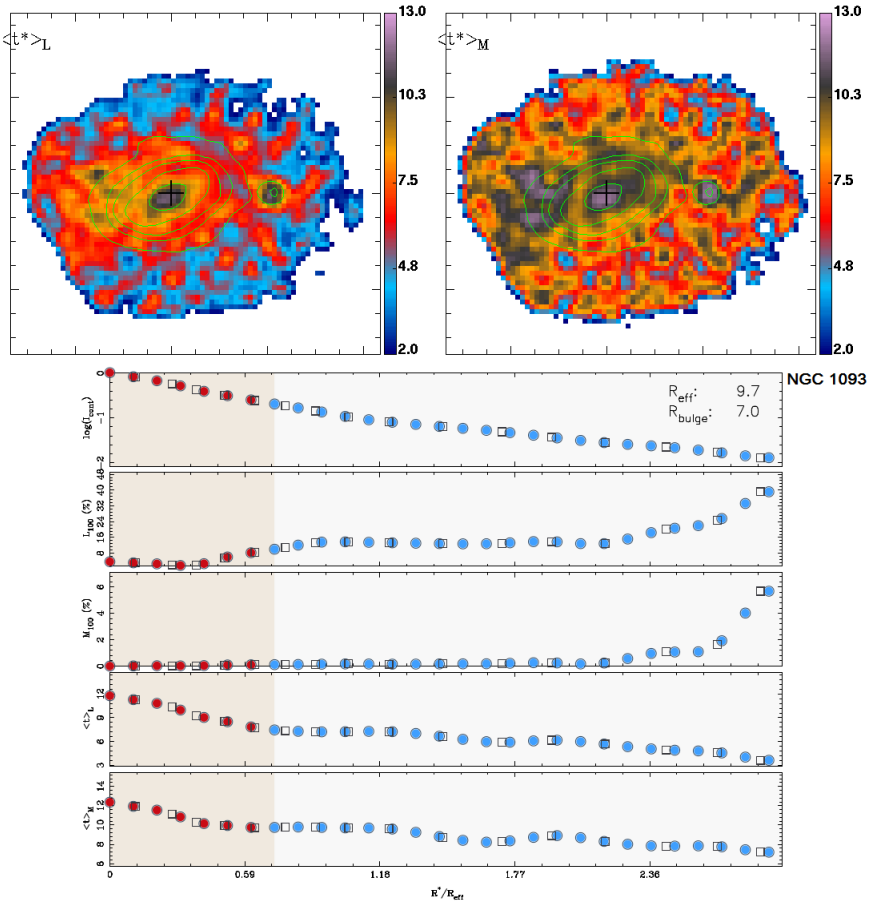
<t*>L
<t*>M
13.0
10.3
7.5
4.8
2.0
NGC 1093
R_eff: 9.7
R_bulge: 7.0
0.59
1.18
1.77
2.36
R*/R_eff

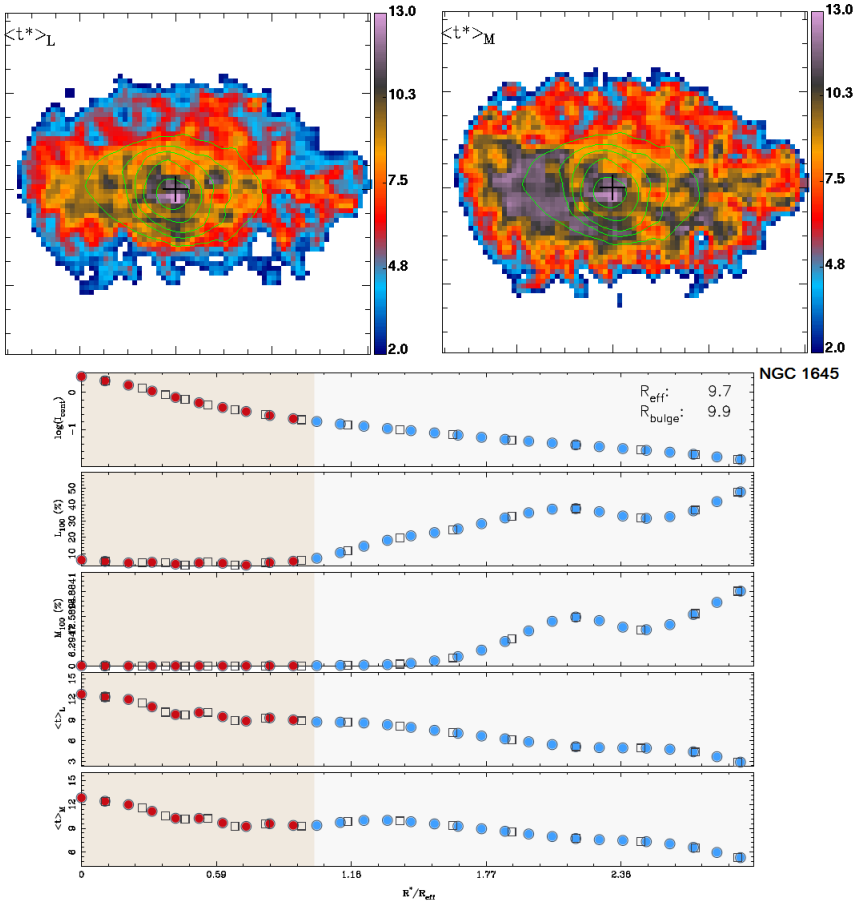
<t*>L
<t*>M
13.0
10.3
7.5
4.8
2.0
NGC 1645
R_eff: 9.7
R_bulge: 9.9
0.59
1.18
1.77
2.36
R*/R_eff

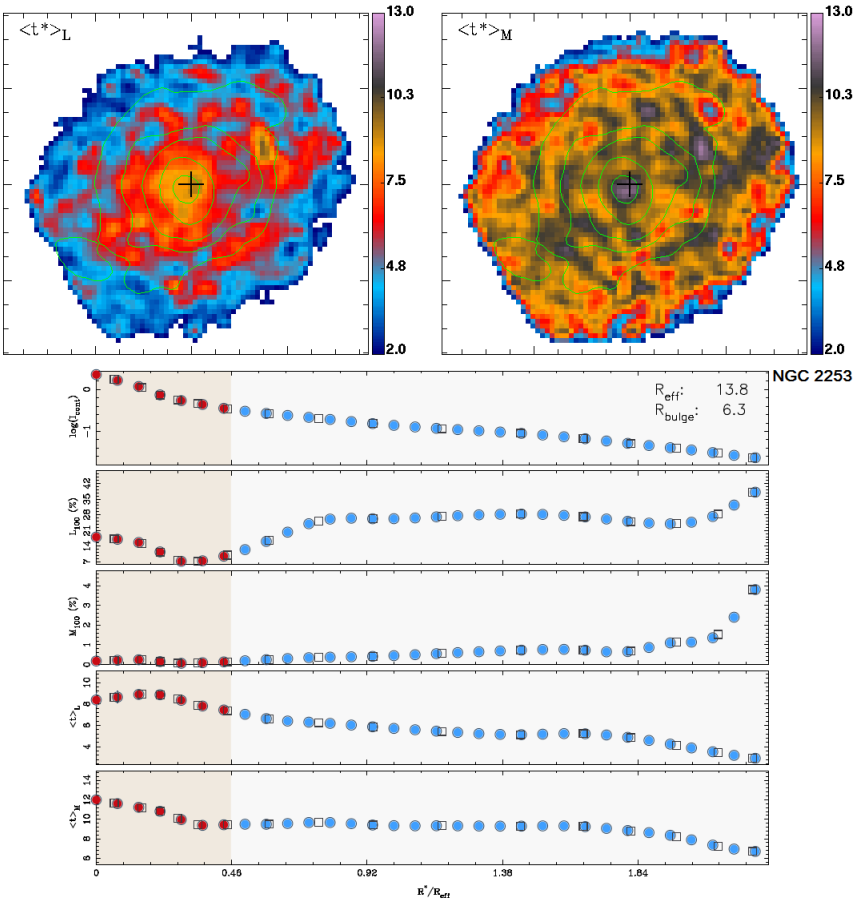
<t*>L
<t*>M
13.0
10.3
7.5
4.8
2.0
NGC 2253
R_eff: 13.8
R_bulge: 6.3
R*/R_eff
<t*>L
<t*>M
13.0
10.3
7.5
4.8
2.0
NGC 2347
R_eff: 11.2
R_bulge: 5.8
R*/R_eff

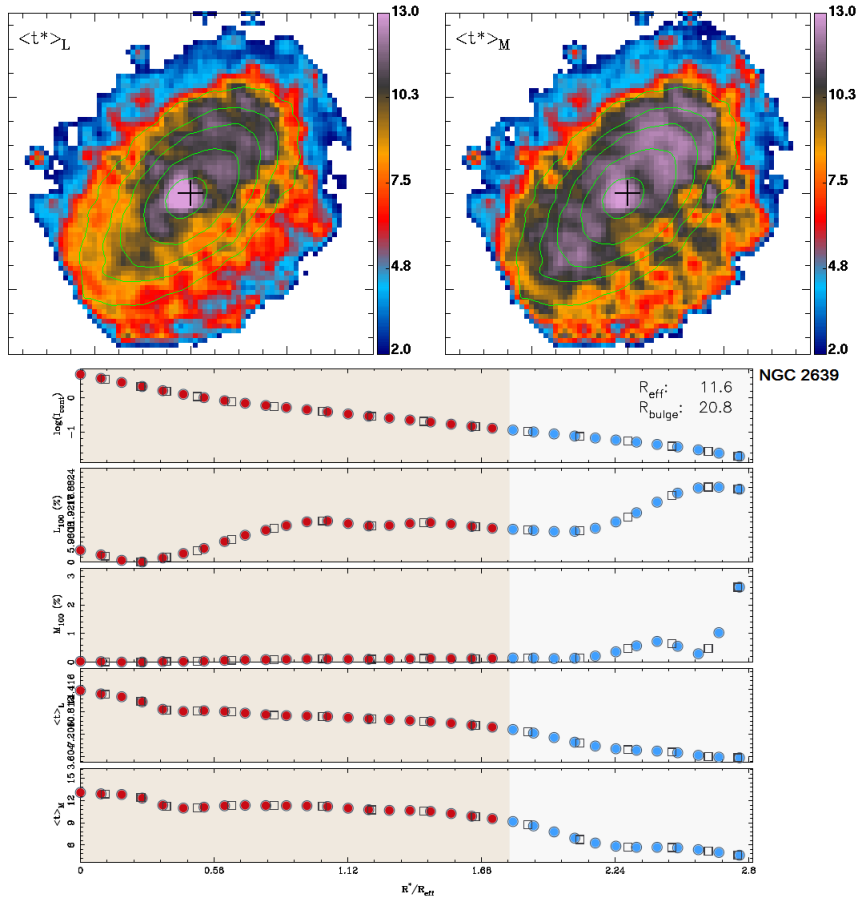
<t*>L
<t*>M
13.0
10.3
7.5
4.8
2.0
NGC 2639
R_eff: 11.6
R_bulge: 20.8
0.56
1.12
1.68
2.24
2.8
R*/R_eff

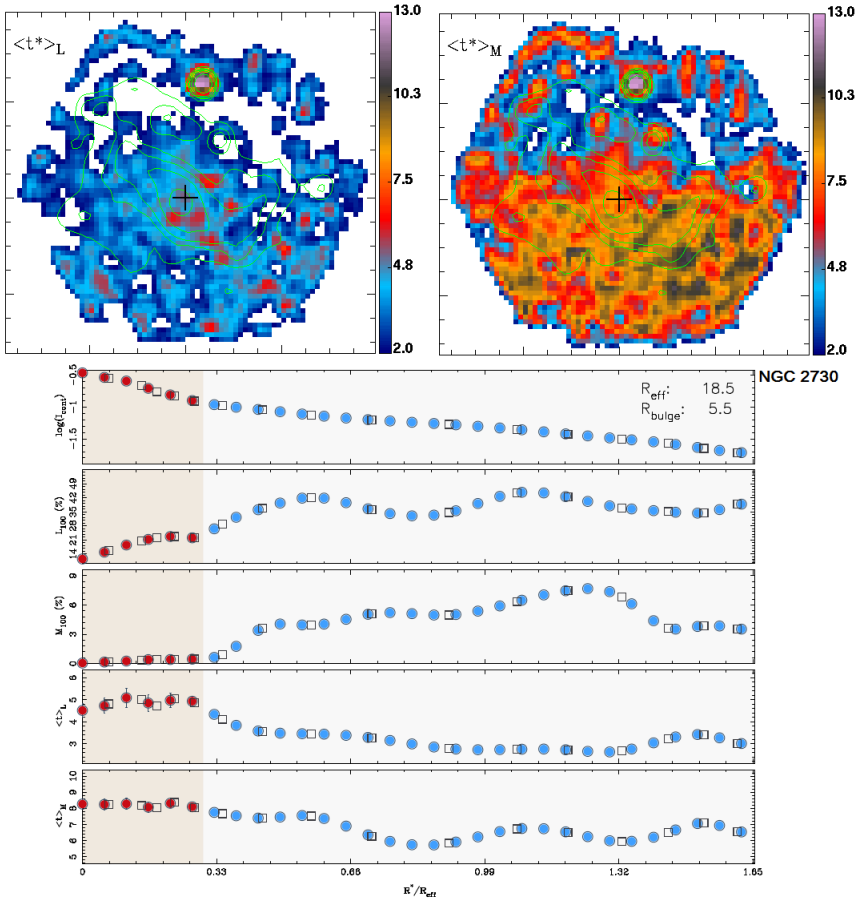
<t*>L
<t*>M
13.0
10.3
7.5
4.8
2.0
NGC 2730
R_eff: 18.5
R_bulge: 5.5
0.33
0.66
0.99
1.32
1.65
R*/R_eff

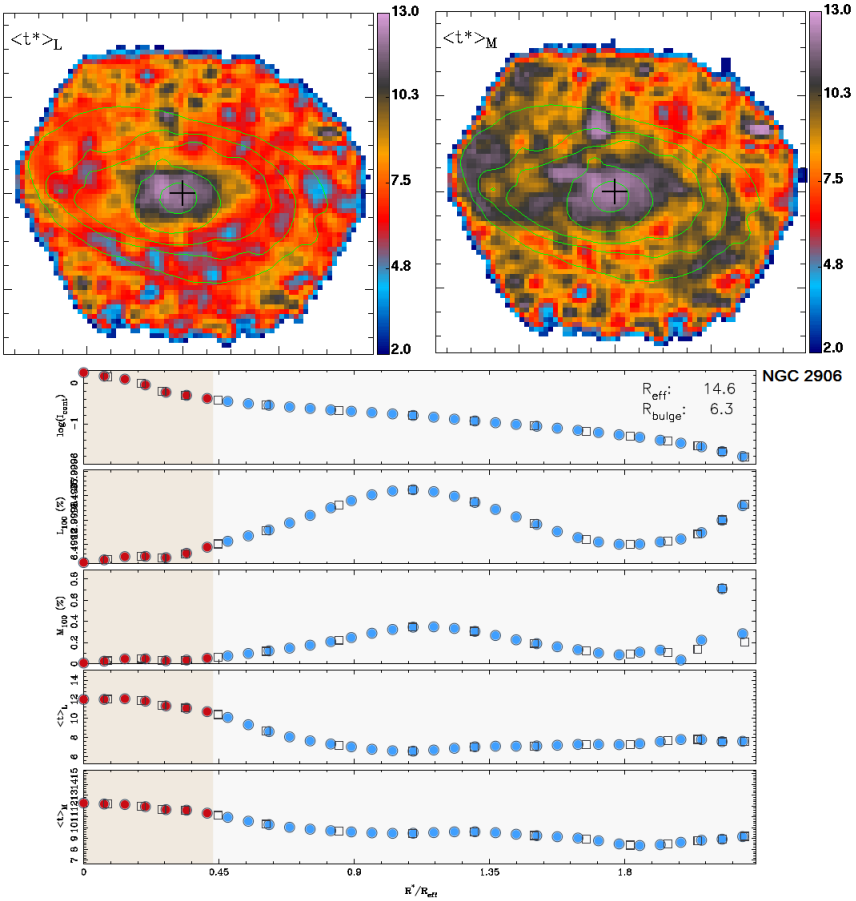
<t*>L
<t*>M
13.0
10.3
7.5
4.8
2.0
NGC 2906
R_eff: 14.6
R_bulge: 6.3
log(τ_mass)
L100 (%)
M100 (%)
<t>L
<t>M
R*/R_eff

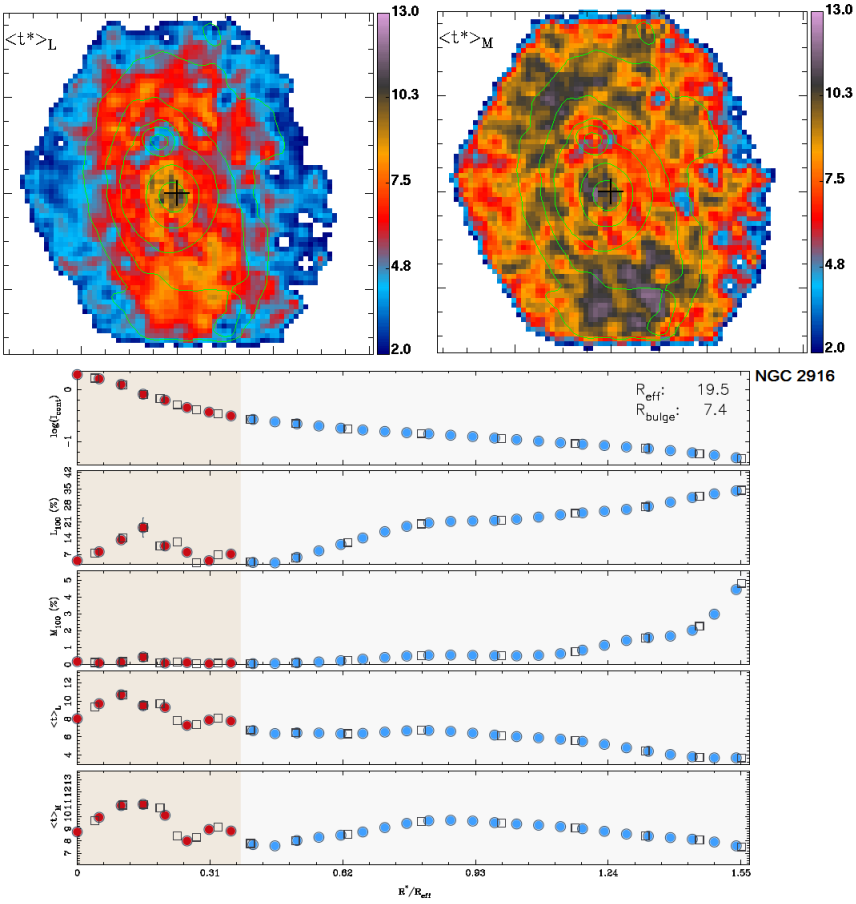
<t*>L
<t*>M
13.0
10.3
7.5
4.8
2.0
NGC 2916
R_eff: 19.5
R_bulge: 7.4
log(τ_mass)
L100 (%)
M100 (%)
<t>L
<t>M
R*/R_eff

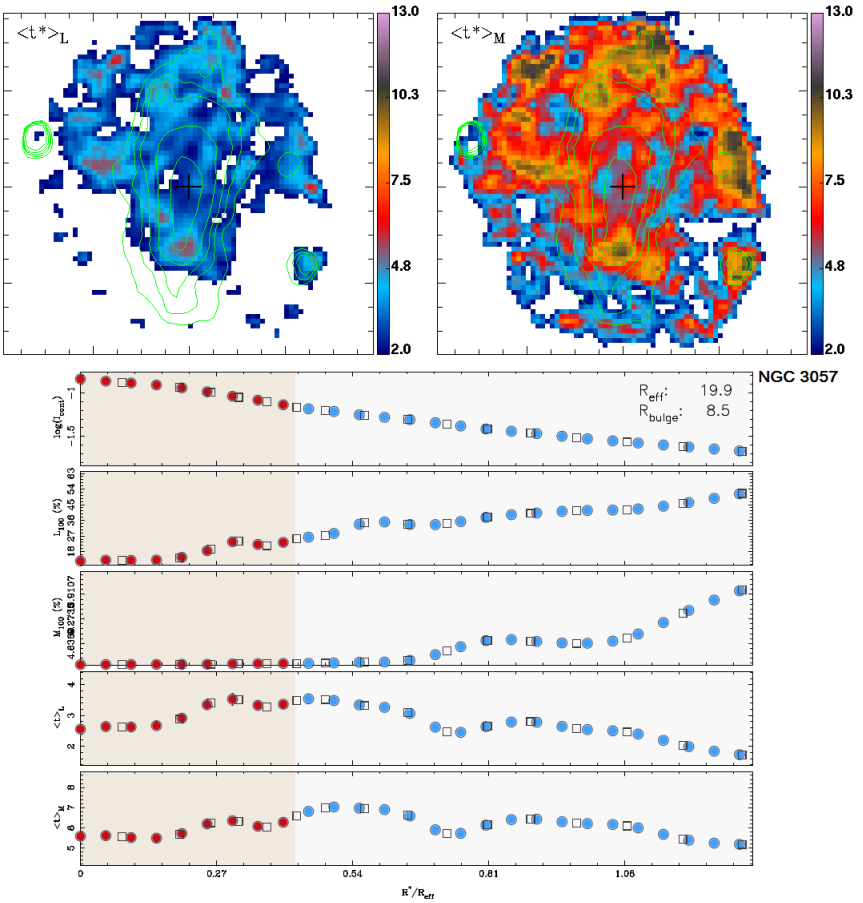
<t*>L
<t*>M
13.0
10.3
7.5
4.8
2.0
NGC 3057
R_eff: 19.9
R_bulge: 8.5
R*/R_eff

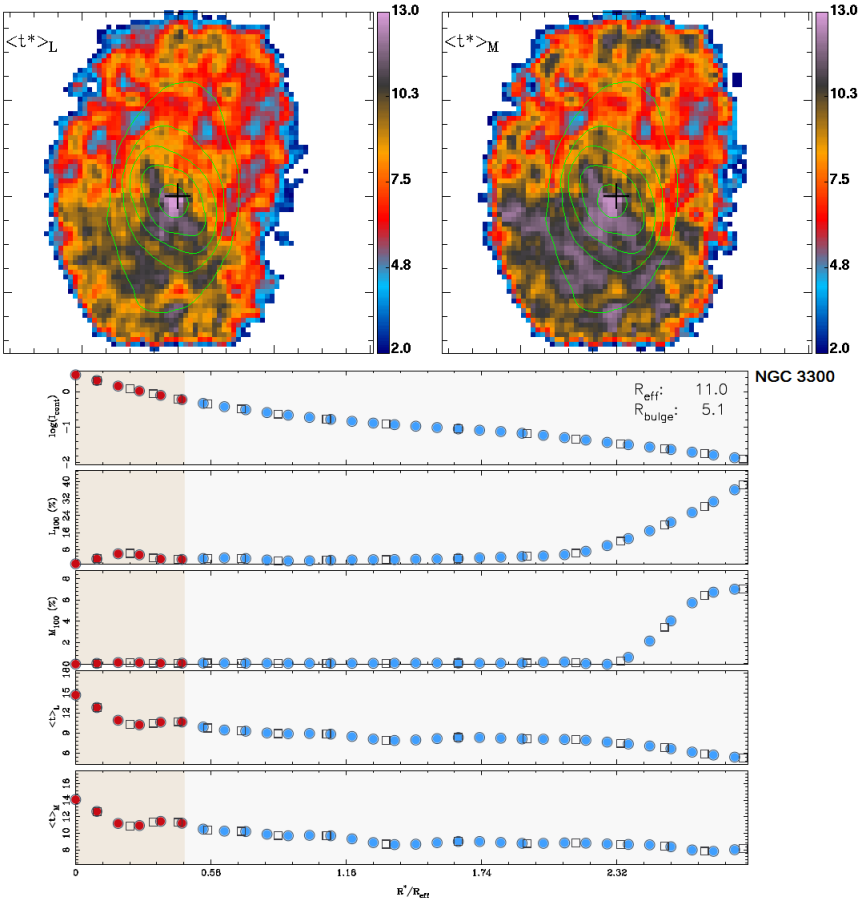
<t*>L
<t*>M
13.0
10.3
7.5
4.8
2.0
NGC 3300
R_eff: 11.0
R_bulge: 5.1
R*/R_eff

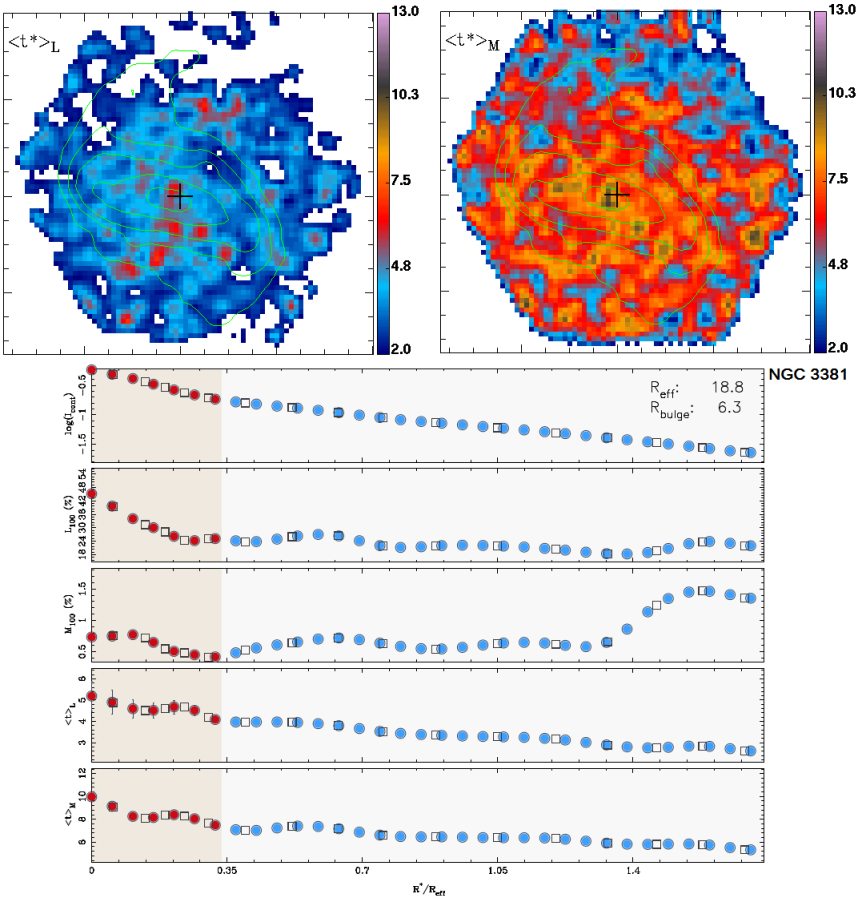
<t*>L
<t*>M
13.0
10.3
7.5
4.8
2.0
NGC 3381
R_eff: 18.8
R_bulge: 6.3
log(t_cons)
i100 (%)
M100 (%)
<t>L
<t>M
R*/R_eff

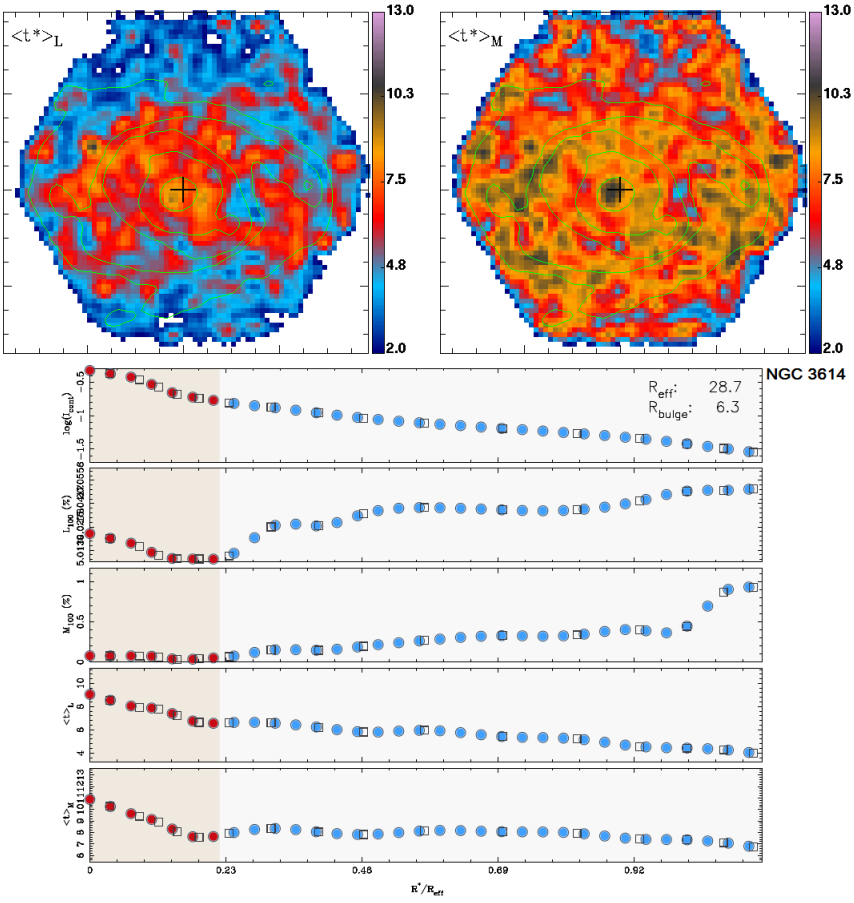
<t*>L
<t*>M
13.0
10.3
7.5
4.8
2.0
NGC 3614
R_eff: 28.7
R_bulge: 6.3
log(t_cons)
i100 (%)
M100 (%)
<t>L
<t>M
R*/R_eff

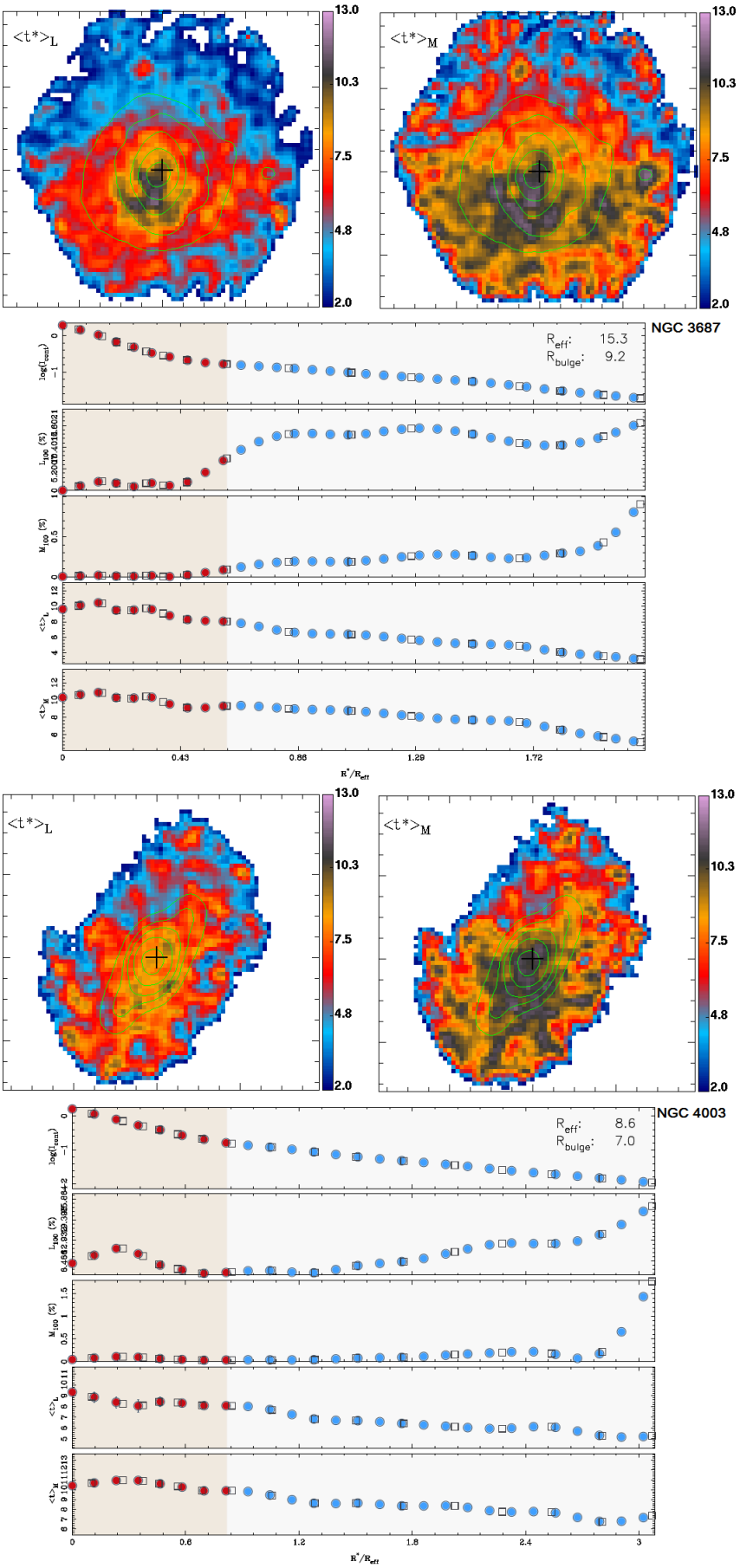
<t*>L
<t*>M
13.0
10.3
7.5
4.8
2.0
NGC 3687
R_eff: 15.3
R_bulge: 9.2
0.43
0.86
1.29
1.72
R*/R_eff
<t*>L
<t*>M
13.0
10.3
7.5
4.8
2.0
NGC 4003
R_eff: 8.6
R_bulge: 7.0
0.6
1.2
1.8
2.4
3
R*/R_eff

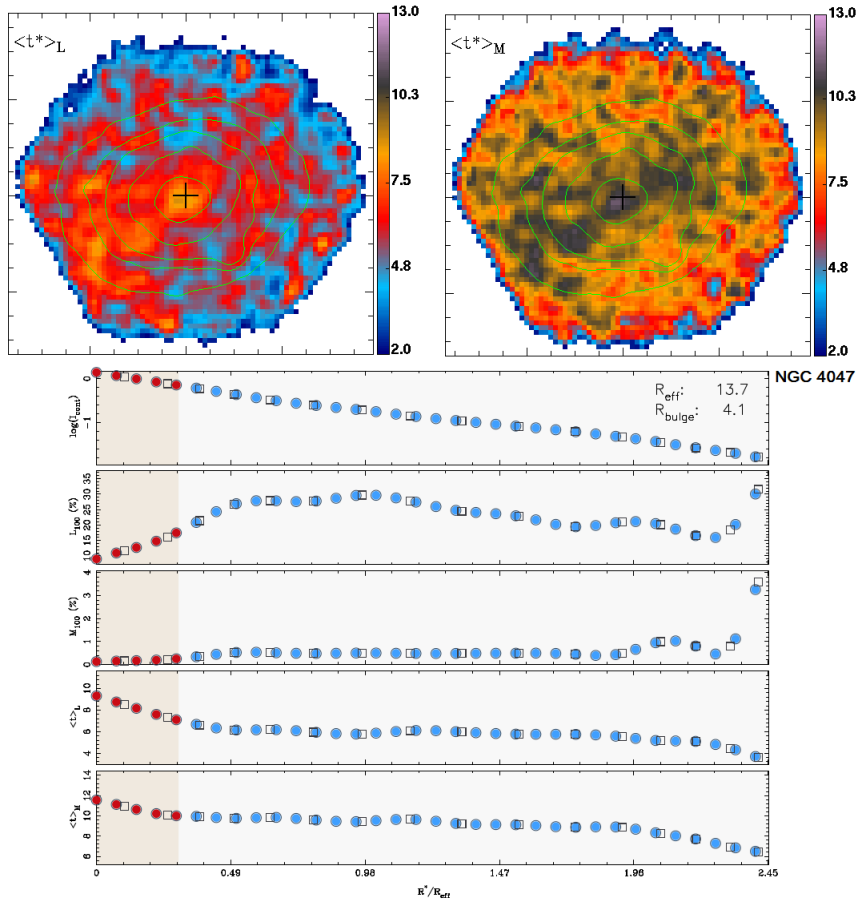
<t*>L
<t*>M
13.0
10.3
7.5
4.8
2.0
NGC 4047
R_eff: 13.7
R_bulge: 4.1
log(t_ssp)
L100 (%)
M100 (%)
<t>L
<t>M
0
0.49
0.98
1.47
1.96
2.45
R*/R_eff

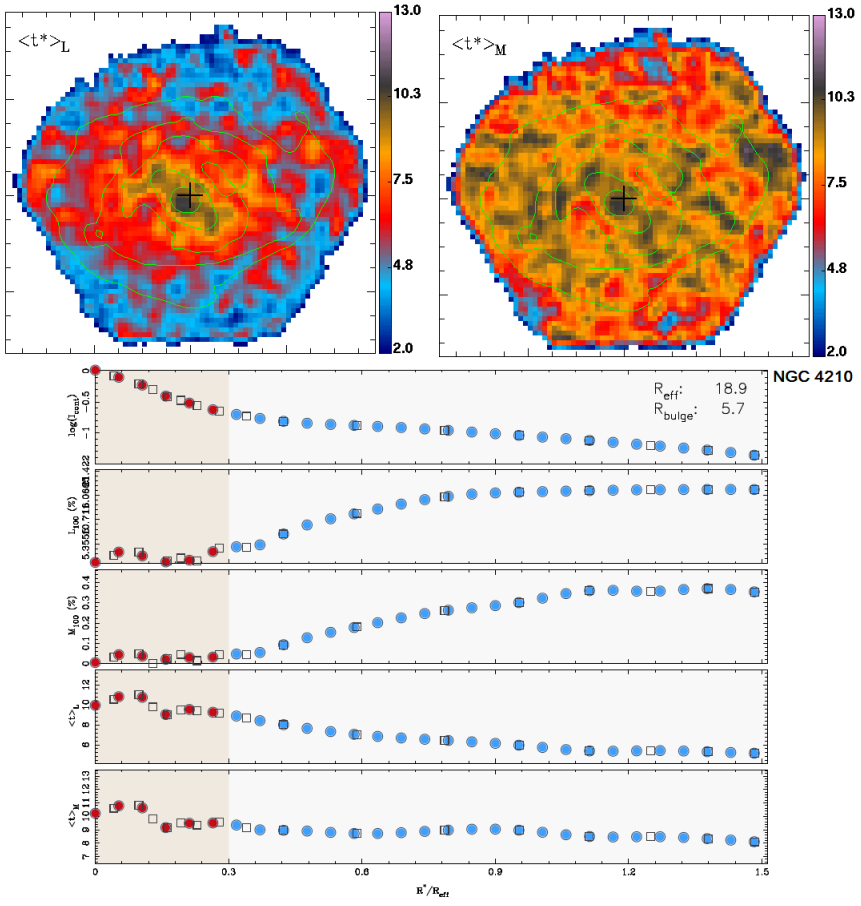
<t*>L
<t*>M
13.0
10.3
7.5
4.8
2.0
NGC 4210
R_eff: 18.9
R_bulge: 5.7
log(t_ssp)
L100 (%)
M100 (%)
<t>L
<t>M
0
0.3
0.6
0.9
1.2
1.5
R*/R_eff

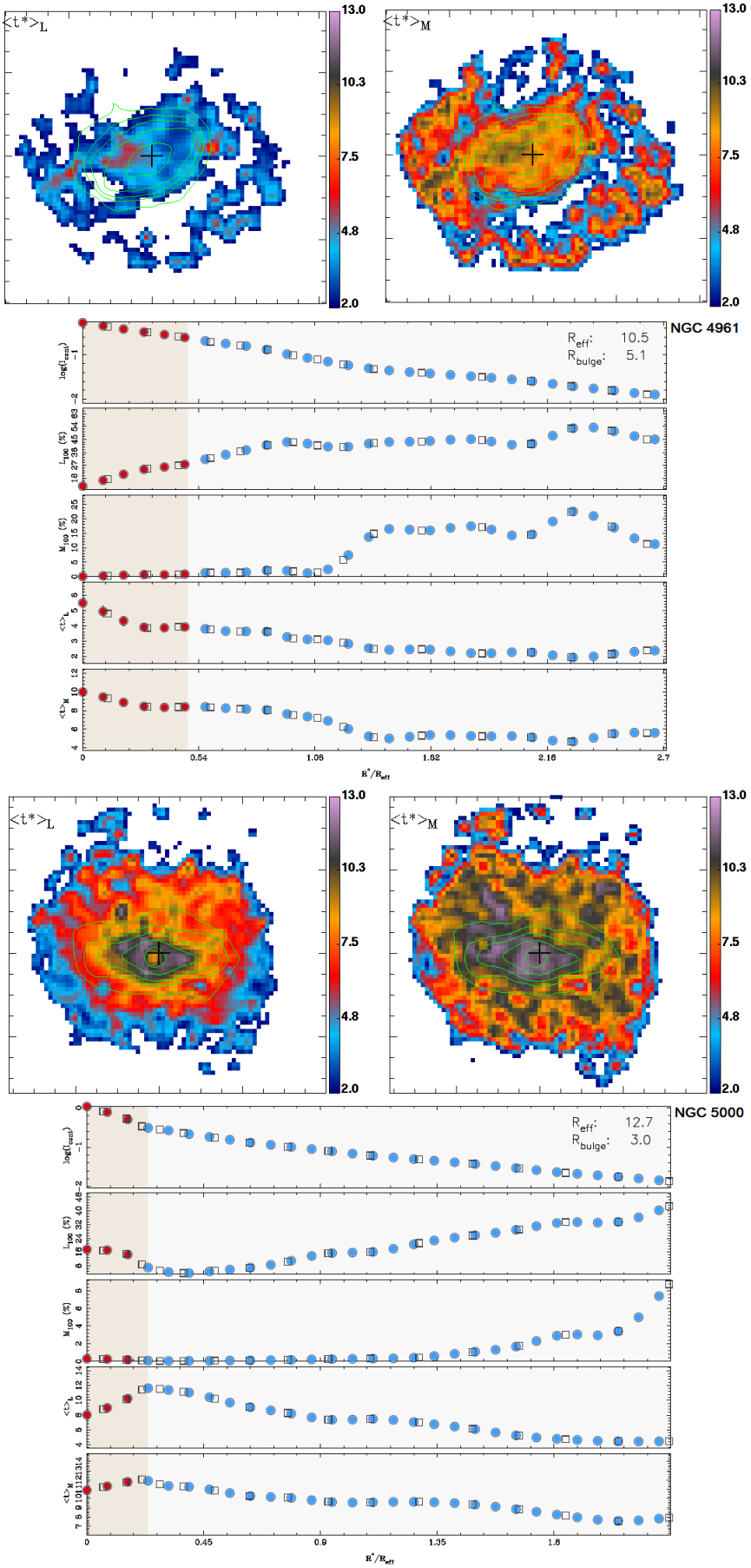
<t*>L
<t*>M
13.0
10.3
7.5
4.8
2.0
NGC 4961
R_eff: 10.5
R_bulge: 5.1
NGC 5000
R_eff: 12.7
R_bulge: 3.0
R*/R_eff

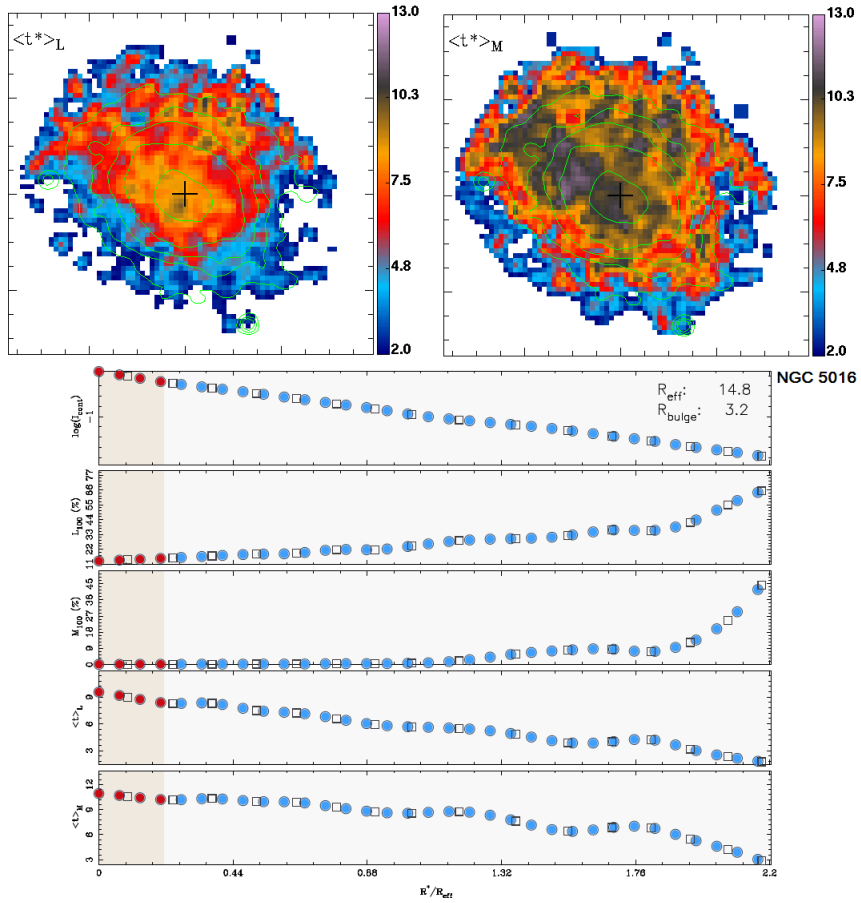
<t*>L
<t*>M
13.0
10.3
7.5
4.8
2.0
NGC 5016
Reff: 14.8
Rbulge: 3.2
R'/Reff

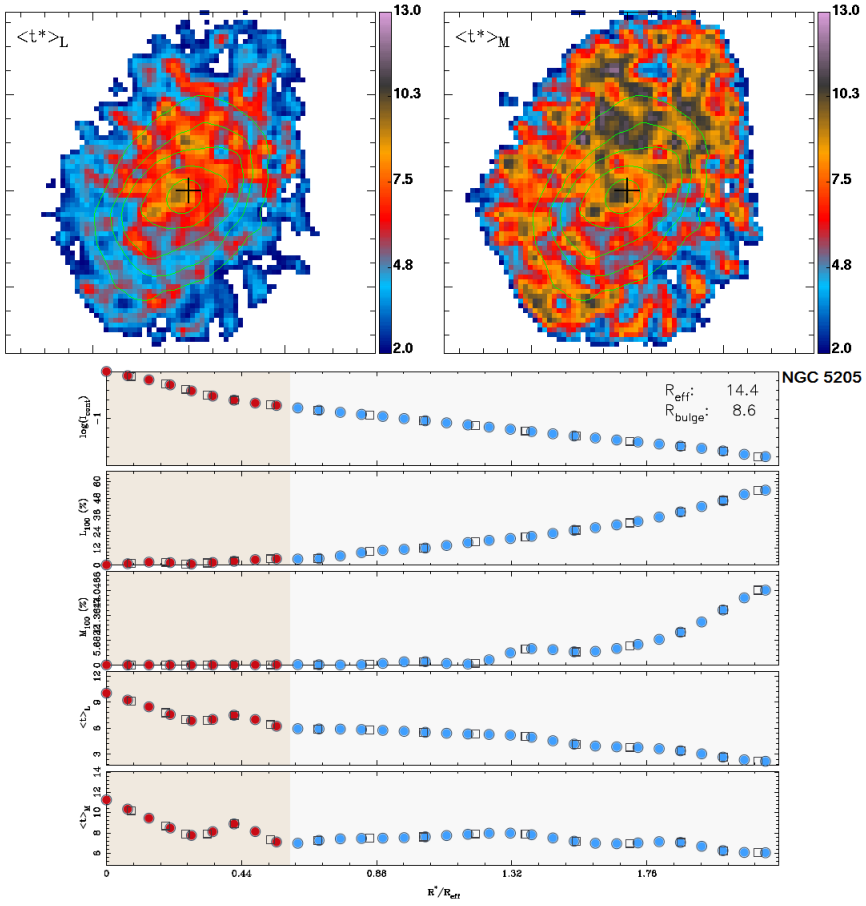
<t*>L
<t*>M
13.0
10.3
7.5
4.8
2.0
NGC 5205
Reff: 14.4
Rbulge: 8.6
R'/Reff

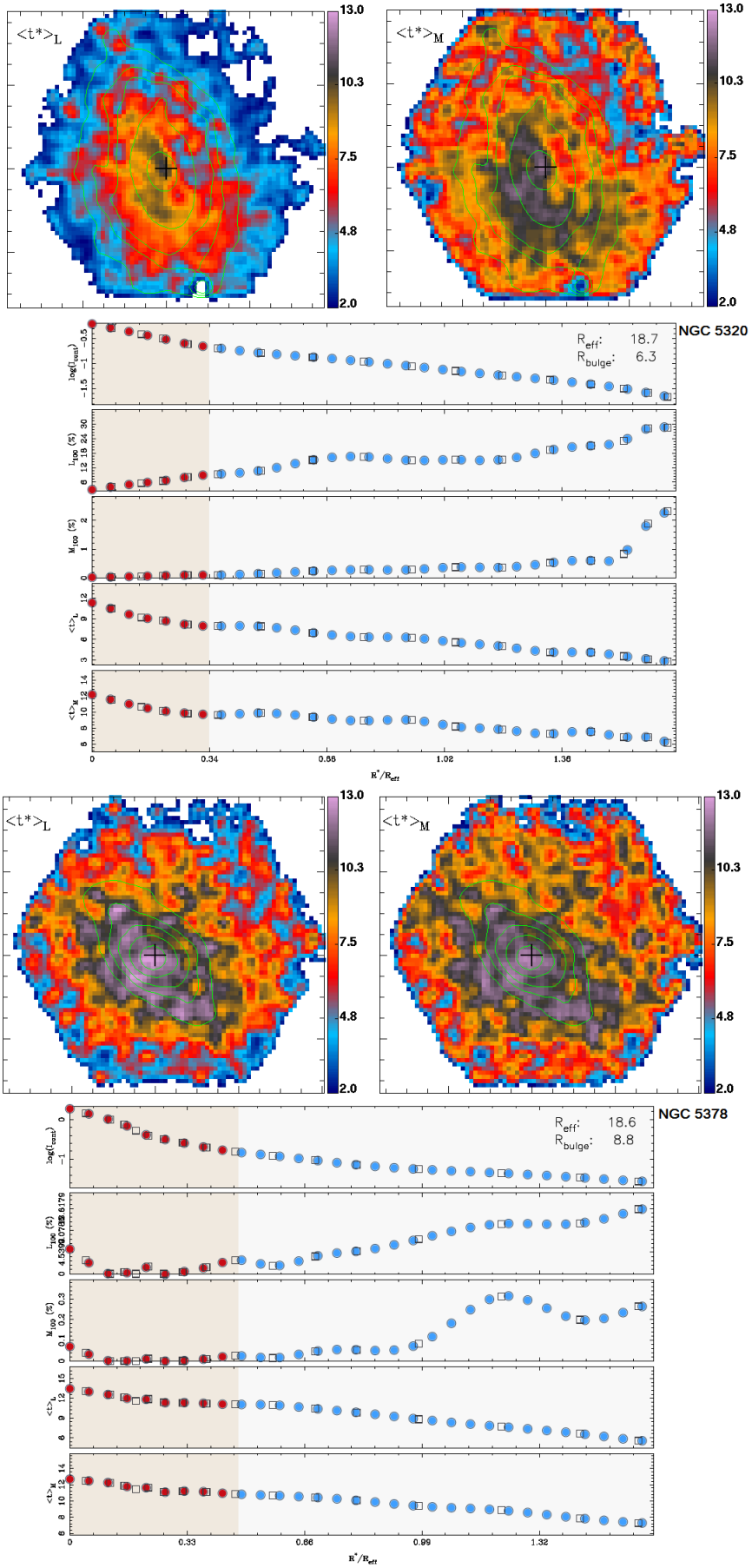
<t*>L
<t*>M
13.0
10.3
7.5
4.8
2.0
NGC 5320
R_eff: 18.7
R_bulge: 6.3
log(I_cont)
I_100 (%)
M_100 (%)
<t>L
<t>M
0
0.34
0.68
1.02
1.36
R*/R_eff
NGC 5378
R_eff: 18.6
R_bulge: 8.8
0.33
0.66
0.99
1.32

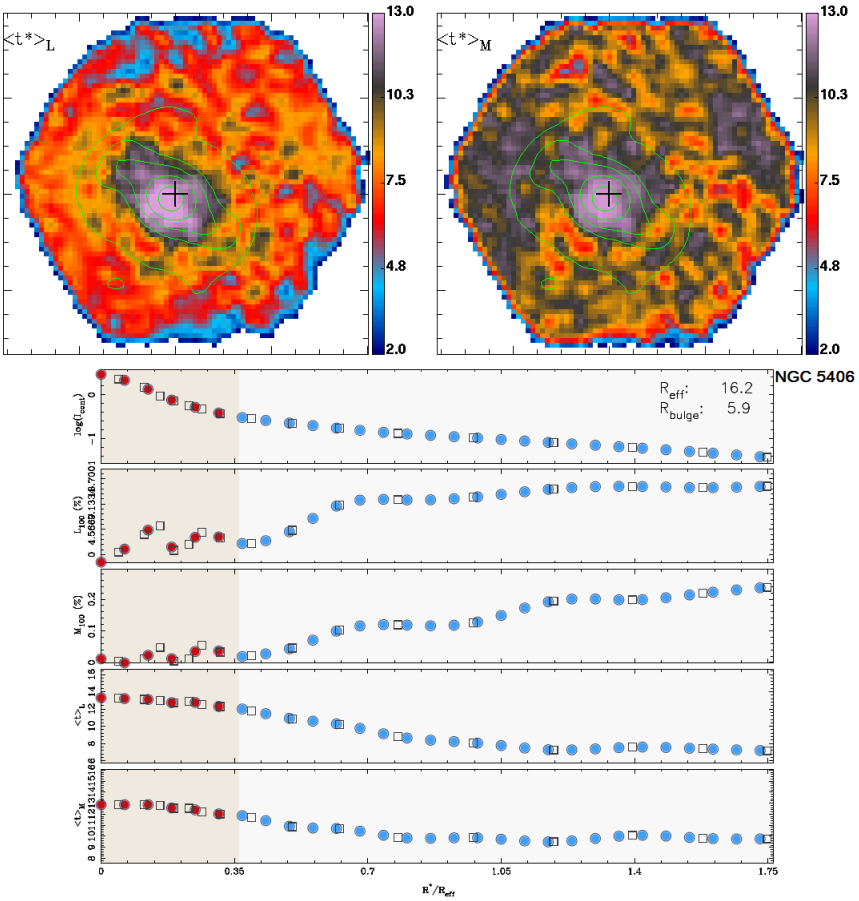
<t*>L
<t*>M
13.0
10.3
7.5
4.8
2.0
NGC 5406
R_eff: 16.2
R_bulge: 5.9
R*/R_eff

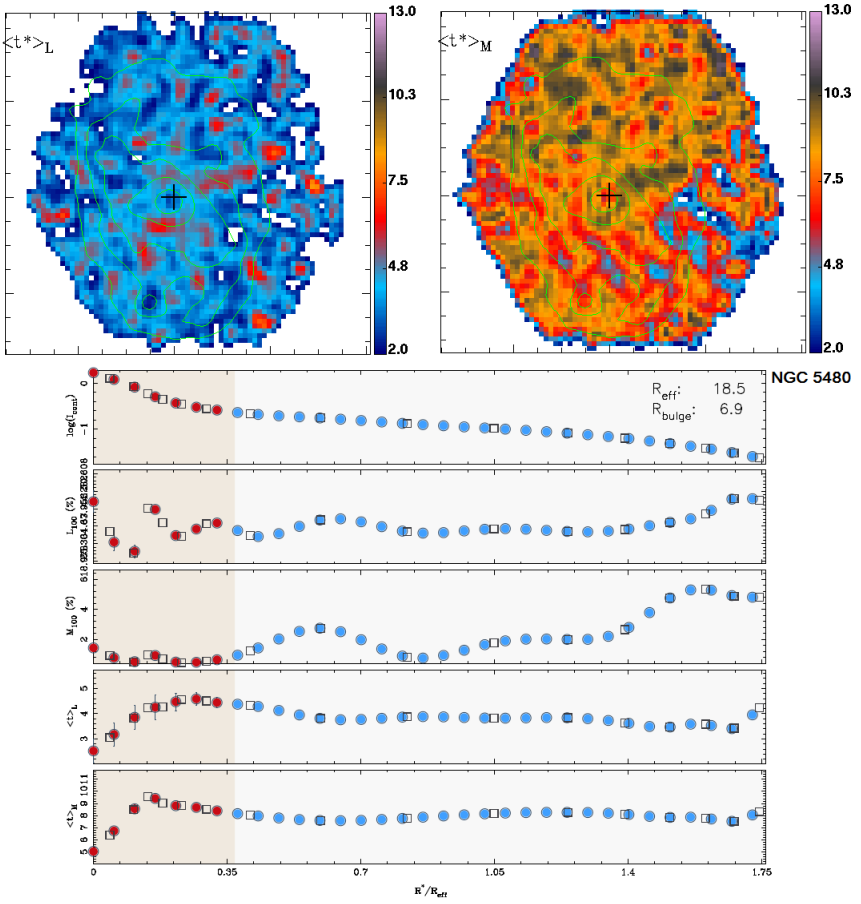
<t*>L
<t*>M
13.0
10.3
7.5
4.8
2.0
NGC 5480
R_eff: 18.5
R_bulge: 6.9
R*/R_eff

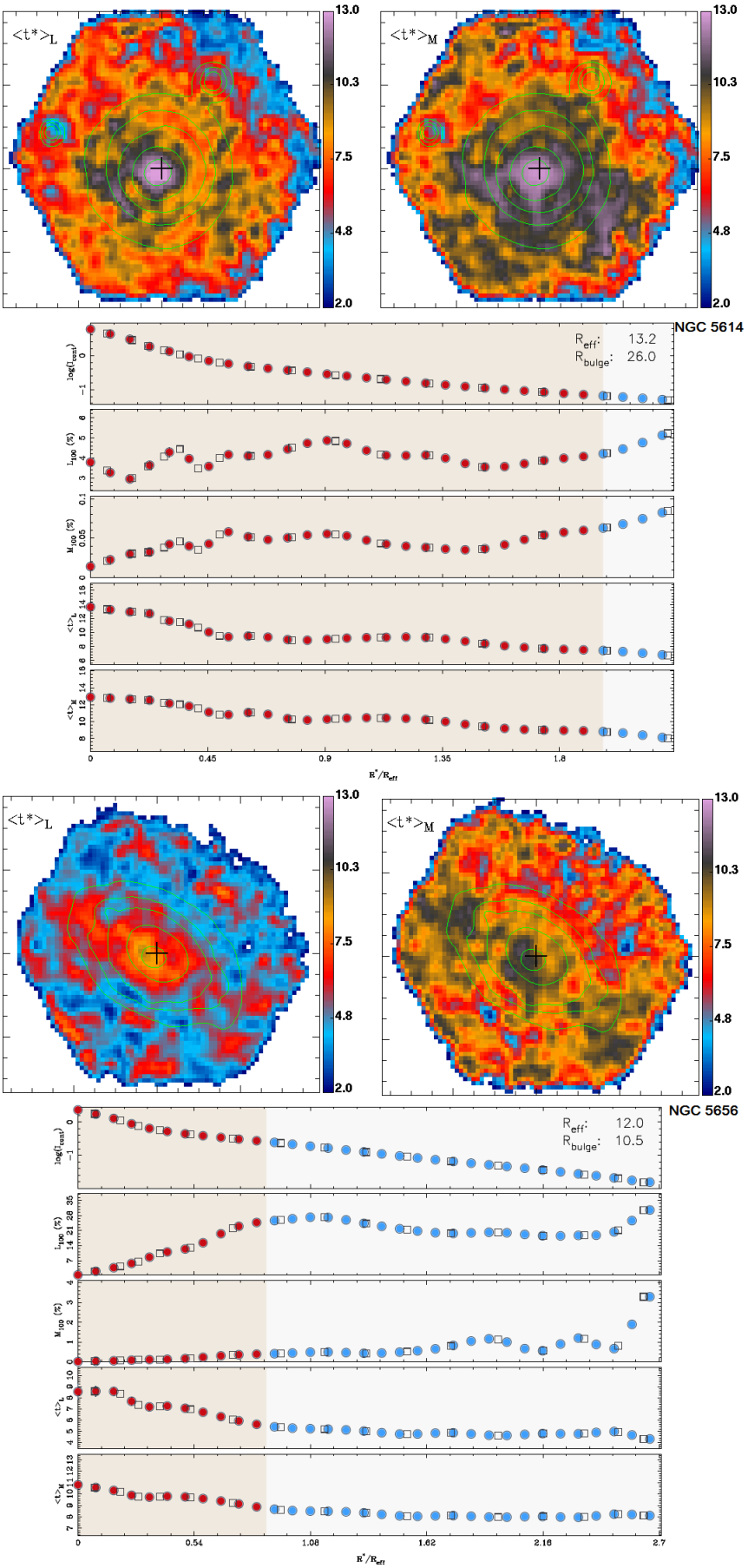
<t*>L
<t*>M
13.0
10.3
7.5
4.8
2.0
NGC 5614
R_eff: 13.2
R_bulge: 26.0
log(t_sfh)
L100 (%)
M100 (%)
<t>L
<t>M
0
0.45
0.9
1.35
1.8
R*/R_eff
NGC 5656
R_eff: 12.0
R_bulge: 10.5
0.54
1.08
1.62
2.16
2.7

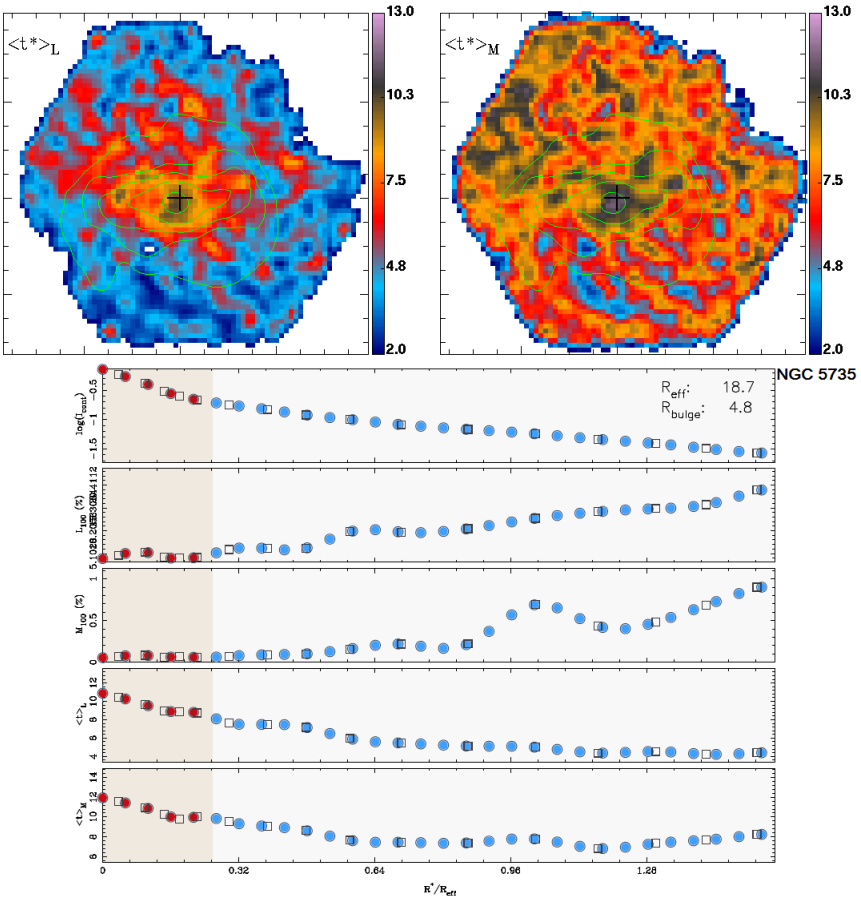
<t*>L
<t*>M
13.0
10.3
7.5
4.8
2.0
NGC 5735
R_eff: 18.7
R_bulge: 4.8
0.32
0.64
0.96
1.28
R*/R_eff

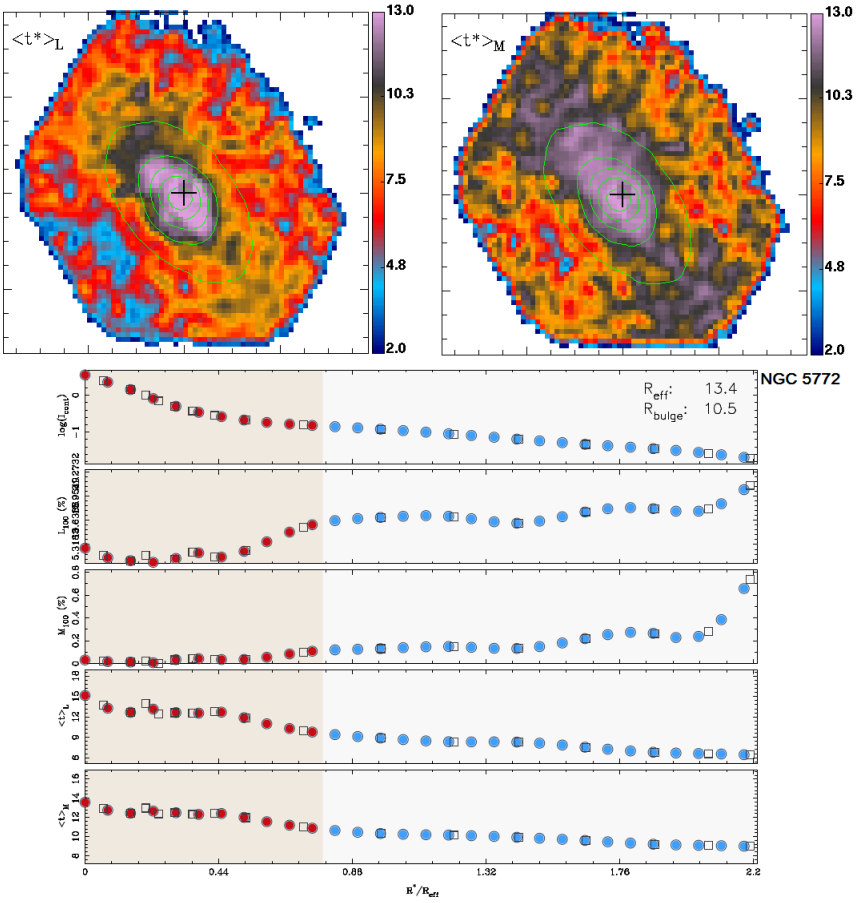
<t*>L
<t*>M
13.0
10.3
7.5
4.8
2.0
NGC 5772
R_eff: 13.4
R_bulge: 10.5
0.44
0.88
1.32
1.76
2.2
R*/R_eff

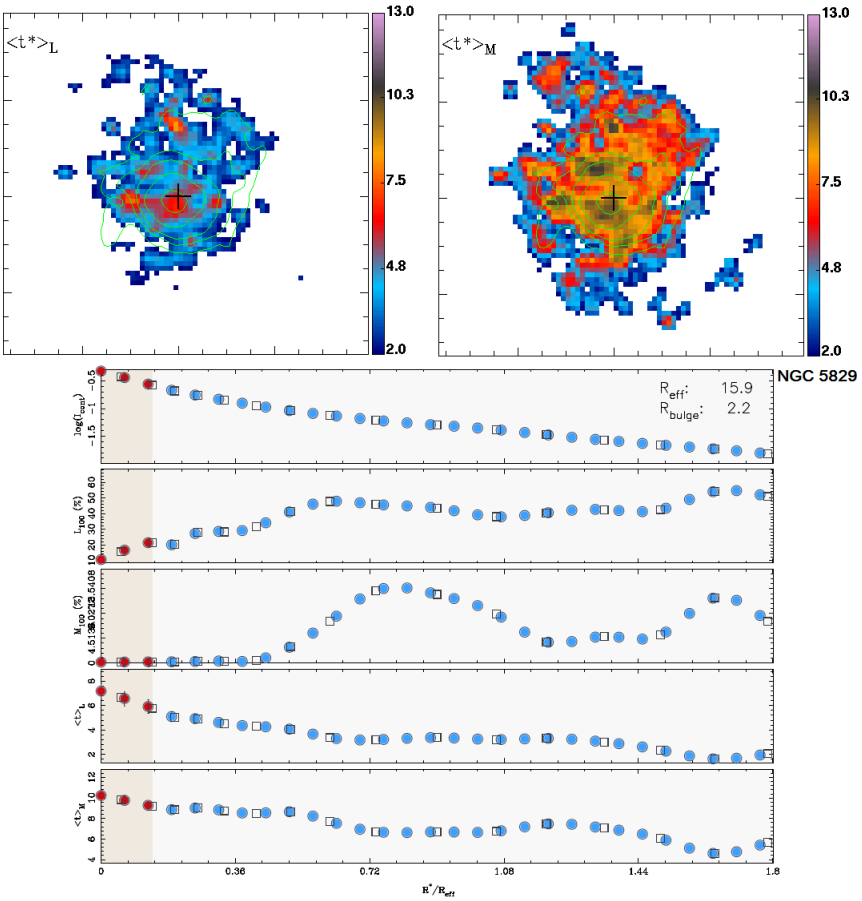
<t*>L
<t*>M
13.0
10.3
7.5
4.8
2.0
NGC 5829
Reff: 15.9
Rbulge: 2.2
R*/Reff

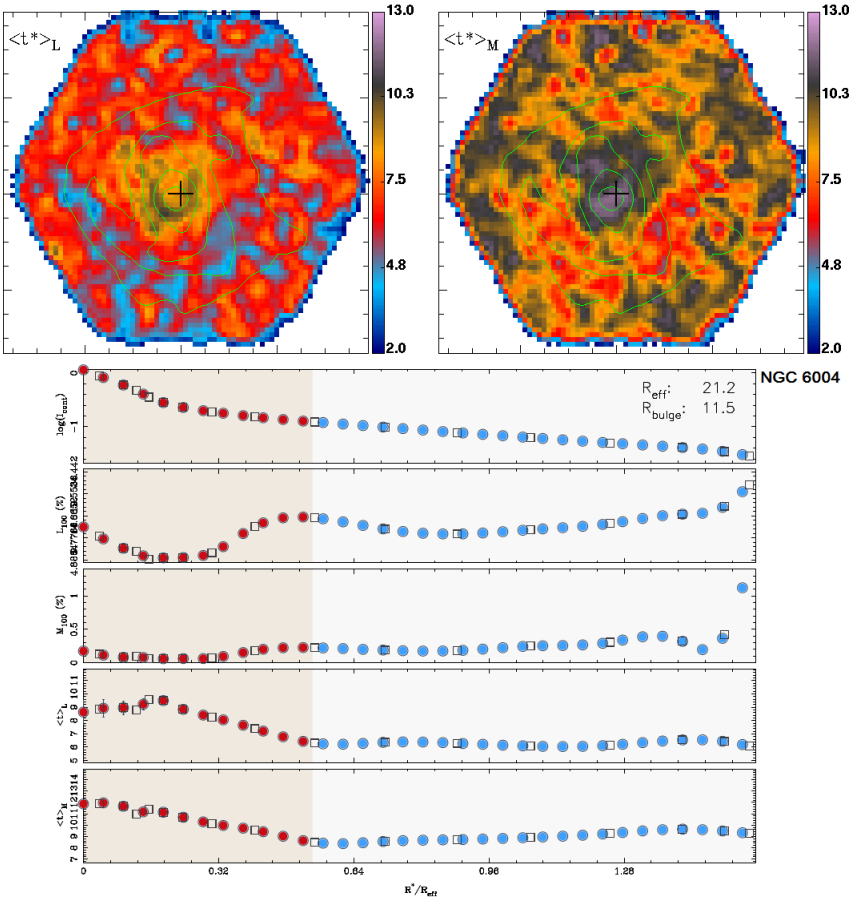
<t*>L
<t*>M
13.0
10.3
7.5
4.8
2.0
NGC 6004
Reff: 21.2
Rbulge: 11.5
R*/Reff

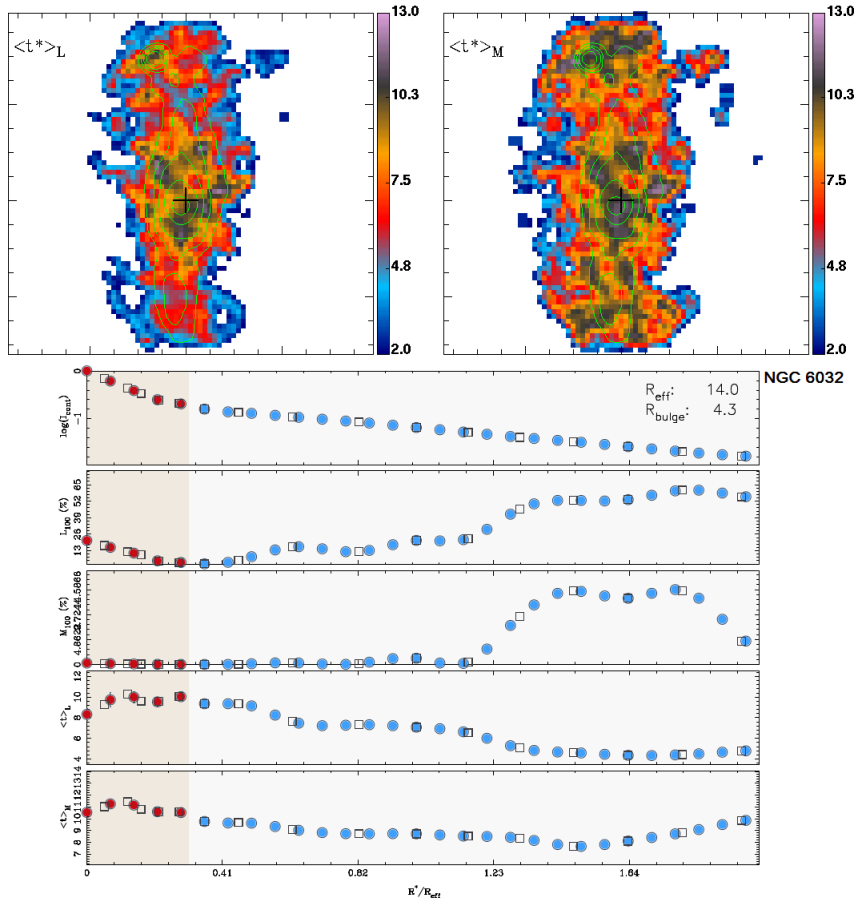
<t*>L
<t*>M
13.0
10.3
7.5
4.8
2.0
NGC 6032
R_eff: 14.0
R_bulge: 4.3
R*/R_eff

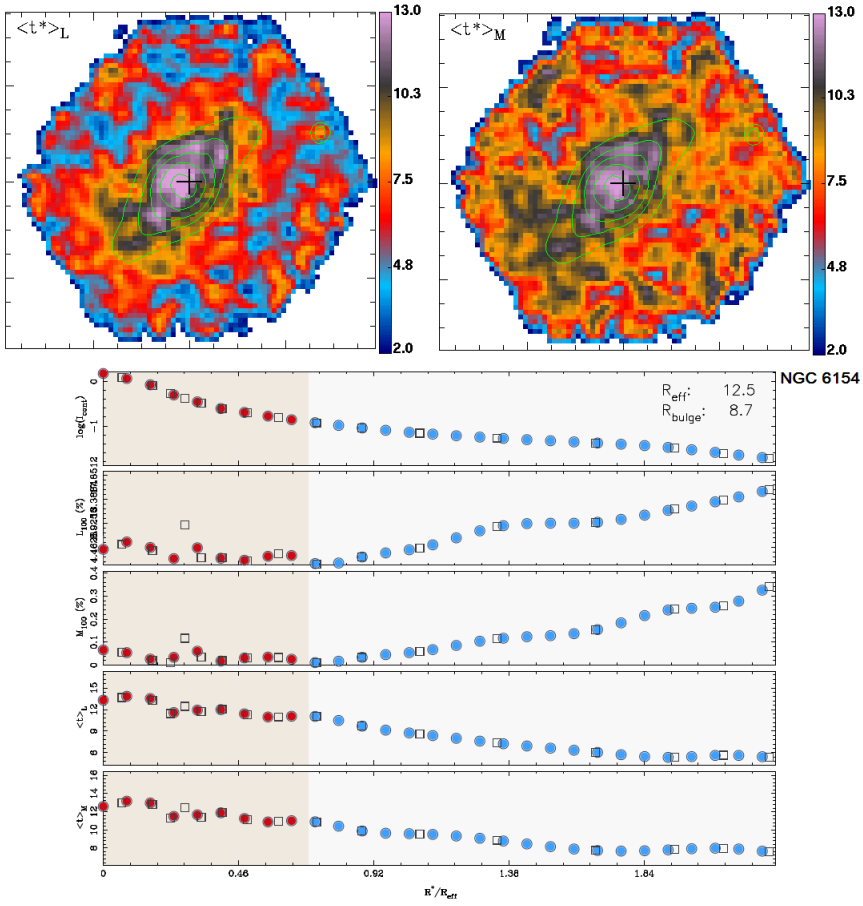
<t*>L
<t*>M
13.0
10.3
7.5
4.8
2.0
NGC 6154
R_eff: 12.5
R_bulge: 8.7
R*/R_eff

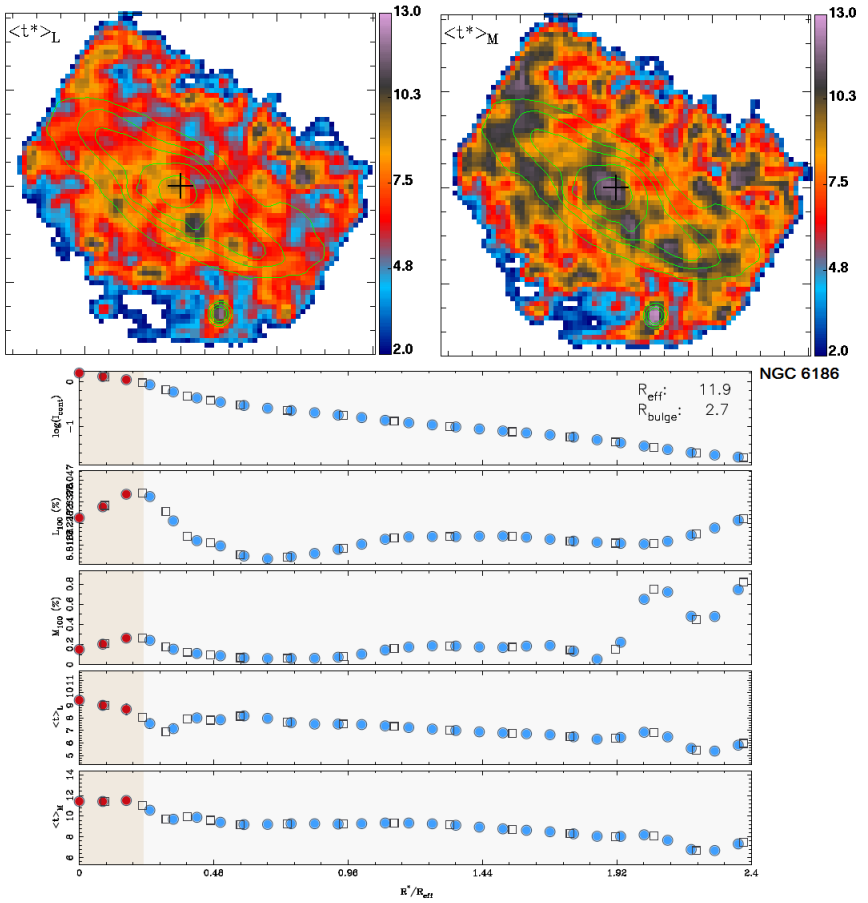
<t*>L
<t*>M
13.0
10.3
7.5
4.8
2.0
NGC 6186
R_eff: 11.9
R_bulge: 2.7
R*/R_eff

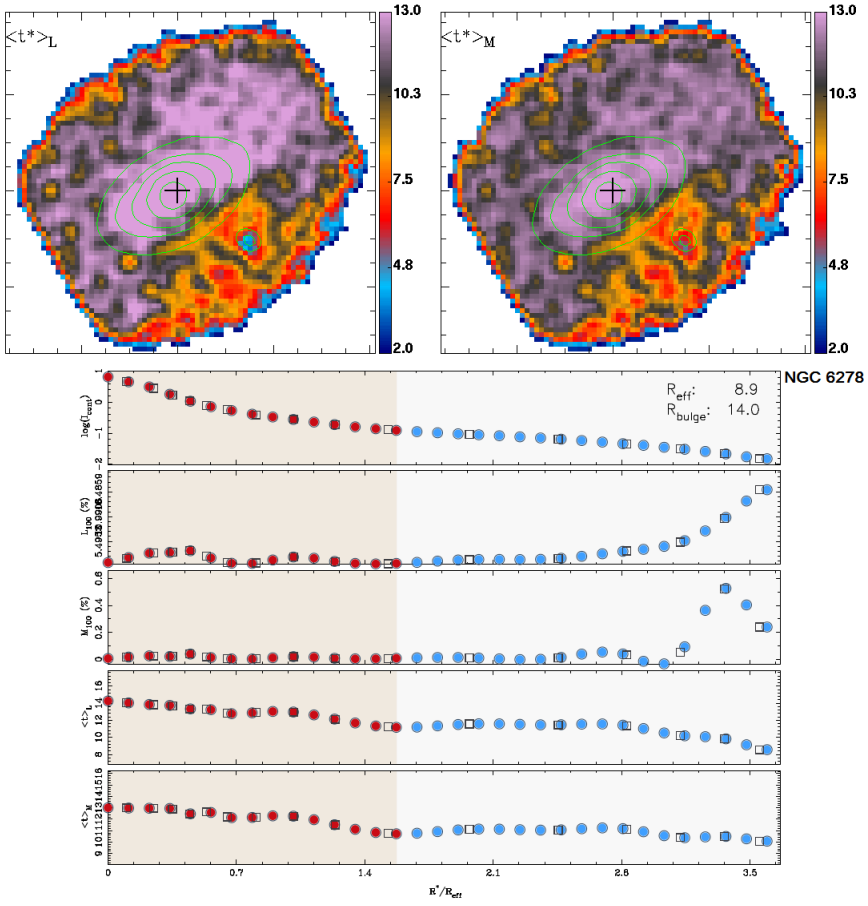
<t*>L
<t*>M
13.0
10.3
7.5
4.8
2.0
NGC 6278
R_eff: 8.9
R_bulge: 14.0
R*/R_eff

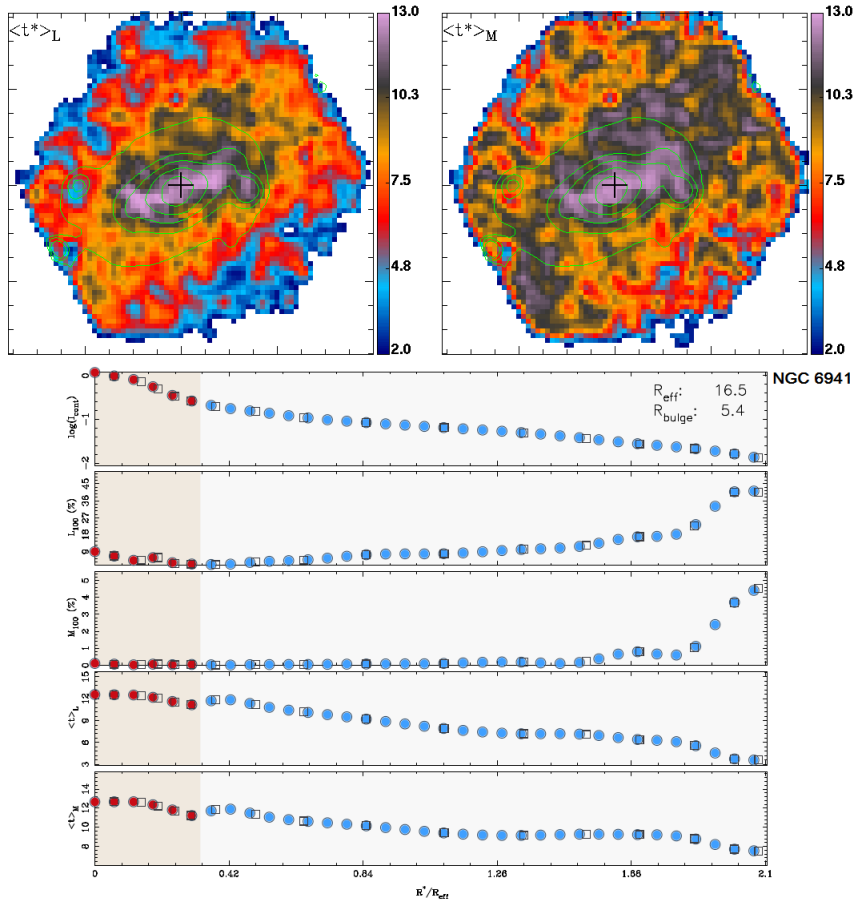
<t*>L
<t*>M
13.0
10.3
7.5
4.8
2.0
NGC 6941
R_eff: 16.5
R_bulge: 5.4
log(τ_sfh)
i_100 (%)
M_100 (%)
<t>L
<t>M
R*/R_eff

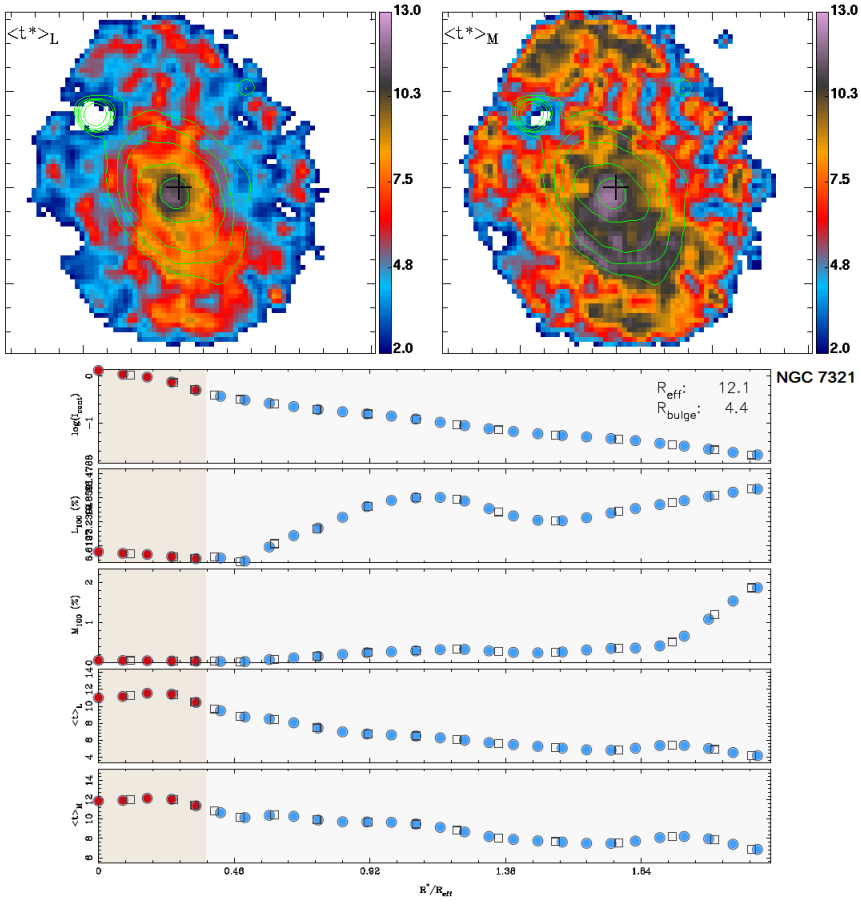
<t*>L
<t*>M
13.0
10.3
7.5
4.8
2.0
NGC 7321
R_eff: 12.1
R_bulge: 4.4
log(τ_sfh)
i_100 (%)
M_100 (%)
<t>L
<t>M
R*/R_eff

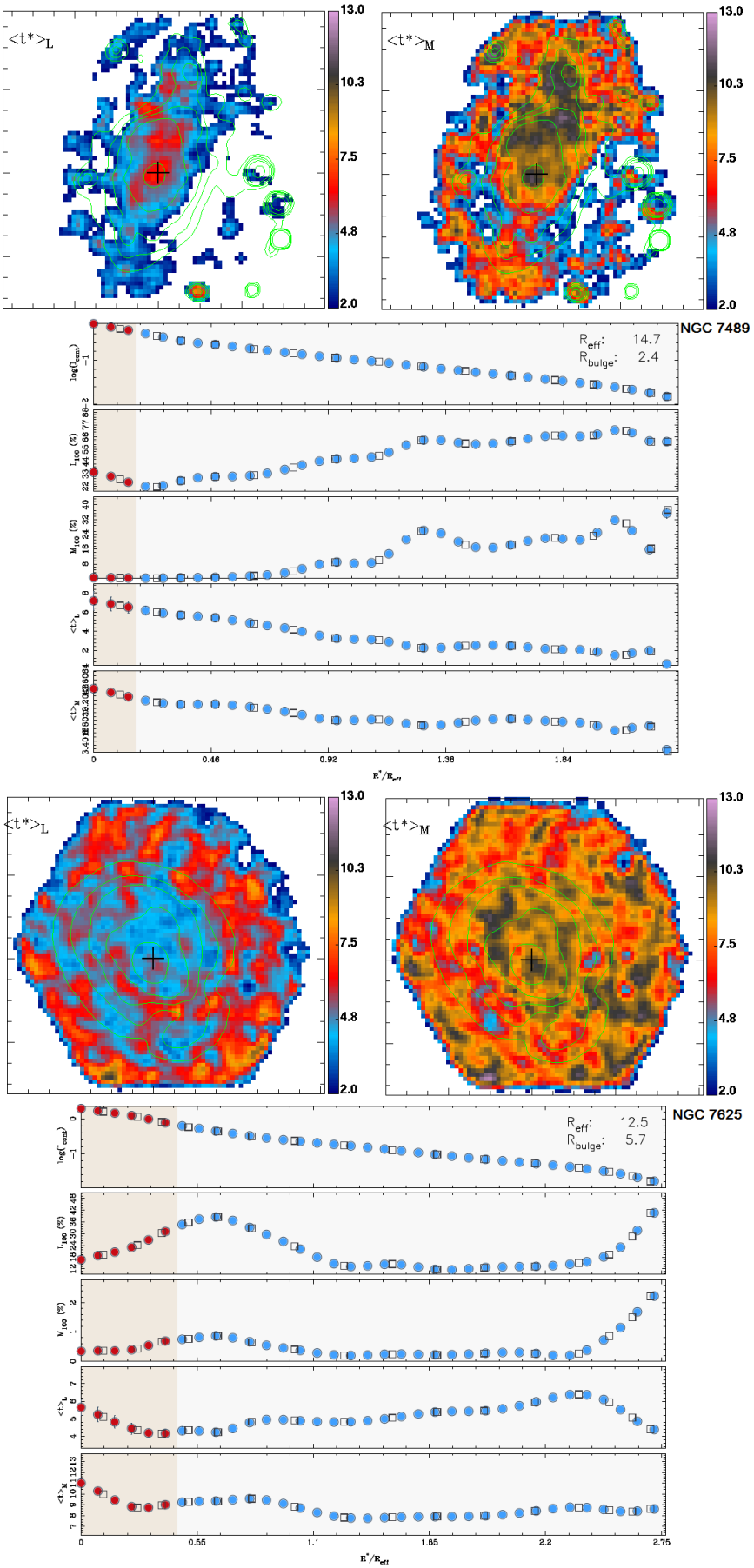
<t*>L
<t*>M
13.0
10.3
7.5
4.8
2.0
NGC 7489
R_eff: 14.7
R_bulge: 2.4
log(τ_cent)
L100 (%)
M100 (%)
<t>L
<t>M
0
0.46
0.92
1.38
1.84
R*/R_eff
NGC 7625
R_eff: 12.5
R_bulge: 5.7
0
0.55
1.1
1.65
2.2
2.75

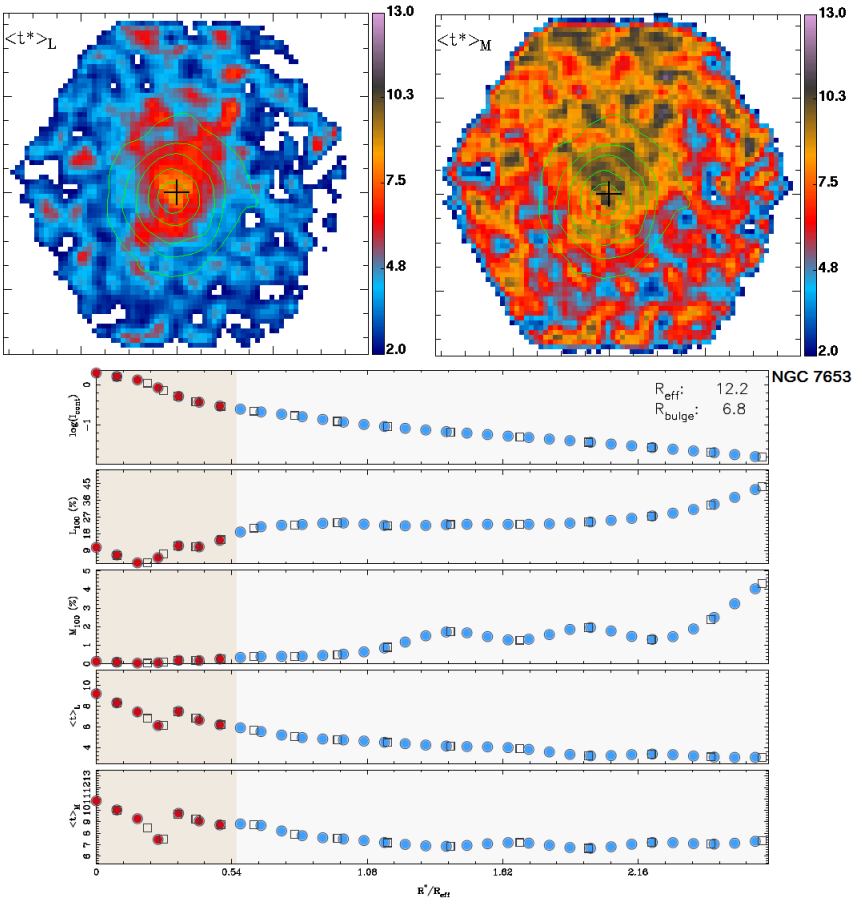
<t*>L
<t*>M
13.0
10.3
7.5
4.8
2.0
NGC 7653
R_eff: 12.2
R_bulge: 6.8
R*/R_eff

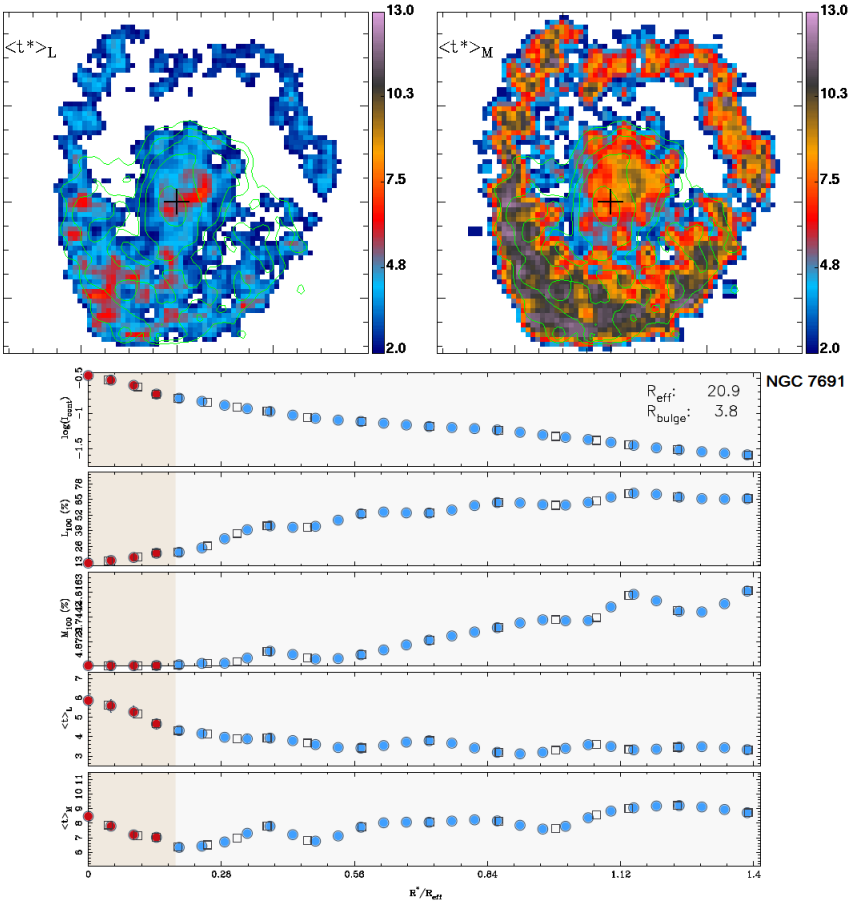
<t*>L
<t*>M
13.0
10.3
7.5
4.8
2.0
NGC 7691
R_eff: 20.9
R_bulge: 3.8
R*/R_eff

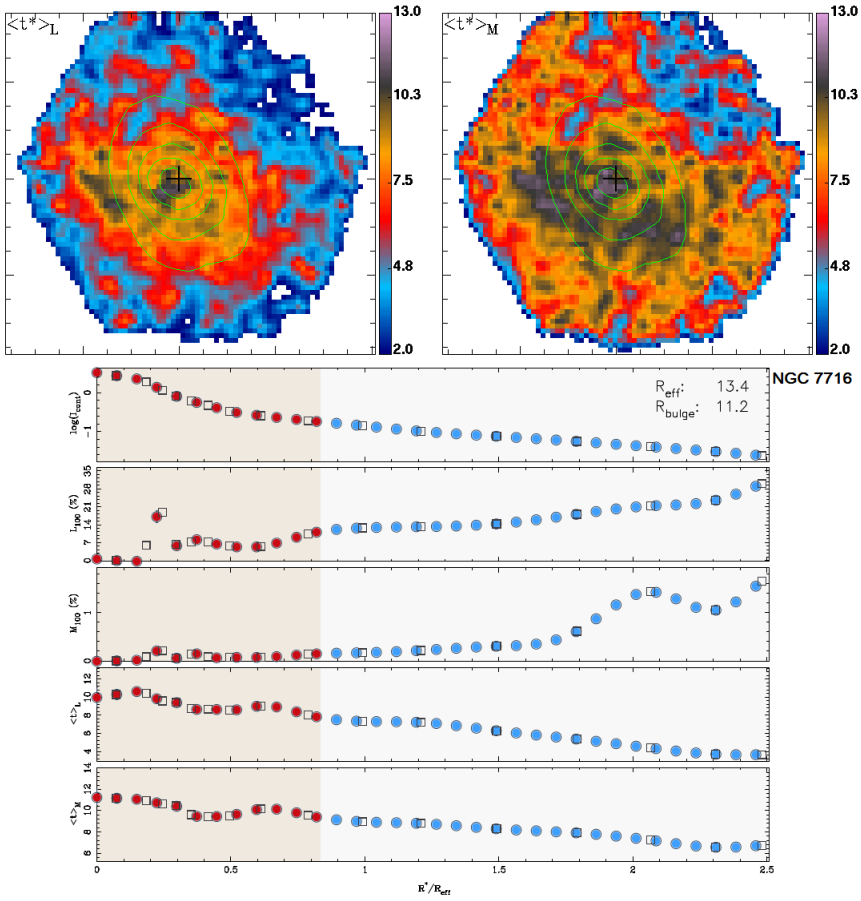
<t*>L
<t*>M
13.0
10.3
7.5
4.8
2.0
NGC 7716
R_eff: 13.4
R_bulge: 11.2
R*/R_eff

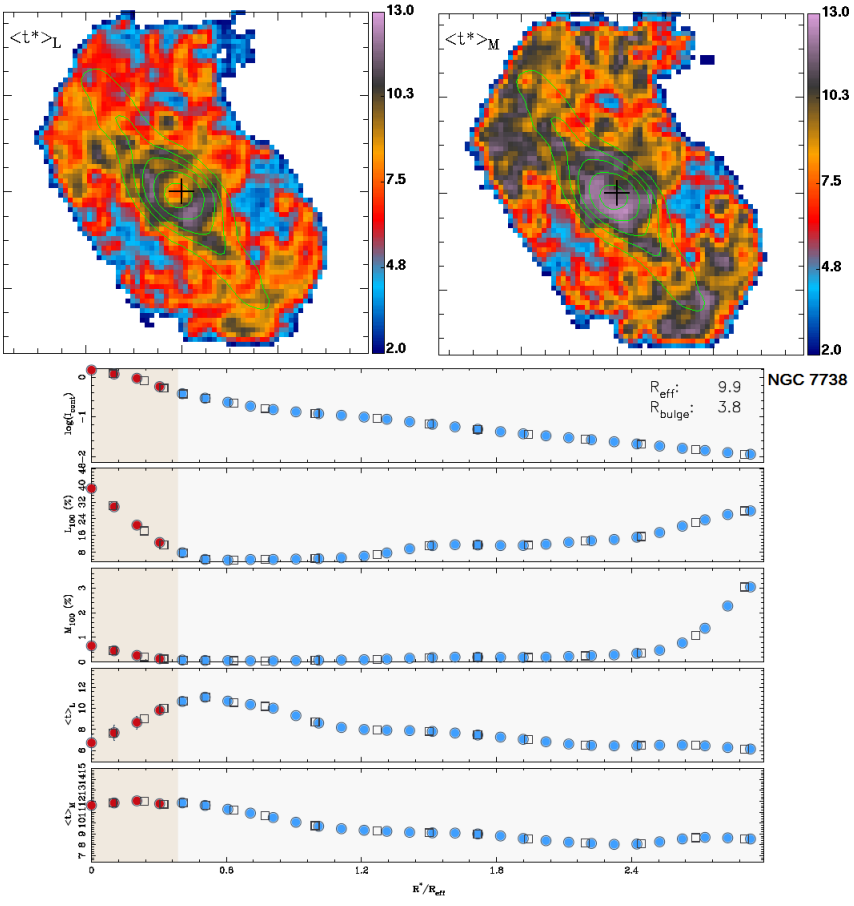
<t*>L
<t*>M
13.0
10.3
7.5
4.8
2.0
NGC 7738
R_eff: 9.9
R_bulge: 3.8
R*/R_eff

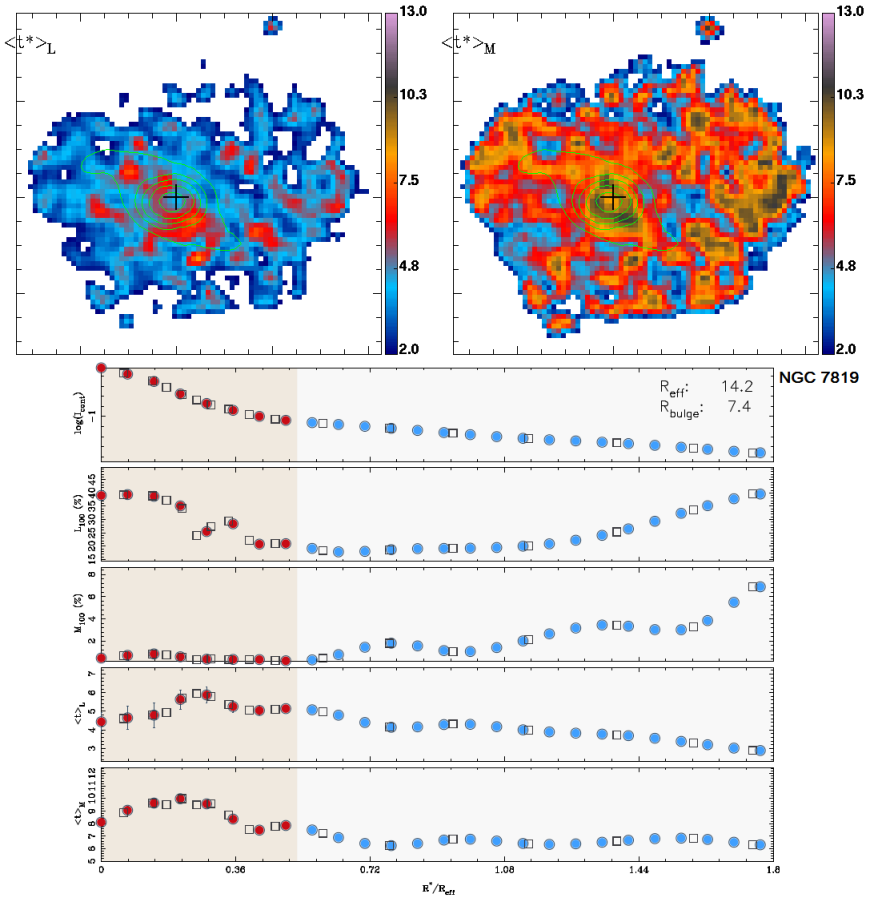
<t*>L
<t*>M
13.0
10.3
7.5
4.8
2.0
NGC 7819
R_eff: 14.2
R_bulge: 7.4
R*/R_eff

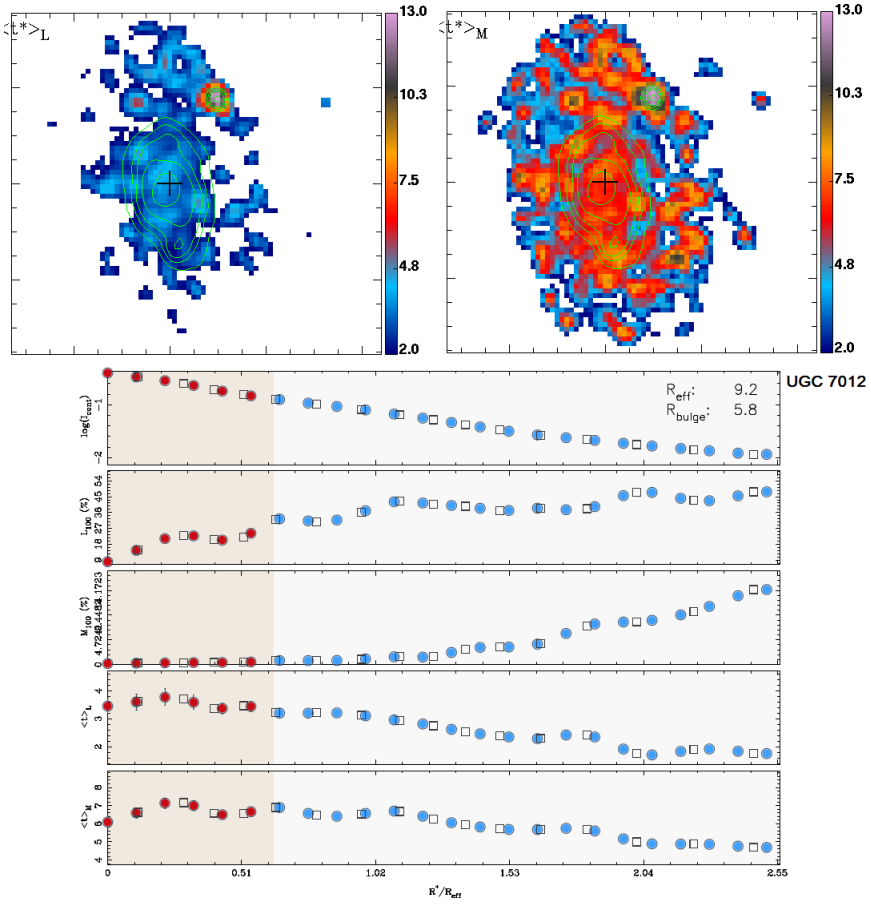
<t*>L
<t*>M
13.0
10.3
7.5
4.8
2.0
UGC 7012
R_eff: 9.2
R_bulge: 5.8
R*/R_eff

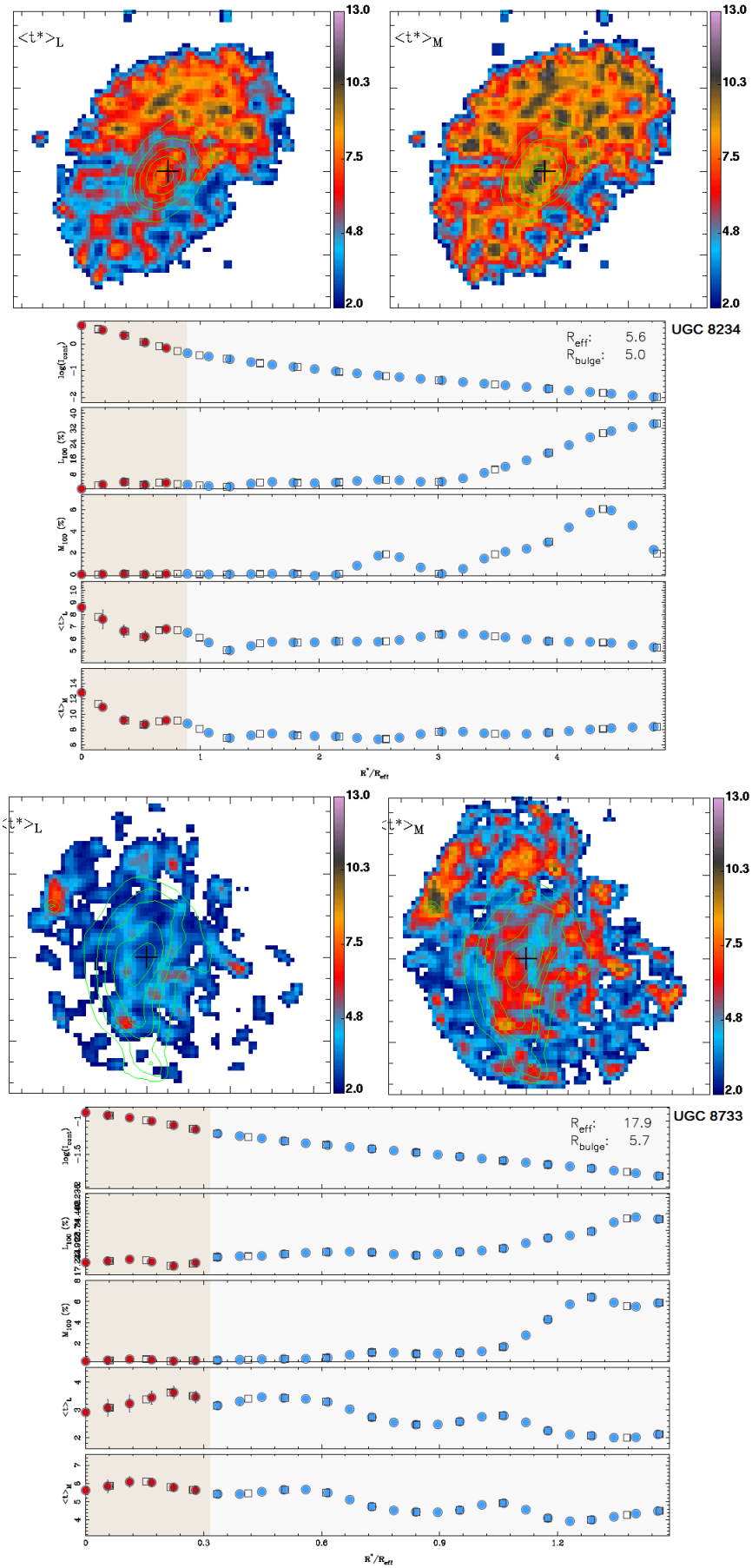
<t*>L
<t*>M
13.0
10.3
7.5
4.8
2.0
UGC 8234
R_eff: 5.6
R_bulge: 5.0
UGC 8733
R_eff: 17.9
R_bulge: 5.7
R*/R_eff

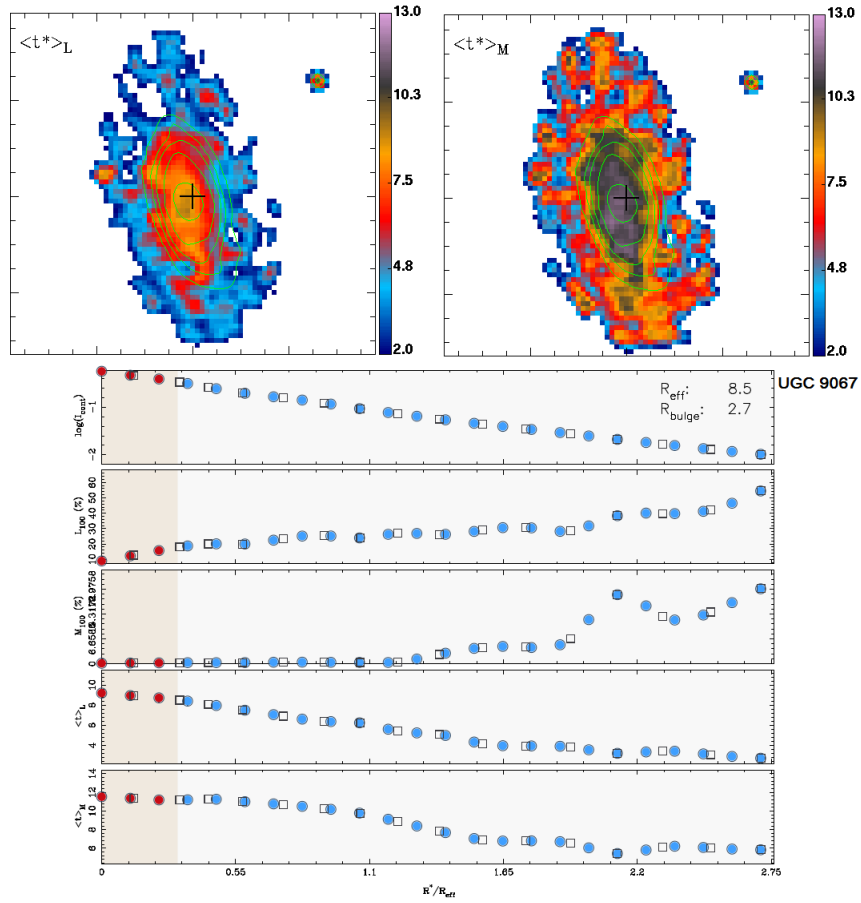
<t*>L
<t*>M
13.0
10.3
7.5
4.8
2.0
UGC 9067
R_eff: 8.5
R_bulge: 2.7
0.55
1.1
1.65
2.2
2.75
R'/R_eff

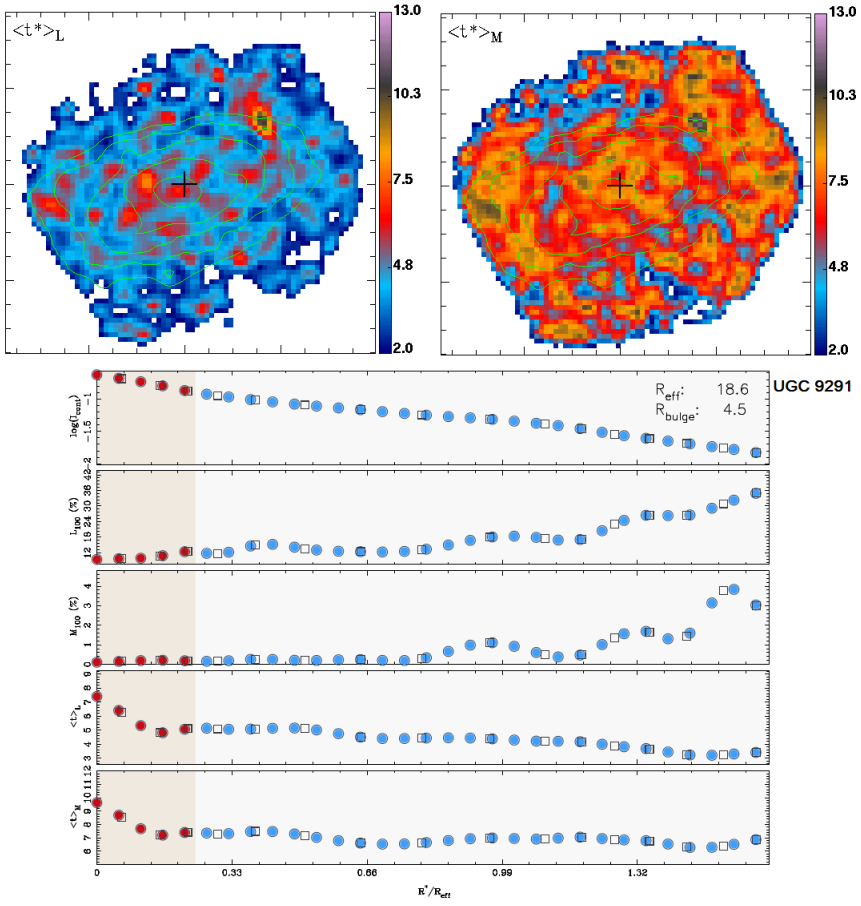
<t*>L
<t*>M
13.0
10.3
7.5
4.8
2.0
UGC 9291
R_eff: 18.6
R_bulge: 4.5
0.33
0.66
0.99
1.32
R'/R_eff

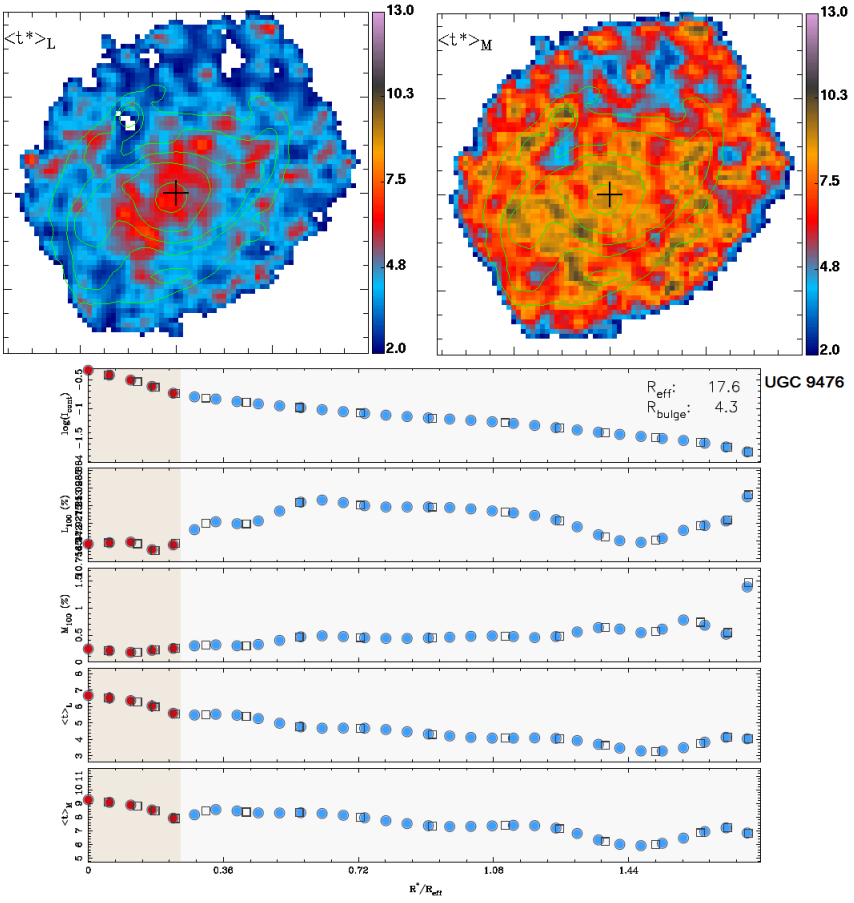
<t*>L
<t*>M
13.0
10.3
7.5
4.8
2.0
UGC 9476
R_eff: 17.6
R_bulge: 4.3
0
0.36
0.72
1.08
1.44
R*/R_eff

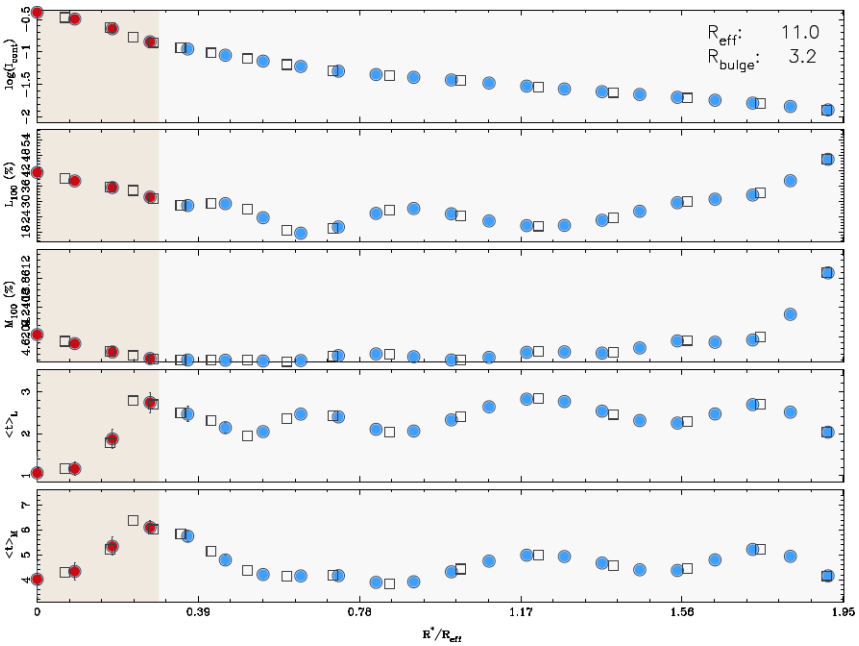
R_eff: 11.0
R_bulge: 3.2
0
0.39
0.78
1.17
1.56
1.95
R*/R_eff

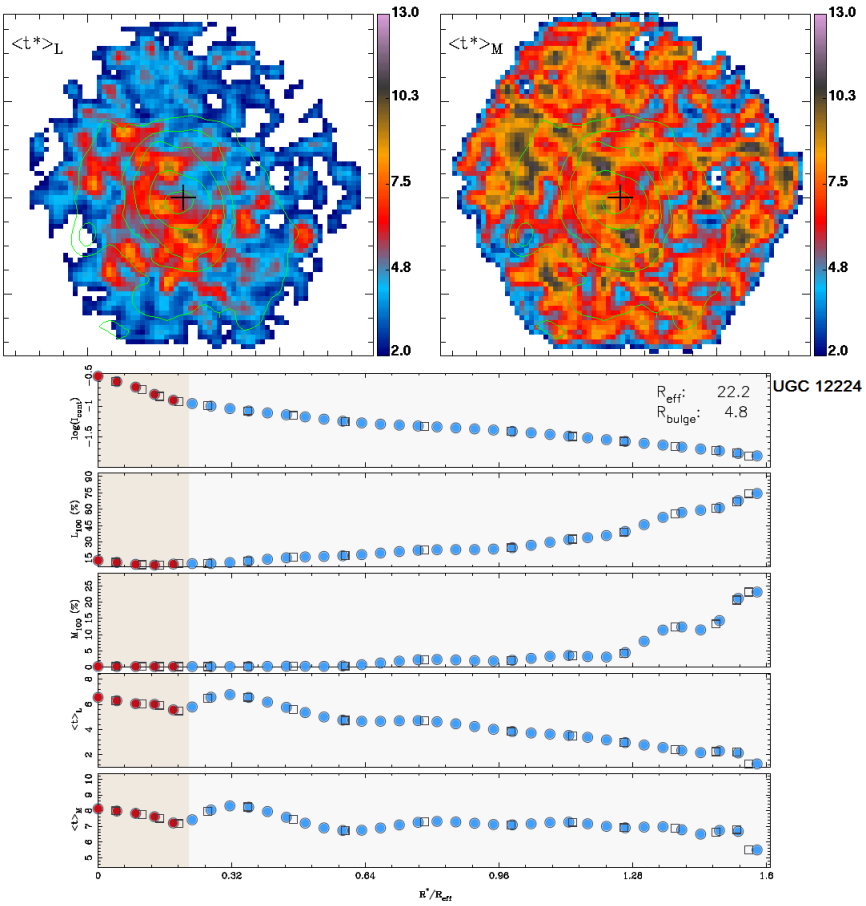

Figure B.1: Top panels: 2D maps are from left to right luminosity- and mass-weighted stellar ages, respectively. From top to bottom, radial profiles of: logarithm of the emission-line free continuum between 6390–6490 Å; luminosity fraction of stellar populations younger than 100 Myr; mass fraction of stellar populations younger than 100 Myr; luminosity-weighted stellar age and mass-weighted stellar age. The bulge region is shown in red (light-shaded area). The black empty squares and colored circles (bulge - red and disk - blue) are, respectively, the measured quantities for each irregular isophotal annulus and the result of a spline interpolation in steps of 1 arcsec.

Appendix C.

Tables

Table C.1 shows the photometric parameters obtained from the surface photometry and profile decomposition for our entire sample. Tables C.2 and C.3 presents the spectroscopic quantities obtained from the spectral synthesis.

Table C.1: Parameters obtained from the photometric decomposition. From left to right: name of the galaxy, total absolute magnitude, effective radius, disk absolute magnitude, disk effective radius, disk central surface brightness, disk scale-length, bar absolute magnitude, bar central surface brightness, bar scale-length, bar Sérsic index, bar-to-total, bulge absolute magnitude, bulge radius, bulge effective radius, bulge R_{80}, surface brightness at bulge effective radius, bulge sérsic index, bulge CI8020 concentration index (R_{80}/R_{20}), distance-independent concentration index (CIP96; see Papaderos et al. (1996)), bulge-to-total, bulge-to-disk and bulge-to-bar (in light).

Galaxy	Total		Disk				Bar				BA/T	Bulge							CIP96	B/T	B/D	B/BA
	M	$r_{\rm eff}$	M	$r_{\rm eff}$	μ_0	α	M	μ_0	α	η		M	$r_{\rm bulge}$	$r_{\rm eff}$	R_{80}	$\mu_{r_{\rm eff}}$	η	CI8020				
IC0776	-18.96	3181.28	-18.88	3739.68	21.79	17.47	-16.49	22.54	9.17	0.45	0.10	-15.06	610.12	524.41	812.31	22.53	0.50	2.10	0.98	0.03	0.03	0.27
IC1256	-21.15	4390.99	-21.03	4677.71	19.87	8.86	-	-	-	-	-	-17.21	932.50	424.86	680.44	19.98	0.60	4.20	0.82	0.03	0.03	-
IC4566	-21.71	5086.38	-21.56	6283.86	19.99	10.12	-18.88	20.77	5.90	0.25	0.07	-19.09	1557.73	616.57	987.47	18.91	0.60	2.42	0.98	0.09	0.10	1.21
NGC0001	-21.43	2562.86	-20.81	4560.57	20.04	10.26	-	-	-	-	-	-20.37	10004.10	1131.12	2299.78	19.36	1.50	3.77	0.80	0.36	0.67	-
NGC0023	-22.28	3093.08	-21.33	6680.20	20.39	15.58	-20.75	20.52	17.44	0.25	0.24	-21.22	3826.51	751.42	1313.59	17.37	0.90	2.49	0.96	0.38	0.91	1.54
NGC0160	-21.96	4993.91	-21.49	6517.47	20.15	12.93	-	-	-	-	-	-20.42	5717.68	1078.02	1988.45	19.05	1.10	3.12	0.93	0.24	0.38	-
NGC0165	-21.35	5683.04	-21.28	6638.37	20.43	12.16	-	-	-	-	-	-19.23	3783.00	825.21	1522.64	19.67	1.10	2.59	0.96	0.14	0.15	-
NGC0171	-21.67	5267.07	-21.56	5755.48	19.79	14.82	-	-	-	-	-	-19.34	5085.25	847.84	1644.37	19.69	1.30	2.90	0.96	0.12	0.13	-
NGC0180	-22.11	7728.63	-22.11	8937.68	20.23	17.85	-18.81	20.89	7.39	0.25	0.05	-18.86	1480.79	596.84	955.85	19.06	0.60	2.36	0.99	0.05	0.05	1.05
NGC0214	-22.04	4446.22	-21.89	5229.43	19.21	11.26	-19.51	20.31	8.96	0.35	0.10	-18.64	1339.58	540.12	864.87	19.07	0.60	2.38	0.99	0.04	0.05	0.45
NGC0237	-20.88	2779.95	-20.61	3173.54	19.42	7.53	-18.84	21.37	11.65	0.35	0.15	-17.84	1543.27	545.64	926.61	20.02	0.80	2.59	0.97	0.06	0.08	0.40
NGC0257	-22.00	5543.45	-21.94	6184.80	19.54	11.74	-	-	-	-	-	-19.40	2431.29	724.70	1231.57	19.07	0.80	2.87	0.97	0.09	0.10	-
NGC0477	-21.47	6179.46	-21.46	6436.62	20.15	11.37	-	-	-	-	-	-18.16	1434.31	651.40	1043.27	19.95	0.60	2.34	0.99	0.05	0.05	-
NGC0776	-21.81	4869.67	-21.67	5909.97	19.73	12.18	-18.48	21.42	8.76	0.25	0.05	-19.44	1490.20	552.17	884.35	18.32	0.60	2.39	0.98	0.11	0.13	2.41
NGC1093	-21.40	3336.75	-21.09	4719.73	19.83	9.09	-19.37	20.56	8.18	0.25	0.15	-18.96	2543.34	709.03	1239.54	19.51	0.90	2.61	0.97	0.11	0.14	0.69
NGC1645	-21.67	3103.11	-21.11	5730.31	20.26	12.28	-19.37	21.32	12.50	0.25	0.12	-20.25	3093.04	853.19	1449.97	18.57	0.80	2.76	0.95	0.27	0.45	2.26
NGC2253	-21.44	3443.9	-21.28	3511.12	18.94	8.87	-	-	-	-	-	-18.76	1922.55	368.53	662.09	18.34	1.00	2.78	0.98	0.09	0.10	-
NGC2347	-21.89	3408.62	-21.60	4374.31	19.11	9.06	-19.80	19.38	6.52	0.25	0.15	-18.99	2176.68	422.12	758.43	18.40	1.00	2.54	0.99	0.07	0.09	0.48
NGC2639	-22.09	2787.07	-21.65	4018.03	18.86	10.45	-	-	-	-	-	-20.77	7560.03	1204.88	2279.69	18.98	1.20	3.41	0.85	0.30	0.45	-
NGC2730	-20.66	5083.17	-20.71	5456.32	20.59	14.15	-	-	-	-	-	-16.96	1411.40	575.98	1006.88	21.06	0.90	2.69	0.98	0.03	0.03	-
NGC2906	-20.71	2370.51	-20.69	2497.88	18.79	9.60	-	-	-	-	-	-17.75	1263.56	249.95	449.07	18.51	1.00	2.53	0.99	0.07	0.07	-
NGC2916	-21.91	5291.42	-21.91	5984.35	19.50	14.23	-	-	-	-	-	-19.01	2457.39	515.13	925.49	18.82	1.00	2.84	0.98	0.07	0.07	-
NGC3057	-18.81	2496.99	-18.77	2627.55	20.99	15.81	-	-	-	-	-	-15.39	684.35	576.28	867.89	22.33	0.40	2.20	0.96	0.04	0.04	-

Table C.1 Continued.

NGC3300	-21.27	2554.09	-21.02	3146.21	18.97	8.51	-18.91	19.30	5.14	0.50	0.11	-18.51	1082.99	336.39	555.20	18.23	0.70	2.48	0.99	0.08	0.10	0.70
NGC3381	-19.83	2621.68	-19.75	2823.14	20.06	13.60	-16.17	22.61	11.83	0.25	0.03	-16.41	593.85	338.53	513.70	20.21	0.45	1.91	0.99	0.04	0.05	1.25
NGC3614	-20.79	5347.43	-20.75	5584.70	20.60	21.42	-16.83	22.44	11.14	0.25	0.03	-16.60	957.18	443.77	732.42	20.74	0.70	2.49	0.99	0.02	0.02	0.81
NGC3687	-20.66	3057.6	-20.41	3620.38	19.94	12.17	-17.77	23.17	22.51	0.25	0.07	-18.56	2732.45	436.43	825.79	18.99	1.20	2.85	0.97	0.14	0.18	2.07
NGC4003	-21.77	4027.07	-21.47	5313.96	19.70	7.42	-18.78	22.07	9.16	0.25	0.06	-19.88	3166.84	965.52	1640.89	19.21	0.80	2.58	0.96	0.18	0.23	2.76
NGC4047	-21.67	3547.38	-21.52	4020.07	19.00	9.80	-19.05	19.93	6.99	0.30	0.09	-17.37	815.28	340.58	544.53	19.35	0.60	2.45	0.99	0.02	0.02	0.21
NGC4185	-21.67	6972.93	-21.68	7362.57	20.25	17.18	-	-	-	-	-	-18.29	3155.48	777.86	1472.15	20.51	1.20	2.91	0.97	0.04	0.04	-
NGC4210	-20.83	3955.17	-20.49	3541.67	19.80	11.13	-	-	-	-	-	-17.38	932.37	410.25	656.98	19.73	0.60	2.47	0.98	0.04	0.06	-
NGC4961	-19.99	2168.43	-19.66	2840.08	20.17	9.37	-18.34	20.69	8.97	0.30	0.22	-16.23	853.28	417.74	689.11	20.99	0.70	2.52	0.98	0.03	0.04	0.14
NGC5000	-21.45	5226.24	-21.29	6116.45	20.23	10.17	-19.08	20.15	4.18	0.70	0.11	-17.84	958.38	392.94	625.77	19.20	0.60	2.32	0.99	0.04	0.04	0.32
NGC5016	-20.86	3122.76	-20.82	3237.40	19.24	9.76	-17.00	21.98	8.62	0.25	0.03	-15.85	448.33	252.58	386.04	20.11	0.45	2.24	1.00	0.01	0.01	0.34
NGC5205	-19.89	2163.82	-19.76	2391.61	19.67	10.46	-	-	-	-	-	-17.47	1871.86	349.15	660.75	19.60	1.20	3.25	0.94	0.11	0.12	-
NGC5320	-20.85	3957.71	-20.81	4013.68	19.75	12.51	-	-	-	-	-	-16.96	1283.40	451.23	788.83	20.53	0.90	2.51	0.99	0.03	0.03	-
NGC5378	-21.10	4483.67	-20.82	6217.12	20.79	18.91	-18.59	21.43	12.16	0.25	0.10	-18.89	2876.28	551.99	1018.17	19.13	1.10	3.16	0.98	0.13	0.17	1.32
NGC5406	-22.32	6200.58	-22.18	7368.36	19.70	12.57	-19.06	20.81	7.14	0.25	0.05	-19.82	2242.06	585.95	995.82	18.19	0.80	2.58	0.99	0.10	0.11	2.01
NGC5480	-20.54	2957.36	-20.42	3041.87	19.51	12.31	-	-	-	-	-	-17.58	1322.61	285.19	512.38	18.96	1.00	2.50	0.99	0.07	0.07	-
NGC5614	-22.41	3933.19	-22.02	5737.80	19.29	12.28	-	-	-	-	-	-21.41	455513.00	1077.94	3193.74	18.67	3.80	3.67	0.92	0.40	0.57	-
NGC5656	-21.45	3001.68	-21.30	3305.74	18.78	8.28	-	-	-	-	-	-19.05	39924.70	422.02	1194.02	18.79	2.90	5.02	0.86	0.11	0.13	-
NGC5735	-21.18	5405.07	-21.19	6187.29	20.37	15.10	-17.82	21.65	7.87	0.30	0.05	-17.33	1148.41	474.81	783.66	20.17	0.70	2.49	0.99	0.03	0.03	0.63
NGC5772	-22.00	4847.15	-21.78	5839.69	19.58	10.44	-	-	-	-	-	-20.27	10704.30	628.48	1336.14	18.25	1.70	2.93	0.98	0.20	0.25	-
NGC5829	-21.35	6594.55	-21.26	7216.70	20.65	12.48	-18.71	20.26	3.80	0.65	0.09	-16.35	664.64	368.67	570.80	20.47	0.50	2.20	1.00	0.01	0.01	0.11
NGC6004	-21.68	6234.81	-21.77	7753.36	20.27	18.34	-	-	-	-	-	-19.09	42171.90	791.96	2214.30	20.24	3.20	3.86	0.95	0.09	0.08	-
NGC6032	-21.13	4563.58	-20.99	4750.89	19.95	9.81	-	-	-	-	-	-18.08	1527.50	395.20	690.89	19.12	0.90	2.80	0.98	0.06	0.07	-
NGC6154	-21.79	5371.14	-21.57	6564.72	20.09	10.41	-	-	-	-	-	-19.88	5463.98	964.85	1825.64	19.39	1.20	3.14	0.94	0.17	0.21	-
NGC6186	-21.11	2774.27	-20.94	3185.70	19.08	8.62	-18.67	18.91	4.02	0.35	0.11	-17.00	444.85	237.46	358.49	18.78	0.40	2.15	1.00	0.02	0.03	0.22
NGC6278	-21.45	1977.84	-21.02	3635.48	19.29	10.45	-	-	-	-	-	-20.31	7501.88	563.29	1145.04	17.90	1.50	3.31	0.93	0.35	0.52	-
NGC6941	-22.22	7075.28	-22.09	8486.28	20.12	13.37	-19.15	20.62	6.07	0.25	0.06	-19.55	2335.38	657.61	1117.60	18.71	0.80	2.60	0.99	0.09	0.10	1.45

Table C.1 Continued.

NGC7321	-22.32	5736.73	-22.24	6250.92	19.25	8.38	-18.24	21.34	5.04	0.25	0.02	-19.03	1823.62	633.70	1045.90	19.09	0.70	2.47	0.99	0.05	0.05	2.08
NGC7489	-22.27	6061.76	-22.26	6270.38	19.24	9.71	-	-	-	-	-	-17.66	658.27	428.73	618.30	19.47	0.30	2.61	1.00	0.01	0.01	-
NGC7625	-20.14	1438.86	-19.92	1820.51	18.88	9.92	-17.97	19.43	7.57	0.35	0.14	-16.88	429.35	274.25	405.90	19.16	0.30	2.32	0.99	0.05	0.06	0.36
NGC7653	-21.50	3442.53	-21.21	4851.69	19.76	11.29	-19.09	20.79	9.71	0.25	0.11	-19.33	1910.14	513.63	872.91	18.39	0.80	2.70	0.98	0.13	0.18	1.25
NGC7691	-21.01	5597.32	-21.01	6039.67	20.51	16.00	-17.37	21.48	6.37	0.30	0.03	-16.09	761.06	419.55	671.88	21.07	0.60	2.39	0.99	0.01	0.01	0.31
NGC7716	-20.79	2316.6	-20.51	3419.92	19.69	12.94	-	-	-	-	-	-19.29	3081.78	403.76	763.96	18.09	1.20	3.26	0.91	0.25	0.33	-
NGC7738	-21.86	4387.85	-21.59	5526.47	19.66	8.13	-19.65	19.43	3.85	0.60	0.13	-19.09	1367.06	519.38	827.32	18.55	0.60	2.29	0.99	0.08	0.10	0.59
NGC7819	-20.83	4613.28	-20.70	5680.95	20.70	12.61	-	-	-	-	-	-18.90	2503.62	704.30	1231.16	19.56	0.90	2.60	0.96	0.17	0.19	-
UGC07012	-19.62	2195.65	-19.18	2906.27	20.78	8.87	-18.20	21.20	8.97	0.40	0.27	-16.87	1212.67	521.87	886.66	20.89	0.80	2.38	0.96	0.08	0.12	0.30
UGC08234	-22.60	3157.66	-21.96	7381.51	19.93	8.73	-20.89	19.67	6.66	0.25	0.21	-21.24	2337.14	782.95	1253.90	17.28	0.60	2.27	0.98	0.29	0.51	1.38
UGC08733	-19.33	3438.75	-19.29	3523.07	21.14	14.39	-	-	-	-	-	-15.63	779.48	524.59	864.39	22.09	0.70	2.37	0.98	0.03	0.03	-
UGC09067	-21.69	4791.29	-21.61	5101.22	19.44	5.83	-18.06	21.30	3.73	0.40	0.04	-17.48	1141.84	542.01	867.98	20.24	0.60	2.11	0.99	0.02	0.02	0.59
UGC09291	-20.29	4301.86	-20.31	4491.49	20.57	13.92	-	-	-	-	-	-15.74	763.62	501.54	803.24	21.81	0.60	2.30	0.99	0.02	0.01	-
UGC09476	-20.75	4475.16	-20.92	5519.55	20.41	15.69	-16.96	22.22	7.84	0.25	0.03	-16.78	851.52	410.60	657.52	20.34	0.60	2.33	0.99	0.03	0.02	0.85
UGC10796	-19.28	2554.25	-19.13	2923.37	20.84	9.26	-16.83	20.60	3.42	0.60	0.10	-15.60	576.92	308.04	489.59	20.91	0.60	2.15	0.99	0.03	0.04	0.32
UGC12224	-20.63	5236.71	-20.72	5866.67	20.77	18.37	-16.28	23.24	9.87	0.25	0.02	-16.43	881.47	407.68	672.85	20.73	0.70	2.51	0.99	0.02	0.02	1.14

Table C.2: Mean values ($\bar{x}$), standard deviation (σ), and standard error of the mean ($\bar{\sigma}$) of some physical quantities obtained from the spectroscopy. From left to right: luminosity and mass fractions of stellar populations younger than 100 Myr for bulge and disk regions.

Galaxy	L100 Bulge			L100 Disk			M100 Bulge			M100 Disk		
	$\bar{x}$	σ	$\bar{\sigma}$	$\bar{x}$	σ	$\bar{\sigma}$	$\bar{x}$	σ	$\bar{\sigma}$	$\bar{x}$	σ	$\bar{\sigma}$
IC0776	23.50	1.65	0.74	37.43	8.22	1.75	0.48	0.13	0.06	6.37	8.58	1.83
IC1256	9.00	2.03	1.01	18.51	7.92	1.55	0.10	0.07	0.04	0.80	1.09	0.21
IC4566	4.22	1.11	0.50	12.15	5.35	1.09	0.04	0.05	0.02	0.46	0.51	0.10
NGC0001	15.94	5.58	1.35	32.23	12.51	3.23	0.22	0.11	0.03	4.13	4.66	1.20
NGC0023	23.10	3.86	1.12	18.93	1.71	0.42	0.38	0.14	0.04	0.38	0.19	0.05
NGC0160	8.86	6.46	1.79	52.86	8.44	1.99	0.12	0.12	0.03	3.33	2.30	0.54
NGC0165	17.62	7.95	2.81	11.16	4.02	0.95	0.26	0.20	0.07	0.32	0.30	0.07
NGC0171	7.18	3.14	0.87	16.71	4.98	1.17	0.09	0.11	0.03	1.03	1.06	0.25
NGC0180	24.88	4.42	1.81	11.31	3.81	0.79	0.33	0.13	0.05	0.29	0.36	0.07
NGC0214	9.37	2.29	0.93	41.40	14.01	2.80	0.11	0.07	0.03	2.63	3.04	0.61
NGC0237	13.26	5.95	2.43	28.88	3.88	0.83	0.23	0.13	0.05	2.83	2.36	0.50
NGC0257	17.43	6.19	2.19	43.26	9.56	1.99	0.25	0.15	0.05	2.24	1.70	0.35
NGC0477	10.07	2.59	1.16	19.74	9.50	1.94	0.14	0.11	0.05	1.09	1.58	0.32
NGC0776	11.62	3.24	1.32	13.91	2.57	0.51	0.13	0.09	0.04	0.23	0.09	0.02
NGC1093	4.07	2.33	0.88	16.78	7.32	1.56	0.04	0.06	0.02	0.82	1.41	0.30
NGC1645	4.53	1.07	0.34	28.87	10.80	2.48	0.05	0.02	0.01	7.21	5.97	1.37
NGC2253	12.35	4.59	1.74	25.91	4.78	0.96	0.15	0.10	0.04	0.83	0.77	0.15
NGC2347	10.96	6.08	2.48	34.22	11.53	2.35	0.13	0.10	0.04	4.23	5.91	1.21
NGC2639	6.17	3.53	0.77	11.96	4.54	1.31	0.08	0.05	0.01	0.57	0.71	0.20
NGC2730	18.45	4.49	1.83	37.46	4.29	0.86	0.28	0.18	0.07	4.81	1.70	0.34
NGC2906	3.30	1.35	0.51	13.12	5.05	0.99	0.03	0.05	0.02	0.22	0.14	0.03
NGC2916	9.36	4.73	1.67	20.32	8.91	1.86	0.15	0.14	0.05	0.95	1.05	0.22
NGC3057	17.13	4.79	1.60	38.92	6.65	1.57	0.73	0.13	0.04	5.30	4.09	0.96
NGC3300	3.92	1.79	0.73	8.76	9.37	1.84	0.04	0.11	0.04	1.04	2.19	0.43
NGC3381	32.06	8.00	3.02	22.27	2.43	0.48	0.61	0.22	0.08	0.79	0.34	0.07
NGC3614	5.24	2.33	0.88	13.56	3.21	0.63	0.06	0.05	0.02	0.34	0.22	0.04
NGC3687	2.23	2.08	0.66	13.02	1.55	0.32	0.03	0.03	0.01	0.28	0.15	0.03
NGC4003	5.94	2.93	1.04	9.18	5.44	1.25	0.06	0.05	0.02	0.21	0.33	0.08
NGC4047	12.97	3.33	1.49	23.91	4.19	0.78	0.18	0.09	0.04	0.65	0.54	0.10
NGC4185	3.69	1.83	0.61	9.15	2.04	0.42	0.04	0.03	0.01	0.13	0.06	0.01
NGC4210	2.38	1.14	0.46	14.33	4.08	0.85	0.03	0.06	0.02	0.26	0.12	0.02
NGC4961	21.20	5.84	2.38	43.27	5.18	1.08	0.47	0.33	0.13	11.55	7.28	1.52
NGC5000	16.38	1.84	1.06	20.03	11.48	2.25	0.22	0.12	0.07	1.33	1.83	0.36
NGC5016	14.24	0.93	0.47	29.98	12.22	2.27	0.14	0.08	0.04	6.47	9.55	1.77
NGC5205	2.13	1.45	0.48	23.74	14.77	3.08	0.03	0.04	0.01	4.21	5.02	1.05

Table C.2 Continued.

NGC5320	5.90	2.14	0.81	16.92	4.88	0.98	0.06	0.05	0.02	0.50	0.51	0.10
NGC5378	1.44	1.67	0.56	7.59	3.68	0.79	0.02	0.02	0.01	0.15	0.11	0.02
NGC5406	1.96	2.06	0.84	9.91	3.16	0.66	0.02	0.01	0.01	0.15	0.07	0.01
NGC5480	31.18	6.47	2.44	31.94	3.54	0.69	0.75	0.38	0.14	2.49	1.43	0.28
NGC5614	3.99	0.47	0.09	4.63	0.56	0.28	0.04	0.02	0.00	0.07	0.09	0.04
NGC5656	11.46	8.39	2.53	22.36	3.64	0.78	0.17	0.14	0.04	0.86	0.65	0.14
NGC5735	4.54	0.80	0.36	11.71	3.96	0.79	0.07	0.06	0.03	0.38	0.26	0.05
NGC5772	4.16	2.67	0.81	12.08	1.78	0.41	0.04	0.03	0.01	0.21	0.13	0.03
NGC5829	16.16	5.48	3.16	41.30	8.23	1.61	0.17	0.11	0.07	6.72	4.51	0.88
NGC6004	9.35	3.52	1.02	13.04	2.33	0.50	0.13	0.08	0.02	0.29	0.21	0.04
NGC6032	11.34	7.26	3.25	32.87	20.83	4.25	0.12	0.13	0.06	5.65	6.08	1.24
NGC6154	3.44	1.18	0.39	8.06	4.03	0.90	0.04	0.02	0.01	0.14	0.10	0.02
NGC6186	16.69	2.55	1.47	9.97	2.64	0.52	0.20	0.13	0.08	0.23	0.22	0.04
NGC6278	1.53	1.01	0.26	4.62	4.84	1.14	0.01	0.03	0.01	0.10	0.17	0.04
NGC6941	5.25	2.51	1.03	12.44	10.32	1.92	0.06	0.06	0.03	0.58	1.09	0.20
NGC7321	3.98	0.88	0.39	15.08	5.49	1.14	0.05	0.06	0.03	0.42	0.46	0.10
NGC7489	30.37	4.61	2.66	50.70	15.92	2.86	0.54	0.23	0.13	13.71	10.51	1.89
NGC7625	22.81	5.37	2.19	20.80	9.85	1.83	0.44	0.17	0.07	0.53	0.48	0.09
NGC7653	8.87	4.25	1.61	25.56	5.23	1.03	0.13	0.09	0.03	1.43	0.88	0.17
NGC7691	15.68	3.65	1.83	53.93	13.64	2.67	0.24	0.11	0.06	6.60	4.62	0.91
NGC7716	6.26	4.96	1.43	17.66	4.88	1.04	0.08	0.09	0.03	0.67	0.50	0.11
NGC7738	25.48	11.17	5.59	11.72	6.79	1.33	0.37	0.26	0.13	0.42	0.73	0.14
NGC7819	30.97	8.09	2.86	24.36	7.33	1.73	0.49	0.26	0.09	2.58	1.68	0.40
UGC07012	18.46	6.16	2.51	39.98	5.11	1.20	0.33	0.14	0.06	5.42	4.52	1.07
UGC08234	2.54	1.58	0.71	11.11	11.05	2.30	0.02	0.05	0.02	1.61	1.91	0.40
UGC08733	17.40	0.98	0.40	23.36	4.57	1.00	0.37	0.14	0.06	2.32	2.23	0.49
UGC09067	12.31	3.50	2.02	30.68	9.41	2.05	0.18	0.14	0.08	6.29	6.95	1.52
UGC09291	10.49	1.31	0.58	18.67	6.78	1.33	0.17	0.10	0.05	0.95	1.01	0.20
UGC09476	13.54	0.75	0.33	19.09	2.65	0.51	0.22	0.08	0.04	0.52	0.22	0.04
UGC10796	36.53	4.20	2.10	26.90	7.05	1.66	2.98	1.67	0.83	3.05	3.42	0.81
UGC12224	10.39	1.81	0.81	30.26	18.19	3.27	0.15	0.09	0.04	4.53	6.14	1.10

Table C.3: Mean values ($\bar{x}$), standard deviation (σ), standard error of the mean ($\bar{\sigma}$), zero point (z_0), error of the zero point, gradient (γ) and error of the gradient for the following physical quantities, from left to right: luminosity-weighted stellar age of the bulge and disk, and mass-weighted stellar age of the bulge and disk, respectively.

Galaxy	Bulge $< t >_L$							Disk $< t >_L$							Bulge $< t >_M$							Disk $< t >_M$						
	$\bar{x}$	σ	$\bar{\sigma}$	z_0	z_0 err	γ	γ err	$\bar{x}$	σ	$\bar{\sigma}$	z_0	z_0 err	γ	γ err	$\bar{x}$	σ	$\bar{\sigma}$	z_0	z_0 err	γ	γ err	$\bar{x}$	σ	$\bar{\sigma}$	z_0	z_0 err	γ	γ err
IC0776	3.84	1.01	0.45	2.927	0.337	7.459	2.248	3.32	1.00	0.21	5.465	0.221	-2.261	0.216	6.12	1.56	0.70	4.379	0.496	14.178	3.305	6.67	1.26	0.27	9.230	0.354	-2.693	0.345
IC1256	8.73	0.77	0.39	9.105	0.007	-3.143	0.045	5.60	1.29	0.25	8.281	0.140	-2.040	0.097	11.23	0.65	0.33	11.712	0.007	-4.007	0.044	8.17	1.12	0.22	10.487	0.137	-1.762	0.095
IC4566	12.50	0.64	0.29	13.084	0.144	-3.526	0.715	7.79	1.72	0.35	11.714	0.182	-2.890	0.123	12.38	0.46	0.21	12.826	0.116	-2.716	0.576	9.31	1.29	0.26	12.214	0.175	-2.136	0.119
NGC0001	5.88	1.04	0.25	7.331	0.178	-1.551	0.163	4.56	0.67	0.17	7.309	0.491	-0.984	0.173	8.84	1.41	0.34	10.799	0.299	-2.099	0.273	7.92	0.49	0.13	7.971	0.573	-0.018	0.202
NGC0023	6.19	1.44	0.42	4.367	0.415	3.429	0.660	6.58	0.46	0.11	7.422	0.299	-0.435	0.150	10.42	1.20	0.35	10.424	0.667	-0.016	1.061	9.15	0.43	0.10	10.373	0.117	-0.632	0.059
NGC0160	10.56	2.19	0.61	13.822	0.245	-7.954	0.506	5.43	0.73	0.17	7.941	0.136	-1.707	0.090	10.87	1.56	0.43	13.172	0.216	-5.612	0.447	9.85	0.64	0.15	8.202	0.393	1.123	0.260
NGC0165	7.48	1.31	0.46	6.172	0.533	5.574	1.892	6.27	1.27	0.30	10.070	0.115	-3.421	0.099	10.11	0.55	0.19	10.358	0.284	-1.050	1.010	8.40	0.57	0.13	9.986	0.133	-1.431	0.114
NGC0171	10.16	1.76	0.49	12.661	0.336	-8.594	0.979	5.82	1.04	0.25	9.588	0.333	-3.605	0.310	10.81	1.34	0.37	12.615	0.327	-6.178	0.952	8.30	0.65	0.15	9.822	0.467	-1.456	0.434
NGC0180	8.91	2.37	0.97	10.266	1.643	-12.230	12.254	7.84	1.72	0.36	11.958	0.211	-5.475	0.262	11.84	2.04	0.83	13.543	1.206	-15.374	8.996	9.49	1.01	0.21	11.772	0.180	-3.03	0.222
NGC0214	10.10	1.39	0.57	11.754	0.289	-9.956	1.436	5.08	1.20	0.24	7.849	0.167	-2.312	0.129	11.80	0.73	0.30	12.663	0.159	-5.212	0.788	9.11	0.42	0.08	9.549	0.185	-0.37	0.144
NGC0237	6.07	0.74	0.30	6.548	0.185	-1.973	0.626	4.01	0.56	0.12	5.108	0.185	-0.684	0.108	9.67	0.48	0.19	9.670	0.111	-0.006	0.378	7.65	0.84	0.18	9.388	0.286	-1.077	0.166
NGC0257	7.22	1.17	0.41	8.657	0.104	-6.675	0.403	4.37	0.57	0.12	5.566	0.195	-1.026	0.157	10.42	0.76	0.27	11.177	0.295	-3.502	1.144	8.59	0.73	0.15	7.203	0.322	1.183	0.260
NGC0477	8.38	0.95	0.42	8.702	0.606	-2.613	3.989	5.22	1.46	0.30	8.529	0.145	-3.231	0.130	10.76	1.12	0.50	11.876	0.460	-8.988	3.028	7.88	0.89	0.18	9.667	0.206	-1.749	0.186
NGC0776	10.28	0.63	0.26	9.934	0.128	2.099	0.646	6.49	1.59	0.32	9.798	0.448	-2.820	0.354	11.84	0.42	0.17	12.176	0.084	-2.074	0.425	8.82	1.17	0.23	11.222	0.342	-2.046	0.271
NGC1093	9.88	1.55	0.59	11.930	0.107	-6.635	0.288	5.99	1.17	0.25	8.969	0.173	-1.653	0.090	10.93	1.09	0.41	12.348	0.131	-4.580	0.354	8.63	0.86	0.18	10.753	0.169	-1.179	0.088
NGC1645	10.45	1.49	0.47	12.485	0.296	-4.385	0.539	6.14	1.81	0.42	12.100	0.244	-3.045	0.120	10.67	1.37	0.43	12.563	0.248	-4.084	0.452	8.23	1.44	0.33	12.818	0.330	-2.345	0.162
NGC2253	8.34	0.74	0.28	8.879	0.284	-2.502	1.090	5.19	1.05	0.21	7.755	0.179	-1.867	0.122	10.63	1.10	0.41	12.063	0.148	-6.630	0.570	8.94	0.87	0.17	10.726	0.281	-1.299	0.192
NGC2347	10.64	1.68	0.68	12.776	0.078	-9.522	0.289	5.50	1.89	0.39	10.094	0.120	-2.931	0.071	11.69	0.69	0.28	12.505	0.050	-3.630	0.186	8.92	1.58	0.32	12.719	0.187	-2.423	0.111
NGC2639	10.63	1.62	0.35	13.059	0.237	-2.818	0.235	5.22	1.55	0.45	15.965	0.834	-4.701	0.362	11.23	0.94	0.21	12.587	0.169	-1.569	0.167	6.38	1.47	0.42	16.352	1.118	-4.363	0.485
NGC2730	4.85	0.54	0.22	4.665	0.121	1.367	0.738	3.14	0.45	0.09	3.739	0.190	-0.620	0.181	8.21	0.45	0.18	8.271	0.074	-0.423	0.452	6.65	0.63	0.13	7.343	0.301	-0.716	0.287
NGC2906	11.57	0.65	0.24	12.263	0.146	-3.370	0.593	7.49	0.83	0.16	8.194	0.425	-0.526	0.297	11.88	0.45	0.17	12.347	0.053	-2.286	0.216	9.40	0.65	0.13	10.835	0.166	-1.074	0.116
NGC2916	8.77	1.25	0.44	9.662	0.707	-4.970	3.293	5.68	1.10	0.23	8.367	0.317	-2.761	0.307	9.55	1.12	0.39	10.136	0.704	-3.273	3.281	8.71	0.73	0.15	8.795	0.447	-0.088	0.443
NGC3057	3.00	0.49	0.16	2.478	0.108	2.580	0.451	2.66	0.56	0.13	4.305	0.154	-1.874	0.167	5.87	0.49	0.16	5.433	0.121	2.169	0.507	6.17	0.60	0.14	7.781	0.258	-1.83	0.281
NGC3300	11.64	1.81	0.74	13.605	0.762	-8.643	2.763	7.98	1.13	0.22	10.412	0.235	-1.445	0.129	11.93	1.28	0.52	13.227	0.593	-5.710	2.150	9.03	0.74	0.15	10.588	0.150	-0.926	0.082
NGC3381	4.64	0.61	0.23	5.068	0.114	-2.674	0.596	3.29	0.47	0.09	4.408	0.045	-1.073	0.040	8.49	0.91	0.34	9.509	0.267	-6.375	1.391	6.39	0.61	0.12	7.819	0.090	-1.373	0.081
NGC3614	7.75	1.00	0.38	9.000	0.079	-11.975	0.626	5.44	0.81	0.16	7.421	0.073	-2.911	0.100	9.07	1.33	0.50	10.809	0.143	-16.690	1.138	7.83	0.46	0.09	8.656	0.129	-1.221	0.178
NGC3687	9.22	0.93	0.29	10.337	0.239	-3.813	0.688	5.45	1.29	0.27	9.364	0.120	-2.862	0.084	9.97	0.73	0.23	10.814	0.201	-2.869	0.579	7.77	1.25	0.26	11.483	0.213	-2.714	0.149
NGC4003	8.44	0.70	0.25	8.965	0.177	-1.287	0.365	6.33	0.80	0.18	8.543	0.181	-1.121	0.087	10.45	0.54	0.19	10.870	0.208	-1.021	0.427	8.15	0.85	0.19	10.568	0.172	-1.221	0.083
NGC4047	8.18	1.08	0.48	9.297	0.022	-7.669	0.125	5.68	0.65	0.12	6.843	0.153	-0.842	0.101	10.71	0.80	0.36	11.513	0.074	-5.537	0.417	8.97	0.93	0.17	10.789	0.195	-1.311	0.129
NGC4185	11.09	0.98	0.33	12.454	0.092	-8.050	0.455	8.42	0.99	0.21	11.234	0.112	-3.317	0.125	11.16	0.73	0.24	12.114	0.152	-5.625	0.755	9.93	0.48	0.10	11.190	0.081	-1.487	0.091
NGC4210	9.89	0.87	0.35	10.539	0.471	-4.871	2.937	6.35	1.12	0.23	8.979	0.201	-2.919	0.208	9.96	0.77	0.32	10.602	0.385	-4.830	2.399	8.72	0.36	0.07	9.360	0.097	-0.711	0.101
NGC4961	4.40	0.84	0.34	5.226	0.219	-3.455	0.761	2.64	0.62	0.13	3.968	0.157	-0.820	0.090	8.91	0.83	0.34	9.759	0.199	-3.554	0.693	6.03	1.29	0.27	8.597	0.442	-1.588	0.255
NGC5000	9.08	1.39	0.80	7.974	0.113	14.027	1.113	7.18	2.30	0.45	11.706	0.229	-3.704	0.169	11.34	0.69	0.40	10.876	0.016	5.852	0.161	9.46	1.21	0.24	11.830	0.130	-1.94	0.096
NGC5016	8.97	0.85	0.42	9.567	0.023	-5.860	0.179	5.30	1.87	0.35	9.185	0.138	-3.197	0.103	10.56	0.62	0.31	10.922	0.017	-3.595	0.138	7.85	2.00	0.37	11.874	0.264	-3.314	0.197
NGC5205	7.77	1.31	0.44	9.409	0.353	-5.911	1.070	4.53	1.26	0.26	8.075	0.188	-2.561	0.129	8.84	1.37	0.46	10.487	0.441	-5.964	1.339	7.21	0.61	0.13	8.303	0.284	-0.786	0.195
NGC5320	9.35	1.32	0.50	11.040	0.176	-10.559	0.915	5.60	1.60	0.32	9.664	0.097	-4.006	0.090	10.70	0.99	0.37	11.949	0.142	-7.810	0.739	8.36	1.09	0.22	11.076	0.119	-2.672	0.110
NGC5378	11.98	0.90	0.30	13.164	0.157	-5.541	0.614	8.52	1.79	0.38	13.841	0.073	-5.090	0.066	11.68	0.69	0.23	12.596	0.115	-4.250	0.451	9.21	1.15	0.24	12.597	0.077	-3.237	0.070
NGC5406	12.90	0.53	0.22	13.378	0.087	-3.100	0.468	8.54	1.53	0.32	11.952	0.398	-3.252	0.353	12.59	0.38	0.16	13.007	0.107	-2.686	0.570	10.13	0.62	0.13	11.239	0.246	-1.054	0.219
NGC5480	3.90	0.92	0.35	2.918	0.240	6.081	1.234	3.81	0.30	0.06	4.239	0.083	-0.406	0.074	7.95	1.58	0.60	6.423	0.792	9.421	4.075	7.93	0.35	0.07	7.802	0.132	0.127	0.117
NGC5614	9.69	1.78	0.35	12.278	0.309	-2.737	0.280	7.14	0.82	0.41	12.883	0.394	-2.760	0.189	10.61	1.24	0.24	12.558	0.133	-2.057	0.121	8.50	0.71	0.36	14.924	0.476	-3.086	0.228
NGC5656	7.22	1.11	0.34	8.766	0.123	-3.732	0.251	4.87	0.34	0.07	5.517	0.124	-0.361	0.067	9.80	0.66	0.20	10.658	0.085	-2.056	0.172	8.18	0.28	0.06	8.695	0.114	-0.286	0.061

Table C.3 Continued.

NGC5735	9.67	1.04	0.47	10.779	0.167	-10.366	1.278	5.45	1.22	0.24	8.024	0.239	-2.832	0.242	10.84	0.95	0.42	11.911	0.164	-10.033	1.253	7.84	0.79	0.16	8.908	0.321	-1.171	0.325
NGC5772	12.27	1.55	0.47	14.377	0.328	-5.624	0.742	7.82	0.99	0.23	11.116	0.144	-2.202	0.093	12.20	0.80	0.24	13.283	0.156	-2.892	0.353	9.75	0.56	0.13	11.595	0.054	-1.231	0.035
NGC5829	6.55	1.16	0.67	7.184	0.018	-10.005	0.218	3.27	0.95	0.19	5.021	0.150	-1.791	0.138	9.77	0.87	0.50	10.251	0.003	-7.600	0.041	7.07	1.27	0.25	9.319	0.272	-2.304	0.251
NGC6004	8.21	1.07	0.31	9.524	0.284	-5.044	0.924	6.27	0.27	0.06	6.174	0.120	0.091	0.109	10.45	1.15	0.33	12.160	0.075	-6.560	0.243	8.98	0.48	0.10	7.594	0.089	1.307	0.080
NGC6032	9.52	0.94	0.42	8.876	0.432	4.542	2.478	6.25	1.74	0.35	10.069	0.296	-3.251	0.232	10.81	0.50	0.22	10.950	0.310	-0.968	1.777	8.76	0.64	0.13	9.260	0.317	-0.425	0.249
NGC6154	12.17	1.15	0.38	13.598	0.326	-4.455	0.856	7.25	1.82	0.41	12.645	0.416	-3.642	0.268	11.87	0.86	0.29	12.947	0.267	-3.363	0.701	8.69	1.04	0.23	11.643	0.294	-1.993	0.189
NGC6186	9.03	0.99	0.57	9.393	0.033	-4.294	0.302	7.00	0.76	0.15	8.326	0.147	-1.022	0.102	11.46	0.56	0.33	11.422	0.040	0.423	0.369	8.77	0.94	0.18	10.495	0.170	-1.323	0.118
NGC6278	12.87	0.99	0.26	14.305	0.127	-1.828	0.137	10.86	0.97	0.23	14.226	0.610	-1.275	0.226	12.13	0.77	0.20	13.276	0.123	-1.454	0.133	10.83	0.42	0.10	11.974	0.283	-0.432	0.105
NGC6941	12.10	0.73	0.30	12.827	0.174	-4.777	0.947	7.91	2.22	0.41	12.992	0.226	-4.186	0.172	12.23	0.64	0.26	12.947	0.205	-4.711	1.113	9.66	1.08	0.20	11.993	0.191	-1.925	0.145
NGC7321	11.13	0.65	0.29	11.292	0.364	-1.000	1.798	6.15	1.47	0.31	9.372	0.284	-2.432	0.198	11.89	0.44	0.20	12.065	0.241	-1.067	1.188	8.72	1.17	0.24	11.280	0.234	-1.934	0.163
NGC7489	6.84	0.97	0.56	7.171	0.005	-4.847	0.054	3.27	1.50	0.27	6.083	0.184	-2.300	0.134	11.47	0.94	0.54	12.139	0.025	-9.821	0.280	7.20	1.71	0.31	10.141	0.345	-2.399	0.252
NGC7625	4.75	0.82	0.33	5.534	0.108	-3.910	0.448	5.19	0.64	0.12	4.179	0.217	0.631	0.125	9.53	1.01	0.41	10.617	0.329	-5.422	1.360	8.48	0.62	0.11	9.065	0.261	-0.368	0.151
NGC7653	7.34	1.24	0.47	8.664	0.466	-5.369	1.575	4.01	0.86	0.17	6.054	0.118	-1.276	0.069	9.30	1.15	0.43	10.130	0.661	-3.364	2.233	7.29	0.58	0.11	8.181	0.229	-0.557	0.133
NGC7691	5.34	0.79	0.39	5.932	0.108	-8.214	1.213	3.57	0.35	0.07	4.048	0.097	-0.601	0.112	7.62	0.86	0.43	8.360	0.156	-10.283	1.743	7.95	0.87	0.17	6.296	0.181	2.096	0.209
NGC7716	9.17	0.93	0.27	10.307	0.228	-2.777	0.471	5.63	1.41	0.30	10.421	0.147	-2.858	0.084	10.21	0.77	0.22	11.068	0.233	-2.085	0.483	7.92	0.88	0.19	10.861	0.114	-1.755	0.065
NGC7738	8.23	1.56	0.78	6.689	0.061	10.187	0.324	7.88	1.58	0.31	11.050	0.255	-1.905	0.139	11.82	0.41	0.21	11.726	0.156	0.620	0.824	9.28	1.12	0.22	11.394	0.256	-1.269	0.140
NGC7819	5.10	0.69	0.24	4.746	0.291	1.440	0.985	3.92	0.61	0.14	5.638	0.125	-1.474	0.102	8.76	1.01	0.36	9.345	0.584	-2.371	1.978	6.61	0.38	0.09	6.841	0.230	-0.197	0.188
UGC07012	3.53	0.51	0.21	3.600	0.110	-0.246	0.334	2.44	0.57	0.13	3.856	0.097	-0.895	0.058	6.66	0.61	0.25	6.487	0.284	0.638	0.858	5.74	0.76	0.18	7.698	0.118	-1.237	0.070
UGC08234	7.16	1.15	0.51	8.163	0.469	-2.812	1.073	5.82	0.42	0.09	5.824	0.199	-0.001	0.064	10.16	1.77	0.79	12.039	0.725	-5.285	1.660	7.53	0.59	0.12	7.035	0.264	0.175	0.086
UGC08733	3.30	0.55	0.22	2.961	0.084	2.382	0.495	2.69	0.53	0.12	3.887	0.125	-1.334	0.130	5.84	0.49	0.20	5.851	0.161	-0.095	0.948	4.78	0.59	0.13	6.020	0.289	-1.387	0.197
UGC09067	8.95	0.92	0.53	9.192	0.005	-2.035	0.030	4.97	1.81	0.39	8.640	0.212	-2.397	0.126	11.36	0.54	0.31	11.529	0.012	-1.466	0.078	8.02	2.12	0.46	12.259	0.335	-2.77	0.198
UGC09291	5.80	1.19	0.53	7.045	0.387	-11.645	2.945	4.28	0.66	0.13	5.658	0.080	-1.468	0.078	8.13	1.13	0.50	9.321	0.352	-11.112	2.680	6.88	0.39	0.08	7.363	0.129	-0.515	0.126
UGC09476	6.23	0.69	0.31	6.760	0.092	-4.650	0.660	4.32	0.67	0.13	5.645	0.138	-1.296	0.124	8.74	0.71	0.32	9.381	0.123	-5.693	0.889	7.40	0.80	0.15	8.960	0.187	-1.533	0.168
UGC10796	1.71	0.91	0.46	0.849	0.235	6.307	1.379	2.39	0.34	0.08	2.255	0.154	0.120	0.125	4.95	1.15	0.57	3.861	0.182	7.968	1.069	4.58	0.55	0.13	4.494	0.308	0.075	0.250
UGC12224	6.09	0.62	0.28	6.538	0.072	-5.005	0.655	4.14	1.46	0.26	7.269	0.130	-3.465	0.131	7.75	0.62	0.28	8.181	0.073	-4.819	0.665	7.13	0.55	0.10	7.971	0.167	-0.93	0.169